This is to certify that the

dissertation entitled

Processing, Microstructure and Thermomechanical
Behavior of Superelastic Nickel-Titanium Thin Films
Sputter-Deposited at Elevated Temperatures

presented by

Li Hou

has been accepted towards fulfillment
of the requirements for

Ph.D. degree in Materials Science

Major professor

Date 4/17/98

PROCESSING, MICROSTRUCTURE AND THERMOMECHANICAL BEHAVIOR OF SUPERELASTIC NICKEL-TITANIUM THIN FILMS SPUTTER-DEPOSITED AT ELEVATED TEMPERATURES

By

Li Hou

A DISSERTATION

Submitted to
Michigan State University
in partial fulfillment of the requirements
for the degree of

DOCTOR OF PHILOSOPHY

Department of Materials Science and Mechanics

1998

ABSTRACT

PROCESSING, MICROSTRUCTURE AND THERMOMECHANICAL BEHAVIOR OF SUPERELASTIC NICKEL-TITANIUM THIN FILMS SPUTTER-DEPOSITED AT ELEVATED TEMPERATURES

By

Li Hou

Near-equiatomic NiTi is capable of fully recoverable strains associated with the formation and reversion of a stress-induced martensite phase from a B2 (CsCl) parent phase. Recently, sputter-deposited NiTi thin films have drawn attention for potential application to microactuators in microelectromechanical systems (MEMS). As-sputtered NiTi films are amorphous when deposition temperature is below $0.4T_m$ and an additional thermal treatment is required to achieve the crystalline B2 phase. The objective of this study was to investigate the microstructure and thermomechanical behavior of crystalline NiTi films where were directly produced by sputter deposition at elevated substrate temperatures.

A series of NiTi films were sputter deposited at various substrate temperatures between 573 K and 773 K using a $Ni_{51}Ti_{49}$ alloy cathode. In order to study the effects of grain boundaries and precipitates on deformation behavior, some as-sputtered crystalline films were given a thermal treatment to form diverse microstructures which were systematically examined by transmission electron microscopy. Electron microdiffraction and XRD methods were employed to identify precipitate structures. Phase transformation characteristics were obtained by electrical resistivity and DSC measurements. Stress-strain experiments were conducted in uniaxial tension on free-standing NiTi films. Finally, fracture surfaces and the microstructure of deformed films were examined by TEM and SEM for the purpose of verifying structural stability.

A fully crystallized NiTi film could be produced at a deposition temperature of 623 K which is about 150 K lower than the minimum temperature to form B2 phase by post-deposition annealing in a reasonable time. Crystalline films displayed microstructures consisting of very fine columnar B2 grains with 0.1-0.3 μm in-plane diameter and dispersed Ni_4Ti_3 particles. Films deposited at 703 K and 723 K exhibited well-defined transformational superelasticity. The stability of microstructure against permanent deformation was found to result from the combination of a fine-grained structure with moderate-sized transgranular precipitates. As a practical demonstration of applicability to MEMS systems, a prototype electrically-excitable NiTi/polyimide actuating element was fabricated by hot-substrate deposition and a pattern-etch technique.

To my Wife and Daughter with Appreciation

ACKNOWLEDGMENTS

I am deeply grateful to Dr. David S. Grummon, my major professor, for his advice and continuing support. Dr. Thomas J. Pence is greatly acknowledged for sharing invaluable ideals in our NiTi thin film group meetings. Sincere appreciation is expressed to my other guidance committee members: Dr. Kali Mukherjee and Dr. Subhendra D. Mahanti for their important comments and valuable suggestions.

I would like to thank Dr. Andre Y. Lee for his generosity in providing liberal access to the Minimat™ microtensile apparatus. I also like to thank Dr. John Mansfield in University of Michigan for his instruction of manipulating Jeol 2000 FX TEM in his laboratory.

Mr. Syed Shahzaman is acknowledged for his kindly help in Photolithography Laboratory at Dept. of Electrical Engineering, Michigan State University. I am grateful to my colleagues in the NiTi Thin Film Group, Dr. Xiaochuang Wu for his assistance in using Mark™ finite element analysis software, and Mr. Jinping Zhang for his help in characterizing the X-ray spectra of precipitates.

Finally, I would like to thank my wife, Jiefei, for her support and patience during the preparation of this work.

TABLE OF CONTENTS

LIST OF TABLES viii

LIST OF FIGURES ix

INTRODUCTION 1

CHAPTER 1. BACKGROUND 5

1.1. Thermoelastic Martensitic Transformation 6
  1.1.1. General Characteristics 6
  1.1.2. Crystallography of Martensitic Transformation 8
  1.1.3. Frictional Work and Stored Elastic Energy 10
  1.1.4. Shape Memory and Superelasticity 13
  1.1.5. The Clausius-Clapeyron Equation for Uniaxial Stress 14

1.2. Transformations in NiTi Alloys 17
  1.2.1. Martensitic and R-Phase Transformations 17
  1.2.2. Diffusional Transformations 21
  1.2.3. The Effects on Phase Transformations 23

1.3. Deformation of Metallic Crystals 26
  1.3.1. Role of Grain Boundaries in Plastic Deformation 26
  1.3.2. Precipitation Hardening 29

1.4. Deformation of NiTi Alloys 31
  1.4.1. Recoverable Tensile Strains 31
  1.4.2. Slip Deformation 37
  1.4.3. Factors Influencing SME and Superelasticity 39

1.5. Formation and Structures of Thin Films 42
  1.5.1. Sputter Deposition 42
  1.5.2. Influence of Temperature on Phase Formation 44
  1.5.3. Structural Zone Models 46
  1.5.4. The Secondary Grain Growth in Thin Films 48

1.6. Studies on NiTi Films and the Purpose of Present Work 49

CHAPTER 2. EXPERIMENTAL METHODS 58

2.1. Sputter Deposition Facility 58

2.2. Fabrication of NiTi/Polyimide Prototype Microactuator 60
  2.2.1. Crystallizing NiTi by Post-Deposition Annealing 60
  2.2.2. Metallization of Kapton by Hot-Substrate Deposition 62
  2.2.3. Photolithography Process 64

2.3. Preparation of Free-Standing NiTi Films 65
  2.3.1. Sputter Deposition Procedure 65
  2.3.2. Thermal Treatment of As-Sputtered NiTi Films 66

2.4. Characterization of NiTi Films 67
  2.4.1. Energy Dispersive X-Ray Microanalysis (EDX) 67
  2.4.2. Film Thickness Measurement 68
  2.4.3. Electrical Resistimetry 68
  2.4.4. Differential Scanning Calorimetry (DSC) 69
  2.4.5. X-Ray Diffraction (XRD) 69
  2.4.6. Transmission Electron Microscopy (TEM) 69
  2.4.7. Tensile Tests 72
  2.4.8. Scanning Electron Microscopy (SEM) 74

CHAPTER 3. RESULTS AND DISCUSSION 75

3.1. Microstructure of As-Sputtered NiTi Films 75
  3.1.1. TEM Observation 75
  3.1.2. Thin Film Microstructure: Discussion 78
  3.1.3. Formation of Texture 81
  3.1.4. Growth of Precipitates 82

3.2. Microstructure of Annealed NiTi Films 86
  3.2.1. Morphology 86
  3.2.2. Structure of Precipitates in Annealed Films 88

3.3. Phase Transformation Characteristics 91
  3.3.1. Phase Transformations in As-Sputtered Films 91
  3.3.2. Phase Transformations in Annealed Films 94

3.4. Deformation Behavior of NiTi Films 96
  3.4.1. Ultimate Elongation of NiTi Films 96
  3.4.2. Isothermal Stress-Strain Curves of NiTi Films 97
  3.4.3. Classification of Stress-Strain Curves 99
  3.4.4. Thermomechanical Behavior of NiTi Films 101
  3.4.5. Transformational Superelastisity 104

3.5. Fractography of NiTi Films 107

CONCLUSIONS 109

APPENDICES 247

A.1. Electrically-Excitable Shape-Memory Actuator 247
A.2. Thermodynamic Analysis by Jacobian Notation 251

BIBLIOGRAPHY 254

LIST OF TABLES

Table 1-1 Austenite-to-martensite lattice correspondences of NiTi [after Matsumoto *et al.* 1978]. 112

Table 1-2 The 24 habit plane variants and related correspondence variant-combinations. The habit plane indices were calculated from the phenomenological crystallographic theory, and correspond to the experimental data for solution-treated specimens [after Miyazaki *et al.*, 1978]. 113

Table 2-1 Sputter-deposition conditions and resultant film compositions. The notation 'H---' is used in the present work where the 'H' signifies 'hot deposition' and three digits signify the substrate temperature of deposition in Kelvin. The substrate for all films were quartz except for film H698 which was deposited on Kapton film. 114

Table 2-2 Heat-treatment conditions of annealed NiTi films. For annealed NiTi films, the notation 'A-' is used where the 'A' represents 'annealing' and a digit designates the detailed heat-treatment path as indicated in the table. 115

Table 3-1 Summary of microstructures of as-deposited NiTi films. In the table, D_{B2}, D_{ptt} and PS, respectively, designate the in-plane grain diameter of the B2, the diameter of precipitates in longitudinal direction, and precipitate spacing. 116

Table 3-2 Summary of NiTi matrix and precipitate morphologies of annealed NiTi films. In the table, D_{B2}, D_{ptt} and PS, respectively, designate the in-plane grain diameter of the B2, the diameter of precipitates in longitudinal direction, and precipitate spacing. 117

Table 3-3 Phase transformation temperatures of as-deposited NiTi films. 118

Table 3-4 Transformation characteristics of the film H703 obtained from electrical resistivity and DSC measurements. 119

Table 3-5 Phase transformation temperatures of annealed NiTi films. 120

LIST OF FIGURES

Figure 1-1	Schematic drawings of a two-variant matensitic transformation [Chang, 1993]. (a) The lattices of the parent phase and the martensite. (b) The Bain distortion, which converts the parent phase into the martensite, does not yield an undistorted plane associated with the habit plane. (c) A lattice invariant shear, through a reversible manner of twinning, produces an undistorted plane. (d) The rigid body rotation, which brings the transformed lattice back, so that the interface is in contact with the parent. lattice	121
Figure 1-2	A schematic representation showing the influence of frictional work and stored elastic energy on thermoelastic martensitic transformations [modified from Salzbrenner and Cohen, 1979].	122
Figure 1-3	Schematic drawings summaries the influence of frictional force and stored elastic energy on thermoelastic martensite transformations.	123
Figure 1-4	Upper figure: schematic drawing of shape-memory effect: (*a-c*) the deformation is accomplished by detwinning or reorientation of variants in martensite lattice. M is twinned martensite and M' is deformed martensite. Bottom figure: (*a-c*) the deformation is accomplished by transformational twining in the austenite.	124
Figure 1-5	The steps illustrating the transition from B2 to B19' lattices [modified from Hehemann and Sandrock, 1971]. (a) B2 lattices; (b-c) an orthorhombic distortion; (c-d) a monoclinic shear; (e) two shuffle models.	125
Figure 1-6	An illustration representing geometry relationships between planes and directions in twinning [Reed-Hill, 1964].	126
Figure 1-7	The self-accommodation morphology of the monoclinic martensite, and a model describing crystallographic relationships between the martensite variants in the triangular morphology [Miyazaki *et al.* 1989].	127
Figure 1-8	The schematic diagram showing physical property changes associated with R-phase and martesitic transformation: (a) lattice distortion, (b) electrical resistivity change, and (c) latent heat exchange.	128
Figure 1-9	Self-accommodating morphology and corresponding schematic variants-combination of rhombohedral phase proposed by Miyazaki and Wayman [1988].	129

Figure 1-10 (a) Ni-Ti equilibrium phase diagram proposed by Massalski [1987]; (b) Ni-Ti phase diagram in the vicinity of stoichiometric composition proposed by Wasilewski *et al.* [1971]. 130

Figure 1-11 Isothermal time-temperature-transformation (TTT) diagram for $Ni_{52}Ti_{48}$ alloy [Nishida, Wayman and Honma, 1986]. 131

Figure 1-12 The effect of Ni-concentration on the electrical resistivity vs. temperature curves for NiTi alloys quenched from 1073 K [Nishida and Honma, 1984]. The M_s temperature decreases rapidly with the increase of nickel content. 132

Figure 1-13 Electrical resistivity vs. temperature curves [Wu, Lin and Chou, 1989], of $Ni_{51}Ti_{49}$ alloy aged at 673 K after a 1073 K, 2 hour solution-treatment for various times, showing the effects of aging on M_s temperatures. 133

Figure 1-14 The effect of specimen thickness on the normalized flow stress in polycrystalline (a) Al, (b) Cu, (c) Cu-13Al (at.%), and (d) Fe [Miyazaki, Shibata and Fujita, 1979]. 134

Figure 1-15 Three types of crystallographic relationships between the lattice of the precipitate and the lattice of the matrix [Hirsch *et al.*, 1977]. (a) coherent with negative misfit; (b) semi-coherent, and (c) incoherent. 135

Figure 1-16 Interactions between dislocations and precipitates. (a) In lightly aged alloys, the closely spaced stress fields make the dislocation unable to bend between the particles. The dislocation has to move out of its slip plane by climbing or cross-slipping. (b) In over-aged alloys, the particles are much wider apart. The dislocation can bend around each precipitate and leaving dislocation loops [Orowan, 1948]. (c) A schematic representation showing sheared Ni_3Al particles by passing dislocations in a Ni-19% Cr-6% Al alloy after 2 % deformation [based on Gleiter and Hornbogen, 1965]. 136

Figure 1-17 A diagram schematically illustrating an idealized deformation route from a B2 single crystal to a B19' single crystal where the transformation twinning and detwinning of martensite are well separated. (a-b) The martensitic transformation proceeds through the movement of parent/martensite interface. (b-c) The deformation is realized by the coalescence of favorable twin variants with respect to applied stress. 137

Figure 1-18 The orientation dependence of recoverable tensile strain for NiTi single crystals in B2-to-B19' transformation: (a) The values predicted from the lattice deformation matrix [Saburi and Nenno, 1981]. (b) The measured values from solution-treated single crystals [Miyazaki *et al.* 1984]. Numbers in parentheses indicate the measured results and contour lines represent predicted values. 138

Figure 1-19 (a) The orientation dependence of recoverable strain for B2-to-R transition at a temperature of (T_R - 35) K. Solid circles indicate the experimental data, whereas contour lines indicate calculated values; (b) The temperature dependence of the recoverable strain for various orientations. The recoverable strain in all directions increases gradually as temperature decreases from T_R [Miyazaki, Kimura and Otsuka, 1988]. 139

Figure 1-20 (a) The effect of tension cycling on superelasicity characteristics in $Ni_{49.5}Ti_{50.5}$ alloy [Miyazaki *et al* 1986]; (b) The effect of grain size on superelasticity in $Ni_{50.5}Ti_{49.5}$ alloy [Saburi, Yoshida and Nenno, 1984]. 140

Figure 1-21 Schematic representation of (a) planar diode sputter deposition [modified from Thornton, 1982], and (b) planar magnetron [modified from Ahmed, 1987]. 141

Figure 1-22 A schematic illustration of the effect of substrate temperature on phase formation for a hypothetical polymorphic material [Thornton, 1977]. 142

Figure 1-23 Structural zone models for physical vapor deposition processes. (a) The model proposed by Movchan and Demchishin [1969] for electron beam evaporations; (b) The model proposed by Thornton [1974] for sputtered metal coatings. 143

Figure 1-24 A computer modeling of film growth using 2D hard spheres by Muller [1985]. (a-c) show the influence of temperature on packing density of films. (d) displays that the temperature effects packing density while the deposition rate changes the transition temperature of density-to-unity density. 144

Figure 1-25 Schematic microstructures and grain distributions for thin films undergoing secondary grain growth [Thompson, 1990]. (a) Microstructure before the secondary grain growth occurs. (b) Intermediate stage in which the grain sizes are bimodelly distributed. (c) After the secondary grain growth microstructure shows crystallographic (fiber) texture. 145

Figure 1-26 Schematic drawing of two devices [Johnson, 1992] using the shape-memory effect of NiTi thin films: (a) a microvalve, and (b) a microactuator. 146

Figure 2-1 Photograph of magnetron sputter machine developed for this study. 147

Figure 2-2 Schematic diagram of magnetron sputter system developed for this study. 148

Figure 2-3 The weight loss characteristics of Kapton in air and helium at a heating rate of 3 K/min [Product Bulletins, DuPont, 1993]. 149

Figure 2-4 Differential scanning calorimetry (DSC) curves of sputter-deposited binary and ternary NiTi films at a heating rate of 20 K/

min showing the crystallization temperature. 150

Figure 2-5 Experimental set-up for *in situ* observation of electrical resistivity change in crystallization annealing of NiTi/Kapton laminate. 151

Figure 2-6 The diagram showing the electrical resistivity of NiTi film as a function of temperature during crystallization annealing treatment at a heating rate of 6.7 K/min. 152

Figure 2-7 Residual gas pressure vs. temperature curves of Kapton film at a heat-up rate of 5 K/min. 153

Figure 2-8 Schematic drawings of substrate heating devices which have been tested in this study. (a) A conventional substrate holder with a heater situated under the substrate. (b) A heating device consists of four 625 watt quartz lamps clustered around the sputter source to irradiate the substrate. 154

Figure 2-9 Schematic illustration showing the exploded view of two-sided substrate heating device. 155

Figure 2-10 A patterning-etching process for fabrication of NiTi/polyimide actuator elements. 156

Figure 2-11 Pattern for making eight NiTi/polyimide actuator elements. 157

Figure 2-12 A plot of substrate temperature and base pressure vs. time for a typical deposition run ($T = 670$ K). 158

Figure 2-13 A quartz-tube vacuum furnace used for heat-treatment of NiTi films. 159

Figure 2-14 A drawing illustrating the preparation of TEM disks. Three sampling locations along the depth of the NiTi thin films could be obtained by a masking technique. 160

Figure 2-15 (a) The reciprocal lattice of the B2 structure in [110] zone. (b) The geometry for calculating the positions of diffracted arcs upon tilting. Where φ is the angle between tilting axis and the arcs in the image plane, θ is the tilting angle of the specimen, d is the distance between the zero-order reciprocal rings and the higher-order reciprocal rings and R is the radius of arcs in the image plane. 161

Figure 2-16 Schematic illustration of tensile test apparatus for evaluating thin NiTi films at various temperatures. 162

Figure 2-17 Finite element grid for analysis of rectangular thin film tensile specimens. 163

Figure 2-18 A contour map obtained from the finite element analysis showing the maximal principal stress of thin film tensile specimen. It can be seen that the maximal principal stress reaches the maximum at edges near the ends of the gauge section. 164

Figure 2-19 A plot of the number of samples fractured versus the normalized x-position where the fracture occurred. Each number is collected from the interval of $(x, x + 0.05)$. 165

Figure 3-1 TEM bright-field (BF) image in (a) showing a completely featureless structure, and the associated selected area diffraction pattern (SADP) in (b) showing a broad, diffuse halo pattern which are normally observed in the amorphous materials. The micrographs were taken from the midplane of the film H573 at a tilt of 0°. 166

Figure 3-2 TEM BF image in (a) and the associated SADP in (b), taken from the interface of the film H598 at a tilt of 0°, showing the amorphous structure. 167

Figure 3-3 TEM BF image and the associated SADP taken from the midplane of the film H598 at a tilt of 0°. The SADP reveals a single-crystal diffraction pattern in the $[110]_{B2}$ zone together with a superimposed diffuse halo pattern scattered from the amorphous background. This initial crystallite has an in-plane size greater than 1 μm. 168

Figure 3-4 TEM BF images and the associated SADP's taken from the surface of the film H598. The BF image (a) and (d), respectively, were recorded at a tilt of 0 and 45°. Elongated grain images in (d) suggests a columnar grain structure. The SADP (b) and (c) were recorded at a tilt of 0 and 30°, respectively, showing a strong (110)fiber-texture. The non-even intensities of the diffraction rings in (b) reflect the restricted in-plane grain orientations. 169

Figure 3-5 TEM BF image and the associated SADP's taken from the interface of the film H623. The SADP (b) and (c) were recorded at a tilt of 0 and 30°, respectively, showing a strong (110) fiber-texture. 171

Figure 3-6 TEM BF images and the associated SADP's taken from the midplane of the film H623. The BF image (a) and (d), respectively, were recorded at a tilt of 0 and 45°. Elongated grain images in (d) implies a columnar grain structure. The SADP (b) and (c) were recorded at a tilt of 0 and 30°, respectively, showing a strong (110) fiber- texture. 172

Figure 3-7 TEM BF image and the associated SADP's taken from the surface of the film H623. The SADP (b) and (c) were recorded at a tilt of 0 and 30°, respectively, showing a strong (110) fiber-texture. 174

Figure 3-8 TEM BF image and the associated SADP's taken from the interface of the film H673. The lenticular precipitates in (a) can be distinguished (indicated by arrow). The SADP (b) and (c) were recorded at a tilt of 0 and 30°, respectively, showing a strong (110) fiber-texture. 175

Figure 3-9 TEM BF images and the associated SADP's taken from the midplane of the film H673. The BF image (a) and (d), respectively, were recorded at a tilt of 0 and 45°. A precipitate particle displays a perfect 'butterfly' shape of the image contrast as indicated by the arrow. Again, elongated grain images in (d) implies a columnar grain structure. The SADP (b) and (c) were recorded at a tilt of 0 and 30°, respectively, showing a strong (110) fiber-texture. 176

Figure 3-10 TEM BF image taken from the surface of the film H673. 178

Figure 3-11 (a) The high magnification image of precipitate with 'butterfly' shaped contrast. The strain fields around Ni_4Ti_3 particles come from the lattice mismatch between particles and B2 matrix. (b) The habit plane of precipitate is $\{111\}_{B2}$ and the maximum mismatch of -2.9 % is along the normal to the precipitate disk. This minus value indicates a tensile strain perpendicular to the precipitate disk [Kainuma and Matsumoto, 1988]. 179

Figure 3-12 TEM BF image and the associated SADP's taken from the interface of the film H723. Extremely fine grains, 25 nm in diameter, were nucleated on very thin initial amorphous layer. The SADP (b) and (c) were recorded at a tilt of 0 and 30°, respectively. The unchanged SADP's upon tilting imply the absence of the grain texture. 180

Figure 3-13 TEM BF image and the associated SADP's taken from the midplane of the film H723. The SADP (b) and (c) were recorded at a tilt of 0 and 30°, respectively. The unchanged SADP's upon tilting display the random grain orientations. 181

Figure 3-14 TEM BF image taken from the surface of the film H723. The precipitates show smaller size than that in the midplane. Three ranges of precipitates can be seen in the low part of the micrograph. 182

Figure 3-15 The micrograph and associated SADP taken at the midplane of the film H703 revealing crystalline B2 grains and transgranular precipitates (indicated by arrows). 183

Figure 3-16 TEM BF image and the associated SADP's taken from the interface of the film H773. The SADP (b) and (c) were recorded at a tilt of 0 and 30°, respectively. The micrographs display extremely fine grains and the random grain orientations. 184

Figure 3-17 TEM BF image and the associated SADP's taken from the midplane of the film H773. The SADP (b) and (c) were recorded at a tilt of 0 and 30°, respectively. The micrographs show coarse precipitates and the random grain orientations. 185

Figure 3-18 TEM BF image taken from the surface of the film H773 showing the coarse grains and precipitates. 186

Figure 3-19 Time-lapse sequence illustrating the development of the Johnson-Mehl microstructure from the untransformed body [Mahin, 1980]. 187

Figure 3-20 A schematic diagram illustrating the formation of columnar grained structures. By means of superposing two-dimension grain growth upon film growth (increasing thickness), a columnar structure can be formed as shown. The shape of the columnar grains is controlled by both the in-plane grain growth rate and the deposition rate. 188

Figure 3-21 A schematic diagram showing the effect of in-plane grain size on texture formation. (a) At higher substrate temperatures the surface and interface energies of grains are not significant due to smaller fraction of the interface and surface areas of the grains and the crystals show random orientations. (b) Films formed at lower temperatures present a strong (110) fiber-texture, i.e., the (110) plane of grains are restricted to parallel to substrate plane, but with no preferred in-plane orientation. 189

Figure 3-22 SADP sampled at the midplane of the film H673. The indices of Ni_4Ti_3 phase were underlined for purpose of distinguishing them from the B2 reflections. The ring pattern in the figure also shows the (110) grain orientation, since the $(310)_{B2}$ reflection having the radius of 64.3 mm absents. 190

Figure 3-23 Two SADP's, each including approximately one grain, sampled at two areas of the midplane of the film H773. (a) $[13\bar{3}]_{B2}$ // $[1\bar{1}1]_{Ni_4Ti_3}$ zone, and (b) $[\bar{1}3\bar{2}]_{B2}$ // $[1\bar{1}0]_{Ni_4Ti_3}$ zone. 191

Figure 3-24 Diagrams showing the size changes of B2 grains and precipitates as a function of deposition temperature in three layers. 192

Figure 3-25 A structural model for Ni-rich NiTi films sputter-deposited at a substrate temperature of 573-773 K. 193

Figure 3-26 Schematic presentations predicting the effects of Ni and Ti diffusions on Ni-rich film microstructure. In Region I, the surface diffusions of Ni and Ti are not active simultaneously. Films deposited at this region are generally amorphous in structure. In sub-region I_2, hyperstoichiometric precipitates may form via Ni surface diffusion in amorphous phase. In Region II, films are mainly of columnar B2 grains. In sub-region II_2, large precipitates may be produced through Ni bulk diffusion and B2/ppt dual-phase may form. In Region III, bulk diffusions for both Ni and Ti start. Films with microstructures similar to that of fully annealed and aged films may result. 194

Figure 3-27 TEM bright-field image of film A1 which was produced by aging the film H623 at 858 K for 1 hour and furnace cooling. 195

Figure 3-28 (a) TEM bright-field image and SADP's of film A2. (b) The inserted picture taken at 45° specimen tilt revealing columnar grain structure. (c), (d) and (e) are SADP's at three tilt angles 0°, 30°

and 45°, respectively, displaying (110) texture. The axis of tilt is indicated in (d) and (e). 196

Figure 3-29 TEM bright-field image and SADP of film A3 which was produced by aging the film H723 at 858 K for 1 hour and furnace cooling. The SADP in (b) was taken at 30° tilt showing random grain orientation. 198

Figure 3-30 TEM bright-field image of film A4 which was produced by aging the film H723 at 813 K for 1 hour and furnace cooling. 199

Figure 3-31 TEM image of the film A5 obtained by annealing film H673 at 988 K for 1 hour and furnace cooling. The size of grains have increased during annealing. Obviously, the bulk diffusion for NiTi grain growth have occurred. 200

Figure 3-32 TEM image shows the microstructure of film A6 produced by annealing the film H673 at 1123 K for 1 hour and furnace cooling. The film is consist of large grains and lenticular precipitates. The precipitates align along well-defined crystallograghic planes of the matrix. Besides, very fine precipitate particles with strain field contrast also can be noticed in the area between the large precipitates. 201

Figure 3-33 TEM image of film A7 obtained by annealing the film H673 at 1073 K for 2 hours and air cooling. The precipitation tends to occur more rapidly at grain boundary areas since the grain boundary is a favorable site for heterogeneous nucleation of precipitation. 202

Figure 3-34 Cross-section SEM micrograph of A7 displaying coarse-grained microstructure. Deep etched surface morphology reveals the crystallographic facets of the grains. 203

Figure 3-35 TEM image of film A8 deposited at 1073 K, 2 hours and 673 K, 1 hour two-stage annealing. 204

Figure 3-36 BF image and two single-crystal SADP's taken from the large precipitate plate in film A3. (a) An isolated precipitate plate in the edge of the TEM foil was examined in favor of excluding diffraction spots from the matrix. (b) The [0-10] zone of Ni_3Ti_2 phase. (c) The [110] zone of Ni_3Ti_2 phase. 205

Figure 3-37 XRD curve of the film A5 recorded at the room temperature (298 K). Besides (110) B2 peak, four peaks match the reflections of Ni_4Ti_3 phase at 2θ angle between 35° and 60° within 2 % error. 206

Figure 3-38 BF images and single-crystal SADP's taken from the film A6. The index of large lenticular precipitates could be completed by assuming that they possess the Ni_4Ti_3 structure. (b) and (d) are SADP's of zone $[0\bar{1}2]_{B2}$ // $[001]_{Ni4Ti3}$ and zone $[230]_{B2}$ // $[221]_{Ni4Ti3}$, respectively, taken from indicated areas in (a) and (c).

The underlined indices represent the diffractions of precipitates. 207

Figure 3-39 XRD curve of the film A7 recorded at 353 K showing (110) B2 peak and two Ni_4Ti_3 phase peaks at 2θ angle between 35° and 60°. The reflections of Ni_4Ti_3 phase are very weak due to its fine size. 208

Figure 3-40 The XRD curves of the film A8, taken from the same specimen at 353 K and the room temperature respectively. The curve (a) identifies the (110) B2 peak and five Ni_4Ti_3 peaks in 2θ angle between 35° and 60°. In the curve (b), the same set of the Ni_4Ti_3 reflections appears, however, the (110) B2 peak splits into two NiTi R-phase peaks: (011) and $(0\bar{1}1)$with a separation about 0.4°. 209

Figure 3-41 Schematic drawings of in-plane views of various microstructure formed in the post-deposition annealing. 210

Figure 3-42 Schematic diagrams illustrating the classification of electrical resistivity vs. temperature curves for NiTi alloys. (a) Two-stage curve involving Martensite ↔ R-phase ↔ Austenite phase transformations. (b, c) The M ↔ R and R ↔ A curves decomposed from the curve (a). Curve (d) represents a two-stage curve with an incomplete austenite → R-phase transition. (e) The curve involving R-phase ↔ Austenite transformation which is the same as the curve (c). (f) The curve involving Martensite ↔ Austenite transformation. 211

Figure 3-43 Electrical resistivity vs. temperature curves of as-sputtered NiTi films deposited at various substrate temperatures. 212

Figure 3-44 Bright-field images of midplane of the films H723 and H673. The micrographs were recorded at 101 K, which is well below their M_s temperatures. (a) The image of film H723. (b) The image of film H673. 213

Figure 3-45 DSC scans (a) and electrical resistivity vs. temperature measurements (b) on film H703 having composition of $Ni_{50.8}Ti_{49.2}$. In (a) the second heating scan from 223 to 373 K is indicated by double arrows. 214

Figure 3-46 Electrical resistivity vs. temperature curves of annealed NiTi films. 215

Figure 3-47 Ultimate elongation curves tested at 423 K for films H673, H723 and A3. According to Clausius-Clapeyron relations shown in Figure 3-61, the critical stresses to induce martensite at 423 K would be 1250, 1035 and 992 MPa for H673, H723 and A3 respectively. Clearly, the yield points in the figure were caused by the significant permanent deformation in the parent phase. 217

Figure 3-48 Ultimate elongation curves tested at 323 K for films H673, H723 and A3. The curves show well-defined three stages: first the elastic deformation of parent phase, then the plateau of parent-to-martensite transformation and finally the elastic deformation of martensite. 218

Figure 3-49 Isothermal stress-strain curves of film H623. The yielding due to the detwinning of martensite variants and stress-induced martensitic transformation did not occur at the stress level above 300 MPa. The thin film behaved as an ordinary metallic material. 219

Figure 3-50 Isothermal stress-strain curves of the film H673. 220

Figure 3-51 TEM bright-field images from deformed film H673. Compared with its original structure, it is seen that the microstructure essentially remained unchanged. 221

Figure 3-52 A series of isothermal stress-strain curves generated from a single tensile specimen of the film H703 at various test temperatures. Arrows indicate the critical stresses for the first and second yieldings. 222

Figure 3-53 Isothermal stress-strain curves of the film H723. 223

Figure 3-54 TEM bright-field images from deformed film H723. Just like its undeformed structure, well-defined precipitate particles and grains without any dislocation can be seen. 224

Figure 3-55 Isothermal stress-strain curves of the film A2. 225

Figure 3-56 Isothermal stress-strain curves of the film A3. 226

Figure 3-57 (a) and (b) TEM bright-field images taken from the deformed film A3. The absence of precipitates inside grains led the formation of dislocations. 227

Figure 3-58 Isothermal stress-strain curves of the film A5. 228

Figure 3-59 TEM bright-field images taken from the deformed film A5. (a) Slip bands which formed by a number of passage of dislocations spread throughout entire grains. The slip bands in different grains tend to align in a common direction which is the direction of maximum shear stress. (b) High density dislocations can be seen. 229

Figure 3-60 Isothermal stress-strain curves of the film A7. The loading curves dose not show any transformation yielding due to the extremely fine Ni_4Ti_3 particles. 230

Figure 3-61 Isothermal stress-strain curves of the film A8. 231

Figure 3-62 TEM bright-field image from the deformed film A7. The microstructure was unchanged in stress-strain cycling. 232

Figure 3-63 TEM bright-field image taken from the deformed film A8. The microstructure was unchanged in stress-strain cycling. 233

Figure 3-64 A schematic σ-ε-T diagram showing six types of stress-strain behavior depending on the deformation temperature relative to the transformation temperatures in polycrystalline NiTi thin films. 234

Figure 3-65 Critical stresses to induce the martensite vs. adjusted deformation temperature curves for NiTi films. 235

Figure 3-66 Tensile yield stress and reversion stress as a function of test temperature for film H703. 236

Figure 3-67 Stress-temperature diagram for film H673. 237

Figure 3-68 Stress-temperature diagram for film H723. 238

Figure 3-69 Stress-temperature diagram for film A3. 239

Figure 3-70 (a) Output of mechanical energy vs. adjusted deformation temperature for NiTi films. (b) Energy efficiency vs. adjusted deformation temperature curves. 240

Figure 3-71 SEM image showing the fractography of film H623. The fracture surface consisting of many microdimples exhibits characteristics of mode I (the opening mode) ductile failure. The fracture is a transgranular one since no feature of columnar grain structure can be seen in the fracture surface. 241

Figure 3-72 SEM image showing the fracture surface of the film H673. The columnar structure is clearly seen and its grain size (abut 0.25 μm) is consistent with that observed by TEM. 242

Figure 3-73 SEM images showing the fractography of film H723. (a) is the fracture surface viewed from surface side, and (b) is the fracture surface viewed from substrate side. The external neck area in surface side of the film reveals a serial of valleys as indicated by arrows, but that in substrate side shows even and flat morphology. 243

Figure 3-74 SEM image showing the fracture surface of film A3. The fracture is mainly transgrainular type but it is also influenced by equiaxial grain structure which was formed in 858 K, 1 hour annealing (i.e., recrystallization) process. 244

Figure 3-75 The fracture surface of film A5 shows large cup-like feature which is due to a greater grain size. Evidently, the combination of large grains and coarse precipitates posses poor structure stability. 245

Figure 3-76 The SEM image showing the fracture surface of the film A7. The fractography shows a flat and straight fracture surface with many small dimples. No neck is found in the edge of fracture surface. The free surface of the film is very smooth. 246

Figure A-1 X-ray diffraction spectra of NiTi film on Kapton substrate sputter deposited at 698 K showing that the NiTi was fully crystallized during the deposition. 248

Figure A-2 Photograph demonstrating electrically-excitable NiTi/polyimide actuator. The prototype microactuator displayed an electrical impedance of 30 ohm. (a) The actuator was deformed into an approximately 100 mm radius hairpin bend at the LN_2 temperature. (b) With the device still immersed in cold nitrogen gas, the application of approximately 3 volts dc induced a rapid and complete recovery of the bending strain. 249

Figure A-3 A series of photographs showing a bending test on a free-standing NiTi strip (film H703). (a) The film could be sharply bent in the LN_2 temperature. (b-c) When the LN_2 flask was removed, the film restored its original flat shape. 250

INTRODUCTION

There are certain intermetallic compounds, such as NiTi, CuAlNi, CuZnAl and AuCd, which undergo first-order shear-dominated hysteretic displacive transformation from a high-symmetry parent phase (an *austenite*) to a lower-symmetry *martensite* phase on loading or cooling. Several of these possess a unique and useful strain-recovery ability, a further subset of alloys, based on ordered equiatomic nickel-titanium, possesses good strength and toughness as polycrystalline engineering materials and have found a number of important industrial uses.

We designate the start and finish temperature of martensitic transformation on cooling as M_s and M_f, and the start and finish temperature of reverse transformation on heating as A_s and A_f respectively.[1] When such an alloy is plastically deformed at below its M_f temperature, deformation up to 5-8 %, far beyond normal metallic elastic limits, can be produced at relatively low stress. Upon heating through its A_f temperature, the specimen may spontaneously recover its original pre-deformed shape, exerting great force if constrained. This behavior has been termed the *shape-memory effect* (SME). Thermoelastic martensitic transformations can also be induced by applying stress to the austenite phase. Within a certain temperature interval, rather large nonlinear elastic strains (5-8 %) can be completely recovered upon unloading at a constant temperature. Such materials are said to show *transformationl superelasticity*[2] which may be viewed as an isothermal shape-memory effect.

---

[1] As discussed in the Figure 3-42b of the Section 3.3.1, for NiTi system involving R-phase transformation, the characteristic temperatures of A_s and A_f actually represent the start and finish temperatures of M → R phase transition.

[2] The terms superelasticity and pseudoelasticity have often been used interchangeably in the literature. Generally, any non-linearity in a stress-strain curve upon unloading can be referred to as pseudoelasticity.

Among the many shape-memory alloys which have been developed as stress-strain-temperature functional materials, nearly equiatomic NiTi alloys are the most commercially important due to their superior mechanical properties, e.g. high ductility (having fracture strains as great as 60 %) [Buehler and Wang, 1968], long fatigue life (up to 10^8 cycles at $\Delta\varepsilon = 0.02$) [Miyazaki, Sugaya and Otuska, 1989], good corrosion resistance (slightly more noble than 316 stainless steel) [Melton, 1990] and biocompatibility [Haasters *et al.*, 1990], although there are some disadvantages in terms of high cost and difficulty in machining. Applications of ingot-metallurgy NiTi alloys utilizing SME can be found in the areas of pipe couplings, fasteners, actuators and electrical interconnection. Applications utilizing superelasticity include eyeglass frames and many medical devices, such as orthodontic arches, stents, kink-resistant guidewires and bendable surgical tools.

Recently, NiTi thin films with a thickness of several micrometers have attracted much attention for use as actuating elements in microelectromechanical systems (MEMS). NiTi shape-memory alloys have a potential advantage over electrostatic, piezoelectric or bimetallic materials because of the large energy output associated with the reverse-martensitic transformation [Johnson, 1991; Wolf and Heuer, 1995]. These transformational displacements, if constrained, generate recovery stresses exceeding 650 MPa [Zhang, 1997]. In this case, one gram force could theoretically be produced by a NiTi strip having a cross-section of 3×5 μm^2. Moreover, in thin film form, due to a large surface-to-volume ratio, heat transfer is fast and the intrinsic disadvantage of slow response in bulk NiTi alloy actuators can in principle be greatly improved [Jardine, 1992].

In conventional NiTi shape-memory alloy manufacturing processes, pure nickel and titanium are melted together under a vacuum or a protective atmosphere to produce NiTi ingots. Then the ingots are forged, rolled or drawn to form NiTi alloy sheets and wires. The minimum dimension of NiTi alloys produced is several tens of micrometers. In

---

In shape-memory alloys a enormous amount of deformation can be completely recovered during the reverse transformation. This type of pseudoelasticity is often specified as superelasticity [Duerig and Zadno, 1990].

contrast, sputter deposition, a vacuum coating process, is able to form NiTi thin films with a thickness less than a few micrometers. Furthermore, NiTi thin films are suitable for batch microfabrication by a standard semiconductor integrated circuit (IC) processing applied to silicon wafers.

A prerequisite of martensitic phase transformations underlying shape-memory effect and superelasticity is an ordered crystalline structure. NiTi films sputter-deposited at an ambient temperature (< 623 K) typically amorphous. Although such as-sputtered amorphous films may be utilized as corrosion-resistant and wear-resistant coatings, a post-deposition anneal at a temperature exceeding 773 K is necessary to achieve crystallization in order to subsequently realize the shape-memory effect associated with martensitic transformation. Recently, much effort has been expended to clarify the dependence of microstructures, phase transformation characteristics and mechanical properties on post-deposition annealing processes. On the other hand, crystalline NiTi films may also be directly produced by the sputter deposition at an elevated substrate temperature. From both fundamental and practical viewpoints, it is interesting to study microstructure and related thermomechanical properties obtained with heated substrate deposition. However, so far no systematic work have been reported in the open literature.

The first goal of this work is to establish a basic understanding of the evolution of microstructure of NiTi films as a function of deposition temperature. It is expected that the structure be different from that of post-annealed films because of the different kinetic conditions involved in the thin film process. The second objective is to qualitatively determine the effects of microstructure (grain size and precipitates) on the phase transformation, thermomechanical behavior and structural stability.

In this study, a series of NiTi films were sputter deposited at various substrate temperatures and characterized by TEM in terms of grain structure, preferred grain orientation and precipitate morphology. Some as-sputtered films were further given a post-deposition annealing process in order to generate diversified set of microstructures for exploring structure effects. The phase transformation temperatures of NiTi films were determined by four-point resistivity measurements. The thermomechanical response of the films was evaluated by isothermal tensile tests in a temperature-strain window where the films exhibited the shape-memory effect and/or superelasticity. Finally, NiTi films that had experienced cyclic deformation were reexamined by TEM and SEM for the purpose of predicting the structural stability against permanent deformation. In addition, some subtle experimental issues, such as depositing crystalline NiTi thin films onto a polymeric (Kapton[3]) substrate and the measurement of stress-strain curves of NiTi thin films are detailed.

The present work has demonstrated that a fully crystallized NiTi film could be produced at a deposition temperature of 623 K. This is about 150 K lower than the minimum crystallization temperature for a post-deposition annealing processes. As-sputtered films displayed very fine columnar-grained structures having in-plane grain sizes of 0.1-0.3 μm. Such fine grained structure is not readily attainable by the prevailing NiTi thin film processes. Films sputter-deposited at 723 K displayed perfect superelasticity in that 2.6 % transformational strain, at a stress level of 700 MPa, could be completely recovered upon unloading. These results suggest that hot-substrate deposition is a viable alternative NiTi thin film process route, which has advantages in terms of eliminating the post-deposition annealing, depressing the maximum process temperature and producing favorable ultrafine grained structures.

The main body of the present thesis is organized into three chapters. Chapter 1 forms the background necessary for discussing the experimental results obtained. The experimental arrangements, procedures and analytical methods employed in this study is covered in Chapter 2. Chapter 3 presents the experimental results and discussion.

---

[3] Kapton is a commercial name of a series of pruducts produced by DuPont.

CHAPTER 1

BACKGROUND

This study mainly deals with the thermoelastic NiTi thin films. The background necessary for understanding the experimental data of NiTi thin films presented in this study should include following three categories:

(1) Thermoelastic martensitic transformation: This has been well established for bulk alloys and is the basis of shape-memory effect and transformational superelasticity of NiTi thin films.

(2) Mechanical response of metal crystals: In NiTi thin films three kinds of deformations occur, namely, the elastic deformation attributed to elasticity displacing individual atoms from their equilibrium positions, permanent deformation caused by dislocation-mediated slip between crystal lattice planes, and recoverable deformation due to stress-induced displacive transformation from the parent phase to the martensite.

(3) The formation and structure of thin films: The kinetic conditions governing thin film formation during vapor deposition processes are quite different from those for melt-solidification process.

In this chapter, general aspects of thermoelastic transformation are first described from thermodynamic and crystallographic viewpoints in Section 1.1. Then the special features of displacive transformations (martensitic and R-phase transformations), as well as diffusional transformations in near-equiatomic NiTi alloys, are briefly reviewed in Section 1.2. Section 1.3 and 1.4, respectively, cover the characteristics of permanent and recoverable deformations occurring in metallic crystals and NiTi alloys. Section 1.5

provides a review of thin film formation process and the correlation between process conditions and resultant film structure. Finally, in Section 1.6 the current state of knowledge regarding NiTi thin films is summarized and the objectives of this work are proposed. The organization of this chapter can be illustrated as follows:

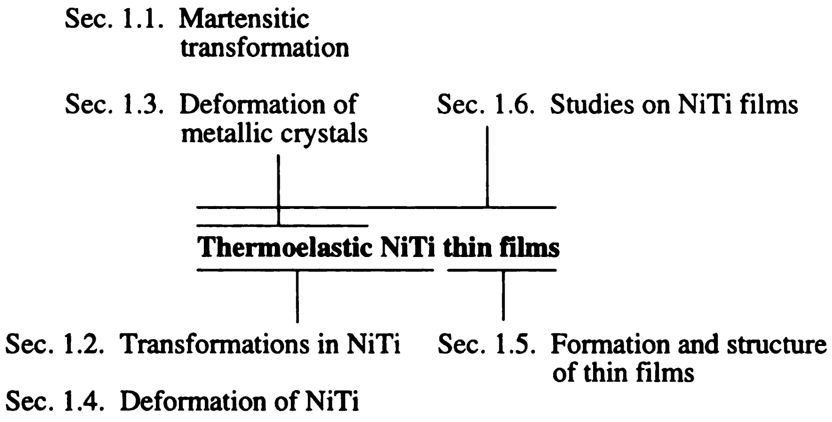

1.1. Thermoelastic Martensitic Transformation

1.1.1. General Characteristics

There are two main types of phase transformation in the solid state: diffusional and displacive. *Diffusional transformations* are those in which a new phase can only be formed by moving atoms over a long range. The new phase often has chemical composition different from that of the parent phase. Since long distance atomic migration is involved, the transformation is not only dependent upon the temperature but also dependent upon the length of time. On the other hand, in *displacive transformations*, the atoms undergo a cooperative atomic rearrangement over distances smaller than interatomic distances. Because no long-range atomic movement is necessary, the progress is only dependent upon temperature and the motion of the interface between the two phases is only limited by the speed of sound in the lattice.

Martensitic transformations are first-order,[4] displacive phase transformations. The *martensite* phase is formed upon cooling from a high temperature parent phase called the *austenite*. Martensitic transformations are of two types: thermoelastic and non-thermoelastic. For *thermoelastic transformations* the interface is quite mobile and the renucleation of the parent phase during reverse transformation is not necessary. The martensite plates form and grow continuously upon cooling, and shrink and revert to the initial parent phase orientation upon heating by the exact reverse path. Just as stated by Tong and Wayman [1974], the first martensite plate appearing at M_s is generally thought to be the last one to disappear at A_f, and the martensite plate appearing last at M_f is the first to disappear at A_s. In contrast, for *non-thermoelastic transformations*, the interface between the parent phase and martensite is relatively immobile. It does not undergo inverse movement during heating, but instead the parent phase must be renucleated within the martensitic phase. As a result, the parent plate does not maintain the original parent phase crystal orientation [Kessler and Pitsch, 1967].

From energetic considerations, the thermoelastic transformation satisfies a condition of local energy balance between chemical and non-chemical forces. Chemical forces are attributed to the difference in Gibbs free energy between the parent phase and martensite, and act as a driving force promoting the phase with lower energy at each temperature. Non-chemical forces arise from three main contributions: interface energy, stored elastic strain energy, and frictional work [Ortin and Planes, 1988 and 1991]. The interface energy is caused by the lattice distortion in both phases in the interface area. The stored elastic strain energy is associated with the accommodation of transformational shape and volume changes. This energy is accumulated inside the lattices of the transforming specimen during the forward (cooling) transformation, and released during the reverse

---

[4] According to Ehrenfest's classification [Swalin, 1961], a first-order transformation is one for which the Gibbs free energy G as a function of a given state variable (V, P, T) is continuous, but the first derivative of the G with respect to the state variable is discontinuous. Other examples of first-order transitions are vaporization and fusion.

transformation. The frictional work is the energy dissipated in the specimen as heat and acoustic emission [Baram and Rosen, 1981] due to interfacial motion either during the growth or during the shrinkage of martensite plates. Upon cooling, when a given temperature is reached, the interfaces move a certain distance into the parent phase, such that the chemical energy released is equal to the sum of interface energy and elastic energy created in the lattices, plus the energy that is dissipated by frictional work. Further progress of the forward transformation requires further decrease in the temperature.

Based on thermodynamic equilibrium formalisms, any dissipative processes such as frictional work should be neglected, otherwise there will be some deviation from the equilibrium. Compared to the elastic strain energy, the interface energy is very small in a thermoelastic transformation, due to a coherent nature of martensite/parent interface [Wayman, 1983]. If the frictional work and interface energy are ignored, the state of a system can be described merely by a thermal and an elastic term. This is the origin of the terminology: *thermoelastic*. As will be discussed later, the temperature and external stress are interchangeable state variables which can induce the martensite transformation.

1.1.2. Crystallography of Martensitic Transformation

The crystallography of martensitic transformations is now well understood in terms of the phenomenological theory of Lieberman, Wechsler and Read [1955]. The basic assumption of the theory is that the martensite/parent phase interface (habit plane) should be macroscopically undistorted in order to minimize strain energy during phase transformation. According to this theory, the transformation consists of three operational processes:

(1) A Bain distortion which forms the martensite lattice parameters and symmetry from the parent lattice.

(2) A lattice invariant shear, which maintains the lattice structure, and in combination with the Bain distortion, produces an undistorted interface.

(3) A rigid body rotation which brings the transformed lattice back in contact with the parent lattice.

Figure 1-1 schematically represents a simplified two-variant martensitic transformation in terms of these three operations [Chang, 1993]. Figure 1-1a shows the lattices of the parent phase and the martensite. In Figure 1-1b, a Bain distortion, which converts the parent phase into the martensite, but does not yield an undistorted plane associated with the habit plane. A lattice invariant shear, through a reversible mechanism such as twinning, produces an undistorted plane as shown in Figure 1-1c. Finally, a rigid body rotation is shown in Figure 1-1d. There is an invariant-plane strain associated with martensitic transformations as indicated in Figure 1-1d by the vector $\boldsymbol{m}$.

In general, thermally induced martensite consists of a twin-related, multiple-variant combination called *self-accommodating* morphology (an example is the triangular morphology shown in Figure 1-7, Section 1.2.1 for NiTi alloy). The combination of variants breaks down the invariant-plane strain into many smaller portions and arranges them in such a way that the total stored elastic strain energy created by lattice invariant shear is a minimum.

The shape reversibility in the reverse transformations is ensured by the combination of three characteristics inherent in shape-memory alloys:

(1) Thermoelastic nature: All phase transformations which are able to show the shape-memory effect are thermoelastic ones [Delaey, Krishnan and Tas, 1974]. As mentioned earlier, in this case no renucleation in the parent phase occurs during the reverse transformation because of the mobile interface. The first martensite plate appearing at M_s is the last one to disappear at A_f, and the martensite plate appearing last at M_f is the first to disappear at A_s [Tong and Wayman, 1974]. The martensite plates shrink and revert to the parent phase upon heating along the same path as they have formed. In this circumstance the original orientation of parent plates is retained in the reverse transformation.

(2) Large difference in lattice symmetry: The parent lattices of shape-memory alloys have higher symmetry (cubic-based B2 or DO_3) compared to that of martensites (monoclinic, B19 etc.). While a large number of crystallographically equivalent martensite variants can form from the parent phase (a maximum of 24 martensite variants can form from a cubic NiTi parent phase), variants of the parent phase formed in the reverse transformation are highly restricted.

(3) Ordered structure: All shape-memory alloys have an ordered parent phase except for the ones which exhibit fcc ↔ fct transformations [Gokin, 1984]. Coupled with the restriction of lattice symmetry, only one orientation of austenite can form in martensite lattices to avoid creation of 'wrong' ordered structures which raise the free energy of the lattice. In case of the fcc ↔ fct transformations, instead of the ordering, its reversibility stems from the fact that the lattice correspondence is unique in the reverse transformation due to very simple lattice change and lower symmetry of the fct phase [Otsuka and Shimizu, 1977].

1.1.3. Frictional Work and Stored Elastic Energy

In thermoelastic martensitic transformations, there is a temperature hysteresis associated with the transformations, and there is a temperature range over which the martensite and the parent phase co-exist. The hysteresis and the co-existence of the martensite and the parent phase can be explained by the effects of the frictional work and the stored elastic energy respectively [Van Humbeeck *et al.*, 1990].

Salzbrenner and Cohen [1979] investigated the influences of the frictional resistance and the elastic strain energy on thermoelastic martensitic transformations in Cu-14Al-2.5Ni (w/o) alloy. In their work, a single-interface transformation from the parent phase β_1 with a DO_3 structure to martensite γ_1' with a 2H structure was achieved by cooling a single crystal ($20 \times 6 \times 6$ mm^3) at a rate of 5-10 K/min, in a temperature gradient of 5 K/cm along the length of the specimen. During a given gradient-cooling/single-interface experiment, the temperature of the interface consecutively passing four spot-welded thermocouples and was found to remain the same. Based on their observations, the fraction of martensite vs. temperature curves can be represented in Figure 1-2a, where T_g and T_r, respectively, are designated as martensite growth and martensite reversion temperatures, and T_0 is the temperature at which the parent and the martensitic phase have the same chemical free energy. In this case, elastic energy was not generated since the transformational shape changed merely against atmospheric pressure.[5] Furthermore, there was no change in interface energy because the area of parent/martensite interface that extended across the specimen section remained the same during interface motion. Evidently, the hysteresis was caused by frictional resistance to interfacial motion and T_0 lies between T_g and T_r. If we assume that the friction force is the same in both directions, T_0 can be taken as

$$T_0 = \frac{T_g + T_r}{2} \tag{1.1}$$

The same single crystal could also be made to undergo multiple-interface transformations into many martensitic variants by cooling it uniformly instead of in a temperature gradient. As shown in Figure 1-2b, the stored elastic energy depressed the martensitic transformation and enhanced the reverse transformation. The martensitic transformation was completed at a lower temperature ($M_f < M_s$), and the reverse transformation 'prematurely' starts at lower temperature ($A_s < A_f$). The thermodynamic equilibrium temperature can be approached by

$$T_0 = \frac{M_s + A_f}{2} \tag{1.2}$$

which was proposed by Tong and Wayman [1974; Wayman and Tong, 1977]. Since at M_s and A_f, where the first martensite plate appears in forward transformation and the first

---

[5] The martensite produced is internally twinned. However, the contribution of the strain energy in the twin-related martensite to the system is negligible [Salzbrenner and Cohen, 1979].

formed martensite disappears in the reverse transformation respectively, there is no elastic strain energy involved.

Transformation observations were also made on polycrystalline specimens with different grain sizes (*D* = 0.5, 4.0 mm). Figure 1-2c and Figure 1-2d show a downward trend in the transformation temperatures with decreasing grain size. As expected, this is due to increasing elastic constraint of grain boundaries [Salzbrenner and Cohen, 1979]. Similar phenomena were observed in surface-constrained Nitinol[6] alloy samples by Hedayat, Rechtien and Mukherjee [1992]. In their work the adhering carbon coating and TiC carbide layer formed after annealing introduced a constraint force against martensitic transformation. The *in situ* TEM examination suggested that during the martensitic transformation the last martensite to form was close to the constrained surface.

Based on the preceding discussion, we can summarize the influence of the frictional force and the stored elastic energy on a thermoelastic martensite transformation. Figure 1-3a shows an ideal transformation in which neither frictional work nor stored elastic energy is involved. Figure 1-3b and Figure 1-3c are curves where only the frictional force or elastic strain energy exists. Finally, Figure 1-3d represent general cases where both the frictional force and elastic strain energy exist. The curves in Figure 1-3a, 3b. 3c and 3d, respectively, correspond to the simplest, unfolding 2, unfolding 1 and dual unfolding models for phase transition proposed by Pence and Ivshin [1994]. It is interesting to note that the relative values of M_s and A_s for a system are only determined by the magnitudes of frictional force and stored elastic energy. The former tends to make $A_s > M_s$ while the latter tends to make $M_s > A_s$.

---

[6] A commercial name *Nitinol* was given to a series of near-equiatomic Ni-Ti compounds. Nitinol stands for nickel titanium, Naval Ordinance Laboratory [Robinson, 1987].

1.1.4. Shape Memory and Superelasticity

Typical uniaxial stress-strain response of the shape-memory process is schematically shown in the upper drawing of Figure 1-4.[7] When the specimen is cooled below M_f, thermally-induced martensite forms in a self-accommodating configuration containing twin-related variants (only two variants are shown for the purpose of simplicity, in real materials up to 24 variants are formed) and there is no macroscopic shape change (point *o*). Upon loading, the specimen first deforms elastically (point *o-a*). Then deformation proceeds through the movement of the intervariant boundaries, in a process often called detwinning; i.e., reorientation of a martensitic structure (point *a-c*). After removing the load, the deformed shape remains except for a small elastic recovery (point *c-d*). However, if the remaining variants revert to the parent phase of the original orientation upon heating (point *d-o*), due to the specific correspondence between the parent lattice and each martensite variant, the remaining plastic strain is recovered.

Transformational superelasticity is the other unique deformation manifestation of shape-memory alloys as shown in the bottom drawing of Figure 1-4. At a temperature $T > A_f$, the specimen is in the austenite phase (point *o*). The loading initially produces elastic distortions of the austenite (point *o-a*). At point *a*, *stress-induced martensite* (SIM) starts to form and it spreads in the specimen under increasing load (point *a-c*). Unlike thermally-induced martensite in which the variants are equally distributed in a self-accommodation morphology, stress-induced martensite consists mainly of the most favored variants with respect to the applied stress. Unloading the specimen first results in elastic unloading of martensite phase (point *c-d*). The martensite becomes unstable as the stress drops and the specimen starts to transform back to austenite through reverse movement of martensite/austenite interface (point *d-e*). Eventually, the specimen returns to zero strain due to the elastic recovery of the parent phase (point *e-o*).

---

[7] The inserted microstructure drawings only roughly describe the austenite-to-martensite structure change. See Figure 1-1 or Figure 1-17 for more precise representation.

1.1.5. The Clausius-Clapeyron Equation for Uniaxial Stress

Analogous to classical Clausius-Clapeyron equation describing the effect of a hydrostatic pressure on transformation temperature, a relation describing the effect of a uniaxial load on the temperature of a stress-induced thermoelastic martensitic transformation has been developed by Wollants *et al.* [1979, 1993]. Next, we briefly review the transformation thermodynamics involving the external loading as a state variable.

Assuming that the tensile specimen which undergoes phase transformation contains one mole of material, the specimen has length L and is subject to a uniaxial load F. Other symbols have their usual meanings in the thermodynamics. Since no chemical composition change occurs during martensite transformation the system may be treated a single-component system.

From the first law of thermodynamics

$$dU = \delta Q - \delta W \qquad (1.3)$$

where δQ and δW represent infinitesimal amount of heat and work respectively. They are not state variables since they are dependent on the particular path chosen. However, the difference between them is a state variable. If only reversible work PdV and FdL are considered, then

$$dU = \delta Q - PdV + FdL \qquad (1.4)$$

We apply the second law of thermodynamics,

$$dS = \frac{\delta Q}{T} \qquad (1.5)$$

which produces the equation combining the first and second laws,

$$dU = TdS - PdV + FdL \qquad (1.6)$$

On the other hand, the generalized Gibbs free energy function,[8] which involves *FL*-work, is

$$G^{gen} = U + PV - TS - FL \qquad (1.7)$$

In order to shift the independent variables from the set (S, V, L) in Equation 1.6 to the set (T, P, F), we apply a Legendre transformation, i.e., differentiate Equation 1.7 and using Equation 1.6, we obtain,

$$dG^{gen} = -SdT + VdP - LdF \qquad (1.8)$$

In the state (T, P, F), if the parent phase and the martensite reach the equilibrium condition,

$$G^{gen,\,P} = G^{gen,\,M} \qquad (1.9)$$

After an infinitesimal change in temperature and loading, in the state ($T + dT$, P, $F + dF$), the system again attains the equilibrium condition,

$$G^{gen,\,P} + dG^{gen,\,P} = G^{gen,\,M} + dG^{gen,\,M} \qquad (1.10)$$

From Equation 1.9 and 1.10, we have,

$$dG^{gen,\,P} = dG^{gen,\,M} \qquad (1.11)$$

Substituting Equation 1.8 for the parent phase and the martensite respectively, at an isobaric environment (i.e., at atmospheric pressure) $dP = 0$, we find that,

$$-S^{P}dT - L^{P}dF = -S^{M}dT - L^{M}dF \qquad (1.12)$$

---

[8] The generalized variables which are involving *FL*-work are superscripted with 'gen' in the present study.

After rearranging the last equation, the Clausius-Clapeyron equation for a uniaxial loading can be obtained:

$$\frac{dF}{dT} = -\frac{\Delta S^{P\to M}}{\Delta L^{P\to M}} \tag{1.13}$$

where $\Delta S^{P\to M} = S^M - S^P$ and $\Delta L^{P\to M} = L^M - L^P$. Substituting $F/A = \sigma$ and $\Delta L^{P\to M}/L = \varepsilon^{P\to M}$ into Equation 1.13 in favor of engineering applications, noting that $AL = V$, the following equation is obtained,

$$\frac{d\sigma}{dT} = -\frac{\Delta S^{P\to M}}{V\varepsilon^{P\to M}} \tag{1.14}$$

The term of $\Delta S^{P\to M}$ needs to be replaced by a measurable value. From the definition of the generalized enthalpy function

$$H^{gen} = U + PV - FL \tag{1.15}$$

and Equation 1.7 for isothermal martensitic transformations, the following equation can be obtained

$$\Delta G^{gen,\, P\to M} = \Delta H^{gen,\, P\to M} - T\Delta S^{P\to M} \tag{1.16}$$

At the equilibrium condition $\Delta G^{gen,\, P\to M} = G^{gen,\, M} - G^{gen,\, P} = 0$, the Equation 1.16 becomes,

$$\Delta S^{P\to M} = \frac{\Delta H^{gen,P\to M}}{T} \tag{1.17}$$

Substituting Equation 1.17 into Equation 1.14, we obtain the Clausius-Clapeyron equation having state variables of T and σ,

$$\frac{d\sigma}{dT} = -\frac{\Delta H^{gen,P\rightarrow M}}{TV\varepsilon^{P\rightarrow M}} \tag{1.18}$$

The influence of stress σ on transformation temperature T is described by the preceding equation in thermodynamical equilibrium sense. In Chapter 3, this equation is employed to predict transformation strain using measured experimental data.

1.2. Transformations in NiTi Alloys

1.2.1. Martensitic and R-Phase Transformations

The crystal structures of the parent and the martensitic phase in NiTi alloys have been studied by many investigators using X-ray and electron diffraction methods. It has been clear that the parent phase of near-equiatomic NiTi alloys has a CsCl (B2) structure with a lattice constant $a_0 = 0.3015$ nm [Philip and Beck, 1957]. For the crystal structure of martensite in NiTi, different models have been proposed. In 1971, Otsuka, Sawamura and Shimizu (OSS) [1971] and Hehemann and Sandrock (HS) [1971] arrived at virtually the same lattice constants for the martensite. They all agreed that the martensite phase has a distorted monoclinic AuCd (B19) structure (denoted as B19'). The monoclinic crystal of $Ni_{49.75}Ti_{50.25}$ with $a = 0.2889$ nm, $b = 0.4120$ nm, $c = 0.4622$ nm, and $\beta = 96.80°$ reported by OSS [1971] has been widely accepted as the standard unit cell. However, controversy lies in the mode of atomic shuffle occurring during the phase transformation [HS, 1971; OSS, 1971].

The conversion from the parent lattice to the martensite lattice can be illustrated in Figure 1-5.[9] The 'steps' in the figure do not mean actual sequence of the lattice transition. A Bain distortion, which consists of an orthorhombic distortion (Figure 1-5b to c) and a monoclinic shear (Figure 1-5c to d), converts original tetragonal unit cell in B2 lattice (Figure 1-5b) into a monoclinic cell (Figure 1-5d). Due to the different sizes between Ni

---

[9] In HS's work the monoclinic angle is γ, while in OSS's work the monoclinic angle is β. In the present study the second description is used for the comparison of two shuffle models.

and Ti atoms, an atomic shuffle is necessary for atoms to reach their final stable positions in the monoclinic lattice. The shuffle proposed by HS is $(010)_M[00\bar{1}]_M$ type with magnitude of $\frac{1}{8}[00\bar{1}]_M$, whereas that proposed by OSS is $(001)_M[010]_M$ type (Figure 1-5e).

There are total 12 *lattice correspondences* (also called correspondence variants of the martensite) between the parent cell and the martensite as summarized in Table 1-1 [Matsumoto *et al.*, 1987]. Figure 1-5 shows the variant 6. In the Table 1-1, the numbered correspondences with and without prime symbols (e.g. 6 and 6') represent correspondence variants having an opposite monoclinic shear along $\mathbf{c}_M$ axis in the $(\mathbf{bc})_M$ plane.

Based on the unit cell parameters of the parent and the martensitic phase and the phenomenological crystallographic theory, twinning modes in the martensite of NiTi have been predicted by calculation by several groups. The calculated results were then compared with experimental data. The deformation twinning has been described by three types: Type I, Type II and compound twin as graphically illustrated in Figure 1-6 [Reed-Hill, 1964]. Type I twinning has a rational K_1 plane and η_2 direction; Type II twinning has the rational K_2 plane and η_1 direction, and the compound twinning has all rational K_1, K_2, η_1 and η_2. With the aid of limited TEM and electron diffraction results, Knowles and Smith (1981) first proposed $\langle 011 \rangle$ Type II twinning. By using the X-ray diffraction data obtained from NiTi single crystals Matsumoto *et al.* [1987] confirmed Knowles and Smith's prediction. A $\{11\bar{1}\}$ Type I twinning mold was also frequently observed in TEM and it was thought to be caused by 'thin foil effect'[10] [Matsumoto *et al.*, 1987; Chang, 1993].

Using the $\langle 011 \rangle$ Type II twinning as a lattice invariant shear, the 24 *habit-plane variants* (or plate variants) shown in Table 1-2 can be calculated [Miyazaki *et al.*, 1978]. The habit plane variant 1(+) is the combination of lattice correspondences 1-2, and so on. The first and second numbers of the correspondence variant-combinations designate the

---

[10] The thin foil mentioned here is the area near perforated area of TEM disks. The thickness in such areas is usually under 0.5 μm. However, the thickness of thin films for NiTi research is typically 2-10 μm.

variant of the 'major' and 'minor' regions respectively. The calculated habit planes in Table 1-2 fit well with experimentally obtained data for solution-treated NiTi specimens. Miyazaki, Otsuka and Wayman [1989] observed a typical triangular self-accommodating morphology consisting of three variants in age-treated NiTi specimens as shown in Figure 1-7. They found that the magnitudes of the habit plane indices of 0.78, 0.39 and 0.48 in age-treated specimens (Figure 1-7) correspond to that of 0.89, 0.22 and 0.40 in solution-treated specimens (Table 1-2). Three junction planes between 1(-), 1'(+) and 2'(-) domains in Figure 1-7 were determined by trace analysis to be one (011) Type I twinning plane and two $\langle 011 \rangle$ Type II twinning planes. They calculated the average shape-strain matrix for the triangular morphology and found that the shear components of the matrix approached zero. Thus it was justified that the triangular morphology satisfied the self-accommodating conditions. Miyazaki, Otsuka and Wayman [1989] also investigated the change in morphology during loading. Upon stressing the triangular morphology was changed into the most favorable variant with respect to the principal shears through the motion of the interfaces between the variants.

Besides the parent phase and the martensite, an intermediate rhombohedral phase (R-phase) may appear upon cooling, prior to the martensitic transformation in NiTi systems. Hwang *et al.* [1983] studied the R-phase transformation in $Ti_{50}Ni_{47}Fe_3$ alloy and proposed a transformation sequence upon cooling as follows: parent phase (B2) → incommensurate phase[11] (I) → commensurate phase (R-phase) → martensite (M). Figure 1-8b [Hwang *et al.*, 1983] schematically shows an electrical resistivity vs. temperature curve in which the R-phase transformation and the martensitic transformation are well separated. Figure 1-8a [Ling and Kaplow, 1981] and Figure 1-8c show the rhombohedral angle, α, vs. temperature curve and differential scanning calorimetry (DSC) curves.

---

[11] According to the study conducted by Hwang *et al.* [1983], on cooling from room temperature the initial 1/3(110) and 1/3(111) superlattice reflections deviated slightly from the exact 1/3 positions relative to the parent B2 structure. They described such phase with non-integral fraction of a reciprocal lattice vector of the parent phase as *incommensurate* phase.

Upon cooling, the incommensurate phase starts to form at T_R' where the resistivity abruptly increases as shown in Figure 1-8b and 1/3-(110)-type superlattice reflections appear in select area diffraction pattern (SADP). In fact, the superlattice reflections are not located in the exact 1/3 positions. There is no heat release associated with the B2-to-incommensurate transformation due to its second-order nature. The onset temperature of incommensurate-to-commensurate (R-phase) transformation is termed T_R, which is a few degrees below T_R' and is close to the inflection point. At T_R, the cubic lattice begins to distort into the rhombohedral lattice (Figure 1-8a) and the superlattice reflections lock into precise 1/3 positions and a finite latent heat starts to evolve (Figure 1-8c). The rhombohedral angle continuously decreases upon further cooling until the martensite starts to form at the M_s temperature where the resistivity sharply drops.

Upon heating, the resistivity slowly increases up to the inflection point A_s. At A_f the heating curve intersects the cooling curve and then shows a small hysteresis for the R-phase ↔ B2 transformation. As detailed in Section 3.3.1, the A_s and A_f in this case do not represent the onset and the completion temperature of M-to-B2 transformation, but rather that of M-to-R transformation. The DSC curve peak, with a shoulder indicating a convolution of the M → R and R → B2 phase transformation enthalpies, is seen in Figure 1-8c. In contrast with the martensitic transformation in which the thermal hysteresis exceeds 10 K the hysteresis of R-phase transformation is only 1.5 K.

Miyazaki and Wayman [1988] investigated the shape-memory mechanism associated with the R-phase transition using age-treated $Ni_{50.5}Ti_{49.5}$ alloy. They observed four distinct vaiants of the R-phase, designated as A, B, C and D in correspondence with the elongated axes $[\bar{1}11]_{B2}$, $[\bar{1}\bar{1}1]_{B2}$, $[111]_{B2}$ and $[\bar{1}1\bar{1}]_{B2}$, respectively. The surface traces of specimen indicated $\{011\}_{B2}$ and $\{001\}_{B2}$ plane-type compound twins. Figure 1-9 shows self-accommodating morphology and a corresponding four-variant combination of rhombohedral phase proposed by Miyazaki and Wayman [1988].

1.2.2. Diffusional Transformations

At high temperatures, sufficient atomic mobility leads to diffusional transformation and precipitate particles which are formed in NiTi alloys with composition deviating from equiatomic stoichiometry. Several Ni-Ti phase diagrams have been plotted which display an eutectoid decomposition of NiTi phase into $NiTi_2 + Ni_3Ti$ at lower temperatures (903 K), as seen in Figure 1-10a [Massalski, 1987; Taylor and Floyd, 1952]. A steep solvus boundary on the Ti-rich side indicates a very limited solubility for titanium in the compound. However, Wasilewski *et al.* [1971] reported that the NiTi phase may remain down to the room temperature with a very narrow composition range as shown in Figure 1-10b. In Ni-rich side, besides Ni_3Ti phase, metastable phases Ni_3Ti_2 and $Ni_{58}Ti_{42}$ (i.e., Ni_4Ti_3 phase[12]) also exist. These metastable phases were later confirmed by Van Loo, Bastin and Leenen [1978], Nishida, Wayman and Honma [1986] and Kim, Moine and Stevenson [1986]. It is generally agreed that the microstructures of near-equiatomic NiTi alloys are primarily B2 NiTi with small amounts of other phases distributed in the matrix. The formation of these phases tends to move the composition of supersaturated matrix toward stoichiometry and also create strain fields associated with volume changes and interface coherency effects, and thus profoundly influences phase transformation temperatures and deformation properties.

Nishida, Wayman and Honma [1986] studied the precipitation behavior of $Ni_{50}Ti_{50}$ and $Ni_{52}Ti_{48}$ bulk alloys, and constructed an isothermal time-temperature-transformation (TTT) diagram for $Ni_{52}Ti_{48}$ alloy as illustrated in Figure 1-11. In furnace-cooled $Ni_{50}Ti_{50}$ alloy, no secondary phase was found except for some $Ni_2Ti_4O_x$ particles.[13] However, in the $Ni_{52}Ti_{48}$ alloy, the precipitation took place and its sequence could be written as:

---

[12] The precipitation Ni_4Ti_3 has been denoted as $Ni_{56}Ti_{44}$ [Nishida and Honma, 1984] or $Ni_{14}Ti_{11}$ [Nishida, Wayman and Honma, 1984] according to the chemical composition analysis of energy dispersive X-ray (EDX). Later, the notation Ni_4Ti_3 prevailed in the literature based on its crystal structure [Sabrui, Nenno and Fukuda, 1986].

[13] Nevitt (1960) concluded that oxygen is soluble interstitially in $NiTi_2$ up to 15 at.%. $Ni_2Ti_4O_x$ phase is isomorphous with $NiTi_2$. It has an fcc structure with lattice constant increasing slightly from 1.132 nm ($NiTi_2$) to 1.134 nm (Ni_2Ti_4O). Chang (1993) showed that most of grain boundary precipitates in sputtered

$$T < 953\text{ K:}\quad \text{NiTi (supersaturated)} \rightarrow \text{NiTi (matrix)} + Ni_4Ti_3 \rightarrow \text{NiTi (matrix)} + Ni_3Ti_2 \rightarrow \text{NiTi (matrix)} + Ni_3Ti \tag{1.19}$$

$$953 < T < 1023\text{ K:}\quad \text{NiTi (supersaturated)} \rightarrow \text{NiTi (matrix)} + Ni_3Ti_2 \rightarrow \text{NiTi (matrix)} + Ni_3Ti \tag{1.20}$$

$$T > 1023\text{ K:}\quad \text{NiTi (supersaturated)} \rightarrow \text{NiTi (matrix)} + Ni_3Ti \tag{1.21}$$

Intermetallic precipitates play an important role in near-equiatomic NiTi alloys when Ni-content is greater than about 50.3 %.[14] It is well known that fine precipitates can severely depress martensitic transformation temperatures. On the other hand, the precipitation process, i.e., aging after the solution treatment, may be utilized to improve the deformation properties of NiTi alloys. Metastable Ni_4Ti_3 is the most important one because it readily forms at an aging temperature as low as 623 K, and has a strong effect on martensitic transformation and deformation behaviors. The Ni_4Ti_3 phase has a lenticular morphology and a rhombohedral cell structure with $a_0 = 0.661$ nm and $\alpha = 113.65°$. The orientation relationship between the B2 matrix and the Ni_4Ti_3 phase has been determined to be $(100)_{Ni4Ti3} // (142)_{B2}$ and $[001]_{Ni4Ti3} // [0\bar{1}2]_{B2}$ and the precipitation habit plane is $\{111\}_{B2}$ [Nishida, Wayman, Kainuma and Honma, 1986]. In the early stages of precipitation, the Ni_4Ti_3 phase is coherent with the matrix and generates internal stress fields due to the mismatch of d-spacing between the Ni_4Ti_3 phase and B2 matrix.

$Ni_{51.0}Ti_{44.4}Cu_{4.6}$ film are $Ni_2Ti_4O_x$ due to oxygen diffusion along the grain boundaries during post-deposition annealing.

[14] For bulk NiTi alloys, the chemical composition is generally determined by the weight percentage of nickel and titanium elements to be melted together for ingot. The chemical analysis is also frequently employed (e.g., in the works of Nishida, Wayman and Honma, 1986; Miyazaki, Igo and Otsuka, 1986). For NiTi films, energy dispersive X-ray (EDX) is mostly used for composition measurement, although flame atomic absorption was also used (Busch, *et al.*, 1990). Determining accurate compositions is difficult especially in films. For this reason, M_s temperature may be used as a reference of composition because it is very sensitive to Ni-contant in Ni-rich side. However, only the M_s of solution-treated NiTi may give a reasonable estimation since the M_s is also strongly influenced by structure defects (Section 1.2.3).

The Ni_3Ti_2 phase usually appears at higher aging temperatures (> 1000 K) after a short period of annealing (1 hour). It has a rectangular plate-like shape. The unit cell was deduced to be monoclinic with $a = 0.414$ nm, $b = 0.828$ nm, $c = 1.352$ nm, and $\gamma = 89.3°$. The orientation relationship between the Ni_3Ti_2 phase and the B2 matrix is as follows: $(100)_{Ni3Ti2} // \{100\}_{B2}$, $[001]_{Ni3Ti2} // \langle 001 \rangle_{B2}$ or $(001)_{Ni3Ti2} // \{100\}_{B2}$, $[210]_{Ni3Ti2} // \langle 001 \rangle_{B2}$ [Nishida and Wayman, 1986].

1.2.3. Effects on Phase Transformations

Martensitic transformation in NiTi alloys can be either thermally-induced (decreasing the temperature) or stress induced (applying an external load). In this section, the effects on thermally-induced martensitic transformation are discussed, and the effects on stress-induced martensitic transformation will be addressed in the Section 1.4.3. Several factors influencing the temperature M_s are listed as follows:

(1) Composition: Since solution-treated NiTi alloys have no special internal structures such as precipitates and dislocations, in such systems the M_s can sometimes directly reflect the effect of chemical composition on the phase transformation. It has been verified that the M_s strongly depends upon composition on Ni-rich side in quenched specimens after solution treatment. It decreases with the increase of Ni-content at a rate over 100 K/at.%, primarily due to the fact that the extra nickel atoms in B2 lattice change relative chemical energies of the parent phase and the martensite. Figure 1-12 illustrates electrical resistivity vs. temperature curves for specimens having various nickel concentrations quenched into ice water from 1073 K [Nishida and Honma, 1984]. In the case of Ti-51.8 at.% Ni specimen, the M_s was depressed beyond the range of measurement.

(2) Precipitates: The internal strain fields associated with Ni_4Ti_3 precipitates created during the aging process have a strong tendency to depress the M_s temperature, since the distorted parent lattice imposes a constraint force on the growth of martensite variants (The

strain fields associated with Ni_4Ti_3 will be further discussed in Section 3.1.1). Wu, Lin and Chou [1989] studied variation of M_s with aging time in $Ni_{51}Ti_{49}$ alloy as shown in Figure 1-13. Curve (a), which is similar to the curve (d) in Figure 1-12, is a typical resistivity feature of solution-treated specimens where only the martensitic transformation takes place. The M_s was low due to a high Ni-content in NiTi solution. In curve (b), after one hour of aging the R-phase transition appears and the M_s is dramatically depressed (over 50 K) below the measurement range although the formation of Ni_4Ti_3 may reduce some Ni-content in the matrix. In curves (b-g) the M_s increases with increasing aging time. This is caused by the combination of stress field relaxation due to the growth of precipitates and the depletion of Ni concentration in the matrix.

(3) Dislocations: Similar to the effect of strain fields created by the precipitation, the strain fields associated with dislocations which are introduced by either cold-work [Lin *et al.*, 1991], or thermal cycling, impede the development of martensite and thus depress the M_s temperature. Miyazaki, Igo and Otsuka [1986] observed that the M_s decreased about 25 K after 100 thermal cycles in all solution-treated specimens irrespective of Ni-content. TEM images revealed that the density of dislocations in the specimens increased with increasing number of thermal cycles. Jean and Duh [1995] confirmed above result in both solution-treated $Ni_{50.5}Ti_{49.5}$ and $Ni_{47}Ti_{50}Cu_3$ alloy.

(4) Grain size: Motohashi *et al.* [1991] developed a process involving sequential stages of intermediate annealing and cold rolling followed by recrystallization. They found that the M_s temperature of $Ni_{50.7}Ti_{49.3}$ alloy increased from 200 K to 241 K when grain size decreased from 21.7 μm to 4.0 μm. Gil, Manero and Planell [1995] reported similar results in Ni-42Ti wt.% (or $Ni_{53}Ti_{47}$) alloy. The M_s monotonically rose from 260 K to 270 K when the perimeter of grains, P, decreased 14 μm.[15] The increment in M_s was attributed to grain boundaries that acted as nucleation sites for martensite.[16]

---

[15] Gill *et al.* [1995] did not mention the initial grain perimeter P_0 in their paper.

[16] However, in Cu-14Al-2.5Ni (w/o) alloy as discussed in Section 1.1.3, M_s decreases as grain size decreases due to increasing elastic constraint of grain boundaries [Salzbrenner and Cohen, 1979].

(5) Impurities: Metallurgical process contamination with impurities decreases M_s considerably. Oxygen is usually introduced from sponge titanium used as a raw material. Almost all of the oxygen appears as precipitates of Ti_4Ni_2O. The oxide phase depletes the Ti content in the matrix, and relatively increases the Ni concentration, thus decreases the M_s [Shugo, Hanada and Honma, 1985]. Other impurities, such as nitrogen from the atmosphere and carbon from graphite crucibles also depress the M_s but to a lesser degree, because of the preferential consumption of titanium in formation of TiC and Ti_4Ni_2N precipitates [Gokin, 1984].

(6) Ternary elements: As mentioned above, any structural defects (precipitates, dislocations) and impurities tend to lower the M_s. The highest M_s that has been achieved in Ni-Ti binary alloys by carefully controlled processing is around 353 K [Melton, 1990]. However, the addition of certain amount (> 5 %) of specifically selected ternary elements such as hafnium which substitutes for Ti [Johnson, Martynov and Minners, 1995], and palladium [Quandt *et al.*, 1995; Miyazaki *et al.*, 1995] which substitutes for Ni, can raise the M_s temperature to well above 373 K.

The R-phase and martensitic transformations are two competing transformations on cooling from the parent phase. Whether or not the R-phase appears prior to the martensitic transformation depends on the relative magnitudes of M_s and T_R. Any factors which can depress M_s and/or can raise T_R may encourage R-phase transformation. Factors that lower the M_s with respect to the T_R are:

(1) Introducing finely dispersed Ni_4Ti_3 precipitates by aging Ni-rich alloys after solution treatment [Wu, Lin and Chou 1989].

(2) Introducing rearranged dislocations by annealing specimens below the recrystallization temperature (about 773 K) after cold work [Miyazaki *et al.*, 1982].

(3) Adding (< 5 at.%) a third element such as iron, aluminum or copper to the binary Ni-Ti alloy [Edmonds and Hwang, 1986].

1.3. Deformation of Metallic Crystals

1.3.1. Role of Grain Boundaries in Plastic Deformation

Effects of grain boundaries on yielding behavior have been widely studied in bicrystals since they are the simplest form of polycrystals. One configuration of bicrystal has two grains A and B bound by a boundary being parallel to the tensile axis (equistrain bicrystal). For each point six components of strain must be specified for arbitrary deformation of a grain: three tensile (ε_x, ε_y and ε_z) and three shear (γ_{xy}, γ_{yz} and γ_{zx}) [Taylor, 1938]. But only five of these are independent because the dilational strains are related through the constant-volume condition ($\varepsilon_x + \varepsilon_y + \varepsilon_z = 0$). To avoid the development of voids between, or overlaps of the grains, the following plastic compatibility conditions must be satisfied at the grain boundary region in order to provide continuity of strains across it [Livingston and Chalmers, 1957; Hook and Hirth, 1967]:

$$\varepsilon_x^A = \varepsilon_x^B \tag{1.22}$$

$$\varepsilon_z^A = \varepsilon_z^B \tag{1.23}$$

$$\gamma_{xz}^A = \gamma_{xz}^B \tag{1.24}$$

Two types of bicrystals are interesting: symmetric and non-symmetric ones. In the former, two crystals (A and B) are symmetric with respect to the boundary, while in the latter the orientations of the two crystals are independent to each other. For symmetric bicrystals, the operation of the slip systems in the two crystals is compatible. The grain boundary does not have any effect on deformation, i.e., the bicrystal behaves like a single crystal, as has been reported in zinc bicrystals by Gilman [1953]. However, for non-symmetric bicrystals the deformation cannot be accomplished by the operation of one system per grain. The activation of multiple-slip systems have been observed along the grain boundary of Fe-3Si (at.%) bicrystal [Hirth, 1972].

The polycrystal is made up of identical crystals differing only in their orientations. Optical microscopy examination of previously polished surface of deformed polycrystals showed that for small grains the deformation is essentially by a multiple slip even at small strains of 1-5 % [Honeycombe, 1968]. For very large grains, the center region of a grain may be deform on a single slip system, but this will soon change with increasing deformation. The displacements must be continuous across grain boundaries and as a result, the grains deform in a cooperative manner. In general, the flow stresses of polycrystals are higher than those of single crystals of the same materials, since the deformation in a grain aggregate is essentially through multiple slip from the start of the deformation. Similar to the free-surfaces which serve as dislocation sources for slip in single crystals, the grain boundaries are major sources of dislocations for plastic deformation in polycrystals [Murr, 1975].

A well-known description of the grain-size dependence of yield stress is the Hall-Petch relationship [Hall, 1951; Petch, 1953] which has the form

$$\sigma_y = \sigma_0 + kD^{-n} \tag{1.25}$$

where σ_y is the yield stress, σ_0 is a frictional stress required to move dislocations, and D is the average grain diameter. The index n, normally 0.5 in bcc metals, but is not so well defined in other systems [Honeycombe, 1968]. According to Petch's explanation [Petch, 1953], plastic deformation commences first in a single grain. When an applied stress reaches yielding point, a Frank-Read dislocation source becomes unpinned and sends out dislocation loops. The dislocation loops run up to the boundary, and form piled-up arrays of dislocations. The pile-up produces a stress concentration in the adjacent grains. If this stress concentration is sufficiently large, dislocations in a neighboring grain will become activated and emit dislocation loops. In this way the yield spreads, grain by grain, through the specimen. As indicated in Equation 1.25, the yield point is inversely proportional to the square root of grain size. This is due to the fact that a polycrystal with smaller grains allows less number of dislocations to pile-up, and imposes less stress concentration.

The Hall-Petch relationship has been applied to many systems with varying degrees of success. Care must be taken when using this equation, such as:

(1) The specimens should be true polycrystals. The numbers of dislocation pile-up tend to be greatly reduced in the grains residing in free surface, since the dislocations are drawn toward the surface and leave the lattice by image-force. Kocks [1976] calculated that wire specimen which has 100 grains per cross section has about 1/3 of its grains at the free surface. This is a significant value and could have an important effect on the mechanical properties. A criterion to assume polycrystallinity suggested by him would be to have a fraction of surface grains less than 10 %. In this case the diameter of cylindrical specimen with equiaxed grains has to be at least 30-40 times the grain diameter.

(2) Specimens having different grain size should have the same level of purity and texture, since impurities may segregate at boundaries and change the flow stress.

In conventional metallurgy, the dimensions of a specimen are generally much greater than the diameter of the grains. Consequently, when such a specimen is stretched, most grains are constrained by surrounding grains except for a very small fraction of the grains that reside near the free surface of the gauge section. However, when the dimensions of specimens become comparable to the diameter of the grains, such as in the case of thin films, a considerable portion of constrained grain boundaries are replaced by free surfaces. In these circumstances, slip tends to occur more easily due to reduced constraint force. This point has been confirmed by Miyazaki, Shibata and Fujita [1979]. They investigated the flow stress of polycrystalline Al, Cu, Cu-13 Al (at.%) and Fe as a function of the grain size and specimen thickness, and found that the yield stress decreased as the specimen thickness decreased when specimen thickness to grain size ratio, *t/d*, is below 5-15 (see Figure 1-14).

1.3.2. Precipitation Hardening

Precipitation from a supersaturated solid solution is a very versatile and common strengthening technique. The basic requirement of precipitation system is that the solubility of solid solutions should decrease as temperature decreases, in other words, the phase diagram must show a declining solvus line. Fine scale precipitates are generally produced by following three steps:

(1) Solutionizing any soluble particles by heating the alloy to the monophase region and maintaining it for a sufficiently long time.

(2) Quenching the alloy so that the formation of coarse precipitates is avoided, and a supersaturated solid solution is formed.

(3) Aging the alloy at moderate temperature to precipitate finely dispersed particles.

The crystallographic relationships between the lattice of the precipitate and that of the matrix can be coherent, semi-coherent or incoherernt, as schematically shown in Figure 1-15 [Hirsch *et al.*, 1977]. A coherent precipitate has a one-to-one correspondence between the precipitate and matrix lattices. The exact spacing of lattices may or may not be the same, and the latter case introduces some elastic strains in both phases (Figure 1-15a). A semi-coherent precipitate has typically one set of coherent interfaces and one set of semi-coherent interfaces (Figure 1-15b). The misfits on semi-coherent interface are taken up by an array of boundary dislocations. An incoherent precipitate has a completely different crystal structure from the matrix and there is no specific orientation relationship between two lattices (Figure 1-15c).

Precipitate hardening is governed by interactions between moving dislocations and precipitate particles. For coherent and semi-coherent precipitates, when precipitate particles lie across slip planes along which dislocations pass, dislocations must behave in one of two ways: (a) take a path around the particles, and (b) cut through the particles. Accordingly, there are two prevailing mechanisms of hardening: internal strain hardening and chemical hardening as described below.

(1) Internal strain hardening: Internal stress fields arise from a slight misfit with respect to the matrix. In lightly aged alloys, the average distance between particles, i.e., the 'wavelength' of the internal stress field, is small. When a dislocation moves on a slip plane containing precipitate particles, the closely spaced stress fields make the dislocation unable to bend between the particles since a dislocation line always tends to reduce elastic energy by shortening its length. The dislocation has to move out of its slip plane by climbing or cross-slipping (Figure 1-16a). This is the peak-aged condition which provides the highest yield stress. In over-aged alloys, the particles are much wider apart. It is easier for dislocations to bow around each precipitate, leaves dislocation loops behind (Figure 1-16b) [Orowan, 1948]. Orowan [1948] showed that the initial flow stress, τ_0, varies inversely with the interparticle spacing, Λ, as shown below

$$\tau_0 = \tau_s + \frac{2T}{b\Lambda} \tag{1.26}$$

where τ_s is the critical resolved shear stress of the matrix, b is the magnitude of Burgers vector and T is the line tension of the dislocation.

(2) Chemical hardening: Figure 1-16c schematically shows sheared Ni_3Al particles formed by passing dislocations in a Ni-19Cr-6Al at.% alloy after 2 % deformation [Gleiter and Hornbogen]. For this process, sufficient energy must be supplied to break favorable bonds within the particles and increase the area of newly formed antiphase boundary. Whether dislocations cut through the precipitate particles or take a path around them depends on the applied stress and the nature of the precipitate. Meyers and Chawla [1984] pointed out that the precipitates tend to be cut when the specific interface energy of the particle and matrix is low and the particle size is very fine.

1.4. Deformation of NiTi Alloys

1.4.1. Recoverable Tensile Strains

Recoverable tensile strains in single crystals of NiTi depends on the crystal orientation with respect to the tensile axis, transformation shape strain, and the detwinning strain. In a NiTi polycrystal, the deformation of each grain is constrained by neighboring grains. The strain field may not be homogenous due to the different orientations of the grains. Its recoverable strain is the spatial average of those inhomogenous strains that may be recovered in each grain by reverse transformation. In this section, we calculate the tensile strains solely caused by, respectively, the B2-to-twin-related B19' martensitic transformation, and the detwinning of B19' variants in NiTi single crystals. The sum of these two strains in the most favorable direction is shown to be consistent with the maximum recoverable tensile strains reported in literature. The recoverable strain of NiTi polycrystals is also discussed.

Figure 1-17 schematically illustrates an idealized deformation route from a single crystal of B2 NiTi to a single crystal of the B19' phase where the transformation twinning and the detwinning in twin-related martensite are well separated. From Figure 1-17a to 1-17b, the martensitic transformation proceeds through the movement of parent/martensite interface. The orientation of the interface is controlled by the requirement of an undistorted interface. The strain associated with this process is referred to as *transformation shape strain*. From Figure 1-17b to 1-17c, the deformation is realized by the coalescence of favorably oriented twin variants with respect to applied stress. Macroscopically, martensitic transformations are accompanied by a shearing deformation along the habit plane (Figure 1-17a). But it is not a pure shear since there is a component perpendicular to the habit plane. The term of *invariant plane strain* is used to describe shape changes where planes and straight lines are preserved during the transformation.

In Figure 1-17a, $\boldsymbol{d}_1$ is the unit vector in the direction of the shape change, $\boldsymbol{p}_1$ is the unit vector normal to the invariant plane (habit plane) and m_1 is the magnitude of deformation. The deformation $m_1\boldsymbol{d}_1$ (corresponding to $\boldsymbol{m}$ in Figure 1-1, Section 1.1.2) may be decomposed into two components:

$$m_1\boldsymbol{d}_1 = m_1{}^p\boldsymbol{d}_1{}^p + m_1{}^n\boldsymbol{p}_1{}^n \tag{1.27}$$

Where $m_1{}^p\boldsymbol{d}_1{}^p$ and $m_1{}^n\boldsymbol{p}_1{}^n$ represent the shear and dilatational components respectively. $m_1{}^n$ is simply the volume change of transformation since a shear component does not attribute a volume change. From the lattice parameters of B2 and B19' and X-ray diffraction data, Matsumoto *et al.* [1987] found consistency between predictions of the phenomenological theory and experimental results for $\{\overline{0.721}\ 1\ 1\}\langle 01\ \bar{1}\rangle$ Type-II twinning, and calculated the crystallographic data for $Ni_{49.8}Ti_{50.2}$ alloy as follows:

Habit plane ($\boldsymbol{p}_1$): $(-0.8889\ \ 0.4044\ \ 0.2152)_{B2}$

Direction of shape strain ($\boldsymbol{d}_1$): $[0.4345\ \ 0.4874\ \ 0.7574]_{B2}$

Magnitude of shape strain (m_1): 0.1308

From above data[17], the angle between the normal of the habit plane and the direction of shape strain is found to be 91.49°, the magnitudes of shear strain $m_1{}^p = 0.1307$, and normal strain $m_1{}^n = 0.0034$.[18]

In order to calculate the tensile strain associated with the transformation, Otsuka *et al.* [1976; Otsuka and Shimizu, 1986] modified Schmid and Boas's formula for slip and mechanical twinning [Schmid and Boas, 1950] by adding a dilatational contribution written as follows:

$$\varepsilon = \sqrt{1 + 2m_1^p \sin\chi_0 \cos\lambda_0 + \left(m_1^p \sin\chi_0\right)^2} - 1 + m_1^n \sin\chi_0 \tag{1.28}$$

---

[17] The correspondence variant 2' in Table 1-1 was chosen for calculating the data [Matsumoto *et al.*, 1987]. The habit plane variant in this case is 2'(+) (see Table 1-2).

[18] Since pure shear strain does not have any contribution to the volume change of austenite-to-martensite phase transformation, the normal strain (= 0.0034) here is corresponding to the volume change (= 0.0041) of the Bain distortion represented in Figure 1-5, Section 1.2.1. The slight difference between these two values was probably caused by experimental errors.

where λ_0 is the angle between the tensile axis and the shear direction, χ_0 is the angle between the tensile axis and the habit plane. We can simplify this expression by conditions

$$(m_1{}^p \sin\chi_0)^2 \ll 1, \text{ and } \quad m_1{}^n \sin\chi_0 \approx 0$$

The Equation 1.28 becomes:

$$\varepsilon = \sqrt{1 + 2m_1^p \sin\chi_0 \cos\lambda_0} - 1 \tag{1.29}$$

Using the power series expression

$$\sqrt{1+x} = 1 + \frac{1}{2}x - \frac{1\cdot 1}{2\cdot 4}x^2 + \frac{1\cdot 1\cdot 3}{2\cdot 4\cdot 6}x^3 - \cdots \tag{1.30}$$

for the right hand side of Equation 1.29 and truncating the higher power terms, since

$$x = 2m_1{}^p \sin\chi_0 \cos\lambda_0 \le 2m_1{}^p(0.5) = m_1{}^p = 0.13$$

is fairly small. We obtain

$$\varepsilon \approx m_1{}^p \sin\chi_0 \cos\lambda_0 \tag{1.31}$$

Therefore, the transformation strain is approximately proportional to the product of the shear strain and the Schmid factor. When the Schmid factor is 0.5, i.e., in the most favorable orientation, the tensile strain solely caused by transformation shape strain is $\varepsilon = 0.5m_1{}^p = 0.0654$.

The detwinning strain can be easily calculated from the crystallographic data as shown in Figure 1-17b. Since two twin regions have different volume fractions, $x = 0.27$ and $(1\text{-}x) = 0.73$, two opposite detwinning directions would lead to different detwinning strains. Using $\{\overline{0.721}\ 1\ 1\}\langle 01\ \bar{1}\rangle$ Type-II twinning as a lattice invariant shear, the twinning elements for variant 2' are [Matsumoto *et al.*, 1987]:

$$K_1 = (\overline{0.721}\ 1\ 1)_M, \qquad \eta_1 = [0 1 \bar{1}]_M$$

$$K_2 = (0 1 \bar{1})_M, \qquad \eta_2 = [\overline{1.571}\ 1\ 1]_M$$

gives the twinning strain $s = 0.280$. The detwinning strains (= average twinning strains of two twin regions) are $\boldsymbol{s}_1 = [0, 0.145, -0.145]$ in the favored direction and $\boldsymbol{s}_2 = [0, -0.053, 0.053]$ in the other direction. The magnitudes of $\boldsymbol{s}_1$ and $\boldsymbol{s}_2$ are $s_1 = 0.204$ and $s_2 = 0.075$ respectively. If the Schmid factor is 0.5, the magnitude of the tensile strains in the favored direction and in the other direction, respectively, would be 0.1022 and 0.0375.

The total recoverable strain, which is the strain associated with the transition of detwinned B19' single crystal-to-B2 single crystal, is the sum of the transformation shape strain and detwinning strain (Figure 1-17c). The recoverable shear strain would be

$$\boldsymbol{y} = m_1\boldsymbol{d}_1 + \boldsymbol{s}_1 \tag{1.32}$$

The magnitude of $\boldsymbol{y}$ is calculated to be 0.221 for the favored twinning direction and 0.163 for the opposite direction. Accordingly, by assuming the Schmid factor to be 0.5, we obtain the maximum recoverable single-crystal tensile strains of 0.1105 for the favored direction and 0.0815 for the opposite direction.[19]

The recoverable tensile strains of B2-to-B19' transformation for NiTi single crystals in different directions have been calculated from the lattice deformation matrix and measured experimentally. Saburi and Nenno [1981] predicted orientation dependence of recoverable tensile strain using the lattice deformation matrix as shown in Figure 1-18a. Saburi, Yoshida and Nenno [1984] and Miyazaki *et al.* [1984] measured the dependence of recoverable tensile strain on crystallographic orientation in $Ni_{50.5}Ti_{49.5}$ single crystals. The strains of solution-treated specimens for various orientations were in good agreement with the values calculated from the lattice deformation matrix. The maximum recoverable tensile

---

[19] In single crystal NiTi, the recoverable strain depends on crystallographic orientation. The maximum recoverable strain mentioned here is referred as the recoverable strain in the most favored direction.

strain is greater than 0.105 as shown in Figure 1-18a and 1-18b which is consistent with the result of preceding calculation ($y = 0.1105$).

From the previous discussion, it is apparent that: (a) The maximum tensile recovery capacity of single-crystal NiTi is 0.1105. (b) For the NiTi system we cannot predict the recoverable strain only from the transformation shape strain, since the detwinning strain also needs to be taken into consideration.[20]

In analogy to the deformation of polycrystals by slip (Section 1.3.1), the transformation twinning and the rearranging of variants in a polycrystalline shape-memory alloy also take complex forms in grain boundary regions in order to maintain grain boundary compatibility. Bhattacharya and Kohn [1996] proposed a general theoretical prediction of recoverable strains for polycrystalline shape-memory alloys by utilizing the Taylor estimate. They found that the recoverable strains of a polycrystal depends not only on the texture of the polycrystal and the transformation strain of the underlying martensitic transformation, but critically on the change of symmetry during the underlying phase transformation. In cubic-to-tetragonal transformations occurring in NiAl and FeNiC alloys, the number of martensite variants, *k*, is 3. In this case the range of deformations that each grain can undergo by rearranging variants is too small to allow cooperative deformation between grains except for special textures. Hence, even though single crystals of Ni-37Al (at.%) can recover tensile strains up to 13 % [Enami *et al.*, 1981], polycrystals can only recover 0.2 % strain in compression [Kim and Wayman, 1992]. In contrast, in the cubic-to-monoclinic transformation occurring in NiTi alloys, the large change in symmetry ($k = 12$) provides a great range of cooperative deformations. Thus significant recoverable strains can be expected in NiTi polycrystals. Bhattacharya and Kohn [1996]

---

[20] Otsuka *et al.* [1976] calculated the orientation dependence of $\beta_1 \rightarrow \beta'_1$ transformation strain in Cu-Al-Ni alloys by using the Equation 1.27. In their work, the measured elongation always slightly exceeded the calculated ones. This might due to the fact that the contribution of the detwinning strain was not included into the consideration.

estimated that NiTi alloys have at least 2 % recoverable strain in any polycrystal and at least 2.4 % along the length in ribbons with the Eucken-Hirsch texture.[21]

The recoverable tensile strain observed experimentally in NiTi polycrystals is in a range of 5.5-8 % [Ling and Kaplow, 1981; Miyazaki, Otsuka and Suzuki, 1981; Saburi, Tatsumi and Nenno, 1982]. The discrepancy is probably caused by the different levels of material texture and/or microstructure defects (such as precipitates and dislocations).

NiTi alloys also exhibit the shape-memory effect and superelasticity associated with R-phase transformation, although the recoverable strain is limited to 1 % due to small change of rhombohedral angle (see Figure 1-8a). The mechanical behaviors associated with the R-phase transformation have been investigated in single-crystals [Miyazaki, Kimura and Otsuka, 1988] and polycrystals [Miyazaki and Otsuka, 1984, 1986]. In a single-crystal, of course, the recoverable strain associated with the R-phase transition is dependent on crystallographic orientation. The maximum and minimum values were found in $[\bar{1}11]_{B2}$ and $[001]_{B2}$ dirctions respectively as shown in Figure 1-19a [Miyazaki, Kimura and Otsuka, 1988]. The recoverable strain is also strongly dependent on the temperature, based on the fact that the rhombohedral angle, α, is a function of temperature at $T \leq T_R$ (Figure 1-8a). The temperature dependence of the recoverable strain for various orientations was calculated using the B2 → R lattice distortion matrix as shown in Figure 1-19b [Miyazaki, Kimura and Otsuka, 1988]. The recoverable strain in all directions increases gradually as temperature decreases from T_R. For $Ni_{50.2}Ti_{49.8}$ alloy, the temperature rate for B2 → R transformation is greater than that for R → M transformation (15.5 vs. 5.3 MPa/K, Stachowiak and McCormick [1988]).

---

[21] Eucken-Hirsch texture is a sheet texture in which all grains align the [001] direction perpendicular to the plane of the ribbon and either the [100] or the [110] direction along the length of the ribbon [Eucken and Hirsch, 1990].

1.4.2. Slip Deformation

Unlike most polycrystalline intermetallic compounds which often have limited ductility at room temperature due to their few and difficult slip systems, B2 NiTi alloys have significant ductility up to 50 % [Moberly *et al.*, 1990]. The permanent deformation mechanism of B2 NiTi system is outlined as follows.

B2 is an ordered bcc compound with CsCl structure. In bcc metals, slip directions are in general the closest packed direction, i.e., $\langle 111 \rangle$. Perfect dislocations may be dissociated in order to reduce the energy. There are two possible ways for $\langle 111 \rangle$ dislocations to dissociate in the B2 lattice [Li and Szpunar, 1992]. One way is

$$\langle 111 \rangle \rightarrow \langle 110 \rangle + \langle 001 \rangle \tag{1.33a}$$

followed by

$$\langle 110 \rangle \rightarrow \langle 100 \rangle + \langle 010 \rangle \tag{1.33b}$$

Each of these dislocation components is perfect and the motion of a dislocation does not disorder the structure. The other way is

$$\langle 111 \rangle \rightarrow \tfrac{1}{2}\langle 111 \rangle + \tfrac{1}{2}\langle 111 \rangle \tag{1.34}$$

These two partial dislocations with the same Burgers vectors are elastically repulsive, but in the ordered structure, separation of partial dislocations will produce a ribbon of antiphase boundary (APB) between them with an associated APB energy. The width of this ribbon r_0 can be obtained from the balance of the elastic energy of the repulsion between the partial dislocations and the APB energy.

Li and Szpunar [1992] found that at room temperature the equilibrium separation $r_0 =$ 0.045 nm for B2 NiTi, which is smaller than the lattice parameter ($a_0 = 0.301$ nm). Such a small separation implies that the APB energy is so high that the dissociation of two repulsive $\frac{1}{2}\langle 111 \rangle$ is impossible. The high APB energy is attributed to a perfect order at room temperature since the ordering temperature, T_c, of NiTi alloy is 973 K [Wang, Buehler and Pichart, 1965]. Therefore, at room temperature the $\langle 111 \rangle$ dislocations tend to dissociate in the way represented by Equation 1.33. The $\langle 100 \rangle$ slip vector in NiTi has been experimentally observed by Mori and Fujita [1984].

At high temperature the APB energy decreases greatly due to the loss of lattice ordering energy, and the second dissociation described by Equation 1.34 may operate. Koskimaki, Marcinkowki and Sastri [1969] observed that the $\frac{1}{2}\langle 111 \rangle$ dislocations were introduced as interfacial dislocations by a second phase which precipitated at about 900 K.[22] Li and Szpunar [1992] concluded that although the slip system in ordered NiTi alloy is $\langle 100 \rangle\{011\}$, but when the temperature rises to near the order-to-disorder transition temperature, the slip system shifts to $\frac{1}{2}\langle 111 \rangle\{1\bar{1}0\}$.

Moberly *et al.* [1990] investigated the plastic deformation of $Ni_{47}Ti_{50}Fe_3$ alloy at room temperature. $\langle 010 \rangle$ type dislocations started to appear after 1 % elongation, and $\{114\}\langle 22\bar{1} \rangle$ mechanical twinning, which was first proposed in NiTi alloy by Goo *et al.* [1985], could be identified in a 10 % cold worked bar. Both dislocation density and twin density increased with an increase in cold working up to 40 %.

Generally, five independent slip systems (ISS) are needed to maintain boundary strain compatibility requirements [Mises, 1928]. $\langle 010 \rangle$ dislocations provide for only three ISS in B2 materials and thus two more ISS must come on other sources [Moberly *et al.*, 1990]. From TEM observation, they suggested that the fourth ISS was provided by mechanical twinning which occurred on only one set of parallel planes, and the newly oriented twins could in turn undergo dislocation slip to provide additional slip systems.

The ductility of martensite NiTi is also greater than 50 %, as reported by Miyazaki, Otsuka and Suzuki [1981] and Miyazaki, Kohiyama and Otsuka [1991]. However, no detailed slip system for B19' NiTi has been proposed. It is found that the critical stress for

---

[22] The second phase was not identified. However, it might be Ni_4Ti_3 phase which precipitated at a similar temperature [Koskimaki, Marcinkowki and Sastri, 1969].

slip in the parent phase is generally greater than that in the martensite [Miyazaki *et al.*, 1983; Miyazaki, Kohiyama and Otsuka, 1991].

1.4.3. Factors Influencing SME and Superelasticity

If slips in the martensite and B2 lattice occur during stressing, NiTi will not fully return to its original shape on heating or/and unloading. To realize a perfect shape-memory effect and superelasticity, any permanent deformation must generally be avoided.[23] Superelasticity occurs at $T > A_f$, according to Clausius-Clapeyron equation the stress level for superelasticity would be greater than that for shape-memory effect which occurs at $T < M_s$. Consequently, it is more difficult to achieve the superelasticity which requires a higher yield point (for slip) of both the martensite and B2 phase.

As will be seen in Section 3.4, in order to enhance the performance of NiTi alloys, a modification of microstructure should have a selected influence on the flow stresses of the B2 and martensite, and the critical stress to induce the martensite. In other words, it should increase the former to a greater degree than the latter. Several microstructural factors affecting NiTi deformation behavior are summarized below:

(1) Solid solutions: B2 and B19' lattices are ordered lattices [Gokin, 1984]. In solution-treated Ni-rich alloys, extra nickel atoms substitute the sites normally occupied by titanium atoms and introduce elastic distortion around them due to the difference in size between nickel and titanium atoms. The strain fields of the distortion restrict the motion of dislocations thus raise the flow stress. Miyazaki, Kohiyama and Otsuka [1991] observed that both flow stresses of the parent and martensite phase of solution-treated specimens (Ni-concentration between 50.0 and 52.0 at.%) monotonically increased as the nickel content increased at the approximately same rate of 400 MPa/Ni at.%, and the flow stress of parent phase is about 100 MPa greater than that of martensite. However, they did not

---

[23] In the case of superelasticity, unrecoverable strain can also be caused by retained martensite after unloading [Miyazaki *et al.*, 1984].

report the effect of composition on the critical stress to induce martensite. Saburi, Tatsumi and Nenno [1982] recognized that as nickel content increased the alloys tended to show superelasticity. Perfect superelasticity was observed even in quenched $Ni_{51.3}Ti_{48.7}$ alloy after solution treatment in which it could be assumed that no precipitates and few dislocations existed.

(2) Precipitates: Fine precipitates produced in the aging process can suppress permanent deformation during stress-induced martensitic transformation by raising the flow stress for slip and thus enhance superelasticity. Miyazaki *et al.* [1982] reported that after an aging treatment in polycrystal NiTi alloys at 673 K, Ni-rich specimens ($Ni_{50.6}Ti_{49.4}$ and $Ni_{51.6}Ti_{48.4}$) showed superelasticity; while stoichiometric specimens ($Ni_{49.8}Ti_{50.2}$ and $Ni_{50.1}Ti_{49.9}$) did not because of the absence of the precipitates. In NiTi single crystals superelasticity could similarly be achieved only after aging treatments [Miyazaki *et al.*, 1983].

On the other hand, fine precipitates reduce the recoverable strains. In the work conducted by Saburi, Tatsumi and Nenno [1982], the recoverable tensile strain in polycrystalline $Ni_{51.3}Ti_{48.7}$ alloy is 5.3 % in solution treated state, but only 3.7 % in 773 K, 1 hour aged sample. Similar results were found in single crystals. Miyazaki *et al.* [1984] investigated the dependence of recoverable strain on crystallographic orientation in $Ni_{50.5}Ti_{49.5}$ single crystals. The recoverable strains of solution-treated specimens for various orientations were in agreement with the values calculated from the lattice deformation matrix. But the recoverable strains of aged specimens were only about half of the calculated values. They speculated that the strains were reduced by untransformed regions or the regions with un-detwinned multi-variants of martensite around the finely dispersed precipitates.

(3) Dislocations: A great quantity of dislocations can be introduced by cold work or cyclic deformation in NiTi systems. Filip and Mazanec [1994] studied influence of work hardening on deformation. A cold-rolled $Ni_{49.5}Ti_{50.5}$ specimen with 20 % reduction

exhibited superelasticity, but the critical stress to induce martensite, as well as the slope of plateaus associated with stress-induced martensitic transformation, and the reorientation of martensite variants, was higher compared with usual superelasticity curves. Zadno and Duerig [1990] stated that cold-worked NiTi alloys exhibit nearly hysteresis-free linear superelasticity with recovered strains as high as 4 %. The plateau is so steep that it almost merges into the elastic slope. Miyazaki *et al.* [1986] investigated the effect of tension cycling on superelasticity characteristics in NiTi alloys. The stress-strain curves of furnace-cooled $Ni_{49.5}Ti_{50.5}$ alloy show that the plateau becomes steeper and steeper as the number of cycles increases and the change is most rapid in the initial cycling (Figure 1-20a). The steep plateau was believed to be caused by a high density of dislocations which limit B2/B19' interface mobility and resist the reorientation of martensite variants.

Miyazaki *et al.* [1982] proposed a thermomechanical treatment method, i.e., annealing at temperatures below the recrystallization temperature immediately after cold work, for realizing superelasticity in stoichiometric NiTi specimens. TEM image of microstructures prepared this way showed that the high density of dislocations remained in a specimen annealed at 673 K was similar to that in an as-rolled specimen. However, sharp spots in the diffraction patterns implied that the dislocations had been rearranged from the cold-worked state to release strain [Miyazaki, Igo, and Otsuka, 1986]. The detailed mechanism has not been thoroughly investigated, nevertheless, the annealing process improved strain recovery. The maximum recoverable strain of polycrystalline $Ni_{49.8}Ti_{50.2}$ alloy in their study was about 5.2 %, which is comparable to solution-treated specimens reported by Saburi, Tatsumi and Nenno [1982].

(4) Grain size: An experiment conducted by Saburi, Yoshida, and Nenno [1984] clearly demonstrated that the reduction of grain size was effective in improving superelasticity, as shown in Figure 1-20b. Three types of single crystal specimens (dimensions: $1 \times 0.4 \times 20$ mm^3), a polycrystal with grain size of 1 mm, and a polycrystal with grain size of 50 μm, were made from the same ingot of the $Ni_{50.5}Ti_{49.5}$ alloy. The

single crystal specimen did not behave superelastically at any test temperature. As the grain size decreased superelasticity became pronounced. For a specimen with a grain size of 50 μm, there were 200 grains per cross section in the tensile sample and the criterion to assume polycrystallinity was nominally satisfied. Apparently grain boundary constraint played an important role in resisting of slip as discussed in Section 1.3.1.

In short, for NiTi alloy both recoverable deformation which underlies the transformation shape strain and detwinning strain, and ordinary permanent deformation need to be considered. In order to achieve perfect shape-memory effect and superelasticity the NiTi process should result in low critical stress to induce martensite and high flow stress for permanent deformation. The recoverable strain in NiTi single crystal in the most favorable direction is 22.10 % in shearing or 11.05 % in extension, while the maximum recoverable tensile strain in NiTi polycrystals is 8 %. Solid solutions, precipitates, dislocations and grain boundaries have effect of enhancing shape-memory effect and superelasticity. However, they also tend to reduce the magnitude of recoverable strain.

1.5. Formation and Structures of Thin Films

1.5.1. Sputter Deposition

To meet an increasing demand for various functional coatings, e.g. optical, electrical, mechanical and chemical coatings, a large number of deposition techniques have been developed in the last 40 years. Methods of preparing thin films can be divided essentially into two groups, namely, chemical methods and physical methods. The chemical methods basically consist of chemical vapor deposition (CVD), and electroplating. CVD is a chemical process which takes place in vapor phase near or on the substrate so that a reaction product is condensed onto the substrate. Electroplating is an electrochemical process in which two electrodes are immersed in an electrolyte of an ionic salt and positive ions are deposited onto the cathode (substrate). Physical methods are mainly the physical vapor deposition (PVD) processes of evaporation, sputtering and ion plating. In the evaporation process, atoms to be deposited are thermally transported from a source material onto the substrate by various heating methods, such as direct resistance, electron beam (E-beam) or an arc discharge. In the sputtering process, gas ions produced in a glow discharge bombard the source material, called the target or cathode, dislodging atoms which pass into the vapor phase and deposit on the substrate. Ion plating is a hybrid process that combines the benefits of evaporation and sputtering. In ion plating, the coating source can be evaporation or sputtering, the surface to be coated is subjected to a flux of high energy ions and neutrals before and during the deposition.

There are some advantages which make sputter deposition one of the most versatile techniques in thin film technology. First, virtually any material, including metals, ceramics and organics are candidates for a coating. The coating material is transported into the vapor phase by a mechanical rather than thermal or chemical process. Second, sputtering is a relatively high energy process. The energies of sputtered atoms are in the range of 10-40 eV, whereas the energies of evaporated atoms are typically in the range of 0.2-0.3 eV. The momentum of sputtered atoms enhances the mobility of adatoms, and often provides superior film quality and good adhesion between the coating and substrate materials. Finally, the sputtering process has capacity to transfer alloys and compounds into the vapor phase while preserving their composition. This feature is of importance in the fabrication of alloy or compound films where the composition needs to be controlled.

The planar diode shown in Figure 1-21a is the simplest sputtering configuration. The cathode serves as the source of coating material. It is usually water cooled to prevent outgassing and the occurrence of diffusion in the case of alloy cathodes.[24] The substrates facing the cathode are mounted on the anode.[25] By applying a dc (direct current) potential of the order of 1-5 kV across the electrodes, a glow discharge is initiated at an argon

---

[24] Cathode (target) cooling is a necessary requirement to produce an altered layer having the reduced concentrations of high yield species at the surface of an alloy cathode [Bunshah *et al.*, 1982]. At the steady state, this altered layer will provide a vapor flux having the chemical composition of originating solid.

[25] In some cases, the substrates are independantly biased (bias sputtering) or allowed to 'float'.

pressure of 1-10 Pa. Most of the electrical potential between the anode and cathode is consumed in a 'cathode dark space' near the cathode, due to the relatively low mobility of ions compared to the electrons. Positive Ar^+ ions are accelerated by this strong electric field and strike the cathode, and ballistically eject atoms from the surface of the cathode. The sputtered atoms condense as a thin film on the substrate. During ion bombardment, a small number of electrons are also emitted from the cathode, and these electrons are accelerated in the cathode dark space and enter the plasma volume. They collide with argon atoms and generate the volume ionization required to sustain the glow discharge.

Recently, magnetron sputter sources have been developed. Magnetrons can be defined as diode devices in which magnets are situated behind the cathode and the combination of magnetic and electrical fields force electrons into helical trajectories near the cathode surface (Figure 1-21b). In this way, the electron's path length is greatly increased, thus raising the ionization probability. Most magnetron sources operate at a pressure in a range of 0.1-10 Pa and a cathode potential of 300-700 volts. Compared with conventional diode sputtering, magnetron sputtering is capable of high deposition rates and lower operating pressures. This allows longer free path of atoms and reduces collisions therefore gives higher adatom energy.

1.5.2. Influence of Temperature on Phase Formation

Most solid metallic materials are produced by melting/solidification technology which approximate equilibrium condition because of the normally slow cooling rate from high temperature. The resultant phases can generally be predicted from equilibrium phase diagrams. In physical vapor deposition processes, at high substrate temperature, equilibrium phases similar to their melt-produced counterparts form due to sufficient diffusion processes. At low substrate temperatures the surface mobility of adsorbed particles is sufficiently limited that the disordered state may be frozen before the adatoms are able to reach energetically preferred sites, and non-equilibrium metastable phases, which do not exist in equilibrium phase diagram, may form. In this subsection we consider the influence of substrate temperature on phase formation.

Figure 1-22 is schematic illustration of the effect of substrate temperature on phase formation for a hypothetical *polymorphic material*[26] [Thornton, 1977]. Substrate temperature is indicated by the horizontal axis and a series of equilibrium phases α, β and γ are shown along the vertical axis. The stable phase at a given temperature will be the one with minimum Gibbs free energy, G, given by the relation $G = H - TS$.[27] At high temperature, the $-TS$ term dominates and the phase with larger entropy S will be more stable. Thus, high temperature phases are characterized by large entropies, i.e., more open and disordered structures and in the limit become an amorphous liquid.

At low substrate temperatures, a highly disordered, amorphous-like phase forms because of low mobility of atoms. However, whether or not an amorphous film forms also depends on the nature of atomic bonding. It is found that in contrast to elements forming covalent bonds such as in compounds, pure metals form crystallites even at liquid helium temperature [Buckel, 1959; Mader, Nowick and Widmer, 1967]. The cause of the difference is that in covalently-bonded materials the formation of crystalline structure requires a relatively large displacement of atoms due to their small coordination number. On the other hand, the formation of close-packed structures for pure metals needs only small displacements which may occur even at very low temperatures.

When substrate temperature is elevated to an intermediate level ($0.3 < T/T_m < 0.5$, where T_m is the melting point in Kelvin) [Thornton, 1977], diffusion processes become significant. Diffusivity generally obeys the Arrhenius law:

$$D = D_0 \exp\left(-\frac{Q}{RT}\right). \tag{1.35}$$

---

[26] Polymorphic materials, such as iron and tin, are capable of existing in more than one solid phase.

[27] The equation $G = H - TS$ only provides a thermodynamic tendency at given temperature. Whether a stable phase forms also depends on the kinetic conditions, i.e., the diffusion process.

Since surfaces have higher energy than the bulk, the extra energy reduces the amount of activation energy which must come from other sources before the atom will diffuse. The activation energies for surface and bulk diffusions can be ordered as

$$Q_{\text{surf.}} < Q_{\text{bulk.}} \tag{1.36}$$

From Equation 1.35 and 1.36, evidently, surface diffusion is favored when substrate temperature is not high enough. The adatom mobility in growing film surfaces is generally adequate to form equilibrium phases even at relatively low substrate temperatures where equilibrium phases are impossible to form in the bulk via bulk diffusion.

When deposition is done at high substrate temperatures ($0.5 < T/T_m < 1$) [Thornton, 1977], diffusion through the volume tends to overpower the surface diffusion, a structure characteristic of conventional melting/solidification processing results.

From preceding discussion it is clear that the structure of thin films is governed by both the thermodynamics which determines the driving force, and the kinetics which defines the available rate controlling mechanisms at a given temperature. Low substrate temperatures limit kinetic processes and result in amorphous phase in alloys and compounds. Moderate substrate temperatures only promote the surface diffusion and produce equilibrium phases having unique columnar-grained structure (as will be discussed in Section 3.1.2). High substrate temperatures greatly remove the kinetics limitation through bulk diffusion process. The structures formed usually display equiaxed grain morphology similar to that formed in the melting/solidification process.

1.5.3. Structural Zone Models

Structural zone models are empirical diagrams representing the morphology of coatings with respect to deposition conditions (substrate temperature and working-gas pressure). The resultant film structures are primarily controlled by shadowing effects,[28] surface diffusion, and bulk diffusion. For many pure metals the activation energy for moving adatoms is proportional to the melting point [Brophy, Rose and Wulff, 1964]. Therefore, various atomic processes can be expected to occur over different temperature regions of T/T_m in zone models.[29]

Movchan and Demchishin [1969] proposed a structure zone model based on their experimental observations for electron beam evaporation as shown in Figure 1-23a. The model predicts three regions which depend on the substrate temperature. In Zone 1 ($T/T_m < 0.3$), the film consists of tapered crystals with domed tops which are separated by voided boundaries. The crystals have a high dislocation density and poorly defined structure. Zone 2 ($0.3 < T/T_m < 0.5$) consists of columnar grains separated by distinct and dense boundaries. The films have properties similar to cast metals and in this region the surface diffusion dominates. Zone 3 ($0.5 < T/T_m < 1$) consists of equiaxed grains with a bright surface. The films are formed through bulk diffusion and have properties similar to a fully annealed metal.

Thornton [1977] extended this zone classification to sputter deposition by adding an axis to account for working gas pressure as shown in Figure 1-23b. A transition zone (Zone T) between Zone 1 and Zone 2, consisting of a dense array of poorly defined fibrous grains without voided boundaries, was also proposed. A higher working gas pressure tends to shift the zone structures toward lower T/T_m since the higher argon pressure increases the chance of collision between sputtered particles and argon atoms and reduces the energy of condensing particles. Thus, at a given substrate temperature denser films will form at low argon pressure conditions. Thornton [1977] further proposed a generalized

---

[28] Shadowing effect is a geometric interaction between the rough growing surface and the angular directions of the coating flux.

[29] In structural zone models the substrate temperature is usually normalized as a fraction of the absolute melting point of the metals.

schematic representation showing the superposition of effects of coating-flux shadowing, surface diffusion and bulk diffusion.

A computer model of film growth using two-dimensional (2D) hard spheres by Muller [1985] demonstrated that a transition from low packing density films (0.7) to unity density films occurred as a function of temperature and deposition rate (Figure 1-24). It was assumed in his model that depositing spheres intersect the growing surface at random positions and stick in place except for relaxation into nearby 'pockets'. This would produce a structure having 'pipes' inclined along the angle of incidence of spheres. If a thermal activation process was added to simulate the temperature dependence, a dense microstructure can be formed at the equivalent temperature of $0.3T_{\mathrm{m}}$.

1.5.4. Secondary Grain Growth in Thin Films

Grain growth in polycrystalline metals is accomplished through grain boundary migration which results from the diffusion of atoms across the grain boundary region.[30] The driving force for *normal grain growth* lies in the interface energy of the grain boundaries. As the grains grow in size and their numbers decrease, the grain boundary area diminishes and the total interface energy is lowered.

Recently, Thompson [1990] developed a concept of *secondary grain growth.* Secondary grain growth is a grain growth mode in which only a subpopulation of grains grow at the expense of a static matrix of grains. The driving force for the secondary grain growth is the surface energy anisotropy of the grains. Generally, closely packed planes have a relatively low surface energy since the bonding forces of an atom within those planes are utilized so fully by neighbors in its own plane that the absence of similar atoms outside that plane introduces only relatively little local distortion. The most densely packed

---

[30] The grain growth in polycrystals should be referred as the coalescence which describes the grain growth in non-crystalline matrix (will be discussed in Section 3.1.2). However, the term of grain growth is more prevail in the literature.

planes in bcc are (110), in fcc are (111), and in hcp with ideal c/a ratios they are (0002). These are the planes which have the lowest surface energy.

In thin films, if the major diameter of grains is comparable to film thickness, a considerable part of the grain boundary is replaced by free surfaces or the interfaces between the film and substrate as seen in Figure 1-25a. The rate of grain growth in this case is a function of not only grain size relative to the mean grain size as the situation of normal grain growth, but also the surface energy of grain relative to the average surface energy of grains. The grains with orientations that lead to low surface energies have an energetic advantage over others during growth (Figure 1-25b). Finally, a uniform crystallographic orientation, i.e., texture may develop (Figure 1-25c). Secondary grain growth in thin films has been experimentally observed in several systems, e.g., Si [Thompson and Smith, 1984], Ge [Palmer, Thompson and Smith, 1987] and Au [Wong, Smith and Thompson, 1986].

1.6. Studies on NiTi Films and the Purpose of Present Work

Since the near-equiatomic NiTi alloy, or Nitinol was first developed by Buehler and Wang at the U.S. Naval Ordnance Laboratory [1968], this unique material has been extensively studied by many researchers. By the late 1980's, the phase transformation characteristics, crystallographic aspects and thermoelastic deformation behaviors of bulk NiTi alloys were well established.

Studies of NiTi thin films relevant to the shape-memory effect commenced in the 1980's and much effort has been expended to clarify the dependence of microstructures and phase transformation temperatures on thin film process conditions. Shifts in composition with respect to the sputter target, and the structural and transformation characteristics of sputtered $Ti(Ni_{1-x}Cu_x)$ films were investigated [Chang, Simpson and Grummon, 1989; Chang *et al.*, 1990; Chang and Grummon, 1997]. In their work, single layer (SL) films and periodic multilayer (PML) films, respectively, were fabricated by sputtering from

$Ti_{50}Ni_{45}Cu_5$ ternary targets and by co-sputtering from alternating ternary and pure titanium targets. Atomic composition analysis showed that titanium loss due to preferential resputtering was compensated for by periodic multilayering with pure titanium. Precipitates in annealed SL films produced marked effect on its martensitic transformation behavior, whereas the PML films showed evidence of appropriate phase transformations during DSC, resistivity, and cold-stage TEM experiments. The crystal structure of ternary precipitate $(Ni+Cu)_2Ti$ found in $Ti_{47.5}$ $(Ni+Cu)_{52.5}$ films was identified by Chang and Grummon [1991] using convergent beam electron diffraction (CBED).

Busch *et al.* [1990] deposited NiTi films using a dc magnetron sputtering. The temperature of unheated substrates during deposition was approximately 423 K due to glow discharge heating. As-sputtered films were amorphous in structure and did not exhibit any shape memory characteristics. The heating curve of differential scanning calorimetry (DSC) of as-sputtered film exhibited one distinct exothermic peak at 753 K which corresponds to the crystallization of the film from amorphous structure. Below this temperature, even to 723 K, the film still remained amorphous. Films annealed at 823 K for 30 minutes showed appropriate B2 diffraction peaks in X-ray diffraction spectra. A free-standing annealed film with a thickness of 10 μm demonstrated a shape-memory recovery in a conventional bending test.

Moberly *et al.* [1992] conducted an *in situ* observation of the crystallization of as-sputtered amorphous NiTi films in high voltage electron microscope. A electron accelerating voltage of 1500 kV was used in order to observe crystallization in film regions as thick as 1.5 μm. The crystallization process occurred over a range of temperatures from 773 K to 873 K. The nucleation of crystallites in thicker regions of TEM specimens, which occurred prior to nucleation in thinner regions, implied that nucleation did not proceed preferentially at surface, but rather homogeneously in the bulk of films.

Ishida, Takei and Miyazaki [1993] sputtered NiTi films under various argon pressures and cathode powers. They found that argon gas pressure had a critical effect on the mechanical properties of the films although the cathode power also affected it. The films formed at a high argon pressure (13.3 Pa) were brittle due to its porous structure, while the films formed at a low argon pressure (0.67 Pa) exhibited a good shape-memory behavior comparable to that of bulk NiTi alloys after annealing. The high argon pressure decreased the energy of sputtered atoms by collision and limited surface diffusion. This result was consistent with the Thornton's structural zone model [Thornton, 1977].

Hua, Su and Wuttig [1993] investigated the effects of isothermal annealing on NiTi/SiO_2/Si heterostructure by cross-sectional TEM observations. The amorphous structure remained in the film annealed at 733 K for 1 hour. The crystallites formed at annealing temperatures of 833 K and 933 K had average grain sizes of 50 nm and 200 nm respectively. Two kinds of nucleation centers were suggested. One was homogeneous nucleation in the bulk of the film, the other was heteronucleation at the film/substrate interface. The grain morphology displayed a columnar structure.

Gyobu *et al.* [1996] studied the influence of chemical composition and heat-treatment on phase transformations in sputtered NiTi films. During crystallization heat treatment, no precipitation occurs in near-equiatomic NiTi films, whereas $NiTi_2$ particles precipitated in the Ti-rich films and Ni_4Ti_3 precipitated in the Ni-rich films. The R → B19' or B2 → B19' transformation temperatures of 773 K, 1 hour annealed films reached the maximum at the equiatomic composition, decreased with increasing Ni-content in the Ni-rich side, and kept constant in the Ti-rich side.

There are only few reports in the literature relating to NiTi films sputter-deposited at elevated substrate temperatures to directly form crystalline NiTi films. Ikuta *et al.* [1990] deposited NiTi thin films at various substrate temperatures and observed that crystalline films were formed only at temperatures exceeding 673 K. At lower substrate temperatures, the films were amorphous and no significant crystalline peaks were found in X-ray diffraction spectra. Gisser *et al.* [1992] employed X-ray diffraction method and observed that crystalline films with (110) texture were produced by sputter deposition of NiTi alloy onto (100) silicon substrate at a temperature range of 623-733 K. Krulevitch *et al.* [1996] sputter-deposited 1.3-μm and 5.1-μm thick Ni-Ti-Cu films at 723 K. The films have excellent shape-memory properties, but the columnar microstructure of the films showed a significant increase in surface roughness with film thickness. Recently, F. Chang, [1997] showed that the stiffness of the substrate may affect the minimum temperature to produce crystalline NiTi. Fully crystalline NiTi films could be formed on Kapton film whose elastic modulus is only 1.6 GPa [Product Bulletin, DuPont, 1993] at substrate temperature as low as 560 K.

In parallel with the fundamental investigation, several prototypes based on shape-memory NiTi thin films were proposed and developed. A micro-planar spring of NiTi film was fabricated by Walker, Gabriel and Mehregany [1990]. In their study, 2 μm-thick NiTi film was deposited onto a silicon wafer which had been coated with a 3 μm-thick polyimide film (Kapton). The as-sputtered film was annealed at 623 K for 1 hour. A wet-etch was used to give a zigzagged spring pattern of the film. After releasing the film pattern using a plasma etch to remove the polyimide spacer, the spring pattern displayed some curling due to residual stress. The curled film then returned to its original, unreleased configuration after applying a heating current. Some researchers argued that the 'shape-memory effect' observed in the film may actually be caused by thermal expansion effects since the NiTi film should have remained amorphous at 623 K [Ikuta *et al.*, 1990]. A lack of basic structure analyses made this study uncertain. Nevertheless, that study demonstrated the compatibility of sputtered NiTi films with current silicon-based micromachining technology.

Kuribayashi, Yosaaki and Ogawa [1990] fabricated a NiTi thin film actuator showing a *two-way shape-memory effect.*[31] They conducted a constrained-aging anneal which was

---

[31] In two-way shape-memory effect, the shape change of specimens also occurs on cooling. The two-way shape-memory can be generated by different methods such as deformation cycling [Schroeder and Wayman, 1977] and constraint aging [Nishida and Honma, 1984]. In the case of constraint aging, Ni_4Ti_3 precipitates

directly adopted from that for bulk material [Nishida and Honma, 1984]. Ni-rich films with 10 μm thickness were sputtered onto NaCl plates which were washed off in distilled water. The free-standing films were annealed at 1073 K for 10 minutes, and then were curled to 3.7 mm diameter and constrained in a glass pipe for a second annealing at 673 K for 6 hours to produce desired precipitates. The aged films were then cut into a horseshoe-like shape for testing. The film horseshoe demonstrated a reversible bending motion with a maximum frequency of 5 Hz when passing a rectangular wave of electrical heating current through its pads.

Johnson [1991] reported two prototype devices developed at the NiTi Alloy Company using the shape-memory effect in NiTi thin films. One device has a membrane of NiTi stretched over an orifice to form a valve as shown in Figure 1-26a. The membrane was heated by a dc current. An operating prototype has been cycled more than two million times in their laboratory and a cycling rate of twenty Hz could be attained. The other one is a microactuator for a mirror to be used as a refreshable optical storage device shown conceptually in Figure 1-26b. Some other types of silicon-based microvalves were also explored [Johnson *et al.*, 1992; Ray *et al.*, 1992].

A thermomechanical NiTi/Si composite thin film switch was fabricated and tested by Kim, Su and Wuttig [1995]. In their work 1 μm NiTi film was deposited onto 90 μm silicon substrate and the composite was given a heat treatment at 873 K. The deflections of a cantilever composite were observed by cycling it between low and high temperature. It is believed that the volume change of about 0.5 % during B2-to-R or B2-to-B19' transformation was fully accounted for such deflections.

The development of residual stresses in NiTi films sputtered on (110) silicon wafer during isochronal and isothermal annealing of both amorphous and crystalline films has been studied using a scanning laser substrate curvature method [Grummon, *et al.* 1995;

---

grow preferentially under constraint stress. On cooling, the growth of martensite variants will be biased by the internal stress fields associated with the precipitates and gives a macroscopic shape strain.

Zhao, 1996; Zhang and Grummon 1996, Zhang, 1998]. The sputter-deposited thin films showed large compressive intrinsic stresses which tend to increase with increasing deposition temperature. Stress-relaxation induced by austenite-to-martensite transformation on cooling can be fully recovered on heating at rates as high as 50 MPa/K. This effect may form the basis for reversible cyclic actuation of NiTi/Si composites applicable to silicon-based microelectromechanical system.

Krulevitch *et al.* [1996] quantitatively compared several microactuation schemes and investigated the thermomechanical properties of Ni-Ti-Cu thin films using the wafer-curvature method. The ternary films exhibited recoverable stresses up to 510 MPa and transformation temperatures above 305 K. A fatigue test, which was measured by the curvature of chips transferred between two water baths one at room temperature and another at 353-373 K, revealed that the stresses up to 350 MPa could be sustained for thousands of cycles. Two micromachined devices, a microgripper and microvalve, were also demonstrated.

Since NiTi films are expected to be utilized as force-displacement functional components, their thermomechanical responses are of interest. In order to evaluate deformation properties of NiTi thin films, one must overcome two difficulties. The first difficulty is to suppress contamination during the sputter deposition and post-deposition crystallization/annealing processes, since even a trace of impurities incorporated into the films will make them brittle. The second is the preparation and handling of free-standing thin film specimens, which are 1000 times thinner than conventional tensile specimens. Probably for these reasons, only very recently has deformation data of the NiTi thin films became available. Miyazaki *et al.* [1994], Ishida *et al.* [1995] and Nomura and Miyazaki [1995] studied the effects of chemical composition, heat treatment and deformation cycling on deformation properties associated with martensite and R-phase transformations using iso-stress tests. Miyazaki *et al.* [1994] reported an achievement of superelasticity in an annealed (at 973 K) and aged (at 773 K) $Ni_{49.7}Ti_{50.3}$ film. Recoverable strain (including elastic strain) about 4 % was attained at an applied stress greater than 600 MPa.

Grummon, Nam and Chang [1992; Nam, 1995] proposed a superelastic NiTi surface coating approach to prevent fatigue crack initiation and improve the fatigue lifetime of polycrystalline copper. NiTi thin films were deposited onto the gauge section of polycrystalline copper dog-bone specimens by ion beam sputtering in which nickel and titanium atoms are sputtered off by argon ions generated from a Kaufman-type ion source. After crystallization annealing, the specimens were subjected to fatigue cycling under a constant strain amplitude at various temperatures with respect to the phase transformation temperatures of the films. The development of fatigue cracks was observed by optical microscopy and SEM. All crystalline film coated specimens showed improved fatigue crack initiation lifes over bare copper specimens. The greatest increase in fatigue life, about 100 % improvement over bare specimens, was found in $Ni_{49.6}Ti_{50.4}$ film coated specimens. The ability of NiTi crystalline film to suppress fatigue crack initiation was believed to be attributed to both superelastic deformation and ductility of the NiTi films.

Typically, the M_s of NiTi binary alloys are near ambient or sub-ambient. In order to extend the application of NiTi thin films to higher ambient temperatures as well as achieve a high cycle-rates, it is necessary to increase the transformation temperatures. Partial substitution of nickel or titanium by a ternary element additions has been found to be an effective way. Miyazaki *et al.* [1995] sputtered Ti-26.4Ni-21.8Pd (at.%) ternary thin films. The transformation temperatures of the films were characterized by the DSC measurement. For the ternary films the martensitic and austenite transformation peak temperatures were 385 K and 401 K, respectively. Johnson, Martynov and Minners [1995] sputtered ternary alloy films using a Ti-50Ni-10Hf (at.%) target having a M_s temperature of 393 K. It was found that the M_s of deposited films could be adjusted in a temperature range from 373 to 473 K by placing additional Ti or Hf pieces on the target's surface. The dependency of transformation temperatures upon the Ni/Pd ratio in sputtered $Ti(Ni_{1-x}Pd_x)$ films with $x = 0, 0.2, 0.6$ and 1.0 was investigated by Quandt *et al.* [1995]. The A_f and M_f temperatures, respectively, were increased with the increment of the palladium content from 305 K and 235 K in NiTi film to 843 K and 771 K in TiPd film. The study showed an achievement of widely adjustable transformation temperatures, from room temperature to over 773 K, which are the highest transformation temperatures ever realized in shape-memory thin films.

Most NiTi films that have been discussed in the literature have been produced by two steps. The first is the sputter deposition of NiTi onto an unheated substrate ($T < 573$ K) which results in an amorphous NiTi film. The second step is crystallization annealing at temperatures well above 773 K. Alternatively, crystalline NiTi films can be directly produced by sputter deposition at elevated substrate temperatures as suggested by the works of Ikuta *et al.* [1990], Gisser *et al.* [1992], Hou and Grummon [1995], Hou, Pence and Grummon [1995] and Krulevitch *et al.* [1996]. However, so far little detail has been reported in open literature.

The first objective of present work is to establish a basic understanding of the connection between the parameters of hot-substrate deposition processes and resultant microstructure of NiTi films. A series of deposition temperatures were chosen in a range where the surface diffusion of NiTi at growing film dominates and no significant bulk diffusion of NiTi occurs. It is expected that crystalline films with a microstructure different from that produced through bulk diffusion can be formed at relatively low temperatures. From engineering viewpoint, hot-substrate deposition may have advantages in terms of reducing maximum required process temperature, which is critical for deposition of crystalline NiTi films onto polymeric components, and may also produce favorable microstructures unattainable from prevailing two-step NiTi film processes.

The second objective is to clarify the relationship between the microstructure of NiTi thin films and their thermomechanical behavior. Although there is a considerable volume of literature on the subject of deformation of NiTi alloys, the data obtained from bulk specimens cannot always be directly applied to thin films. As mentioned earlier, for a given grain size, slip in lattice tends to become easier when the thickness of specimens decreases (Section 1.3.1). Dislocation slip, which degrades the shape-memory effect and superelasticity may become a controlling factor in thin film cases where dimensions are very small. Ni-rich precipitates in NiTi have been found to exert a strong influence on mechanical response. For this reason, Ni-rich thin films sputtered from $Ni_{51}Ti_{49}$ alloy cathodes are of interest. In order to separate the effects of grain size and precipitate on the deformation, some as-sputtered films were further given a post-deposition annealing at different temperatures to produce microstructures with various combinations of grain size and precipitate morphology.

The completion of above two objectives has identified a basic thin film process/structure/property relationship which provides useful information for achieving an optimum thermomechanical performance of NiTi thin films by controlling process conditions. In parallel with the above study, the fabrication and test of a prototype of electrically excitable NiTi/polymeric actuator has been conducted.

CHAPTER 2

EXPERIMENTAL METHODS

The experiments carried out in the present study consist mainly of two parts: the preparation and the thermomechanical characterization of the NiTi films. The sputter-deposition equipment developed for this study is first discussed (Section 2.1). Then methods used for fabrication of NiTi/polyimide prototype microactuator and the preparation of free-standing NiTi films are presented in Section 2.2 and 2.3. In the second part, several basic characterization methods employed in the present study are briefly described in Section 2.4.

2.1. Sputter Deposition Facility

The sputter machine developed for this study is shown in the photograph in Figure 2-1 and schematically illustrated in Figure 2-2. A polished stainless-steel bell-jar having a volume of about 100 liters was evacuated by a 10 inch diameter silicone-oil diffusion pump (Varian HS-10) with a pumping speed of 4000 liter/sec,[32] backed by a rotary-oil-pump (Welch 1397) through a copper-wool oil vapor trap. In order to establish a stable working pressure around 5×10^{-3} torr in the chamber during coating stage, a 10 inch throttle valve (gate valve) was placed between the chamber and the diffusion pump. Four 1500 watt

---

[32] The pumping speed can be calculated using the following equation [Technical Tables, Vacuum Product, Kurt J. Lesker Company, 1993]:

$$S = \frac{V}{t} \ln\left(\frac{P_0}{P}\right)$$

where S: pumping speed in liter/sec, V: chamber volume in liters, t: time to reduce pressure from P_0 to P, in seconds, P_0: starting pressure in torr and P: ending pressure in torr after t second.

resistive heater tapes were mounted around the chamber wall for baking out the chamber. Copper tubing with 3/8 inch diameter was soldered to an outer copper jacket for water-cooling the chamber wall during coating operation. A *K*-type thermocouple gauge, a capacitance manometer (MKS Baratron) and an ion gauge were connected to the chamber to monitor the pressure in different ranges from the atmospheric pressure to 10^{-7} torr (1.3×10^{-5} Pa), and a Quadrupole mass spectrometer was connected to the chamber to indicate the partial pressure of residual gases and serve as a leak detector.

A Torus-2C magnetron sputter source (Kurt J. Lesker Co.) was powered by an Advanced Energy MDX-1K dc power supply. Most deposition runs in this work were operated at power control mode, i.e., during the entire deposition run the product of cathode voltage and cathode current was kept constant. A stainless-steel substrate holder was originally designed to be electrically insulated from other fixtures in the chamber for a purpose of applying a biasing voltage to the substrates during coating.[33] Argon gas with a purity of 99.9996 % was further purified by passing it though a titanium getter heated to over 1023 K.[34] The flow rate of argon was controlled by a MKS mass flow controller and the outlet of the working gas was located in the vicinity of the sputter source. A stainless-steel shutter which could be manipulated through a rotary feedthrough was placed between the sputter source and substrates. The target-to-substrate distance was kept at 65 mm for all runs.

---

[33] Bias sputtering is the technique of maintaining a negative potential (generally in a range of 50-500 volts) on the substrates during deposition. The positively charged ions (primarily Ar^+) are attracted toward the substrates and give the surface of growing films a low energy bombardment. Bias sputtering has been found to have an effect on suppressing the development of Zone 1 structure at low T/T_m [Bunshah, *et al.*, 1982]. In the preliminary work of this study, the effect of biasing on depressing the deposition temperature to form crystalline NiTi films has been explored. Nine deposition cycles were conducted with substrate temperatures between 523 and 673 K and biases between -15 and -300 volts. It was found that the biasing did not have much effect on promoting crystallization. The films deposited at -15 volt bias showed slightly better quality in teams of ductility which may due to the removal of loosely bonded contamination on the growing surface of the film [Thornton, 1982]. The films formed at the higher bias (≥ 250 volts) displayed severe fracture and separation from the substrates which suggests very high internal stress.

[34] By estimating using the ideal-gas state function, at a typical deposition pressure of 5 millitorr, the partial pressure of impurity gas from working gas is 2×10^{-8} torr (2.6×10^{-6} Pa). Therefore, it is beneficial to utilize the titanium getter in the present work.

2.2. Fabrication of NiTi/Polyimide Prototype Microactuator

2.2.1. Crystallizing NiTi by Post-Deposition Annealing

The Kapton film is synthesized by polymerizing an aromatic dianhydride and an aromatic diamine. It is claimed that there are no known organic solvents for the film [Product Bulletin, DuPont, 1993]. Kapton polyimide film has an ability to maintain its physical, electrical, and mechanical properties over a wide temperature range from 4 K to 673 K. Kapton has been used in a variety of electrical and electronic insulation applications: wire and cable tapes, substrates for flexible printed circuits and as a transformer and capacitor insulation.

Since Kapton is stable at a temperature as high as 673 K, this property makes the polyimide film a useful substrate material for metallizing or coating with crystalline NiTi alloy. In the present study, the feasibility of integrating crystalline NiTi film on Kapton film was explored. First, an attempt was made to sputter NiTi onto Kapton substrate at the ambient temperature[35], followed by annealing the NiTi/Kapton laminate to crystallize NiTi film. In this case, the metallization of Kapton with crystalline NiTi thin film requires that at a given heating rate, the crystallization temperature of NiTi film should be lower than the decomposition temperature of the Kapton. The weight loss characteristics of Kapton in air and helium at a heating rate of 3 K/min is shown in Figure 2-3 [Product Bulletin, DuPont, 1993]. At a temperature of about 773 K, the weight loss increases rapidly which indicates the start of decomposition.

The crystallization behavior of NiTi films sputter deposited using $Ni_{51}Ti_{49}$ and $Ni_{45}Ti_{50}Cu_5$ targets were investigated by differential scanning calorimetry (DSC) at a heating rate of 20 K/min as shown in Figure 2-4.[36] The exothermic peak appearing in each curve represents an amorphous-to-crystalline reaction. The temperatures for start of crystallization of binary and ternary films were 770 K and 759 K respectively. The data

---

[35] It was found from this study that due to the bombardment of sputtered material flux, the temperature of unheated substrate could increase from room temperature to 353 K at the sputter power of 250 watts.

[36] The *heat flow* is defined to be positive if the system release heat to the environment.

show that crystallization temperatures are lower than the Kapton decomposition temperature of the polyimide, since high heating rate in the DSC experiment would have raised the crystallization start temperatures, according to the study made by Chang [1993].[37] From this preliminary examination it seemed worthwhile to conduct a further trial.

Compared with its amorphous structure, crystalline NiTi possesses a lower electrical resistivity as revealed by Ikuta *et al.* [1990]. In their work, resistivities of amorphous and crystalline NiTi films at the room temperature were stated to be 1.77×10^{-3} ohm cm and 0.87×10^{-3} ohm cm respectively. Consequently, a resistivity drop should be accompanied with an amorphous-to-crystalline transition. An *in situ* observation of electrical resistivity change was performed during annealing treatment. When a rapid resistivity drop appeared, the heating power was reduced instantly in order to preserve the Kapton substrate from being overheated. Figure 2-5 shows the set-up of the experiment. The NiTi/Kapton laminate formed in cold-substrate deposition was cut into a dog-bone shape. In the vacuum chamber the specimen was irradiated by two 625 watt quartz lamps powered by a controllable power supply.

Figure 2-6 gives the electrical resistivity curve of NiTi film and temperature curve in annealing at a heating rate of 5.6 K/min. At room temperature, the resistivity of NiTi amorphous film is 1.6×10^{-3} ohm cm. In the temperature between 301 K and 767 K, the coefficient of resistivity is about -6.65×10^{-5} ohm cm/K. The negative temperature coefficient can be attributed to structure recovery on increasing temperature. At 767 K, a large resistivity drop occurred due to crystallization and the temperature was maintained until the resistivity drop slowed down. After crystallization the curve exhibited a positive temperature coefficient, which is normally found in metallic crystals. The crystalline structure of NiTi film was confirmed by X-ray diffraction spectra. However, both NiTi film and Kapton displayed discoloration and brittleness after the crystallization anneal. The

---

[37] In Chang's work [Chang, 1993], crystallization temperature of single-layer NiTi film measured by DSC is increased with increasing heating rate from 749 K at heating rate of 2 K/min to 780 K at heating rate of 50 K/min.

NiTi film then was contaminated since NiTi is very reactive at the elevated temperature.

Figure 2-7 shows the residual gas pressure vs. temperature curves of Kapton film at the heat-up rate of 5 K/min. The residual gas pressures start to increase at the temperature around 700 K. It is possible that before the temperature reached the point at which the weight loss increases rapidly the Kapton had been outgassing significantly.

2.2.2. Metallization of Kapton by Hot-Substrate Deposition

For a given material, compared with the bulk diffusion surface diffusion is important at the lower temperature as discussed in Section 1.5.2. A crystalline film can be formed by surface diffusion in a growing film, while crystallization of an amorphous film can only proceed via bulk diffusion. Thus, it is expected that hot-substrate deposition can produce crystalline NiTi thin films at relatively low temperature. In the study reported by Ikuta *et al.* [1990], crystalline NiTi was produced during deposition at substrate temperature of 673 K.

The condition of successfully depositing crystalline NiTi film onto Kapton is that during deposition the temperature of Kapton substrate should be maintained between the minimum temperature to form a fully crystallized NiTi film and the maximum temperature at which Kapton is stable (= 703 K).[38] A conventional substrate holder (Figure 2-8a) with a heater situated behind the substrate did not work well with polyimide substrates which have poor thermal conductivity. For instance, if the side of substrate facing sputter source was heated to 673 K, the other side of substrate, facing the heater, will have a far higher temperature than the decomposition temperature of Kapton. Another heating device which has been tested, consisted of four 625 watt quartz lamps clustered around the sputter source to irradiate the substrate (Figure 2-8b). Thermocouples were located in front of the substrate and in contact with it. However, the problems encountered were that the

---

[38] The requirement of the stable of Kapton® is not only for preventing polyimide film from thermal damage (decomposition), but also for preventing NiTi film from the contamination by outgassing of the Kapton®.

temperature of substrate was not uniform due to imperfect focusing of quartz lamps and in some local areas the Kapton overheated.

Finally a heating device which has two separately controllable heating elements was developed as shown in Figure 2-9. The front heater was placed between the sputter source and substrate holder. The spacing between heating wires permitted sputtered atoms to pass through the heater and to deposit onto the substrates. The heating wires were shielded by alumina tubes to eliminate contamination of the film and to prevent embrittlement of the heating wires caused by in-diffusion of sputtered atoms. The size of both front and back heaters was made to have an area about four times greater than that of the substrate, so that in lateral direction a nearly uniform substrate temperature could be expected. The substrate temperature was monitored by two shielded thermocouples[39] which were placed in the vicinity of each side of the substrates. By individually adjusting power to the two heaters so that readings from the front and back thermocouples were identical, the true substrate temperature could be read.

Crystalline NiTi film with a thickness of 3.1 μm was successfully sputtered onto Kapton-200NH film (having a nominal thickness of 7.6 μm), at 698 K. The detailed deposition procedure will be described in Section 2.3.1. The as-sputtered NiTi film was confirmed to have crystalline structure (Appendix A.1). NiTi films revealed a shiny mirror-like surface and excellent adhesion. When the film was scratched by a fine metal point such as fine tip of tweezers, only a thin deformed groove was formed and no delaminating or cracking occurred. The composite displayed a 3 to 5 mm radius of curvature at room temperature which was convex on the metal side indicating that the NiTi film maintained a slight residual compressive stress arising from the mismatch in the thermal coefficient of linear expansion between NiTi ($\alpha_{B2} = 11.0 \times 10^{-6}$/K, $\alpha_{B19} = 6.6 \times 10^{-6}$/K) and Kapton ($\alpha = 20 \times 10^{-6}$/K).

---

[39] It was found that during the deposition unshielded thermocouple probe would pick up the wrong signal generated by the plasma.

2.2.3. Photolithography Process

The technique for fabricating a NiTi/polyimide microactuator prototype is directly adopted from conventional integrated circuit (IC) process. The experiment of patterning-etching process was conducted at the Photolithography Laboratory in Department of Electrical Engineering, Michigan State University. Several trials were necessary for establishing proper working parameters. The process used in this study is illustrated in Figure 2-10 and outlined as follows:

(1) An 18 × 18 mm^2 square of NiTi metallized Kapton was cemented onto a 22 × 22 mm^2 square slide cover glass with a collodion solution with the NiTi film facing outward. A moderate pressure was applied on microlaminate until the solution had solidified.

(2) A photoresist [Shipley Co., PR1813] was spun over onto the surface of NiTi film for 30 seconds at 3000 rpm in a spin coating machine. The thickness of photoresist was approximately a few micrometers.

(3) The photoresist was soft-baked for 15 minutes at 358 K in a convection oven.

(4) The specimen was aligned with a pattern photomask and exposed under a 7.6 mw/cm^2 ultraviolet source for 60 seconds by using a Karisuss-MJB3 apparatus. The photomask shown in Figure 2-11 was made by photo fabrication.

(5) The specimen was developed for 35 seconds in a MF319 developer at room temperature [Hoechst Celanese Corp., Chatham, NJ].

(6) Again the microlaminate was post-baked at 393 K for 20 minutes in another convection oven to cure the pattered photoresist.

(7) The NiTi thin film was etched by a mixture of equal parts of a titanium enchant and a nickel enchant [Transene Company, Inc., Rowley, MA] for 3 to 5 minutes.

(8) Finally, the microlaminate was released from slide cover glass and the photoresist was dissolved with the acetone.

2.3. Preparation of Free-Standing NiTi Films

2.3.1. Sputter Deposition Procedure

Several 50 mm diameter, 3 mm thick disk-shaped cathodes (targets) were sliced from a wrought NiTi bar having a nominal chemical composition of Ti-51.0 at.% Ni [Special Metals Corporation, New Hartford, NY] by electrical discharge machining (EDM). The surface of cathodes was ground using 400 grit abrasive grit papers. After cleaning, the cathode plate was clamped onto the water cooled copper heat sink base of the sputter gun. Virgin cathodes were given a preliminary sputter 'wear in' for six hours in order to establish a favorable geometrical configuration prior to deposition. Each cathode was only used for two deposition runs, for a total of about 5 hours, to minimize variations caused by cathode wear.

Free-standing NiTi films were needed for TEM observation and tensile tests. The NiTi films were sputtered onto cleaved potassium chloride (KCl) single crystals, onto micro-polished copper sheets, and onto glass microscope slides. Films could be separated from KCl using water and nitric acid could be used to dissolve the copper sheets. Films on the glass substrates could be manually peeled off. However, the films were very brittle when deposition temperatures were above 623 K. Eventually, high purity NiTi films were deposited on quartz plates. Then good quality free-standing NiTi films could be mechanically separated from the quartz substrates.

Quartz plates with a thickness of 1.5 mm were cut into 22 mm × 22 mm squares. Before loading them onto the substrate holder the plates were cleaned with acetone and methanol successively in an ultrasonic cleaner for five minutes to remove contamination. After setting up the specimens and pumping down the chamber, the chamber wall was baked by heating tapes at approximately 353 K and substrates were baked by two-sided substrate heaters (Figure 2-9) at 623 K. Baking for 18 hours was necessary to drive out water vapor absorbed on the wall of belljar and other fixtures inside the chamber. Then the cooling water was introduced into the tubing surrounding the chamber and power for the substrate heaters was gradually adjusted to the selected deposition temperature. Two hours was allowed to elapse in order to establish steady state heat transfer conditions. During the sputtering the temperature readings from both front and back thermocouples were controlled to within ±5 K of the desired value.

The base pressure attained in the vacuum system was less than 3×10^{-6} torr (4×10^{-4} Pa) at process temperatures between 573 K and 773 K. Argon working gas was bled into the deposition chamber though the preheated titanium getter. The argon pressure was chosen as a minimum to sustain a plasma discharge at each selected temperature. Prior to the exposure of the substrates the water-cooled target was presputtered for 15 minutes at full power lever to clean the target surface and to attain a steady-state sputtering condition. The floating potential of the substrates during the sputter deposition was +6 to +8 volts. After sputtering for 2 hours, which typically yielded NiTi films with thickness between 4 and 7 μm, the substrates were cooled to room temperature in the vacuum chamber at an initial rate of 0.5 K/sec. A plot of the substrate temperature and base pressure vs. time for a typical deposition run is shown in Figure 2-12.

The experimental set-up and deposition procedure for Kapton substrates were essentially the same as that for quartz substrates just described. The deposition parameters and resultant film compositions are tabulated in Table 2-1. For NiTi films produced by the hot-substrate deposition, the notation 'H---' is used in the present work where the 'H' signifies 'hot deposition' and three digits signify the substrate temperature of deposition in Kelvin.

2.3.2. Thermal Treatment of As-Sputtered NiTi Films

Some as-sputtered NiTi films were given a post-deposition anneal at various temperatures between 858 K and 1123 K for the purpose of producing microstructures with a variety of grain sizes and precipitate morphologies. A quartz-tube vacuum furnace was used for annealing as schematically illustrated in Figure 2-13. The vacuum chamber was pumped by an Alcatel 5400 turbomolecular pump having a pumping speed of 400 liters/sec. The external electrical resistance furnace could be raised or lowered around the quartz tube manually. A titanium getter which contained pure titanium wires was set in the center of the quartz tube to reduce oxidation of the NiTi films. Free-standing NiTi films were loaded on a titanium wire rack.

The furnace temperature was maintained by a programmable Omega CN8600 controller. The vacuum chamber the was first linearly ramped to a temperature of 575 K in 8 hours and baked at that temperature for 4 hours, then linearly ramped to selected annealing temperatures in 2 hours. After annealing for one or two hours the power for furnace was shut off. Two cooling methods, radiative and furnace cooling, both were kept in vacuum condition, were used in the present study. In radiative cooling, the furnace was elevated quickly and the hot quartz tube was exposed to the ambient immediately after terminating the annealing. The quench rate achieved was 2.0-1.4 K/sec in the temperature range of 1044-799 K. In furnace cooling, it usually took two hours to cool the specimens down to below 373 K. During the entire annealing process, the base pressure was maintained under 10^{-5} torr (1.33×10^{-3} Pa).

For annealed NiTi films, the notation 'A-' is used where the 'A' represents 'annealing' and a digit designates the detailed heat-treatment path as indicated in Table 2-2.

2.4. Characterization of NiTi Films

2.4.1. Energy Dispersive X-Ray Microanalysis (EDX)

The chemical composition of the NiTi films was determined by the energy dispersive X-ray microanalysis (EDX) using ZAF[40] corrections in a Hitachi S-2500 scanning electron microscope (SEM). The NiTi films and the calibration materials were mounted onto a graphite specimen stage using double-coated carbon conductive tape. The calibration

---

[40] ZAF is a correction method to correct measured relative intensity ratio. In this method three effects are corrected: (1) atomic number effect, Z; (2) absorption of x-rays within the specimen, A; and (3) fluorescence effects, F.

spectrum was acquired from a piece of pure nickel. A piece of standard $Ni_{50.1}Ti_{49.9}$ alloy was used to determine the intensity ratios of Ni and Ti elements. Prior to taking spectrum the LaB_6 filament of the SEM was stabilized for at least one hour. All spectra were collected at 20 kV electron accelerating voltage, 15 mm working distance and 2000 × magnification. The spectra were then analyzed using a ZAF-4 program supplied by Link Analytical Incorporation. For the purpose of checking the accuracy of the analysis, two target alloys having known compositions were also measured at the same time. The compositions of two target alloys indicated in the manufacturer's specification were $Ni_{50}Ti_{50}$ (nominal) and $Ni_{51.3}Ti_{48.7}$, whereas that determined by this study were $Ni_{50.01}Ti_{49.99}$ and $Ni_{50.96}Ti_{49.04}$ respectively. Scatter of about 0.5 at.% are considered to be normal in the ZAF method.

2.4.2. Film Thickness Measurement

The thickness of films was measured using a Dektak II profilometer. The surface profile of thin films on quartz substrates was determined by scanning a fine stylus across a step produced by masking a part of the substrate during deposition. The scanning distance was 3 mm and scanning speed was 1 mm/min.

2.4.3. Electrical Resistimetry

The phase transformation temperatures of free-standing NiTi films were determined from electrical resistivity vs. temperature curves. The curves were measured by four-point electrical resistimetry on the first thermal cycle after cooling the films to the room temperature from high temperature of hot-substrate deposition or annealing. The experimental set-up was similar to that presented by Nam [1995]. A 5 × 1.5 mm^2 strip of NiTi thin film was connected to the fine gauge copper wires which linked to the electrical circuit by pure indium. The measurement cycled between 150 K and 380 K with a ramping rate of 3-5 K/min, achieved by adjusting the flow rate of liquid nitrogen to the test tube, and the dc current of power supply to the heating wire mounted on the test tube. Signals from the voltage drop across the NiTi films and the output of the thermocouples, i.e., temperature were plotted by a HP 7046A x-y recorder.

2.4.4. Differential Scanning Calorimetry (DSC)

A TA Instruments Model 2920 modulating differential scanning calorimeter was employed to determine martensitic and R-phase transformation temperatures and associated enthalpies of the NiTi film sputtered at 703 K. For the measurement, a 10.90 mg NiTi film sample was cut into small pieces and encapsulated into a 5 mm diameter aluminum pan. Another empty pan was used as the blank reference. The pans were cycled between 223 K and 373 K at the rate of 5 K/min. The transformation start and finish temperatures were determined by the tangential extrapolation method.

2.4.5. X-Ray Diffraction (XRD)

The crystal structure of as-sputtered NiTi films on Kapton substrates and free-standing NiTi films were verified by a Scintag XRD 2000 diffractometer using the Cu K_α radiation. The machine was operated at an accelerating voltage of 35 kV and a tube current of 25 mA. The scanning range and the scanning speed were $2\theta = 35\text{-}60^\circ$ and 0.3°/min respectively. In some case the specimens were heated to 353 K during data collection using a custom-built electrical resistive heater mounted at the back side of the sample stage. The temperature of specimens was measured by a *J*-type thermocouple.

2.4.6. Transmission Electron Microscopy (TEM)

TEM disc specimens, 3 mm in diameter, were shaped by a pair of sharp scissors. Then the discs were thinned with a Tenupol-3™ [Struers A/S. Denmark] twin-jet electropolisher using 12 % nitric acid and 88 % methanol by volume at 223 K. Using a masking technique, foils parallel to the plane of the deposit were obtained at three locations along the depth of the film: one at the film/substrate interface, one at the nominal midplane of the film, and one at the free-surface of the film, as shown in Figure 2-14. Conventional microstructure observation, precipitate analysis and grain texture determination were conducted in a Hitachi H-800 TEM operated at 200 kV and equipped with a double-tilt specimen stage. Cooling stage observation was performed in a Jeol 100 CX TEM operated at 100 kV and equipped with a single-tilt cooling stage. Precipitate analysis of as-sputtered NiTi films was made in a Jeol 2000 FX TEM operated at 200 kV, using the smallest available selected area diffraction (SAD) aperture ($d = 30\ \mu m$).

In physical vapor deposition, most deposits exhibit a strong preferred grain orientation at low-to-intermediate deposition temperatures and tend to a more random orientation with increasing deposition temperature [Bunshah, 1982]. Several techniques are available to determine preferred grain orientation (i.e., texture) in thin films. The pole figure method in the X-ray diffraction can provide a detailed orientation distribution. However, it collects diffracted beams from the specimen to a depth of several micrometers and does not resolve the signals from the different layers of the thin films. Electron microdiffraction in TEM may give ambiguous result unless either the textures are very strong or diffraction patterns are taken from many individual grains. In contrast, the method of analyzing diffraction patterns with tilting the specimen over a wide range in the TEM can effectively determine the textures of individual layers if the specimen with various sampling layers can be prepared. Tang and Thomas [1993] have successfully analyzed the texture evolution versus thickness of Cr thin films sputtered onto NiP-coated AlMg substrates using the sample tilt method.

It is known that the reciprocal lattices of thin films with randomly oriented grains can be obtained by rotating the reciprocal lattice of single crystal around the origin, whereas, the reciprocal lattices of thin films with fiber-texture can be obtained by rotating reciprocal lattice of single crystal around the texture axis. In the reciprocal space the former is concentric spheres while the latter consists of layered concentric rings. The selected area diffraction patterns (SADP's) are the intersections of those reciprocal spheres or rings and the Ewald sphere.[41] For the films with randomly oriented grains, there is no change of SADP's upon the specimen tilting. But for the textured films, tilting moves zero-order layer rings away except at the locations along the tilting axis and makes the rings in the adjacent layers intersect the Ewald sphere.

Based on the experimental results made by Gisser *et al.* [1992], NiTi films formed at the elevated temperatures have (110) fiber texture. As a starting point, it is logical to assume that the same texture will present in the present study. Figure 2-15a shows the reciprocal lattices of single-crystal (B2) with zone axis [110] and Figure 2-15b shows the geometric representation for calculating the positions of diffracted arcs.[42] The following formula gives the positions of diffraction arcs:

$$\varphi = \sin^{-1}\left(\frac{d}{R\sin\theta}\right) \tag{2.1}$$

where φ is the angular distance of the arcs measured from the tilting axis in the image plane (Ewald sphere), d is the distance between the zero-order reciprocal rings and higher-order reciprocal rings, R is the radius of diffracted arcs in the image plane and θ is the tilting angle of the specimen. For the (110) texture, at a tilting angle of 30°, angles between the tilt axis and the diffraction arcs in image plane are $\varphi = 90.0°$ for the {110} ring, $\varphi = 35.3°$ for the {211} ring and $\varphi = 26.6°$ for the {310} ring etc. By comparing these calculated results with the tilted diffraction patterns, whether a (110) fiber texture presented could be determined.

---

[41] The Ewald sphere can be considered as a plane because of the short wavelength of the electrons.

[42] Instead of diffracted spots, the diffracted arcs were observed in practice. This is due to a imperfect fiber texture in which the ideal concentric rings of the reciprocal lattice spread into the concentric spherical bands.

2.4.7. Tensile Tests

In the present work, the isothermal tensile tests were carried out in a Minimat™ miniature tensile tester [Expanding Polymer Science] using a strain rate of 6.8×10^{-5} to 3.4×10^{-4} /sec at various temperatures.[43] The machine was equipped with a IBM compatible PC and an electronic controller having displacement or load controlled testing capacity. The 20 N load cell and the displacement of the crosshead were independently calibrated by using standard weights and an extensometer respectively. A pair of grips were designed and machined from a 1000-series aluminum alloy plate as shown in Figure 2-16. The grips were made to be much stiffer than the thin film specimen in order to minimize the elongation caused by the grips. The minimum cross-section of grips was 2×8 mm^2 which is about 1300 times greater than that of specimens. Two design features of the grips were important to make the tensile tests successful as seen in inserted sketches in Figure 2-16: (a) Both grips were rotatable around the joint pin which prevented the specimen being torn and bent due to an imperfect alignment in specimen loading. (b) One surface of the grips was machined with a radius about $R = 50$ mm. This surface provided a great compressive force and eliminated the slippage of the specimen.

The thin film specimens were cut using a pair of fine blade scissors. The gauge length and width of the specimens were approximately 6 mm and 1.5 mm. Test temperatures were maintained within ±2.5 K by a methanol flow, pre-cooled to the desired temperature by liquid nitrogen, for temperatures below ambient, and by an electrically heated chamber at higher temperatures. The lowest temperature that could be controlled in the methanol flow was 198 K which is below the M_f temperatures of most films in this work. For each temperature-series of stress-strain curves, a single specimen was used, with the first of the tests conducted at the lowest temperature in the series. In each case,

---

[43] In bulk NiTi, it has been shown that the strain rate has a strong influence on stress-strain responses [Mukherjee, Sircar and Dahotre, 1985; Shaw and Kyriakides, 1995]. This is because stress-induced phase transformations also liberate heat and the heat transfer in bulk tensile specimens is slow. In the present study, however, the specimens are very thin and the effect of straining rate can be neglected. The temperature of the thin film specimens can be considered equal to that of the surrounding.

after completion of a stress-strain loop, the specimen was heated to 373 K, and then cooled to the temperature selected for the subsequent test with care taken to avoid overshoot. To prevent premature fracture, maximum total strain for any individual test was limited to 4 %.

In conventional tensile tests, the test bar has a reduced gauge cross-section for the purpose of eliminating the stress concentration at the grip areas and an extensometer is attached at the center region of the specimen where a uniform deformation is assumed. In the present work, however, rectangular thin film strips were used as the tensile specimens due to the difficulties of handling the thin films. Besides, the tensile strain was evaluated from the measured crosshead displacement, since the extensometer would impose a considerable constraint force on the thin film specimen. Next, the stress state of tensile specimens is estimated by finite element analysis and the initial sites of fracture are predicted.

The dimensions of the gauge section were approximately 6 mm × 1.5 mm × 6.5 μm. The problem can be treated as the plane-stress state since the thickness of specimens was about 1000 times smaller than other two dimensions and there were no loads applied in the coordinate direction parallel to the thickness. Figure 2-17 shows the finite element grid of the specimens. For boundary conditions it can be assumed that at the ends of gauge section neither x-displacement nor y-displacement exists owing to clamping of grips. In the mid-section of the test strip (A-A plane in Figure 2-17) the nodes have the same x-displacement. For simplicity, elastic deformation is considered in the analysis. Entering mechanical parameters $E = 50$ GPa, $\nu = 0.3$ for NiTi alloys and $\varepsilon = 0.25$,[44] a contour map of the magnitude of the maximum principal stress can be plotted by Marc® finite element analysis package as shown in Figure 2-18. The dashed frame in the background represents the image of the specimen before stretching.

The fractography, which will be discussed in Section 3.5, reveals a well-defined ductile fracture characteristic referred to as dimples. The fracture was formed through void

---

[44] A large tensile strain was chosen in favor of illustrating deformation in each point of the specimen.

nucleation, growth and coalescence under normal tensile stress [Dodd and Bai, 1987]. The sites of the fracture can be predicted from the maximal principal stress contours. As indicated in Figure 2-18, the fracture should start at edges near the ends of the gauge section. Figure 2-19 is a plot of a number of samples fractured vs. the normalized *x*-position where the fracture occurred. It is in agreement with the prediction in spite of some scattering which may be caused by the imperfect by cut edges of the specimens.

2.4.8. Scanning Electron Microscopy (SEM)

The secondary electron images of cross-section of the annealed film and the fracture surface of tensile samples were observed in the Hitachi S-2500 SEM. The SEM was operated at 20-25 kV at a 15 mm working distance. To examine the cross-sectional morphology of the annealed film, free-standing film was mounted in epoxy resin and finally polished using a water suspension of 0.05 μm alumina powders. The polished surface was then chemically etched in a solution consisting of 4 parts HNO_3, 2 parts H_2O and 1 part HF by volume for 15 seconds at the room temperature. To observe the fractography of NiTi films, the fractured films were mounted onto an aluminum stage using carbon conductive tape with the fractured surface upward. To get the best image contrast, the specimen stage was tilted in a range between 20° and 45°.

CHAPTER 3

RESULTS AND DISCUSSION

In this chapter, experimental findings and related discussion are presented. First, the microstructures of as-sputtered and annealed films, respectively, are presented in Section 3.1 and 3.2. The phase transformation characteristics of the films are described in Section 3.3. Deformation behavior of NiTi films is reported in Section 3.4. Finally, the fractography of NiTi films is discussed in Section 3.5.

3.1. Microstructure of As-Sputtered NiTi Films

3.1.1. TEM Observation

On examining three regions of film H573[45] (the interface, midplane and surface), it was found that an amorphous structure formed through the entire thickness of the film. Figure 3-1a and 3-1b, respectively, are a bright-field (BF) image and a corresponding selected area diffraction pattern (SADP) sampled at the midplane of the film. The micrographs show a completely featureless structure (Figure 3-1a) and a broad, diffuse halo diffraction-pattern[46] (Figure 3-1b), which is normally observed in amorphous materials.

Figure 3-2a and 3-2b are BF image and the SADP taken at the interface of the film H598. The micrographs display the same features as shown by the film H573, indicating that the interface of the film H598 has an amorphous structure. Figure 3-3a and 3-3b were

---

[45] As indicated in Section 2.3, the notation 'H---' is used in the present work where the 'H' signifies 'hot deposition' and three digits signifie the substrate temperature of deposition in Kelvin.

[46] The average interatomic distance of amorphous NiTi determined from this pattern is 0.212 nm.

taken at the midplane of the film H598. The SADP reveals a single-crystal diffraction pattern in the $[110]_{B2}$ zone, together with a superimposed diffuse halo pattern scattered from an amorphous undelayer. Since the SADP was taken from the whole scope of the Figure 3-3a, the initial crystallite with an in-plane size of 750 nm is a monocrystal although the image contrast is different within the crystallite. Several such crystallites have been examined. They were all in the [110] zone but with random in-plane orientations. It is clear that at the substrate temperature of 598 K the crystalline NiTi phase started to nucleate on the amorphous precursor near the midplane and with their (110) planes aligned parallel to the plane of the film. At the surface of film H598, a very fine structure of crystal grains, 95 nm in average diameter, can be seen (Figure 3-4a). Strain contrast arising from the precipitates can be discerned (the strain field contrast will be discussed later in this section). The elongated grain images in Figure 3-4d obtained after tilting the specimen through 45° suggest a columnar grain structure. Figure 3-4b and 3-4c are the associated SADP's taken at a tilt of 0° and 30° respectively. Using the method of determining grain orientation described in the Section 2.4.6, a strong (110) fiber-texture can be verified. The non-even intensities of the diffraction rings in Figure 3-4b reflect the restricted in-plane grain orientations.

Figure 3-5a, which is taken at the interface of the film H623, exhibits a fine-grained structure having average in-plane grain size of 85 nm and very fine precipitates 12 nm in length, also showing evidence of strain-field contrast. Careful examination around the perforation area of the TEM foil revealed that the layer first deposited, which had a thickness of less than 200 nm, is amorphous.[47] Figure 3-6a and 3-6d are BF images of the midplane of the film H623 recorded at the tilt of 0° and 45°, respectively, showing the columnar structure. At the surface of the film H623 (Figure 3-7a), a well-defined polycrystalline structure with fine precipitates can be seen. The associated SADP's of each layer indicate that the (110) fiber-texture prevails throughout the bulk of the film.

---

[47] The thickness of amorphous was estimated from the curved edge in perforated areas of TEM foil.

Figure 3-8a, sampled at the interface of the film H673, shows the initial crystallites having the average grain size of 240 nm developed from the very thin amorphous layer. Although having low contrast, precipitates averaging 55 nm in length can be distinguished. Figure 3-9a is BF image taken from midplane of the film H673. The interior of the grain exhibits the fine precipitates 20 nm in length surrounded by strain fields. The precipitates were aligned roughly in the same directions within each grain. As indicated by the arrow A, a perfect 'butterfly' shape of the image contrast arising from lattice misfitting strain field can be seen around a precipitate particle.[48] Again, the columnar structure in the midplane of the film was verified by tilting the specimen (Figure 3-9d). Figure 3-10 gives the BF image of the surface plane. The tilted SADP's (Figure 3-8c and 3-9c) again show the (110) fiber-texture.

Figure 3-11a is a high magnification image of precipitate with 'butterfly' shaped contrast having been shown in Figure 3-9a. The particles could be indexed as the Ni_4Ti_3 phase, as will be discussed in Section 3.1.4. The strain fields around Ni_4Ti_3 particles comes from the lattice mismatch between particles and B2 matrix. The habit plane of precipitate is $\{111\}_{B2}$ and the maximum mismatch, $\delta_m = (d_{(111)NiTi3} - d_{\{111\}B2})/d_{\{111\}B2} =$ -2.9 % [Li and Chen, 1996], is along the normal to the precipitate disk as shown in Figure 3-11b [Kainuma and Matsumoto, 1988]. This minus value indicates a tensile strain perpendicular to the precipitate disk.

A further increase of the deposition temperature above 673 K led to a dramatic change in the microstructure. At interface of the film H723 (Figure 3-12a), extremely fine grains, 25 nm in diameter, were nucleated on very thin initial amorphous layer estimated to be 20 nm in thickness. The unchanged SADP's upon tilting implies the absence of texture (Figure 3-12b, 3-12c). A BF image from the midplane (Figure 3-13a) shows grains with clear and smooth boundaries and the lenticular-shaped precipitates with slightly wavy

---

[48] Ashby and Brown [1963] have predicted the image profiles for particles with spherically symmetrical strain fields. The profiles displayed the characteristic 'butterfly' shape of the image contrast.

boundaries and longitudinal size comparable to the matrix grain sizes. Neither strain contrast nor misfit dislocations was found in the regions surrounding the precipitates. A random grain orientation also appears in the midplane (Figure 3-13b, 3-13c). The surface plane of film H723 exhibits a microstructure similar to that of the midplane except for somewhat larger grains and smaller precipitates (Figure 3-14). Three ranges of precipitates can be seen at the lower part of the micrograph. (The growth of precipitates will be discussed in Section 3.1.4.) Figure 3-15 shows micrograph and associated SADP taken at the midplane of the film H703 revealing crystalline B2 grains and transgranular precipitates which are similar to that of film H723.

The microstructures and the grain orientations in the three layers of the film H773 (Figure 3-16, 3-17 and 3-18) are essentially the same as those of the film H723 except for slightly larger grains and precipitates (270 nm vs. 250 nm for B2 grains, and 220 nm vs. 150 nm for precipitates). Finally, the NiTi matrix and precipitate morphologies of as-deposited NiTi films are summarized in Table 3-1.

3.1.2. Thin Film Microstructure: Discussion

The TEM observation presented in the preceding section revealed that a fully amorphous NiTi film was produced at the deposition temperature of 573 K (film H573). As discussed in Section 1.5.2, amorphous films are generally formed under conditions where the surface mobility of arriving species is very limited. In intermetallic compounds the requirement for coordinated adatom motion to form an ordered crystalline lattice increases the tendency to form amorphous structure. As a result, crystalline NiTi films can only form at high enough temperatures. In the present work, the NiTi crystals started to nucleate at a deposition temperature of 598 K (film H598), and a fully crystalline NiTi film was produced at a deposition temperature of 623 K (film H623).

NiTi crystallites were observed to nucleate on an initially amorphous layer during hot substrate deposition ($T > 598$ K). Generally, the resultant grain size of the initial polycrystals is controlled by three kinetic phenomena: crystal nucleation, growth and coalescence [Thompson, 1994]. The grains nucleate and grow on the untransformed material (the amorphous phase) until they fill space by impinging on one another, followed by grain boundary motion.

For nucleation and growth processes, if crystals are assumed to nucleate at a constant rate, I, at random locations, and to grow isotropically at a constant rate G, the well-known Johnson-Mehl structure results [Johnson and Mehl, 1939]. Mahin, Hanson and Morris [1980] analyzed the Johnson-Mehl model through computer simulation and presented the growth sequence leading to Johnson-Mehl structure as illustrated in Figure 3-19. It has been shown that the final average in-plane grain diameter D is given by [Gilbert, 1962]:

$$D = 1.448\left(\frac{G}{I}\right)^{\frac{2}{3}} \tag{3.1}$$

It can be seen from this equation that a higher nucleation rate and/or lower grain growth rate produce smaller final grain size.

From Figure 3-3, 3-8 and 3-12, it is apparent that the in-plane grain size of the initial crystalline phase rapidly decreases as the deposition temperature is increased. The nucleation rate must therefore increase monotonically as the temperature increases, since both the grain growth and the coalescence are thermally activated processes and would not be expected to decrease as the temperature increases. Furthermore, the nucleation rate must grow faster than grain growth and the coalescence. The higher nucleation rate of NiTi crystals at the higher temperature is also consistent with the TEM observation that a thinner initial NiTi amorphous layer is formed at higher deposition temperatures.

The specimen tilting method indicated a columnar grain structure in films H598, H623 and H673. Such columnar structures are commonly found in thin films formed in physical vapor deposition (PVD) at relatively low substrate temperatures. The grain growth in polycrystals involves grain boundary migration which results from diffusive jumps of atoms across the grain boundary. In normal grain growth, the curvature of the grain boundary provides the driving force which minimizes total grain boundary area. Based on experimental results discussed further in Section 3.2.1, the fine columnar grain structure of NiTi films was found to be stable in a one-hour, 858 K post-deposition annealing process. This fact suggests that little bulk diffusion for significant grain boundary migration would occur in the deposition time/temperature range of the present work ($T \leq 773$ K). However, the activation energy for surface diffusion is lower than that for bulk diffusion. Consequently, even when the temperature is too low for significant diffusion in bulk, the diffusion necessary for grain growth during deposition can occur readily at a free surface.

Srolovitz [1986] coupled grain boundary migration and thin film growth and proposed a statistical model using a Monto Carlo approach for the evolution of grain structure during deposition. The columnar grain structure formed during deposition can be interpreted as follows: Within a certain temperature range, the structure below the free surface is frozen-in because bulk diffusion is sluggish and two-dimensional grain growth develops only at the free surface of growing film. By superimposing two-dimensional grain growth upon film growth (increasing thickness), a columnar structure can be formed as shown in Figure 3-20. The shape of the columnar grains is controlled by relative magnitudes of in-plane grain growth rate and the deposition rate.

The columnar grain structure in films H723 and H773 could not be verified by the tilting method due to large in-plane grain size. However, as mentioned earlier, significant bulk diffusion did not occur in a one hour, 858 K annealing process. It is thus reasonable to conclude that very little bulk diffusion took place in sputter processes even at substrate temperatures of 723 K and 773 K. Thus, the columnar grain structure could also be expected.

Comparing Figure 3-16, 3-17 and 3-18, which were taken from the interface, midplane and surface of the film H773 respectively, in-plane grains grew rapidly in first half of the growth period (from $D_{B2} = 30$ nm to $D_{B2} = 270$ nm), then the grain growth slowed down in the second half (from $D_{B2} = 270$ nm to $D_{B2} = 320$ nm). This fact can be explained as follows: The growth rate of the mean diameter of the grains is proportional to the curvature of the grain boundaries. When grains grow larger, total areas of grain boundaries and thus grain boundary energy becomes smaller and the driving force decreases.

3.1.3. Formation of Texture

It has been shown that the first crystalline grains to form nucleated from the amorphous layer, and that (110) texture developed in the films H598-H673, deposited in the temperature range for which surface diffusion dominates. This means that the atoms in the surface have the ability to arrange themselves into the lowest energy configuration. Consider the disk-shaped initial crystallites having the thickness within which the atoms are able to move via the surface diffusion and having the major diameter of the in-plane grain size. On one side the crystallites are in contact with the amorphous NiTi and on another side they are in contact with the vacuum environment. Because the interface and surface[49] energies of the crystals depend strongly on the crystallographic face, the different orientation of the crystallites will lead to different interface and surface energies [Thompson, 1990].

For the films deposited at higher temperatures ($T \geq 723$ K), the initial grains impinge quickly to form extremely small in-plane grain size ($D_{B2} = 25$ nm) due to the high nucleation rate. In this case, the surface and interface energies for such crystallites are less significant because the interface and surface areas of the disk are a relatively small fraction of the total boundary area. The driving force arising from the surface energy anisotropy is

---

[49] The boundary between the gas phase and the solid or liquid phases is refereed as the surface. The interface is the interphase boundary. In this sense the surface is also the interface but a special interface.

not high enough to align the initial grains to the preferred orientations. The films with random grain orientations are produced as schematically illustrated in Figure 3-21a.

For films deposited at lower temperatures ($T \leq 673$ K), the initial grains have in-plane grain size greater than 85 nm due to a decreased nucleation rate. The interface and surface energies are important because these disk-shaped crystallites have considerable areas in the interface and surface, and grains with orientations that minimize total surface and interface energy are favored. Consequently, (110) texture develops in hot-deposited NiTi films. Moreover, the amorphous substrate and vacuum environment have no interface and surface energy anisotropy for in-plane grain rotations, films formed at lower temperatures present a (110) fiber-texture, i.e., the (110) planes of grains are restricted to being parallel to substrate plane but with no preferred in-plane orientation. This circumstance can be schematically illustrated in Figure 3-21b.

The fine grains ($D_{B2} = 95$ nm) displayed on the surface of the film H598 (Figure 3-4) nucleated from the initial crystalline grains having large in-plane size of $D_{B2} = 750$ nm (Figure 3-3). Locally, the initial large crystalline grains can be considered as single-crystal substrates for the fine grains nucleated on them. As mentioned by Thompson [1990], for polycrystalline films formed on single-crystal substrates there should always be a tendency to form a three-dimensionally constrained relationship, i.e., epitaxial orientations between a grain and the substrate in order to minimize the interface energy. In Figure 3-4b, the selected areas diffraction rings having non-uniform intensity, reflect a constrained in-plane grain orientation. The reasons that fine grains re-nucleated from initially crystalline grains are not clear, however, it may be that the surface diffusion at 598 K is be sufficient for grains continuously growing at large scales.

3.1.4. Growth of Precipitates

The morphologies of precipitate observed in the hot-deposited films are of two types: the fine precipitates surrounded by strain fields as shown in the Figure 3-9a, and coarse transgranular “wavy plates” as shown in Figure 3-17. In order to index the fine precipitates, the SADP taken from the midplane of the film H673 (Figure 3-9b) was magnified as shown in Figure 3-22. The $(110)_{B2}$ ring in the diffraction patterns was used as an internal standard for calibration. Within the variation of 2 %, each diffraction ring in the patterns could be indexed by assuming either the B2 structure of the NiTi with $a_0 = 0.3015$ nm [Philip and Beck, 1957], or the rhombohedral Ni_4Ti_3 structure with $a_0 = 0.6610$ nm and $\alpha = 113.65°$ [Nishida, Wayman, Kainuma and Honma, 1986]. The indices of Ni_4Ti_3 phase were underlined in the Figure 3-25 for a purpose of distinguishing them from the B2 reflections. It is noted that the ring patterns in the Figure 3-22 confirm the (110) grain orientation since the $(310)_{B2}$ reflection having a radius of 64.3 mm is absent.[50]

For the coarse precipitates formed at the midplane of the film H773 (Figure 3-17), two SADP’s were recorded using the smallest SAD aperture in Jeol 2000 FX TEM, as shown in Figure 3-23. The SADP’s were sampled from two areas of the foil each approximately including one grain. The strong reflections in the SADP’s can be indexed using the B2 structure of the NiTi, while the weak reflections (the indices are underlined) can again be indexed using the rhombohedral Ni_4Ti_3 structure. The Figure 3-23a shows $[13\bar{3}]_{B2} // [1\,\bar{1}\,1]_{Ni4Ti3}$ zone and the Figure 3-23b shows $[\,\bar{1}3\,\bar{2}]_{B2} // [1\,\bar{1}0]_{Ni4Ti3}$ zone. Some diffraction spots that do not belong to these zones were reflected from partially sampled neighboring grains. The orientation relationships between Ni_4Ti_3 precipitates and the B2 matrix can be converted to:

$$(\bar{1}01)_{Ni4Ti3} // (3\bar{2}1)_{B2},\ \ [010]_{Ni4Ti3} // [01\bar{2}]_{B2}$$

for the zone $[13\bar{3}]_{B2}$ in Figure 3-23a, and

$$(00\bar{1})_{Ni4Ti3} // (421)_{B2},\ \ [100]_{Ni4Ti3} // [01\bar{2}]_{B2}$$

---

[50] If the lattice planes {*hkl*} are reflected in the image plane (Eward sphere) having the zone axis ⟨*uvw*⟩, the scalar product of the zone axis with each individual reflection {*hkl*} has to be zero, i.e., $uh + vk + wl = 0$ [Heimendahl, 1979].

for the zone $[\bar{1}3\bar{2}]_{B2}$ in Figure 3-23b. The above orientation relationships were first proposed by Nishida and Wayman [1987]. The boundaries between precipitate and matrix are very clear and no boundary dislocation or strain field contrast can be seen. It can be speculated that the precipitates have lost the coherency during ripening. However, the observed orientation relationships between the Ni_4Ti_3 precipitates and B2 matrix, which were established during the nucleation phase of the precipitation, are seen to persist.

Since as-sputtered films have overall composition of 51.0-52.3 at.% Ni, the films are hyperstoichiometric in NiTi. During the hot-substrate deposition, Ni-rich particles will precipitate in the film to reduce the free energy of the matrix. On the other hand, the formation of the second phase creates additional interface energy. There is thus always a tendency to increase the size of the individual particle but decrease the number of particles. The diffusion of Ni atoms makes it possible for Ni-rich precipitate growth to continue.

Several investigations have shown that the Ni_4Ti_3 phase readily precipitates through bulk diffusion in solution-treated Ni-rich NiTi alloys at an annealing temperature as low as 673 K [Nishida and Wayman, 1984; Wu, Lin and Chou, 1989; Xie, Zhao and Lei, 1989]. The TEM micrographs of the film H723 give evidence for growth of Ni_4Ti_3 phase in the films through the bulk diffusion. The sizes of the Ni_4Ti_3 phase is 150 nm in the midplane (Figure 3-13) but 65 nm in the interface (Figure 3-13). The precipitates in the midplane thus apparently coarsened during deposition.

At a given temperature surface diffusion proceeds more rapidly than dose bulk diffusion. It is expected that the precipitates nucleated and grew also via surface diffusion. Ni_4Ti_3 precipitates having a considerable size are observed in the surface of the films H723 (Figure 3-14) and H773 (Figure 3-18). The particles must have developed during the deposition, since after shutting off power to the sputter source and substrate heaters the film was cooled down to below 573 K (where no significant diffusion is assumed) in only few minutes.

Similar to the grain growth of NiTi, the growth rate of precipitates increases as the substrate temperature increases. The BF images of the midplane of films H673 (Figure 3-9) and H723 (Figure 3-13) show that the larger particles in smaller numbers were produced at the higher substrate temperature where the rate of diffusion is greater.

It is interesting to note that the precipitates did not nucleate within extremely fine initial grains (D_{B2} = 25 nm) even at the deposition temperature of 723 K, as shown in Figure 3-12 (film H723). There are a few possible ways to accommodate the extra Ni atoms in the film: forming supersaturated NiTi grains, increasing solubility in grain boundaries and creating a NiTi-Ni_4Ti_3 dual phase. However, the detailed structure is not clear yet at this point due to the difficulty of deconvoluting the precipitate reflections from the B2 reflections.

Experimental observation allows the size changes of B2 grains and precipitates as a function temperature in the three layers to be plotted as in Figure 3-24. There was a rapid change in B2 grain size in the first half of deposition course. Then B2 grain size only increased slightly in the second half of deposition course. It seems that the deposition temperature had strong effects on the microstructure of the initial crystalline layer. Figure 3-25 is a proposed structural model for Ni-rich NiTi films sputter-deposited at the temperature of 573-773 K based on TEM observation conducted in this study.

It is likely that the growth of ordered B2 grains involves the cooperative movement of both nickel and titanium atoms across the grain boundary, whereas the growth of Ni_4Ti_3 phase in the Ni-rich matrix mainly relies mainly on the movement of nickel atoms. The diffusivity of nickel in B2 NiTi is approximately an order of magnitude greater than that of titanium [Bastin and Rieck, 1974]. In amorphous phase, titanium is also thought to be a relatively slower diffuser [Chang, 1993]. For the Ni-rich NiTi system, a possible resultant film structure would be determined by the deposition temperature, and the active regions for surface and bulk diffusion of Ni and Ti. Figure 3-26 schematically represents such relationships.[51] In Region I, the surface diffusion of Ni and Ti are not active simultaneously. Films deposited at this region are generally amorphous in structure. However, in sub-region I_2, hyperstoichiometric precipitates may form via Ni surface diffusion in amorphous phase. In Region II, films consist mainly of columnar B2 grains. In sub-region II_2, large precipitates may be produced through Ni bulk diffusion and B2/ppt dual-phase microstructures similar to that of annealed films A1-A4 which will discussed in the next section may form. In Region III, bulk diffusion for both Ni and Ti dominate. Films with microstructures similar to that of fully annealed and aged films may result.

3.2. Microstructure of Annealed NiTi Films

In this study, the microstructures obtained from hot-deposition at below 773 K basically consist of fine columnar B2 grains and fine Ni_4Ti_3 second phase distribution. According to Ni-Ti phase diagram (Figure 1-10), Ni will redissolve at $T > 900$ K. An additional anneal to as-sputtered films at higher temperature (> 773 K) can provide a variety of additional combinations of grain and precipitate due to the activation of bulk diffusion. In this section, the microstructures of annealed NiTi films are analyzed.

3.2.1. Morphology

The first set of heat treatment experiments was conducted at 858 K for 1 hour. Figure 3-27, 3-28 and 3-29 are TEM bright-field images of films A1[52], A2 and A3 which were produced by aging the films H623, H673 and H723, respectively. They all show a dual-phase microstructure consisting of fine grains and coarse platelike precipitates. It appears that during the annealing the fine precipitates inside grains coalesced into large independent plates (compare the original microstructures in Figure 3-6, 3-9 and 3-13).

---

[51] The temperature boundaries for each regions in Figure 3-26 were estimated from the present work. Since diffusion is controlled by both temperature and time, a given microstucture may be formed either at lower temperature after longer time or at higher temperature after shorter time.

[52] As indicated in Section 2.3, for annealed NiTi films, the notation 'A-' is used where the 'A' represents 'annealing' and a digit designates the detailed heat-treatment path as indicated in Table 2-2.

However, the grain structure of the B2 NiTi phase remains nominally unchanged since neither in-plane grain size nor columnar grain structure has increased (Figure 3-28b). The film texture, of course, should not have been altered in the heat treatment, as is verified by Figure 3-28c, 3-28d, 3-28e and 3-29b.

To explore the minimum temperature for forming a dual-phase structure, the film A4 was produced at an annealing temperature of 813 K. Film A4 also displays the same dual-phase morphology (Figure 3-30). It can be concluded that at the annealing temperature of 813-858 K diffusive processes for B2 grain boundary motion have not become significant, whereas bulk diffusion for precipitate growth was quite rapid.

Figure 3-31 is an image of the film A5 obtained by annealing film H673 (Figure 3-9) at 988 K for 1 hour. The size of B2 grains increased from 0.22 μm to 0.64 μm during the annealing. Obviously, bulk diffusion for NiTi grain growth has occurred. Large lenticular precipitates 180 nm in length started to form within grains. According to the NiTi phase diagram proposed by Wasileski *et al.* [1971] (Figure 1-10b), at 988 K, nickel in excess of 50 at.% should have dissolved in the B2 matrix (the composition of A5 was Ti-51.0 at.% Ni), and the formation of precipitates must have occurred on cooling from 988 K to room temperature. For larger B2 grains (diameters > 0.5 μm) like those in film A5 and other Ni-rich films reported in literature [Nishida and Honma, 1984; Xie, Zhao and Lei, 1989], there seems a tendency for the precipitates to form inside the grains than outside grains (i.e., B2/ppts dual phase) in thermal treatment.

Figure 3-32 shows the microstructure of the film A6 produced by annealing film H673 at 1123 K for 1 hour. The film consists of large grains 2-5 μm in diameter and large lenticular precipitates about 1 μm in longitudinal direction.[53] The precipitates align along well-defined crystallograghic planes of the matrix.[54] In addition, very fine precipitate

---

[53] The sizes of grains and precipitates in the films A6-A8 were measured from the micrographs having lower magnification (10,000 ×). For a purpose of direct comparison, the majority of BF images in this work were prepared at the same magnification (165,000 ×).

[54] The formations of plate- or needle-shaped precipitate particles in such a manner that they are aligned along specific crystallographic planes is called *widmanstätten* structures [Reed-Hill, 1964].

particles with strain field contrast can be noticed in the area between the large precipitates. A band of matrix free of precipitation was left on each side of large precipitates due to the depletion of nickel atoms in these areas.

According to the TTT diagram (Figure 1-11) proposed by Nishida, Wayman and Honma [1986], any Ni_4Ti_3 particle should be dissolved at a temperature above 1023 K. The binary NiTi phase diagram indicates that solutionization should occur at 903 K. Film A7 was produced by annealing film H673 at 1073 K for 2 hours to form single NiTi phase and then subjected to radiative cooling. Figure 3-33 is the BF image of the film A7 showing the microstructure consisting of coarse grains (1.5 μm) and fine precipitates. The fine particles probably grew in the course of the cooling because it took about 5 minutes to cool the film to below 623 K. Precipitation tends to occur more rapidly at grain boundaries since the grain boundary is a favorable site for heterogeneous nucleation. Development of precipitation in grain boundaries depleted the Ni atoms in the vicinity of the boundaries. The coarse grain structure in the film A7 is also confirmed in a cross-section SEM micrograph as shown in Figure 3-34. Deep etched surface morphology reveals the crystallographic facets of the grains.

Film A8 was processed under the conditions similar for that of the film A7 except for an additional 673 K, 1 hour aging treatment. As seen in Figure 3-35, the grain size is about the same as that of film A7 because 673 K was too low for grain growth via bulk diffusion, but the precipitate particles had ripened. This microstructure is similar to that of Ni-rich bulk NiTi alloy formed at low temperature (673-723 K) aging after solution treatment [Nishida *et al.*, 1986; Xie, Zhao and Lei, 1989].

3.2.2. Structure of Precipitates in Annealed Films

The lattice structure of precipitates in annealed films were characterized using either electron diffraction in TEM or the XRD method. Films A1-A4 have the same dual-phase structure. The precipitate plate in film A3 was selected for indexing lattice structure because its greater size. Figure 3-36b and 3-36c are two single-crystal SADP's taken from the region indicated in Figure 3-36a. So as to exclude diffraction spots from the B2 matrix, the SADP's were taken on an isolated precipitate plate situated in the edge of the TEM foil. The precipitate can be indexed by assuming Ni_3Ti_2 phase having a monoclinic cell with constants: $a_0 = 0.441$ nm, $b_0 = 0.882$ nm, $c_0 = 1.352$ nm and $\gamma = 89.3°$ [Nishida and Wayman, 1987]. As a self-consistency check, the magnitudes of the tilt angle between the $[0\bar{1}0]$ zone in Figure 3-36a and the [110] zone in Figure 3-36b, and the theoretical angle between these two zone axes for Ni_3Ti_2 are compared. The former was measured to be 29.5°, while the latter is calculated from crystallographic data to be 26.4°. About 10 % deviation may be caused by improperly adjusted manipulator of double-tilting stage and/or imperfect equalization of diffracted spot intensity at 0° tilt. Thus it is concluded that the precipitates in film A3 are the Ni_3Ti_2 phase.

Figure 3-37 shows the XRD curve of film A5 recorded at room temperature (298 K). Besides the (110) B2 Bragg peak, four peaks match the reflections of Ni_4Ti_3 phase in 2θ angle between 35° and 60° within 2 % error. This indicates that the large lenticular precipitates formed within the grains are Ni_4Ti_3 particles.

Indexing of large lenticular precipitates in film A6 could be completed by assuming that they possess the Ni_4Ti_3 structure. Figure 3-38b and 3-38d are SADP's of zone $[0\bar{1}2]_{B2} // [001]_{Ni_4Ti_3}$ and zone $[230]_{B2} // [221]_{Ni_4Ti_3}$, respectively, taken from areas indicated in Figure 3-38a and 3-38c. The underlined indices represent the diffraction from the precipitates.

Figure 3-39 shows the XRD curve of the film A7. In order to reduce the complexity of the curve, the NiTi film was scanned at 353 K, which is about 40 K higher than its A_f,[55] to eliminate the reflections from the R-phase of NiTi. The spectrum shows the (110) B2

---

[55] The characteristic temperatures associated with the phase transformations will be represented in the Section 3.3.

peak and two Ni_4Ti_3 phase peaks in 2θ angle between 35° and 60°. The reflections of Ni_4Ti_3 phase are very weak due the small particle size (20 nm in length).

The XRD curves of the film A8 are shown in Figure 3-40. Curves (a) and (b) were taken from the same specimen at 353 K and room temperature respectively. The curve (a) identifies the (110) B2 peak and five Ni_4Ti_3 peaks in 2θ angle between 35° and 60°. In curve (b), the same set of the Ni_4Ti_3 reflections appears, however, the (110) B2 peak splits into two NiTi R-phase peaks: (011) and $(0\bar{1}1)$ with a separation about 0.4°. This is due to the B2 → R-phase transformation when the temperature is below T_R. Ling and Kaplow [1981] first found this interesting character in $Ni_{50.13}Ti_{49.96}$ bulk alloy. Recently, Nam [1996] reported similar XRD spectra in a $Ni_{50.3}Ti_{49.7}$ thin film specimen.

The TTT diagram of $Ni_{52}Ti_{48}$ bulk alloy shown in Figure 1-11 [Nishida, Wayman and Honma, 1986] verifies that compared with Ni_4Ti_3, Ni_3Ti_2 phase forms after longer aging process at higher temperature. The Ni_3Ti_2 phase is closer to the thermodynamic equilibrium state, but there is a higher energy barrier for its formation. In $Ni_{52}Ti_{48}$ bulk alloy, it would take over 100 hours for the completion of $Ni_4Ti_3 \rightarrow Ni_3Ti_2$ transition at 858 K. However, at the same temperature it only took one hour to transform Ni_4Ti_3 phase into Ni_3Ti_2 in the films A1-A4. The reasons for enhancing the formation of Ni_3Ti_2 precipitates are not fully understood. Nevertheless, one pronounced difference is the grain morphology. In Nishida, Wayman and Honma's work [1986] the grain size were greater than 100 μm and the Ni_3Ti_2 phase grew within grains and along specified crystallographic planes. However, in the present work the in-plane grain size of films A1-A4 is only about 0.1-0.3 μm and Ni_3Ti_2 particles formed in dual-phase structure. It is likely that the interface energy of the second phase and the matrix or parent grains played an important role in the precipitate formation.

As a summary, the in-plane views of various microstructure formed in the post-deposition annealing are schematically represented in Figure 3-41.

3.3. Phase Transformation Characteristics

3.3.1. Phase Transformations in As-Sputtered Films

In NiTi-based systems, many measurable physical values have been utilized to study the martensitic and R-phase transitions, such as electrical resistivity (ρ), enthalpy (H), internal friction (Q^{-1}) [e.g. Hasiguchi and Iwasaki, 1968; Wu, Lin and Chou, 1990], and magnetic susceptibility (χ) [Loloee, 1995]. Among them measuring electrical resistivity is most widely used because the simplicity of required equipment. For this reason the resistimetry was selected, together with the DSC (for measuring transformation ΔH), as techniques for determining transformation temperatures in the present work. Before discussing the experimental results, it is useful to discuss some general features of resistivity vs. temperature curve related to the phase transformation in NiTi system. By examining a large number of resistivity vs. temperature curves in the literature, it is found that:

(1) Compared with the parent phase and martensite, the R-phase has the highest electrical resistivity. During the R-phase transformation, $\Delta\rho/\Delta T$ becomes negative.

(2) The slope of the curve in martensite region is much steeper than that in austenite and R-phase regions.

(3) The hysteresis of R $\leftrightarrow$ B2 transitions is only about one tenth of that of M $\leftrightarrow$ R and M $\leftrightarrow$ B2 transitions.

Figure 3-42 schematically illustrates the classification of electrical resistivity vs. temperature curves for NiTi. Curve (a) shows a two-stage transformation sequence involving M $\leftrightarrow$ R $\leftrightarrow$ B2 phase transformations as discussed in the Section 1.2.1. Curve (a) can be decomposed into curves (b) and (c), which involve M $\leftrightarrow$ R and R $\leftrightarrow$ B2 transformations respectively. The curve (b) clearly shows that the characteristic temperatures A_s and A_f, respectively, indeed represent the start and finish temperatures of M $\rightarrow$ R transformation. Curve (d) is a two-stage curve but with an incomplete B2 $\rightarrow$ R transition. The martensitic transformation starts within the R-B2 mixture before the completion of the R-phase transition. Curve (e) shows the R ↔ B2 transformation which is essentially the same as the curve (c). This kind of curves can be frequently seen in the literature [e.g. Edmonds and Hwang, 1986; Stachowiak and McCormick, 1988; Wu, Lin and Chou, 1989; Xie, Zhao and Lei, 1989]. Curve (f) reflects the M ↔ B2 transformation. Similar curves have been reported for the Ni-Ti-Cu ternary system [e.g. Edmonds and Hwang, 1986; Chang and Grummon, 1992].

Figure 3-43 shows the electrical resistivity vs. temperature curves for several as-deposited films. Film H573 exhibits a negative temperature coefficient of resistivity in the temperature range of measurement (140-380 K).[56] This is a typical resistivity-temperature behavior of amorphous NiTi as reported by Ikuta *et al.* [1990], Nam [1995], and as discussed in previous crystallization annealing trial in this study (Figure 2-6, Section 2.2.1). The amorphous structure of the film H573 was confirmed by the TEM observation (Section 3.1.1).

The resistivity curve of film H623 shows that the M_s temperature was severely depressed to below the measurement range and only the R ↔ B2 transition occurred. This is the case of curve (e) in Figure 3-42. The curves of this sort have been reported for Ni-rich (≥ 50.5 at.% Ni) bulk NiTi alloys aged at 673-773 K for 1-2 hours after solution treatment [Xie, Zhao and Lei, 1989; Wu, Lin and Chou, 1989]. In the early stage of precipitation, the nickel atoms have not been fully depleted and the matrix has high nickel content which strongly suppresses M_s. Also, small precipitates still remain coherent with parent matrix. The combination of a higher Ni-content matrix and finely dispersed precipitates with coherency strain fields in the film is responsible for depressing the M_s temperature.

Films H673, H723 and H773 all display classical M ↔ R ↔ B2 two-stage transformation sequence commonly observed in Ni-rich bulk alloys aged at 673-773 K for

---

[56] The magnitude of the resistivity of film H573 in Figure 3-43 has been compressed three times with respect to other curves.

≥ 5 hours. Compared with H723 and H773, the H673 has highly dispersed fine precipitates with evidence of strain contrast. The Ni-content of the matrix may still have been hyperstoichiometric since the precipitates were small. Consequently, the M_s of film H673 was more depressed than that of other two films. The films H723 and H773 have similar microstructures, but the latter has a slightly higher Ni-content and thus displays lower M_s temperature.

A cold-stage TEM experiment was conducted to gain a better understanding of the effect of precipitates on martensite transformation. Figure 3-44 shows bright-field images of the midplane of H673 and H723 taken at 101 K which is well below their M_s temperatures. In the film H723 (Figure 3-44a), martensite twins were well-defined and spread over the entire grain regardless of the array of precipitate plates. This implies that the ripening of precipitates relaxes the lattice mismatch stress in particle/matrix interface. In contrast, the martensite twins in the film H673 (Figure 3-44b) were confined in small areas due to the stress field imposed by finely dispersed precipitates. As a result, the microstructure of H723 was more favorable for the formation of martensite thus led a higher M_s temperature. The phase transformation temperatures of as-deposited films are tabulated in the Table 3-3.

Both DSC and electrical resistimetry were performed to study the transformation of film H703. In the DSC scan shown in Figure 3-45a, initial scanning from room temperature to 373 K revealed an endothermic reaction at 314 K associated with the R-phase transformation having an enthalpy, $\Delta H^{R\rightarrow A}$, of 2.8 J/g. In the subsequent cooling scan, two well separated exothermic reactions were found with enthalpies of -3.0 J/g at 310 K and -4.1 J/g at 251 K, which are identified as $\Delta H^{A\rightarrow R}$ and $\Delta H^{R\rightarrow M}$ respectively. Reasons for the low magnitude of the latter datum are unclear, but on a second heating scan from 223 K to 373 K (indicated by double arrows), an endothermic peak at 310 K was found and is associated with the reversion enthalpy, $\Delta H^{M\rightarrow A}$, of 17.8 J/g. A small shoulder appears on this peak which coincides with $\Delta H^{R\rightarrow A}$ on the heating scan, indicating that the overall peak is a convolution of the M → R and R → A transformation enthalpies. The value of $\Delta H^{M\rightarrow R}$ can be calculated, $\Delta H^{M\rightarrow R} = \Delta H^{M\rightarrow A} - \Delta H^{R\rightarrow A} = 15.0$ J/g. Electrical resistivity curves are plotted in Figure 3-45b. The transformation temperatures determined from the electrical resistimetry are in good agreement with that of DSC results. Table 3-4 summarizes the transformation temperatures and enthalpies determined from above experiments.

3.3.2. Phase Transformations in Annealed Films

Films A1-A3 all displayed a similar NiTi-Ni_3Ti_2 dual-phase structure. As expected, they possess the same general type of electrical resistivity behavior (curves *a*, *b* and *c*, Figure 3-46). This type of curve has been defined in the Figure 3-42d as indicating that the martensitic transformation starts prior to the completion of R-phase transformation. Normally, both solution-treated specimens irrespective of the composition, and aged equiatomic specimens reveal this characteristic [e.g. Miyazaki, Igo and Otsuka, 1986; Miyazaki *et al.* 1982]. It is believed that the absence of precipitates in NiTi grains of the films A1-A3 promoted the martensitic transformation. The compositions of B2 grains in these films was very close to equiatomic since the M_s temperatures (= 271-282 K) are very close to those reported for solution-treated $Ni_{49.8}Ti_{50.2}$ (≈ 280 K) [Miyazaki *et al.*, 1982]. The platelike Ni_3Ti_2 particles residing between matrix grains have no effect of depressing the M_s temperature. Film A1 has a greater Ni-content than that of films A2 and A3 (52.3 at.% vs. 51.0-51.1 at.%), however, they all have almost the same M_s temperatures. The greater volume of precipitates in the film A1 (Figure 3-27) substantiates that the extra Ni atoms migrated into the Ni_3Ti_2 phase and maintained the composition of matrix at a relatively constant value. The unique structure of films A1-A3 provides a potential advantage to NiTi films such that the M_s temperature is independent of the composition in a certain range.

The resistivity curve of the film A5 (curve *d*, Figure 3-46) is similar to the curves of film A1-A3 as just discussed. The feature that the martensitic transformation starts prior to the completion of R-phase transformation is primarily due to the depletion of the extra Ni content in the matrix during the formation of coarse Ni_4Ti_3 particles.

Film A6 displayed the two-stage transformation behavior (curve *e*, Figure 3-46), although the composition of the matrix should have been near-equiatomic state due to the formation of large lenticular precipitates. The fine coherent particles with local strain fields are thought to lower the M_s temperature. The changes in resistivity for A → R and R → M transitions on cooling are very slow. This implies that the A → M transition proceeded in a broad temperature range. It is possible that two regions, the region of precipitate-free bands near the large precipitates which may have higher transformation temperatures and the region having fine precipitates which may have lower transformation temperatures, consequently transformed into the martensite on the cooling.

Film A7 showed ill-defined transformation behavior (curve *f*, Figure 3-46). The M_f temperature could not be unambiguously determined from the curve. The strain field surrounding each particles apparently impeded the transformations on cooling.

Both the microstructure and electrical resistivity scan (curve *g*, Figure 3-46) of film A8 are similar to that of bulk Ni-rich materials aged at 773 K after solution treatment [Saburi, Tatsumi and Nenno, 1982]. The dispersed lenticular precipitates with a moderate size enhances the R-phase transition. The rapid change in resistivity resulted from the uniform microstructure which allowed the film to transform in a narrow temperature interval.

3.4. Deformation Behavior of NiTi Films

Thermomechanical properties determine the usefulness of NiTi thin films as a stress-strain-temperature function material. In this section, stress-strain curves made at various temperature are discussed. Then correlation of measured thermoelastic parameters are examined by Clausius-Clapeyron equation. Finally, transformational superelasticity is discussed in terms of stress-temperature diagrams.

3.4.1. Ultimate Elongation of NiTi Films

Figure 3-47 shows ultimate elongation curves of films H673, H723 and A3 at a test temperature of 423 K. Initially, the films were in the B2 state since A_f temperatures for these three films are 309, 313 and 307 K, respectively. Each films display a yielding at a stress over 800 MPa. It is interesting to know whether the yielding was caused by stress-induced martensitic transformation or caused by slip in B2 lattice. According to Clausius-Clapeyron relations (as will be discussed in Section 3.4.4), the critical stresses to induce martensite at 423 K ($\sigma_{T=423K}^{P\to M}$) would be 1250, 1035 and 992 MPa for H673, H723 and A3 respectively. Clearly, the yielding in Figure 3-47, which occurred below the corresponding critical stresses to induce martensite for each films, was caused by significant permanent deformation in the parent phase. In other words, films H673, H723 and A3 at 423 K behave like conventional materials.

Figure 3-48 shows ultimate elongation curves of the same set of films at a test temperature of 323 K. All curves show three well-defined stages: first the elastic deformation in the parent phase, then a plateau associated with the parent-to-martensite transformation, and finally the elastic deformation of the martensite. The curves did not show significant yield in the martensite phase before fracture at stresses above 1000 MPa. Figures 3-47 and 3-48 indicate that the martensite yield point is greater than that of the parent phase. It also can be seen in the Figure 3-48 that the Young's modulus of austenite is 2-3 times greater than that of martensite. Similar result was reported in literature [e.g.

Shaw and Kyriakides, 1995]. The elastic modulus are functions of two things: the nature of atoms and their lattice structure [Smith, 1956]. In this case, austenite and martensite have the same atoms but different lattices and thus result in a great change in elastic modulus.

3.4.2. Isothermal Stress-Strain Curves of NiTi Films

In this section, the isothermal stress-strain curves obtained in this work are reviewed. The transformation temperatures of films were first determined by electrical resistivity measurement. Figure 3-49 shows stress-strain responses of film H623 at test temperature increments of 30 K.[57] Yielding due to the detwinning of martensite variants and stress-induced martensitic transformation did not occur even at stresses above 300 MPa. The thin film simply behaved as an ordinary metallic material. In film H623, the interspacing of precipitates is only 7 nm. High density of fine Ni_4Ti_3 particles which are rigid to deformation apparently blocked the development of martensite variants.

Figure 3-50 exhibits the stress-strain curves of films H673 at test temperature increments of 20 K. The film shows yielding plateaus related to the detwinning of martensite (at $T < M_s$) and stress-induced martensitic transformation (at $T > A_s$). Curves *f*, *g* and *h* display classical transformational superelasticity. Figure 3-51 shows the microstructure of film H673 which had experienced eight load/unload cycles as shown in Figure 3-50. Compared with its original structure (Figure 3-9), it is seen that the microstructure essentially remained unchanged. No dislocations were introduced by stressing that can be seen under high magnification. However, as indicated in Figure 3-50, a strain about 0.2 % was left after the last cycle. The slip at stress concentrations (such as the grip areas) of the tensile specimen, which may not have been detected in the TEM foil,

---

[57] As seen in the Figure 3-49, the difference between the slopes of loading and unloading curves are evident in (a) and (b) but not in (c) and (d). This phenomenon has been reported for gold polycrystalline film by Neugebauer [1960]. The lower slope on loading curves is thought to relate to the creep in grip region and/or uneven fastening of thin film specimen.

and unrecovered martensite after unloading may be responsible for this rather small permanent strain.

Figure 3-52 presents a series of twelve stress-strain curves generated from a specimen of film H703 at deformation temperature increments of 15 K ranging from 198 K (< M_f) to 363 K (> A_f).[58] The curves are substantially similar to those reported for bulk NiTi alloys [e.g., Miyazaki, Ohmi, Otsuka and Suzuki, 1982; Miyazaki and Otsuka, 1986; Shaw and Kyriakides, 1995]. Figure 3-53 shows the stress-strain curves of film H723. Similar to film H703, H723 also displays superior thermoelastic properties in terms of very small residual strains in the superelastic region ($T > A_f$) and less steep slope of yielding plateau (curves *e*-*h*). The deformed microstructure of film H723 is shown in Figure 3-54. Just like its undeformed structure (Figure 3-13), displaying well-defined precipitate particles and grains without any dislocations. Thus the film H723 also possesses a very stable structure against slip during stress-cycling.

Annealed films A2 and A3 possessed NiTi/Ni_3Ti_2 dual phase structure. Their stress-strain responses are shown in Figure 3-55 and 3-56 respectively. Residual strains about 0.2-0.3 % can be seen after unloading. Figure 3-57a and 3-57b are the images of deformed microstructure of film A3. Lack of transgranular precipitates led to the formation of dislocations and thus reduces structural stability against permanent deformation.

Figure 3-58 shows the stress-strain curves of the film A5 which consists of coarse NiTi grains and Ni_4Ti_3 particles. As NiTi grains grew coarser in the film A5, slip bands which formed by passage of a number of dislocations spread throughout entire grains as seen in Figure 3-59a. This is consistent with its very low critical stress for slip ($\sigma_s = 271$ MPa). As seen in the micrograph, the slip bands in different grains tended to align in a common direction in order to accommodate the maximum shear stress.

---

[58] At the highest test temperature $T = 363$ K, the film fractured at 4 % elongation and only the loading curve was recorded.

Figure 3-60 and 3-61 show stress-strain curves of films A7 and A8 respectively. Both films are composed of coarse NiTi grains with but different precipitate morphology. The loading curves of film A7 does not show any transformation yielding due to the high density of fine Ni_4Ti_3 particles with spacing of 12 nm. The film A8 having precipitate spacing of 60 nm shows a limited stress-induced martensitic transformation. The images of the deformed films (Figure 3-62 for A7 and Figure 3-63 for A8) indicate that, the microstructures were virtually unchanged in stress-strain cycling.

It may be concluded that, both small grain size and fine precipitates were found to promote a perfect transformational superelasticity. On the other hand, when the interspacing of precipitates was less than 12 nm (in films H623 and A7), the precipitates tended to impede stress-induced martensite transformation. The combination of fine B2 grains (0.25 μm) and precipitates with moderate interspacing (30-40 nm) in films H703 and H723 provided superior thermoelastic properties.

3.4.3. Classification of Stress-Strain Curves

One striking feature of shape-memory alloys is that in a certain temperature range the stress-strain behavior changes dramatically with temperature as seen in the preceding section. From Figure 3-52 (film H703) the stress-strain behavior of polycrystalline NiTi thin film associated with the martensitic transformation can be classified into six types depending on the value of deformation temperature, T, with respect to transformation temperatures M_f, M_s, A_s, and A_f.[59]

Type I ($T < M_f$, curves *a-c*): In the initial, unstressed condition, the specimen is entirely in the martensite phase with a self-accommodating morphology. Plastic strain due

---

[59] According to a study conducted by Miyazaki and Otsuka [1984], in the regime $T \leq T_R$, the strain associated with R-phase decreases with increasing temperature and reaches the minimum at $T = T_R$. This is consistent with the decrease in rhombohedral distortion with increasing temperature. In the regime $T > T_R$, the associated strain is constant irrespective of the test temperature. Overall, the strain associated with R-phase is so small ($\varepsilon < 0.5$ % in polycrystals) that it is not easy to detect even in the specially-prepared specimen. The strain associated with the martensite dominates the stress-strain behavior of NiTi system. For this reason, the classfication in this work is only focused on the martensitic transformation.

to detwinning and variant coalescence on loading is followed by elastic unloading of the martensite and a large plastic strain. Serrated feature in the loading curve implies the burst progress of variant rearrangement.

Type II ($M_f < T < M_s$, curves *d* and *e*): The martensite and R-phase coexist in this temperature range. Curve (e) reveals variations in the tangent modulus during plastic flow, i.e., two-stage yielding. According to the results reported by Miyazaki and Otsuka [1986], the first yielding is associated with the coalescence of R-phase variants, while the second yielding is caused by the growth of the stress-induced martensite as well as the continuation of variant coalescence in the martensite.

Type III ($M_s < T < A_s$, curves *f* and *g*): The specimen is fully in the R-phase state since only the R-phase is stable in a temperature between M_s and T_R ($> A_s$). The very low initial tangent modulus of the loading curves may be associated with R-phase variant reorientation. Each of these curves shows a nearly flat plateau connected with stress-induced martensite transformation. Only elastic recovery of the martensite occurs upon unloading since the temperature is still below the A_s.

Type IV ($A_s < T < A_f$, curve *h*): The R-phase and austenite coexist in this temperature range. The deformation is caused by stress-induced martensite formation as well as R-phase variant reorientation. After elastic unloading of the martensite, the deformation strain is only partially recovered by M → A reverse transformation because the temperature is above A_s, but below A_f.

Type V ($A_f < T < M_d$,[60] curves *i* and *j*): Since stress-induced martensite is unstable in the absence of external stress at temperatures above A_f, the deformation strain which results from stress-induced martensite tends to be fully recovered upon unloading. The residual strain drops to less than 0.5 % in curve *i*. Further increasing test temperature yields nearly perfect surperelasticity as shown in curve *j*.

---

[60] The M_d temperature is designated as the temperature at which the stress to induce martensite equals the critical stress for slip.

Type VI ($T > M_d$, curves *k* and *l*): As predicted by the Clausius-Clapeyron equation, the critical stress to induce martensitic transformation increases linearly with the temperature. The stress level reaches the flow stress of the specimen and an unrecoverable strain is introduced by dislocation glide.

Figure 3-64 schematically summarizes the six types of stress-strain curve in σ-ε-T space based on the preceding discussion. The classification is also made for other stress-strain curves presented in Section 3.4.2.

3.4.4. Thermomechanical Behavior of NiTi Films

In this section, first the dependence of critical stress to induce martensite with respect to deformation temperature is examined for NiTi films. Then the applicability of Clausius-Clapeyron relation to a practical case is explored by thermodynamics analysis. Finally, the plateau strain associated with stress-induced martensitic transformation is estimated from measured thermoelastic values.

For films H673, H703, H723, A2, A3, A5 and A8, the critical stresses to induce martensite are plotted against the test temperature (given as adjusted deformation temperature $T - M_s$) as shown in Figure 3-65. The critical stresses are measured from their stress-strain curves using the tangent-intercept method. All films tend to give a linearity suggested by the Clausius-Clapeyron equation in the austenite region except for film A8 where the data deviate from linearity at higher stress. According to this linear relation, the temperature approaches M_s ($= T_{\sigma=0}^{P\rightarrow M}$) when tensile stress approaches zero as seen in Figure 3-64.

The Clausius-Clapeyron relation (Equation 1.18) links important parameters associated with thermoelastic phase transformation. For the NiTi system, the measured values and calculated ones using the Clausius-Clapeyron equation have been compared in the literature [Miyazaki and Otsuka, 1984; Stachowiak and McCormick, 1988; Hou and Grummon, 1995]. However, in their work, $\Delta H^{gen,P\rightarrow M}$ (= the heat released during the phase transformation subjected to a stress, σ) was assumed to be equal to $\Delta H^{P\rightarrow M}$ (= the heat released during the stress-free phase transformation which can be conveniently measured by DSC) in order to apply Clausius-Clapeyron formula. The following discussion shows that the difference between $\Delta H^{gen,P\rightarrow M}$ and $\Delta H^{P\rightarrow M}$ can be ignored in such applications.

Starting from Planck-like formula[61] [Perkins, 1975], Wollants, Roos and Delaey [1980] have showed that if the difference in heat capacity of two phases is negligible, $\Delta H^{gen,\,P\rightarrow M}$ is a linear function of T. Based on Clausius-Clapeyron relation (Equation 1.18) a linear T-σ relation can be expected. In this work similar results can be obtained through mathematical manipulation using Jacobian notation.

In (T, σ) domain, the total differential $d\Delta S^{P\rightarrow M}$ can be expressed as follows:

$$d\Delta S^{P\rightarrow M} = \left(\frac{\partial \Delta S^{P\rightarrow M}}{\partial T}\right)_{\sigma} dT + \left(\frac{\partial \Delta S^{P\rightarrow M}}{\partial \sigma}\right)_{T} d\sigma \qquad (3.2)$$

Using the Jacobian notation [Mukherjee and Bieler, 1993], the partial differential teams in Equation 3.2 can be converted to measurable parameters (for details refer to appendix A.2).

$$d\Delta S^{P\rightarrow M} = \frac{\Delta C_F^{P\rightarrow M}}{T} dT + V\Delta\alpha^{P\rightarrow M} d\sigma \qquad (3.3)$$

Where $\Delta C_F^{P\rightarrow M}$ is the difference in iso-force heat capacity of the parent and martensitic phase and $\Delta\alpha^{P\rightarrow M}$ is the difference in thermal expansion coefficient of two phases. In order to estimate the influence of T and σ on transformation entropy, we substitute the

---

[61] Planck was the first to obtain the following formula called Planck equation for the temperature coefficient of the enthalpy function ΔH:

$$\frac{d\Delta H}{dT} = \Delta C_P + \frac{\Delta H}{T} - \frac{\Delta H}{\Delta V}\left(\frac{\partial \Delta V}{\partial T}\right)_P$$

properties of NiTi into Equation 3.3, $\Delta C_F^{P\rightarrow M} \approx \Delta C_P^{P\rightarrow M} = -0.28$ J/mol K,[62] $V = 1.64 \times 10^{-5}$ m^3/mol and $\Delta\alpha^{P\rightarrow M} = -4.4 \times 10^{-6}$ /K.

$$d\Delta S^{P\rightarrow M} = -\frac{0.28}{T}dT - 7.3 \times 10^{-11}\, d\sigma \qquad (3.4)$$

For general application, $T = 273\text{-}373$ K and $\sigma = 0\text{-}600$ MPa. Within this T-σ window the maximum deviation of $\Delta S^{P\rightarrow M}$ predicted by the Equation 3.4 would be 0.10 J/mol which is only 0.9-1.1 % of $\Delta S^{P\rightarrow M}$ values for four NiTi alloys cited in Hedayat, Rechtien and Mukherjee's paper [1992].

It is evident from preceding discussion that for NiTi system the $\Delta S^{P\rightarrow M}$ is rather a weak function of T and σ in the range of consideration. This result suggests two things: (1) It gives a theoretical explanation of the linearity of Clausius-Clapeyron formula, since from Equation 1.14, a linear T-σ relation can be expected if $\varepsilon^{P\rightarrow M}$ is constant. (2) Because of $\Delta H^{gen,P\rightarrow M}/T = \Delta S^{P\rightarrow M}$ (Equation 1.17), and $\Delta S^{P\rightarrow M} \approx (\Delta S^{P\rightarrow M})_{\sigma=0} = \Delta H^{P\rightarrow M}/T_0$, the value $\Delta H^{P\rightarrow M}/T_0$ can be used for $\Delta H^{gen,P\rightarrow M}/T$ in Clausius-Clapeyron formula, where $\Delta H^{P\rightarrow M}$ is the heat released during the stress-free phase transformation which can be conveniently measured by differential scanning calorimetry (DSC), and T_0 is the temperature at which the parent and martensitic phases have the same chemical free energy at zero stress. Equation 1.18 can thus be expressed by measurable values:

$$\frac{d\sigma}{dT} = -\frac{\Delta H^{P\rightarrow M}}{T_0 V \varepsilon^{P\rightarrow M}} \qquad (3.5)$$

For film H703, the critical stress to induce martensite and the stress at which the reverse transformation begins, both determined by a tangent-intercept construction, are plotted as a function of test temperature in Figure 3-66. The measured transformation

---

[62] The values of C_P^P and C_P^M, respectively, were determined to be 9.66 and 9.38 J mol^{-1}K^{-1} from the DSC curve of the film H703 (Figure 3-45).

temperatures from the electrical resistivity measurement are indicated along the temperature axis. Below M_s, it is found that the yield stress declines slightly with temperature, reaching a minimum near M_s. In this range the deformation is caused by detwinning of martensite variants. The stress shows a normal temperature dependence, i.e., it decrease with increasing of temperature since detwinning is a thermally activated process [Miyazaki, Kohiyama and Otsuka, 1991]. Above the M_s, both the stress for martensite formation and the reversion stress rise monotonically with temperature in a linear fashion in agreement with predictions based on the Clausius-Clapeyron equation. The extrapolation of the two lines intersect the temperature axis at around M_s and A_s.

We may estimate the plateau strain ($\varepsilon^{P \to M}$) using the measured values of H and $d\sigma/dT$. It is worth to point out that the Clausius-Clapeyron relation is a thermodynamic equation which describes equilibrium conditions, whereas the transformation in a practical case like NiTi system deviates from the thermodynamic equilibrium as has been discussed in Section 1.1.3. We input following data into the Equation 3.5, $T_0 = (M_s + A_f) / 2 = 283.5$ K (Equation 1.2), $V = 1.64 \times 10^{-5}$ m^3/mol, $\Delta H^{P \to M} = - \Delta H^{M \to P} = - \Delta H^{M \to R} = -1599.0$ J/mol (in this case R-phase is the parent phase of martensite, i.e., P = M in superscript), and $d\sigma/dT = 6.41$ MPa/K which is obtained from the loading curve of Figure 3-66. The calculated value of plateau strain is 5.3 % which compares favorably with the values (= 4.7-5.5 %) reported for bulk NiTi alloys [Miyazaki and Otsuka, 1984; Stachowiak and McCormick, 1988].

3.4.5. Transformational Superelastisity

In this section, a stress-temperature diagram for predicting transformational superelastisity is discussed first. Then mechanical energy output and energy efficiency associated with each superelastic cycle is explored.

Three types of yield phenomena are possible involve in a thermoelastic alloy. The first is attributed to the detwinning of unfavorably oriented matensitic twin variants into favorable ones with respect to the stress axis. The yield stress declines slightly with temperature as shown in Figure 3-66 at $T < M_f$. The second one is related to stress-induced martensitic transformation and the critical yield stress rises linearly with increasing temperature as predicted by the Clausius-Clapeyron equation as shown in Figure 3-66 at $T > A_f$. The third one is a conventional yielding caused by dislocation glide in the parent phase and martensite. As it will be addressed in following, whether or not a material behaves superelastically essentially depends on the relative values of the stress to induce martensite and the critical stress for slip.

Stress-temperature diagrams for films H673, H723 and A3 can be plotted in Figure 3-67, 3-68 and 3-69, respectively, using the data obtained in the preceding sections. In the diagrams the line σ_m represents the critical stress to induce martensite which was measured from corresponding stress-strain curves using the tangent-intercept method as shown in Figure 3-65. The line σ_s is the onset stress for slip which was obtained from the yielding points of ultimate elongation curves at 423 K (Figure 3-63), and by assuming that the change of the critical stress for slip with the temperature was -0.2 MPa/K [Miyazaki, Kohiyama and Otsuka, 1991]. The transformation temperatures A_s and A_f were measured from the resistivity vs. temperature curves (Table 3-3 and Table 3-5).

In the diagrams, T-σ conditions allowing superelasticity is confined by three boundaries:

(1) $\sigma > \sigma_m$, to stress induce the martensitic transformation,

(2) $\sigma < \sigma_s$, to prevent permanent strain, and

(3) $T > A_f$, to eliminate the residual strain created in stress-induced martensitic transformation after unloading.

It is evident that a greater σ_s, a lower σ_m and a lower A_f tend to give a wider T-σ window for superelasticity. As predicted by the stress-temperature diagrams, films H673, H723 and A3 all show superelasticity at $T > A_f$ (Figure 3-67, 3-68 and 3-69, respectively). However, the superelasticity in film H673 and especially in film A3 are not 'perfect' as exemplified by a residual strain after unloading. There are perhaps two reasons making the previous T-σ diagrams unable to predict a perfect superelasticity. First, a very limited amount of permanent deformation, which may be large enough to jeopardize the perfection of superelasticity, can occur in the linear region of stress-strain curve shown in Figure 3-63. Second, some martensite may still be retained in the specimen after unloading as pointed out by Miyazaki *et al.*[1984]. In order to predict perfect superelasticity, a proper way to precisely detect the onset of the stress, where the slip or retained martensite start to occur, is to measure the stress at which the first dimensional change is observed when repeating loading-unloading cycle with small increment of load. Miyazaki, Kohiyama and Otsuka [1991] have reported the stresses for slip both in the parent phase and the martensite for bulk NiTi alloys using such method.

In each superelastic cycle, the area under the loading curve is the work done per unit volume on the specimen (E_{in}), while the area under the unloading curve is the energy density per unit volume which is stored and can be released as mechanical energy upon unloading (E_{out}). The area confined by the loading-unloading loop represents the energy density per unit volume (E_{in} -E_{out}) which is dissipated during the cycle.

Figure 3-70a shows the output of mechanical energy vs. adjusted deformation temperature (T - A_f) for NiTi films. The output energy increases when deformation temperature increases. This is mainly due to the fact that the critical stress to induce martensite increases as temperature increases. The maximum output energy found in this study was 1.7×10^7 J/m^3 which was produced in film H673 at 3.5 % total strain.[63] As a comparison, output energy per unit volume for various available microactuators are given as follows: solid-liquid phase change: 4.7×10^6 J/m^3 [Hale, Hoover and O'Neil, 1971], thermopneumatic actuator: 1.2×10^6 J/m^3 [Zdeblick *et al.* 1994], thermal expansion: 4.6×10^5 J/m^3 [Krulevitch, *et al.* 1996], electromagnetic actuator: 2.8×10^4 J/m^3 [Guckel, *et al.*

---

[63] To avoid the fracture of specimen in grip areas, the total strain was limited to 3.5 % in this work. Therefore, the possible maximum output energy could be greater.

1994], electrostatic actuator: 3.4×10^3 J/m^3 [Fan, *et al.* 1994], and piezoelectric actuator: 1.8×10^2 J/m^3 [Robbins, *et al.* 1991; Tjhen, *et al.* 1991]. Evidently, the NiTi thin film produced in this work displays the highest energy output. Figure 3-70b shows the energy efficiency (E_{out} /E_{in}) as a function of adjusted deformation temperature. For as-sputtered films (H673, H703 and H723), the energy efficiency is increases as temperature increases, while for annealed films no such relation appears. The large residual strain shown in stress-strain curves of annealed films reduced the energy efficiency. The energy efficiency are varied from 47 % (film A3) to 93 % (film H723).

3.5. Fractography of NiTi Films

Fracture surfaces of specimens strained to fracture were examined by the SEM (the ultimate elongation curves of films H673, H723 and A3 are shown in the Figure 3-47). Figure 3-71 shows the fractography of film H623 which displays fibrous characteristic consisting of many microdimples. The fractography exhibits a typical transgranular mode I (the opening mode) ductile failure. The ductile fracture occurs through three stages: First small cavities nucleate at weak internal interfaces, such as second particle/matrix interfaces. These cavities then expand by plastic deformation and finally coalesced by localized necking of the material between adjacent cavities until completely separating specimen into two parts. The force causing such fracture is the principal stress normal to fracture plane. Microscopically, voids were formed through shear in the lattice planes. This is reason for the fracture occurred at near grips of thin film specimens. Since the maximal principal stress reaches the maximum value at the edges near the ends of the gauge section as shown in the contour map of maximal principal stress (Figure 2-18).

The fracture surface of the film H673 is shown in Figure 3-72. The columnar grain structure is clearly seen and the latitudinal dimension of grains (about 0.25 μm) is consistent with that observed by the TEM. This fractography also confirms the columnar grain structure produced by hot-substrate deposition.

Figure 3-73a and 3-73b, respectively, are fractography of film H723 viewed from surface side and substrate side. It seems that the fracture is mainly transgranular one but with some characteristic of intergranular fracture because the fracture surface displayed columnar grains. The external neck area in surface side of film reveals a serial of valleys as indicated by arrows (Figure 3-73a), but the neck in substrate side shows an even and flat morphology (Figure 3-73b). It is understandable from Hall-Petch relationship (Equation 1.25) since the extremely fine (grain size = 25 nm) grains were formed in substrate side of film H723 and impeded plastic deformation. Even in the surface side of the film, the free surface (except the neck area) is quite smooth. This fact implies a very stable microstructure against the permanent deformation.

Figure 3-74 and 3-75, respectively, show SEM images of fracture surfaces of the films A3 and A5. Large cup-like features are perhaps due to a greater grain size and thus greater extent of localized plastic necking. The rough free surface of the film reflects that considerable deformation had remained after ultimate stressing.

Figure 3-76 was taken from the film A7. The fractography shows a flat and straight fracture surface with many small dimples. No neck is found in the edge of fracture surface and the free surface of the film is very smooth. These features are consistent with its very limited plastic strain shown in the stress-strain curves (Figure 3-60), and can be explained by the effect of a high density precipitates resisting dislocation movement.

CONCLUSIONS

Crystalline NiTi thin films, which exhibits a well-defined thermomechanical behavior, have been successfully produced by one-step hot-substrate deposition. The correlation between the microstructure of the films and a key process parameter, substrate temperature, has been systematically examined by TEM. The results have been combined into a grain structure-deposition temperature diagram. The deformation characteristics, including the critical stress to induce martensite and the flow stress for slip have been investigated using tensile tests. Based on obtained thermomechanical data, stress-temperature diagrams have been constructed to predict superelasticity capabilities for NiTi films with diverse microstructures. The correlation between the microstructure and thermomechanical properties has been clarified. Detailed conclusions can be drawn as follows:

(1) Compared with the conventional two-step NiTi film process (sputter deposition plus a crystallization anneal), the hot-substrate deposition technique has been proven to provide advantages in terms of eliminating post-deposition crystallization, decreasing the process temperature to form a crystalline structure ($T = 623$ K in the hot deposition vs. $T > 773$ K in the conventional process), and producing fine-grained microstructure ($D = 0.1$-0.3 μm in the hot deposition vs. $D > 1$ μm in the conventional process).

(2) In hot-substrate deposition, NiTi grains started to nucleate at a substrate temperature of 598 K and columnar grains formed at temperatures from 598 K to the upper limit of this work, 773 K. The columnar-grained structure resulted from surface diffusion processes.

(3) Films deposited at lower temperature ($T \leq 673$ K) exhibited a strong $(110)_{B2}$ fiber texture. The texture vanished when deposition temperature was increased to 723 K. In this case, extremely fine crystallites ($D = 25$ nm) nucleated on an initially amorphous layer.

(4) The variation in Ni_4Ti_3 precipitate morphology with depth in the film and with deposition temperature, suggests that both surface and bulk diffusion for growth of Ni_4Ti_3 occurred during hot-substrate deposition at temperatures between 723 and 773 K.

(5) A unique $NiTi/Ni_3Ti_2$ dual phase structure, which cannot be easily produced by either conventional two-step process or hot-substrate deposition, could be made by giving hot-deposited films an additional heat treatment.

(6) The resistivity-temperature curves could be classified into two categories: B2 $\leftrightarrow$ R $\leftrightarrow$ M and B2 $\leftrightarrow$ M, except for some ill-defined curves. Irrespective of the B2 grain size, films having finely dispersed precipitates in B2 grains displayed two-step phase transformation behavior, whereas the films with coarse precipitates showed single-step transformations.

(7) Both small grain size and fine precipitates were found to promote a perfect transformational superelasticity. On the other hand, when the interspacing of precipitates was less than 12 nm (in films H623 and A7), the precipitates tended to impede stress-induced martensite transformation. The combination of fine B2 grains (0.25 μm) and precipitates with moderate interspacing (30-40 nm) in films H703 and H723 provided superior thermoelastic properties.

(8) The maximum output energy found in this study was 1.7×10^7 J/m^3 which was produced in film H673 at 3.5 % total strain. The energy efficiency are varied from 47 % (film A3) to 93 % (film H723).

It is challenge to realize a perfect superelasticity in NiTi thin films which only have micrometer dimensions. Precipitates and grain boundaries were found to play an important role in resisting permanent deformation and thus promoting superelasticity. However, as the interspacing of precipitates approached 12 nm, the ability of NiTi to form stress-induced martensite tended to be reduced. It is interesting to know whether or not the B2 grain boundaries along (i.e., in precipitate-free NiTi films) are capable of promoting perfect superelasticity. If the answer is yes, then what is the grain size limit which allows the formation of stress-induced martensite? These are questions remaining to be answered in a future study.

Successfully depositing crystalline NiTi onto the polymeric substrates (Kapton) relied on the hot-substrate deposition technique which can produce B2 crystals at a lower temperature, and using a two-sided substrate heating device which can provide a uniform substrate temperature and a reliable temperature reading. Combined with photolithography process, a NiTi/polyimide microactuator prototype was fabricated. In appendix A.1 a robust electrically-excitable shape-memory action move is demonstrated.

Table 1-1. Austenite-to-martensite lattice correspondences [after Matsumoto *et al.*, 1978].

Variant	$[100]_M$	$[010]_M$	$[001]_M$
1	$[100]_A$	$[011]_A$	$[0\bar{1}1]_A$
1'	$[\bar{1}00]_A$	$[0\bar{1}\bar{1}]_A$	$[0\bar{1}1]_A$
2	$[100]_A$	$[0\bar{1}1]_A$	$[0\bar{1}\bar{1}]_A$
2'	$[\bar{1}00]_A$	$[01\bar{1}]_A$	$[0\bar{1}\bar{1}]_A$
3	$[010]_A$	$[101]_A$	$[10\bar{1}]_A$
3'	$[0\bar{1}0]_A$	$[\bar{1}0\bar{1}]_A$	$[10\bar{1}]_A$
4	$[010]_A$	$[10\bar{1}]_A$	$[\bar{1}0\bar{1}]_A$
4'	$[0\bar{1}0]_A$	$[\bar{1}01]_A$	$[\bar{1}0\bar{1}]_A$
5	$[001]_A$	$[110]_A$	$[\bar{1}10]_A$
5'	$[00\bar{1}]_A$	$[\bar{1}\bar{1}0]_A$	$[\bar{1}10]_A$
6	$[001]_A$	$[\bar{1}10]_A$	$[\bar{1}\bar{1}0]_A$
6'	$[00\bar{1}]_A$	$[1\bar{1}0]_A$	$[\bar{1}\bar{1}0]_A$

Table 1-2. The 24 habit plane variants and related correspondence variant-combinations. The habit plane indices were calculated from the phenomenological crystallographic theory, and correspond to the experimental data for solution-treated specimens [after Miyazaki *et al.*, 1978].

Habit plane variant	Correspondence variant combination	Habit plane indices
1(+)	1-2	(-0.89, -0.22, 0.40)
1(-)	1-2'	(-0.89, -0.40, 0.22)
1'(+)	1'-2	(0.89, -0.40, 0.22)
1'(-)	1'-2'	(0.89, -0.22, 0.40)
2(+)	2-1	(0.89, 0.22, 0.40)
2(-)	2-1'	(0.89, 0.40, 0.22)
2'(+)	2'-1	(-0.89, 0.40, 0.22)
2'(-)	2'-1'	(-0.89, 0.22, 0.40)
3(+)	3-4	(-0.40, 0.89, 0.22)
3(-)	3-4'	(-0.22, 0.89, 0.40)
3'(+)	3'-4	(-0.22, -0.89, 0.40)
3'(-)	3'-4'	(-0.40, -0.89, 0.22)
4(+)	4-3	(0.40, 0.89, 0.22)
4(-)	4-3'	(0.22, 0.89, 0.40)
4'(+)	4'-3	(0.22, -0.89, 0.40)
4'(-)	4'-3'	(0.40, -0.89, 0.22)
5(+)	5-6	(0.22, -0.40, 0.89)
5(-)	5-6'	(0.40, -0.22, 0.89)
5'(+)	5'-6	(-0.40, 0.22, 0.89)
5'(-)	5'-6'	(-0.22, 0.40, 0.89)
6(+)	6-5	(0.22, 0.40, 0.89)
6(-)	6-5'	(0.40, 0.22, 0.89)
6'(+)	6'-5	(-0.40, -0.22, 0.89)
6'(-)	6'-5'	(-0.22, -0.40, 0.89)

Table 2-1. Sputter-deposition conditions and resultant film compositions. The notation 'H---' is used in the present work where the 'H' signifies 'hot deposition' and three digits signify the substrate temperature of deposition in Kelvin. The substrate for all films were quartz except for film H698 which was deposited on Kapton film.

Film	Thick-ness (μm)	Base pressure ($\times 10^{-4}$ Pa)	Argon pressure (Pa)	Cathode power (watt)	Cathode potential (volt)	Growth rate (nm/sec)	Film comp. (at.% Ni)
H573	5.0	2.11	0.67	200	582-559	0.62	51.5
H598	4.3	3.73	0.68	200	679-639	0.63	51.2
H623	6.7	2.96	0.67	150-200	638	0.69	52.3
H673	6.3	1.47	0.67	200	556-522	0.71	51.0
H698	3.1	0.66	0.75	250	644-619	0.68	50.8
H703	7.1	0.61	0.75	250	471-460	1.25	50.8
H723	6.7	2.53	0.68	200	593-562	0.72	51.1
H773	4.9	4.00	0.84	200	538-524	0.79	51.4

Table 2-2. Heat-treatment conditions of annealed NiTi films. For annealed NiTi films, the notation 'A-' is used where the 'A' represents 'annealing' and a digit designates the detailed heat-treatment path as indicated in the table.

Film	Composition (at.% Ni)	Dep. temp. (K)	Annealing temperature (K)	Cooling method
A1	52.3	623	858, 1h	Furnace cooling
A2	51.0	673	858, 1h	Furnace cooling
A3	51.1	723	858, 1h	Furnace cooling
A4	51.1	723	813, 1h	Furnace cooling
A5	51.0	673	988, 1h	Furnace cooling
A6	51.0	673	1123, 1h	Furnace cooling
A7	51.0	673	1073, 2h	Air cooling
A8	51.0	673	1073, 2h and 673, 1h	Air cooling

Table 3-1. Summary of microstructures of as-deposited NiTi films. In the table, D_{B2}, D_{ptt} and PS, respectively, designate the in-plane grain diameter of the B2, the diameter of precipitates in longitudinal direction, and precipitate spacing.

Film	Location	Microstructure characteristics	Reference
H573	Midplane	Amorphous;	Fig. 3-5
H598	Interface	Amorphous;	Fig. 3-6
	Midplane	D_{B2} = 750.1 nm, (110) texture; D_{ppt} = 12.2 nm, PS = 6.5 nm;	Fig. 3-7
	Surface	D_{B2} = 94.0 nm, (110) texture; D_{ppt} = 6.3 nm, PS = 6.1 nm;	Fig. 3-8
H623	Interface	D_{B2} = 86.4 nm, (110) texture; D_{ppt} = 12.5 nm, PS = 6.5 nm,	Fig. 3-9
	Midplane	D_{B2} = 98.6 nm, (110) texture; D_{ppt} = 9.4 nm, PS = 6.5 nm;	Fig. 3-10
	Surface	D_{B2} = 101.6 nm, (110) texture; D_{ppt} = 9.4 nm, PS = 5.2 nm;	Fig. 3-11
H673	Interface	D_{B2} = 237.5 nm, (110) texture; D_{ppt} = 56.3 nm, PS = 30.1 nm;	Fig. 3-12
	Midplane	D_{B2} = 221.1 nm, (110) texture; D_{ppt} = 18.8 nm, PS = 18.0 nm;	Fig. 3-13
	Surface	D_{B2} = 252.3 nm; D_{ppt} = 15.6 nm, PS = 15.4 nm;	Fig. 3-14
H703	Midplane	D_{B2} = 235.2 nm; D_{ppt} = 137.5 nm, PS = 30.7 nm;	Fig. 3-3
H723	Interface	D_{B2} = 23.8 nm, random orientations; PS = n/a;	Fig. 3-16
	Midplane	D_{B2} = 247.2 nm, random orientations; D_{ppt} = 150.0 nm, PS = 41.5 nm;	Fig. 3-17
	Surface	D_{B2} = 286.1 nm; D_{ppt} = 62.5 nm, PS = 25.8 nm;	Fig. 3-18
H773	Interface	D_{B2} = 27.4 nm, random orientations; PS = n/a;	Fig. 3-19
	Midplane	D_{B2} = 271.3 nm, random orientations; D_{ppt} = 218.7 nm, PS = 66.4 nm;	Fig. 3-20
	Surface	D_{B2} = 318.8 nm; D_{ppt} = 181.3 nm, PS = 85.6 nm;	Fig. 3-21

Table 3-2. Summary of NiTi matrix and precipitate morphologies of annealed NiTi films. In the table, D_{B2}, D_{ptt} and PS, respectively, designate the in-plane grain diameter of the B2, the diameter of precipitates in longitudinal direction, and precipitate spacing.

Film	Location	Microstructure characteristics	Reference
A1	Midplane	D_{B2} = 116.7 nm; D_{ppt} = 375.2 nm, PS = 258.8 nm;	Fig. 3-30
A2	Midplane	D_{B2} = 207.8 nm; D_{ppt} = 350.5 nm, PS = 877.8 nm;	Fig. 3-31
A3	Midplane	D_{B2} = 232.5 nm; D_{ppt} = 475.0 nm, PS = 1.3 μm;	Fig. 3-32
A4	Midplane	D_{B2} = 218.8 nm; $D_{ppt} > 350$ nm, PS = 1.1 μm;	Fig. 3-33
A5	Midplane	D_{B2} = 638.5 nm; D_{ppt} = 178.2 nm and D_{ppt} = 635.0 nm, PS = 152.9 nm;	Fig. 3-34
A6	Midplane	D_{B2} = 3.7 μm; D_{ppt} = 962.5 nm and D_{ppt} = 15.6 nm, PS = 8.6 nm;	Fig. 3-35
A7	Midplane	D_{B2} = 1.8 μm; D_{ppt} = 19.4 nm, PS = 11.7 nm;	Fig. 3-36 Fig. 3-37
A8	Midplane	D_{B2} = 1.9 μm; D_{ppt} = 122.9 nm, PS = 60.3 nm;	Fig. 3-38

Table 3-3. Phase transformation temperatures of as-deposited NiTi films.

Film	Film composition (at.% Ni)	M_f (K)	M_s (K)	T'_R (K)	A_s (K)	A_f (K)
H573	51.5	n/a	n/a	n/a	n/a	n/a
H598	51.2	n/a	n/a	n/a	n/a	n/a
H623	52.3	n/a	n/a	332	n/a	n/a
H673	51.0	220	248	323	292	309
H703	50.9	235	259	321	295	308
H723	51.1	250	266	322	303	313
H773	51.4	241	261	323	304	360

Table 3-4. Transformation characteristics of the film H703 obtained from electrical resistivity and DSC measurements.

Temp. or heat flow	Electical resistivity method	DSC
A_f	308 K	n/a
A_s	295 K	298 K
T'_R	321 K	n/a
T_R	n/a	319 K
M_s	259 K	263 K
M_f	235 K	231 K
$\Delta H^{R\rightarrow A}$	n/a	298.5 J/mol (2.8 J/g)
$\Delta H^{M\rightarrow A}$	n/a	1897.5 J/mol (17.8 J/g)
$\Delta H^{M\rightarrow R}$	n/a	1599.0 J/mol (15.0 J/g)
$\Delta H^{A\rightarrow R}$	n/a	-319.8 J/mol (-3.0 J/g)
$\Delta H^{R\rightarrow M}$	n/a	-437.1 J/mol (-4.1 J/g)

Table 3-5. Phase transformation temperatures of as-deposited NiTi films.

Film	Film composition (at.% Ni)	M_f (K)	M_s (K)	T'_R (K)	A_s (K)	A_f (K)
A1	52.3	254	282	310	307	314
A2	51.0	247	276	312	306	315
A3	51.1	260	271	314	294	307
A4	51.1	n/a	n/a	n/a	n/a	n/a
A5	51.0	267	282	323	319	329
A6	51.0	184	248	308	278	315
A7	51.0	n/a	223	318	258	289
A8	51.0	228	255	322	318	327

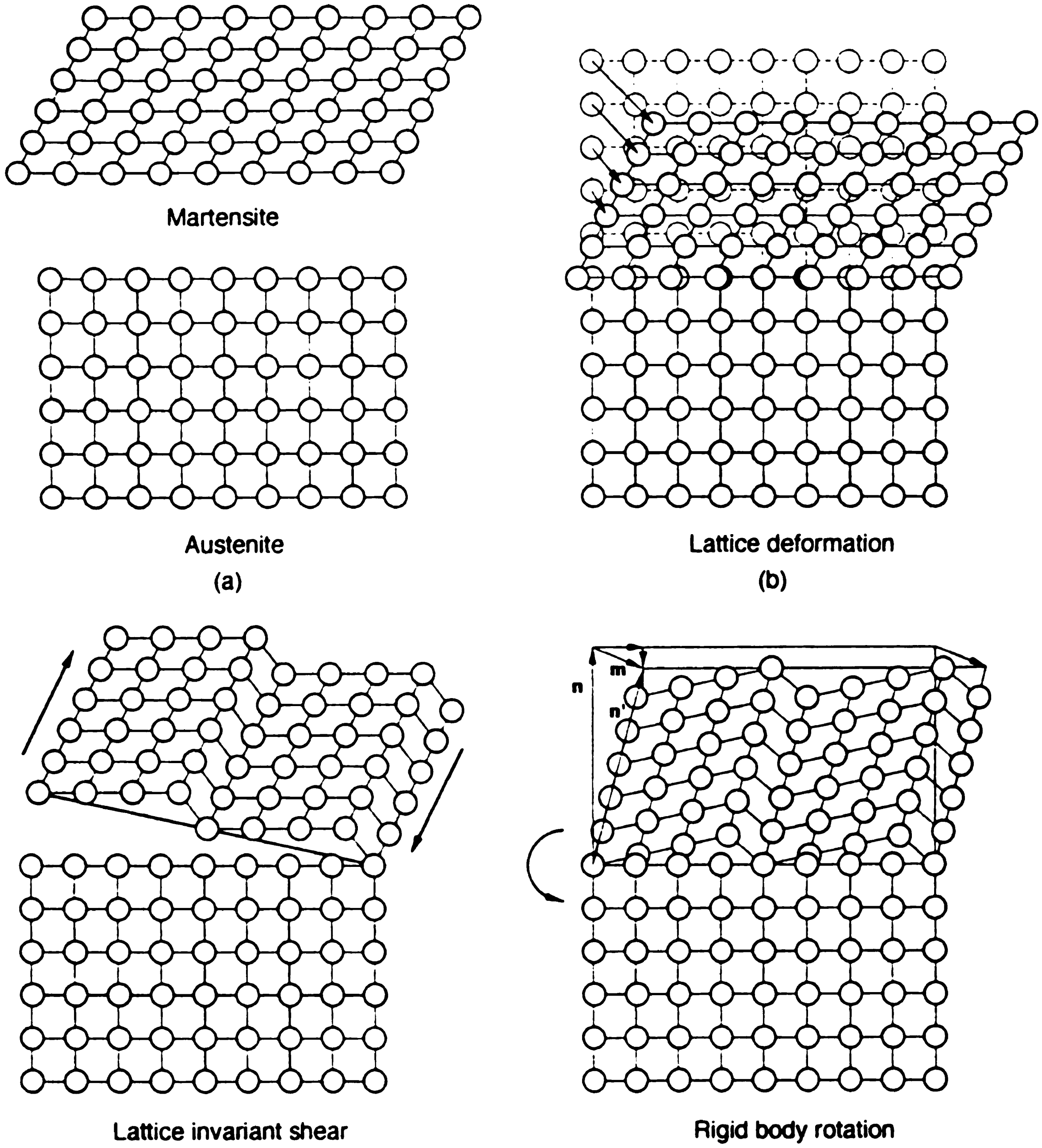

Figure 1-1. Schematic drawings of a two-variant matensitic transformation [Chang, 1993]. (a) The lattices of the parent phase and the martensite. (b) The Bain distortion, which converts the parent phase into the martensite, does not yield an undistorted plane associated with the habit plane. (c) A lattice invariant shear, through a reversible manner of twinning, produces an undistorted plane. (d) The rigid body rotation, which brings the transformed lattice back, so that the interface is in contact with the parent lattice.

(a) Single-crystal, single-interface

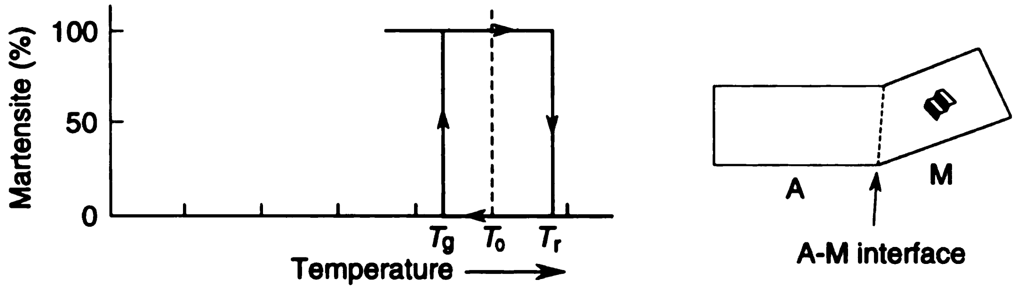

(b) Single-crystal, multiple-interface

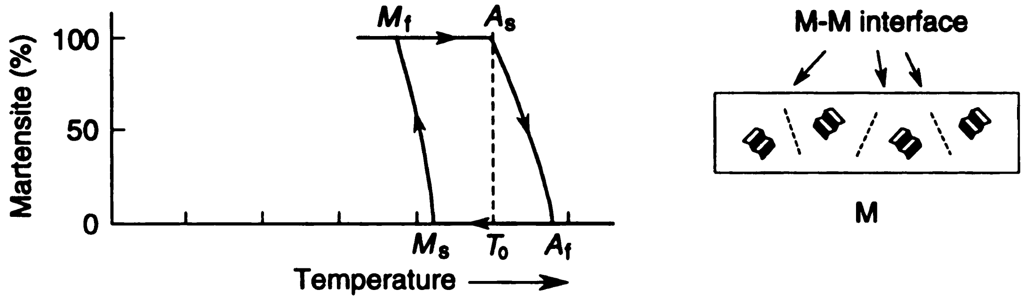

(c) Coarse-grained sample, multiple-interface

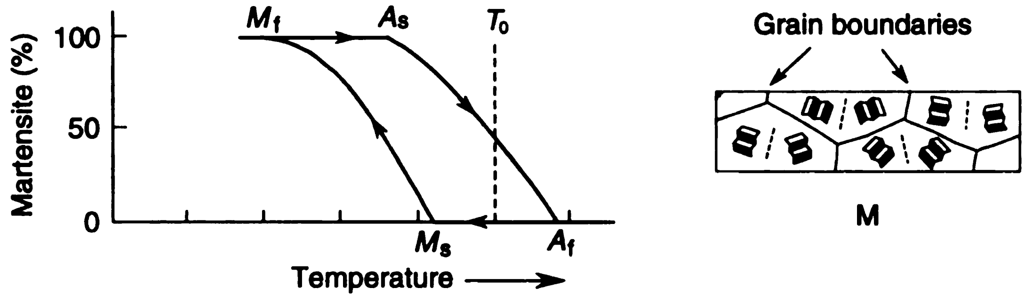

(d) Fine-grained sample, multiple-interface

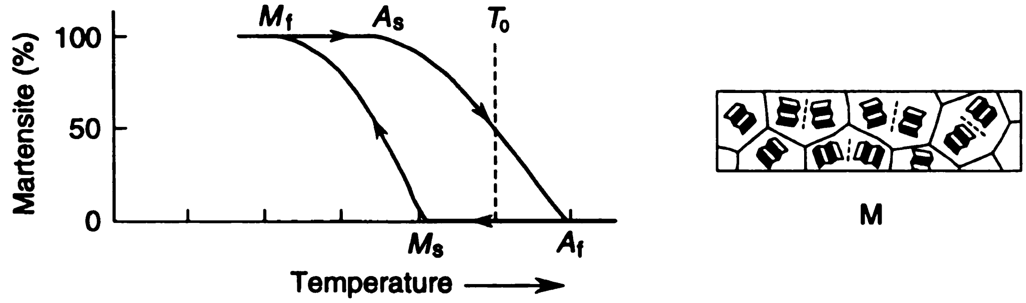

Figure 1-2. Schematic representation of the influence of frictional work and stored elastic energy on thermoelastic martensitic transformation [modified after Salzbrenner and Cohen 1979].

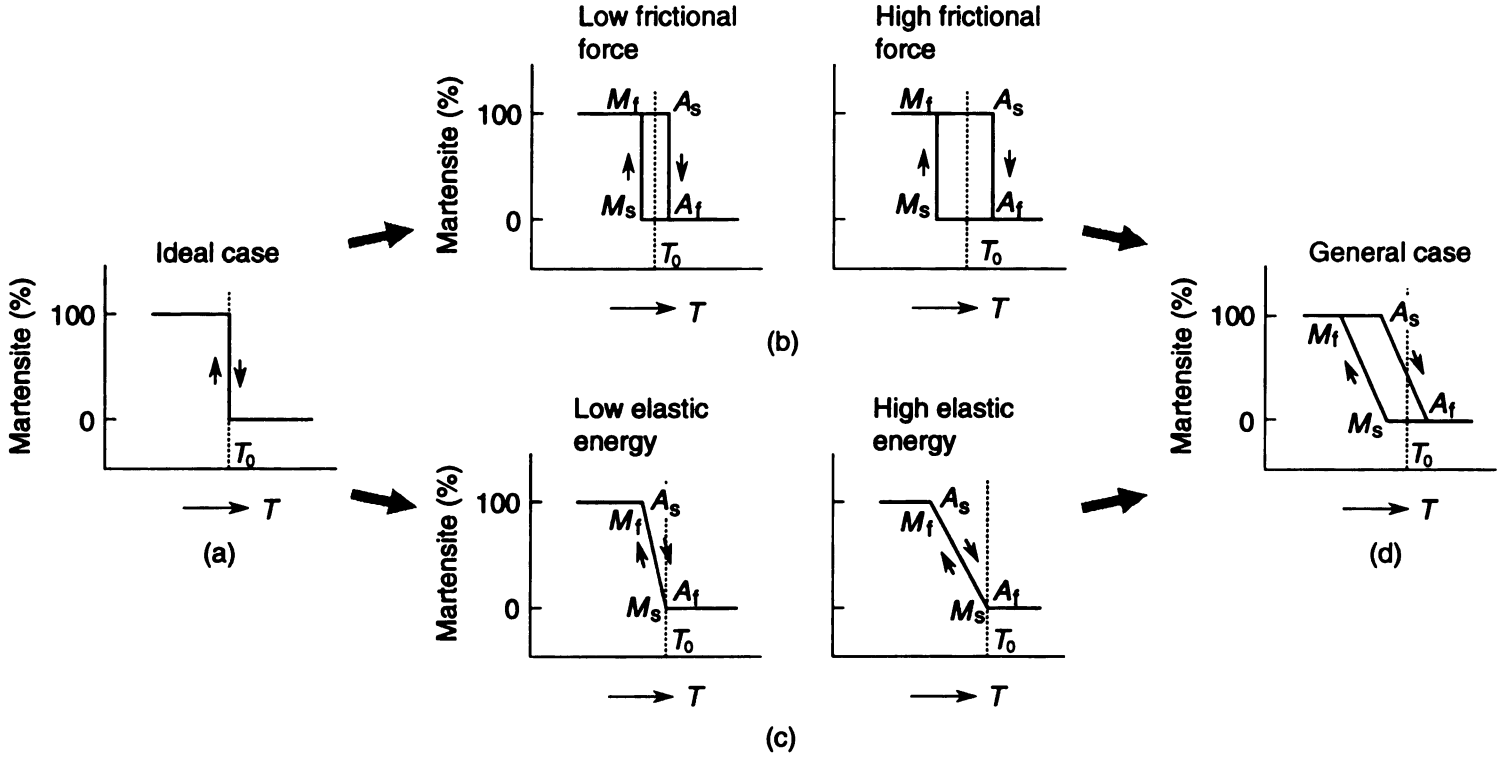

Figure 1-3. Schematic drawings summaries the influence of frictional force and stored elastic energy on thermoelastic martensite transformations.

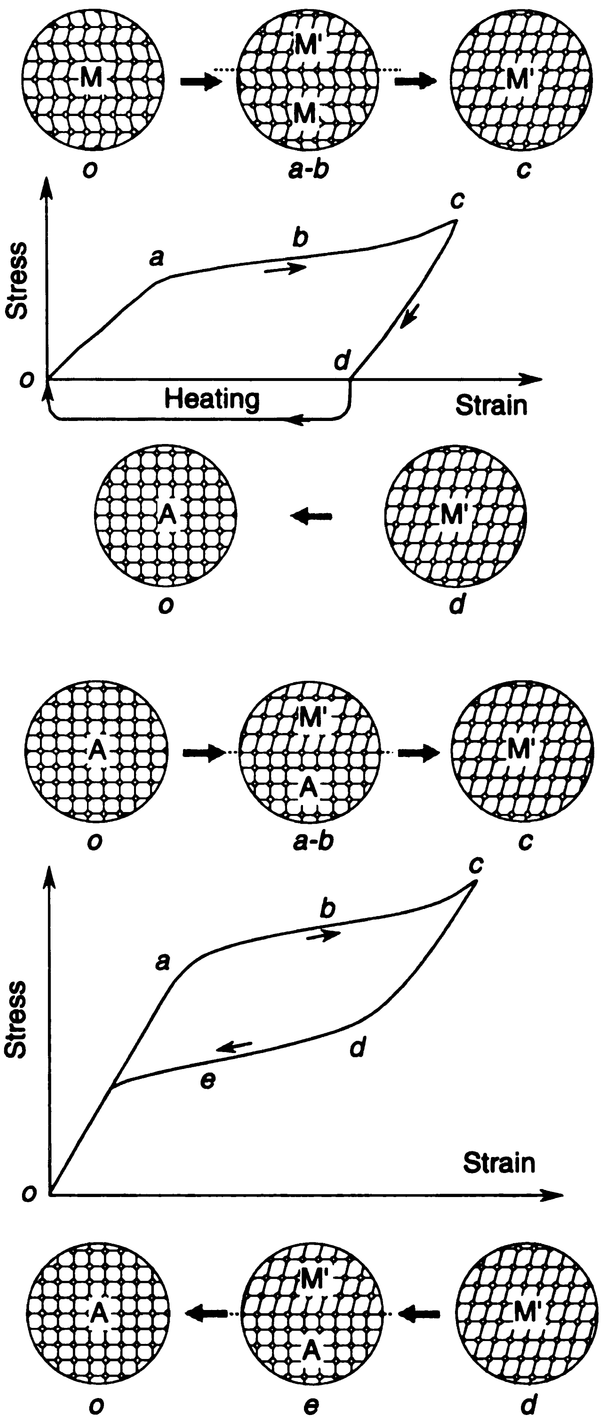

Figure 1-4. Upper figure: schematic drawing of shape-memory effect: (*a*-*c*) the deformation is accomplished by detwinning or reorientation of variants in martensite lattice. M is twinned martensite and M' is deformed martensite. Bottom figure: (*a*-*c*) the deformation is accomplished by transformational twining in the austenite.

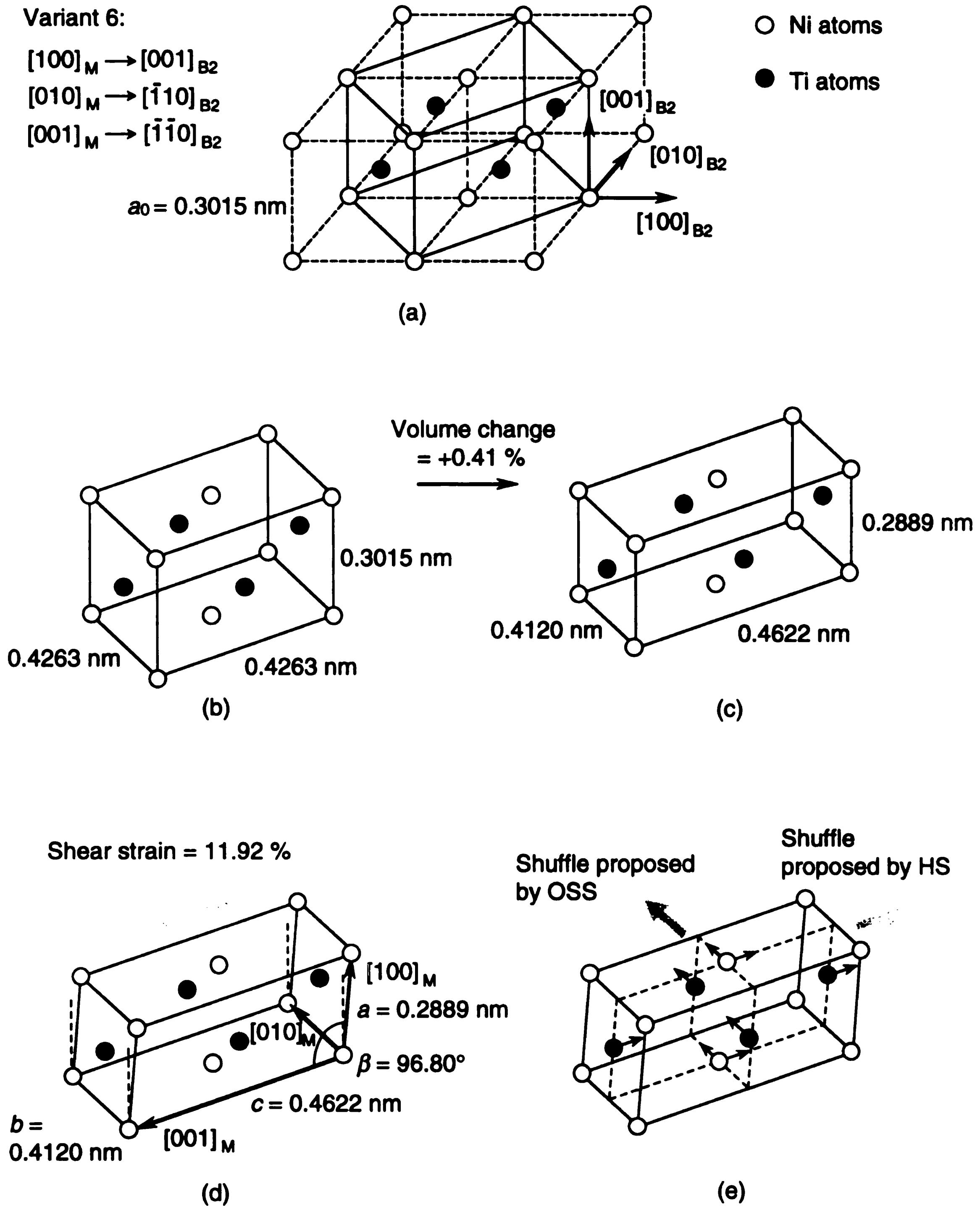

Figure 1-5. The steps illustrating the transition from B2 to B19' lattices [modified from Hehemann and Sandrock, 1971]. (a) B2 lattices; (b-c) an orthorhombic distortion; (c-d) a monoclinic shear; (e) two shuffle models.

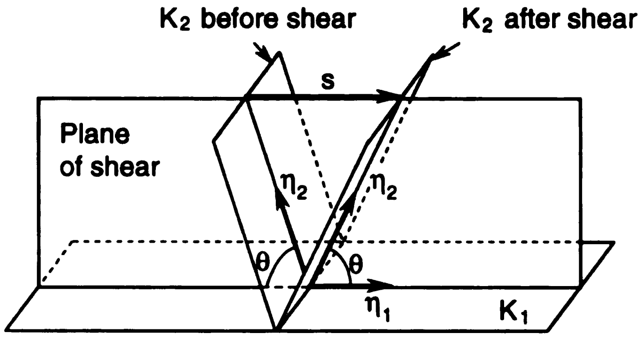

K_1 : Twin plane

K_2 : Second undistorted plane

η_1 : Twining shear direction

η_2 : Intersection of K_2 and the plane of shear

s : Magnitude of twinning shear displacement

Figure 1-6. An illustration representing geometry relationships between planes and directions in twinning [Reed-Hill, 1964].

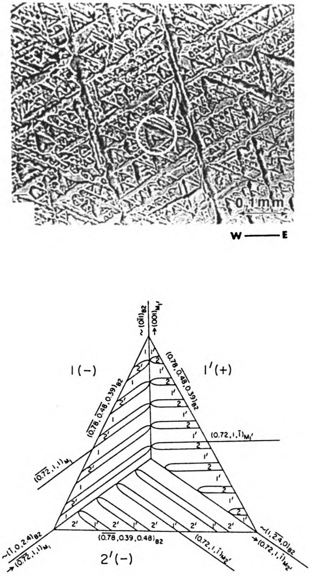

Figure 1-7. The self-accommodation morphology of the monoclinic martensite, and a model describing crystallographic relationships between the martensite variants in the triangular morphology [Miyazaki *et al.* 1989].

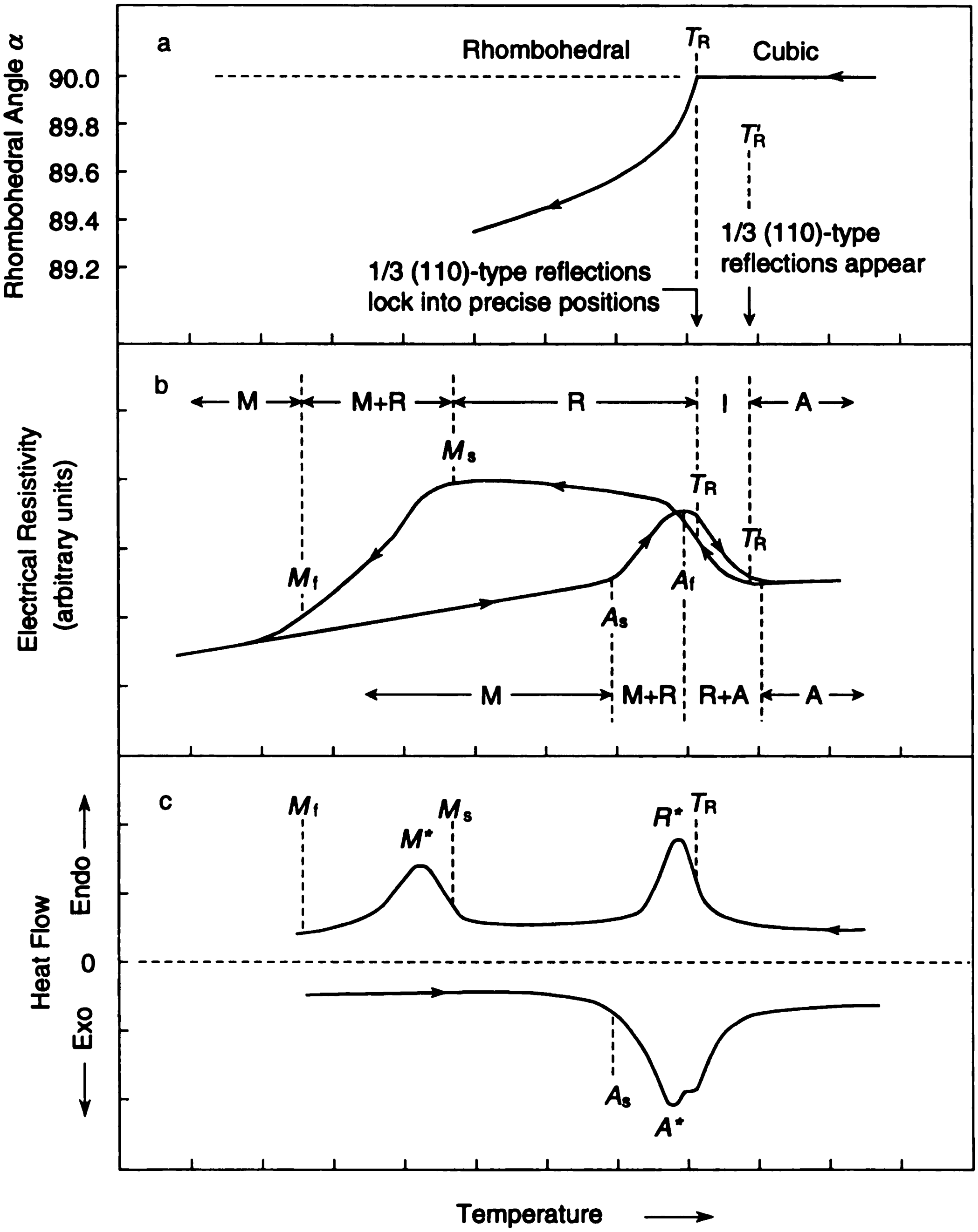

Figure 1-8. Schematic diagram showing physical property changes associated with R-phase and martesitic transformation: (a) lattice distortion, (b) electrical resistivity change, and (c) latent heat exchange.

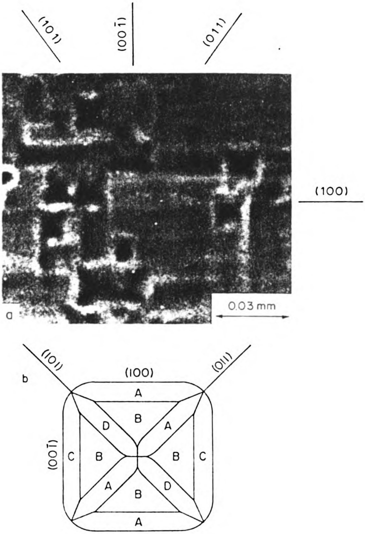

Figure 1-9. Self-accommodating morphology and corresponding schematic variants-combination of rhombohedral phase proposed by Miyazaki and Wayman [1988].

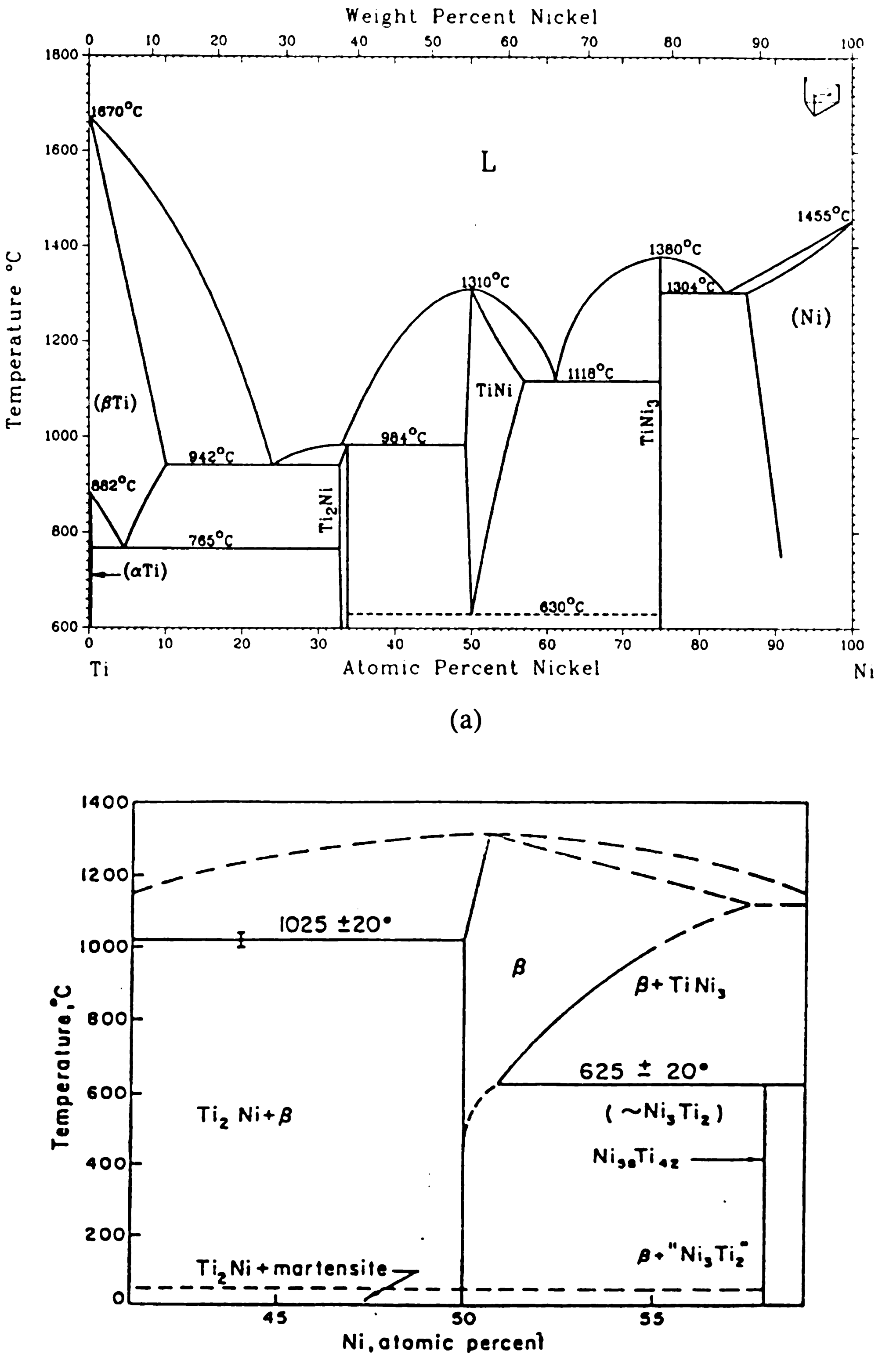

(a)

(b)

Figure 1-10. (a) Ni-Ti equilibrium phase diagram proposed by Massalski [1987]; (b) Ni-Ti phase diagram in the vicinity of stoichiometric composition proposed by Wasilewski *et al.* [1971].

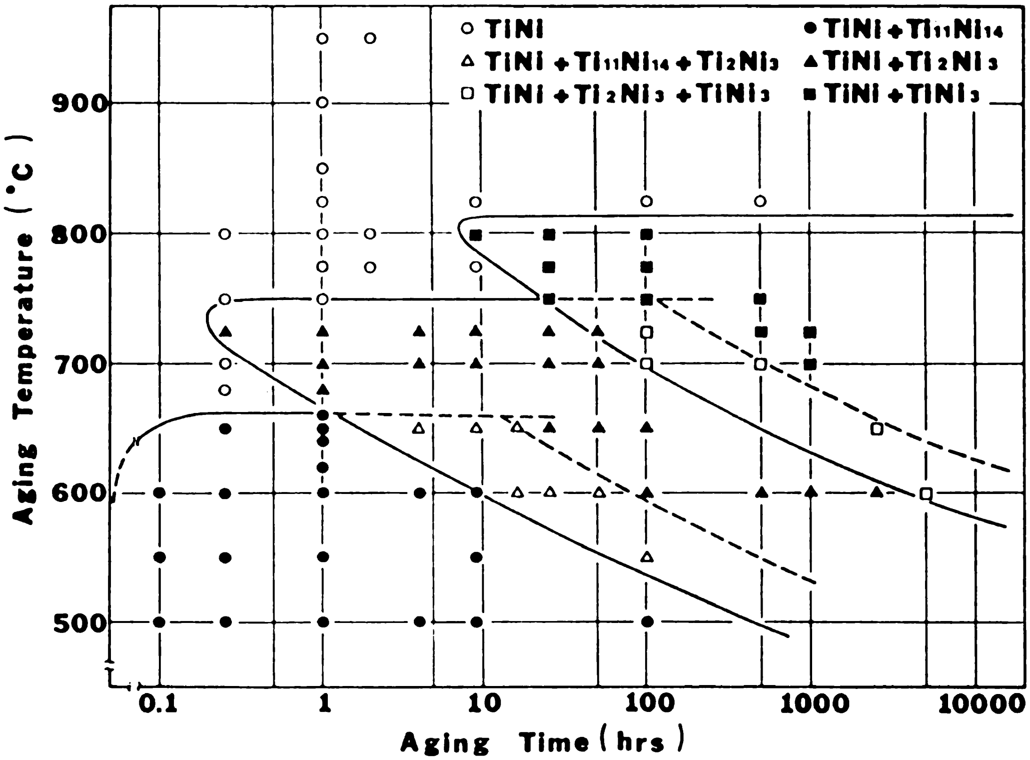

Figure 1-11. Isothermal time-temperature-transformation (TTT) diagram for $Ni_{52}Ti_{48}$ alloy [Nishida, Wayman and Honma, 1986].

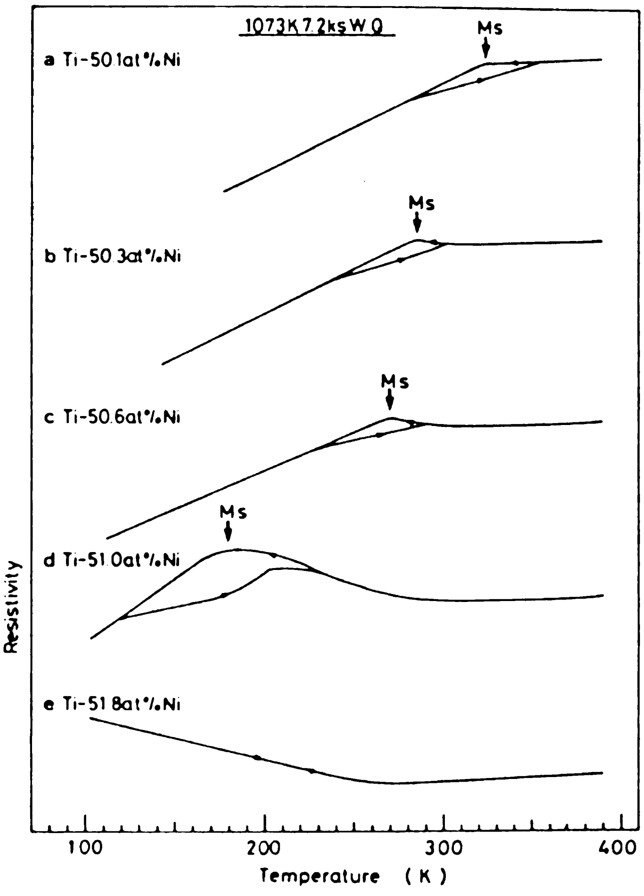

Figure 1-12. The effect of Ni-concentration on the electrical resistivity vs. temperature curves for NiTi alloys quenched from 1073 K [Nishida and Honma, 1984]. The *Ms* temperature decreases rapidly with the increase of nickel content.

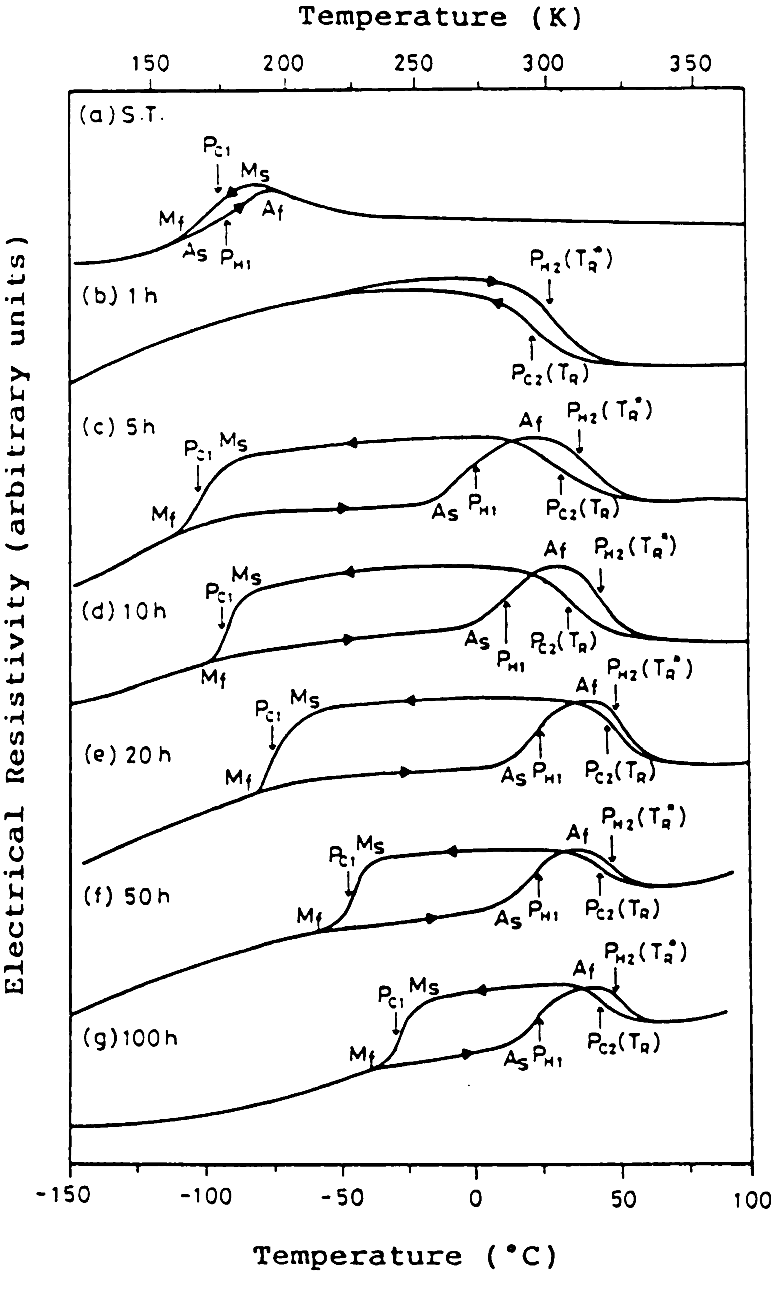

Figure 1-13. Electrical resistivity vs. temperature curves [Wu, Lin and Chou, 1989], of $Ni_{51}Ti_{49}$ alloy aged at 673 K after a 1073 K, 2 hour solution-treatment for various times, showing the effects of aging on M_s temperatures.

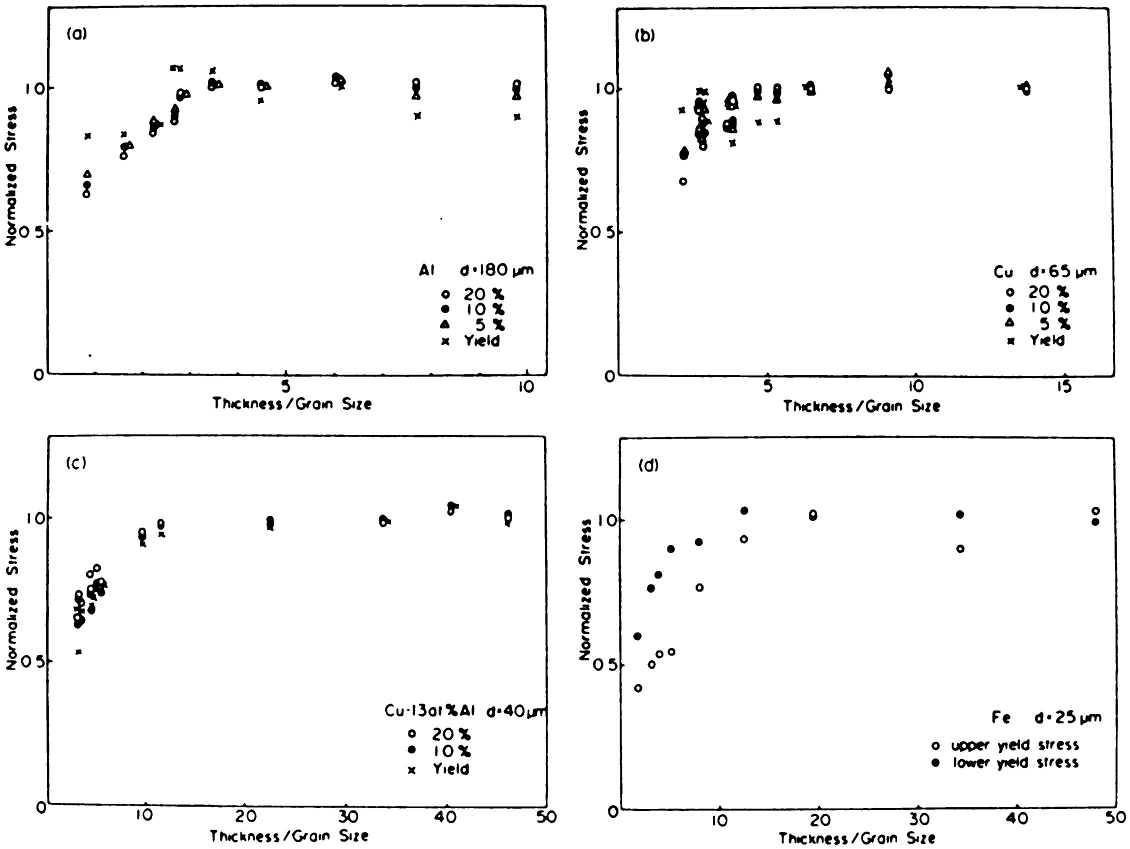

Figure 1-14. The effect of specimen thickness on the normalized flow stress in polycrystalline (a) Al, (b) Cu, (c) Cu-13Al (at.%), and (d) Fe [Miyazaki, Shibata and Fujita, 1979].

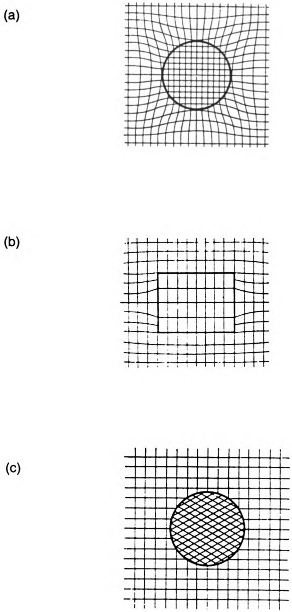

Figure 1-15. Three types of crystallographic relationships between the lattice of the precipitate and the lattice of the matrix [Hirsch *et al.*, 1977]. (a) coherent with negative misfit; (b) semi-coherent, and (c) incoherent.

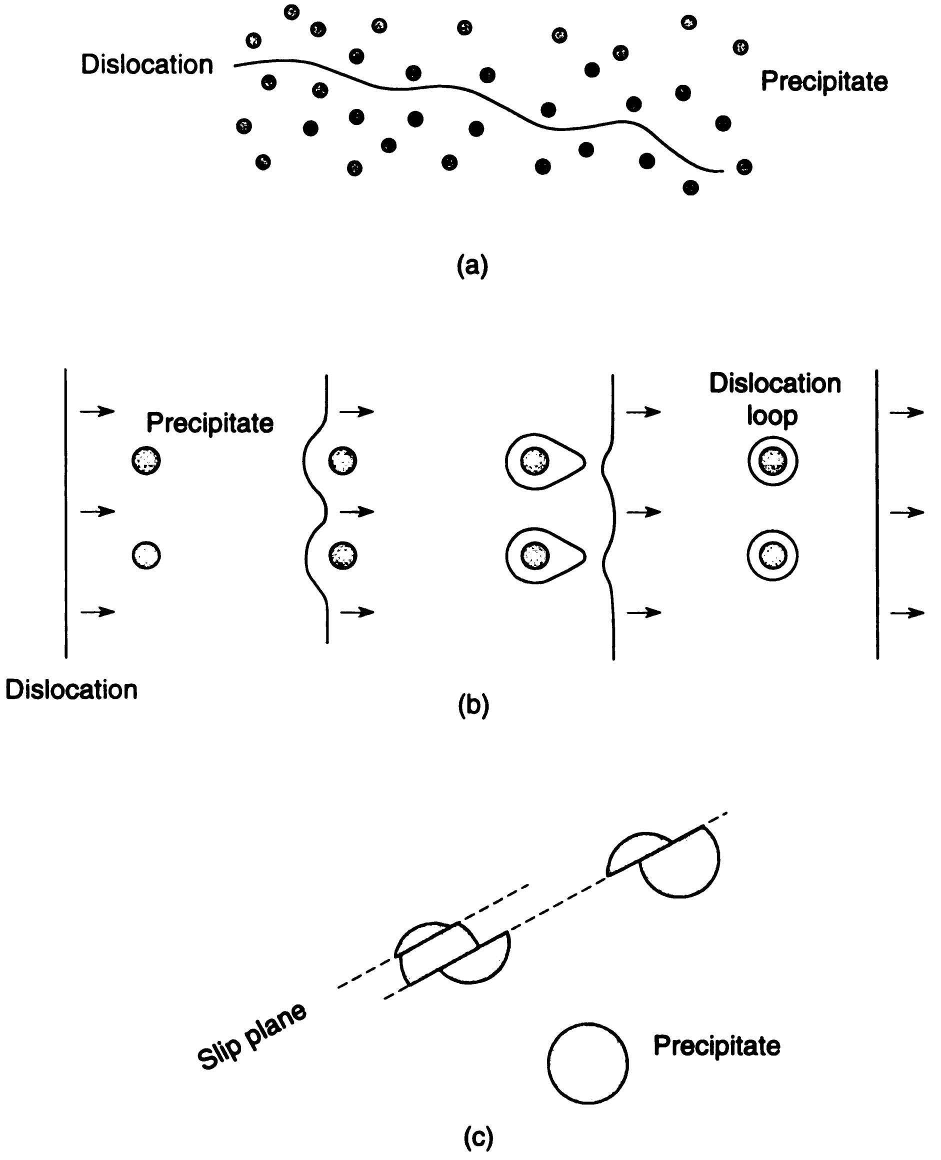

Figure 1-16. Interactions between dislocations and precipitates. (a) In lightly aged alloys, the closely spaced stress fields make the dislocation unable to bend between the particles. The dislocation has to move out of its slip plane by climbing or cross-slipping. (b) In over-aged alloys, the particles are much wider apart. The dislocation can bend around each precipitate and leaving dislocation loops [Orowan, 1948]. (c) A schematic representation showing sheared Ni_3Al particles by passing dislocations in a Ni-19% Cr-6% Al alloy after 2 % deformation [based on Gleiter and Hornbogen, 1965].

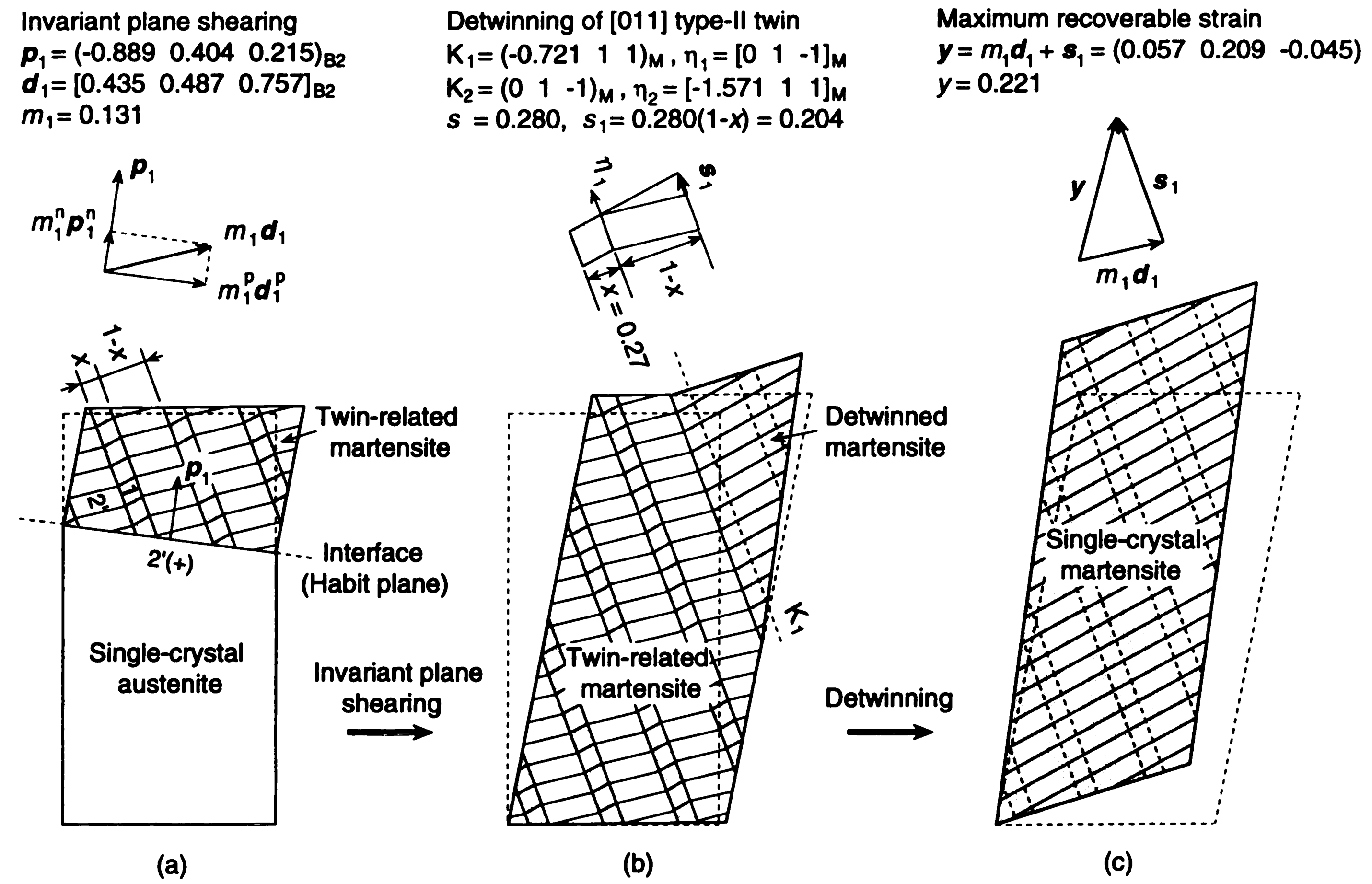

Figure 1-17. A diagram schematically illustrating an idealized deformation route from a B2 single crystal to a B19' single crystal where the transformation twinning and detwinning of martensite are well separated.
(a-b) The martensitic transformation proceeds through the movement of parent/martensite interface.
(b-c) The deformation is realized by the coalescence of favorable twin variants with respect to applied stress.

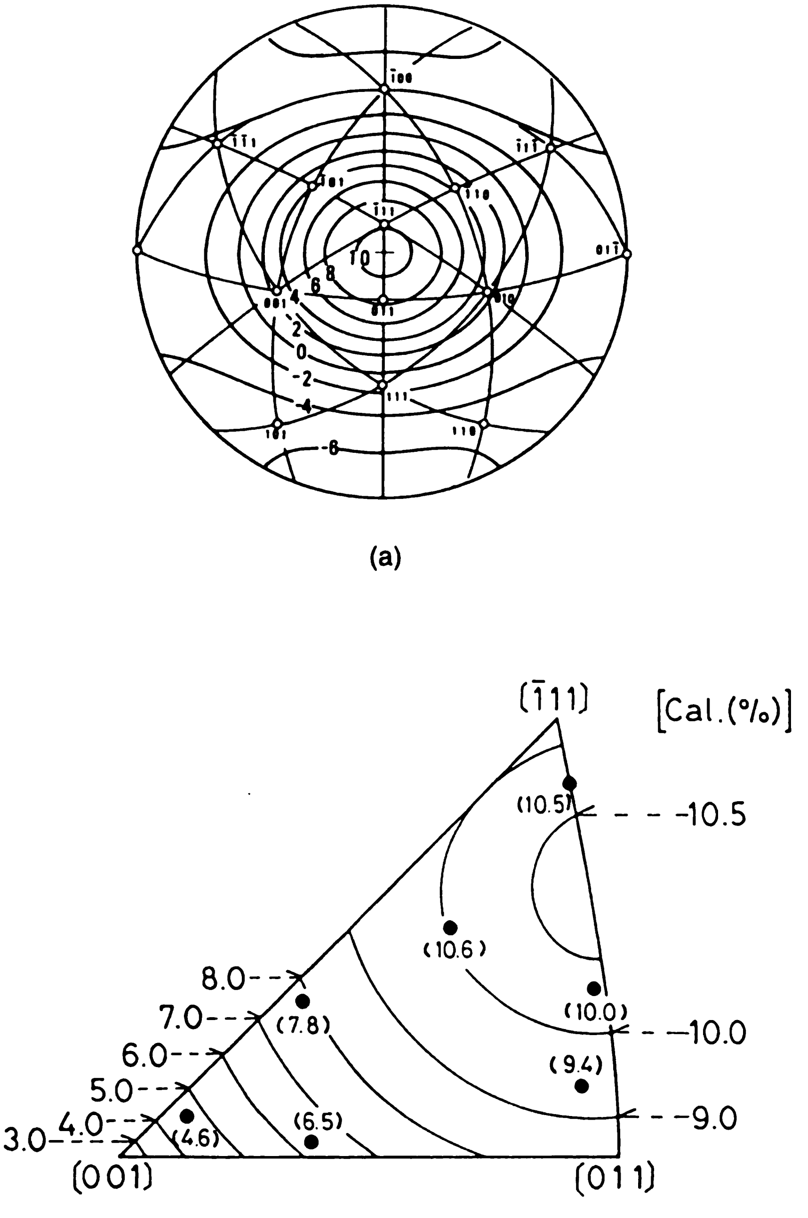

Figure 1-18. The orientation dependence of recoverable tensile strain for NiTi single crystals in B2-to-B19' transformation: (a) The values predicted from the lattice deformation matrix [Saburi and Nenno, 1981]. (b) The measured values from solution-treated single crystals [Miyazaki *et al.* 1984]. Numbers in parentheses indicate the measured results and contour lines represent predicted values.

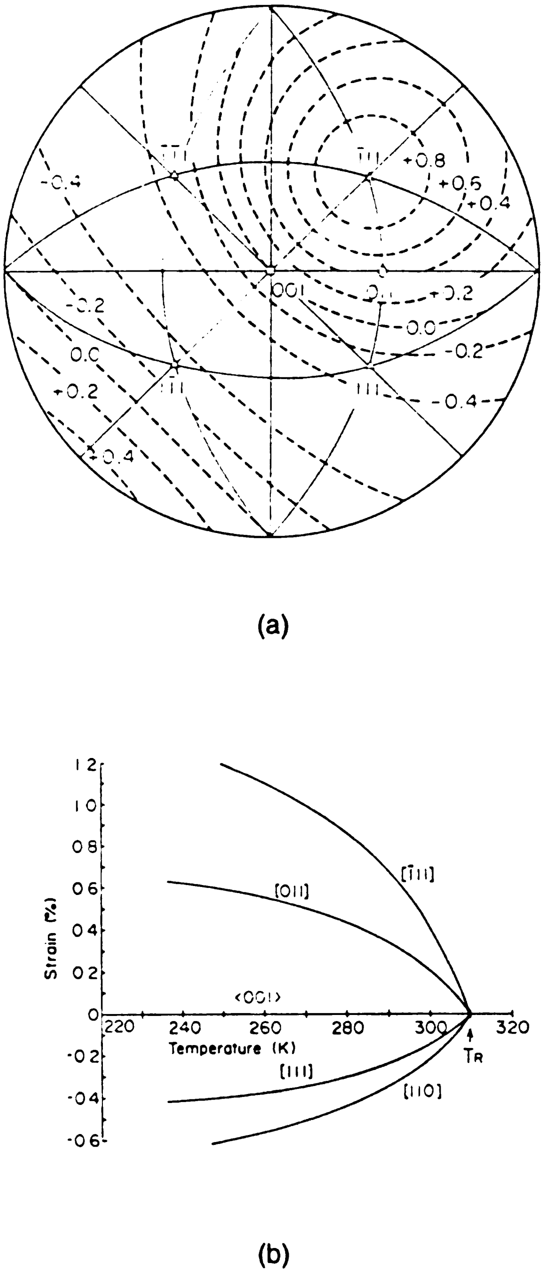

Figure 1-19. (a) The orientation dependence of recoverable strain for B2-to-R transition at a temperature of (*T*R - 35) K. Solid circles indicate the experimental data, whereas contour lines indicate calculated values; (b) The temperature dependence of the recoverable strain for various orientations. The recoverable strain in all directions increases gradually as temperature decreases from *T*R [Miyazaki, Kimura and Otsuka, 1988].

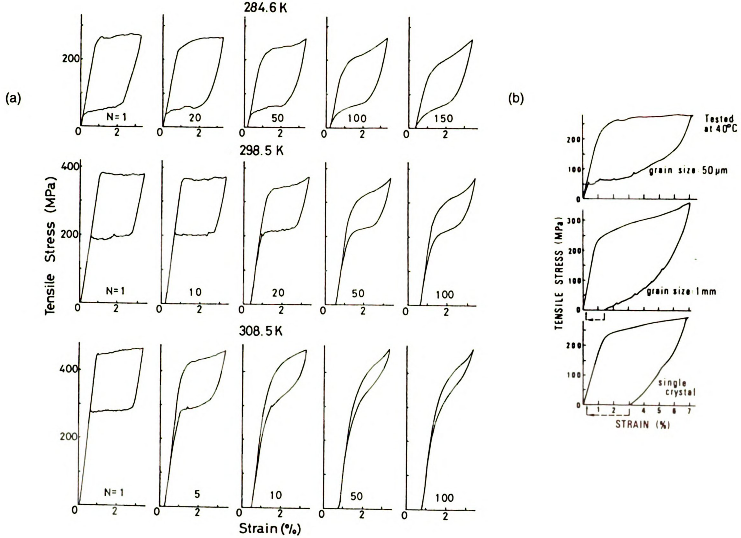

Figure 1-20. (a) The effect of tension cycling on superelasicity characteristics in $Ni_{49.5}Ti_{50.5}$ alloy [Miyazaki *et al* 1986]; (b) The effect of grain size on superelasticity in $Ni_{50.5}Ti_{49.5}$ alloy [Saburi, Yoshida and Nenno, 1984].

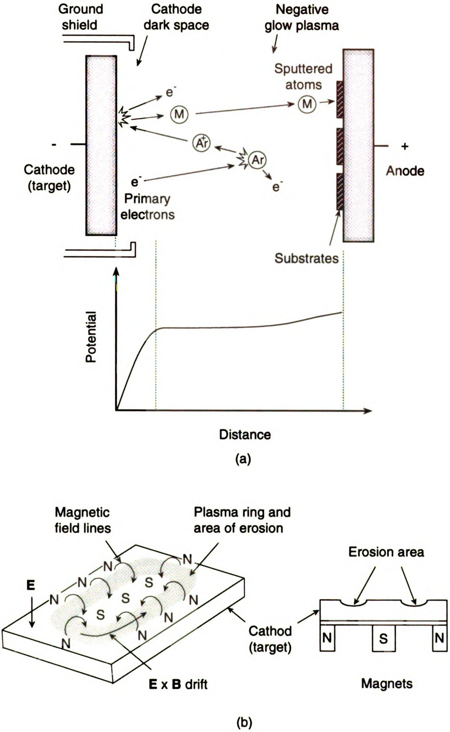

Figure 1-21. Schematic representation of (a) planar diode sputter deposition [modified from Thornton, 1982], and (b) planar magnetron [modified from Ahmed, 1987].

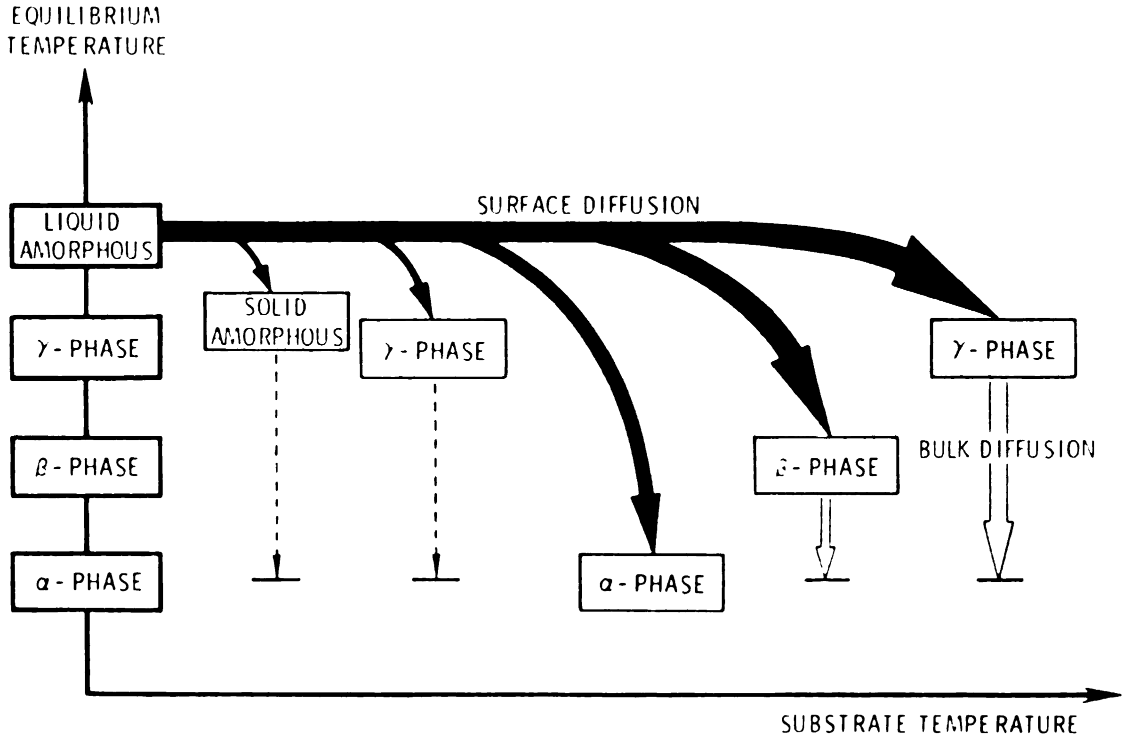

Figure 1-22. A schematic illustration of the effect of substrate temperature on phase formation for a hypothetical polymorphic material [Thornton, 1977].

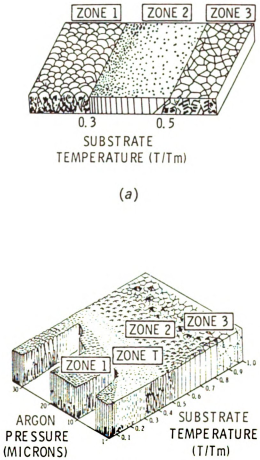

(a)

(b)

Figure 1-23. Structural zone models for physical vapor deposition processes. (a) The model proposed by Movchan and Demchishin [1969] for electron beam evaporations; (b) The model proposed by Thornton [1974] for sputtered metal coatings.

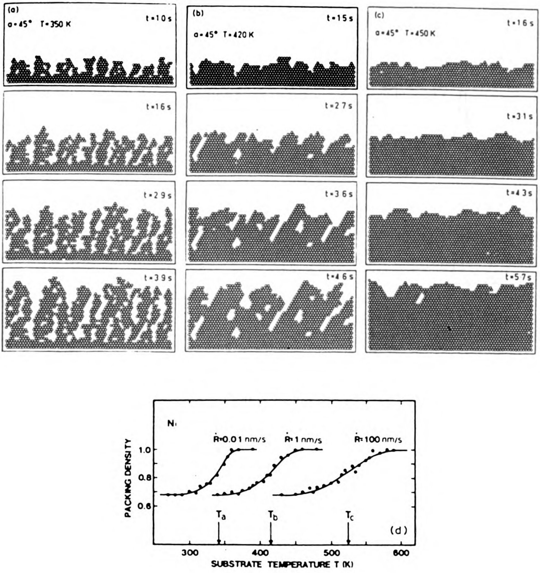

Figure 1-24. A computer modeling of film growth using 2D hard spheres by Muller [1985]. (a-c) show the influence of temperature on packing density of films. (d) displays that the temperature effects packing density while the deposition rate changes the transition temperature of density-to-unity density.

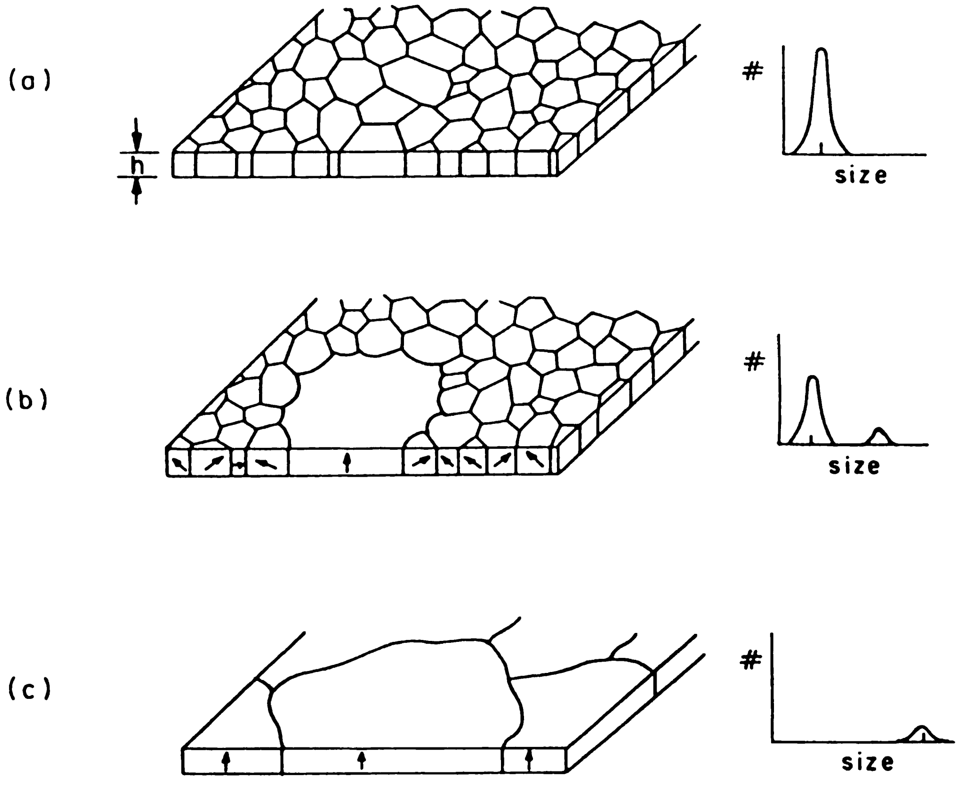

Figure 1-25. Schematic microstructures and grain distributions for thin films undergoing secondary grain growth [Thompson, 1990]. (a) Microstructure before the secondary grain growth occurs. (b) Intermediate stage in which the grain sizes are bimodelly distributed. (c) After the secondary grain growth microstructure shows crystallographic (fiber) texture.

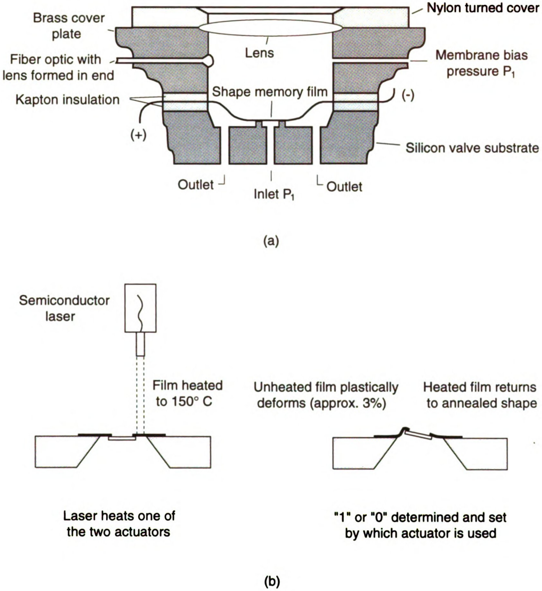

Figure 1-26. Schematic drawing of two devices [Johnson, 1992] using the shape-memory effect of NiTi thin films: (a) a microvalve, and (b) a microactuator.

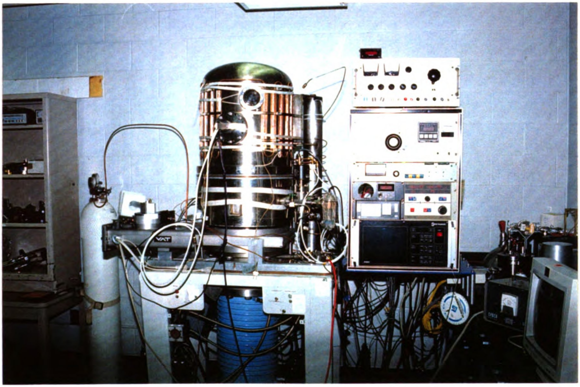

Figure 2-1. Photograph of magnetron sputter machine developed for this study.

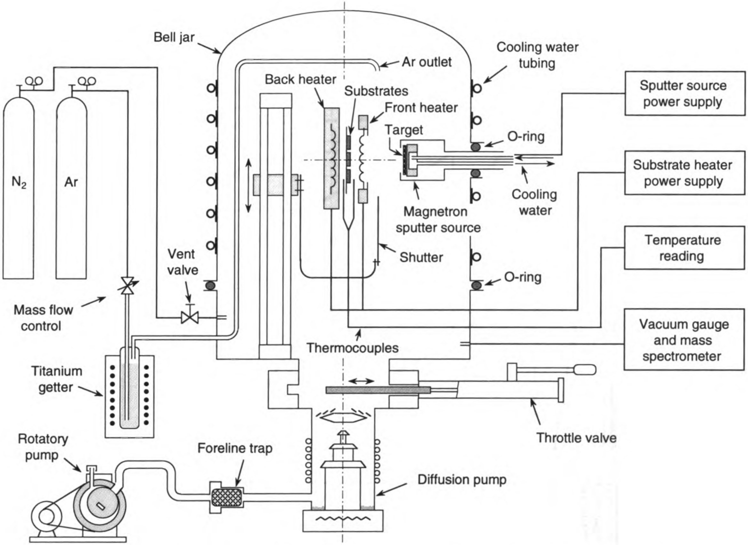

Figure 2-2. Schematic diagram of magnetron sputter system developed for this study.

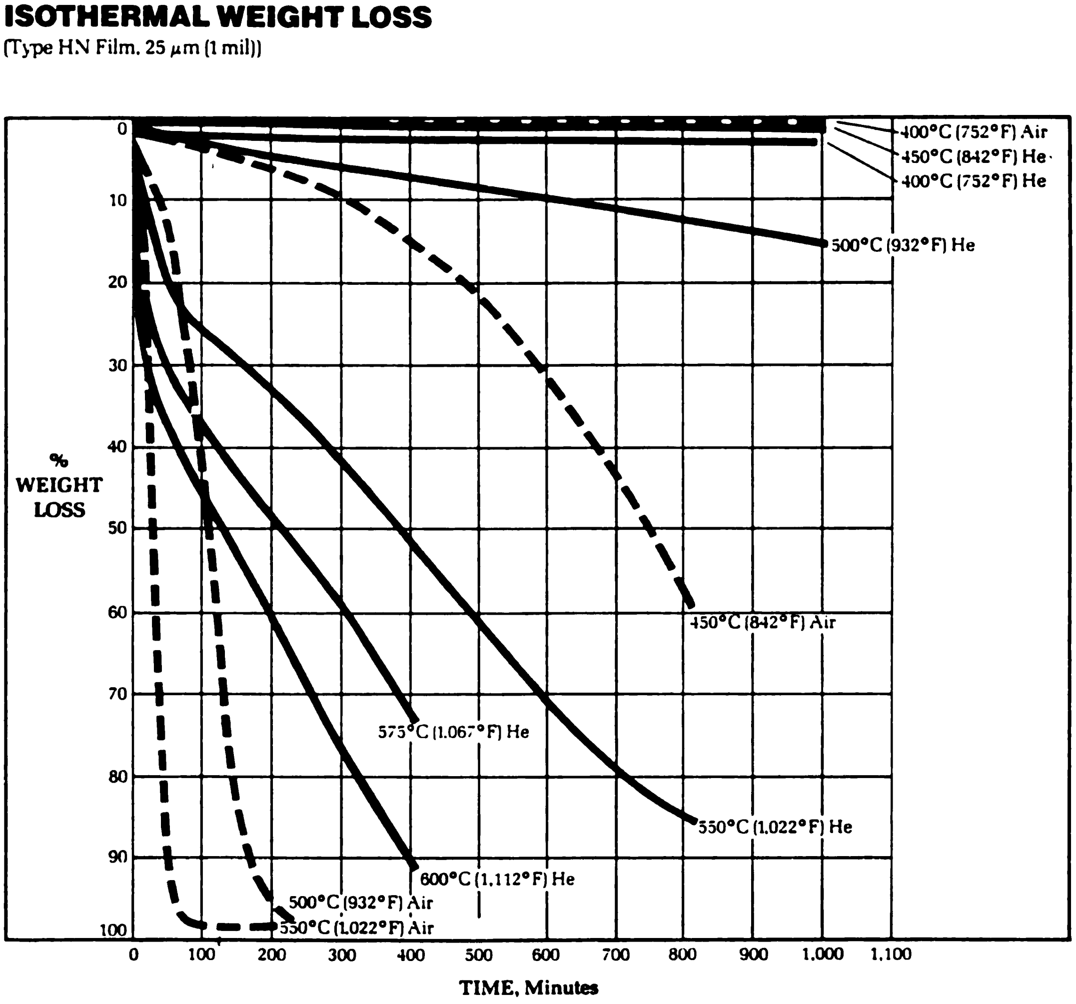

Figure 2-3. The weight loss characteristics of Kapton in air and helium at a heating rate of 3 K/min [Product Bulletins, DuPont, 1993].

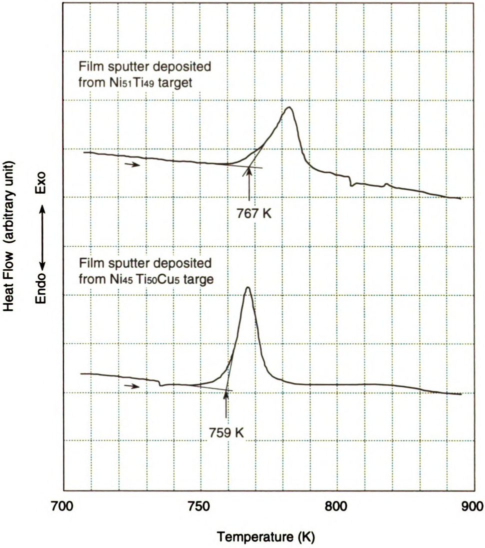

Figure 2-4. Differential scanning calorimetry (DSC) curves of sputter-deposited binary and ternary NiTi films at a heating rate of 20 K/min showing the crystallization temperature.

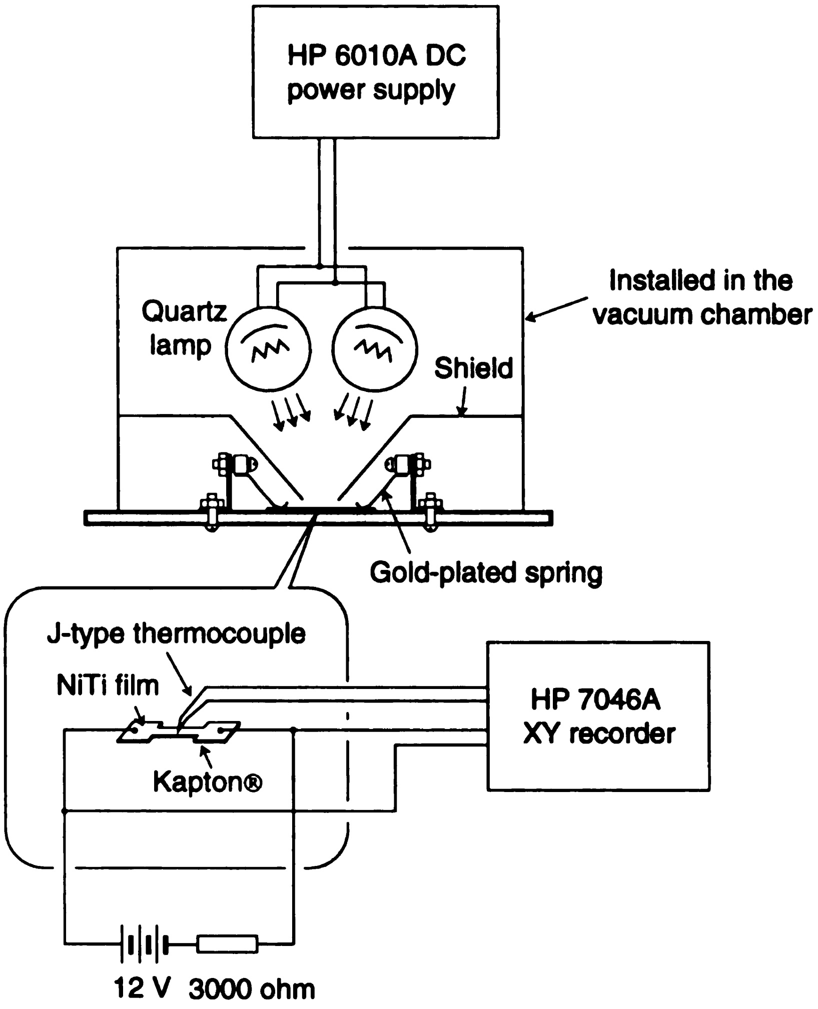

Figure 2-5. Experimental set-up for *in situ* observation of electrical resistivity change in crystallization annealing of NiTi/Kapton laminate.

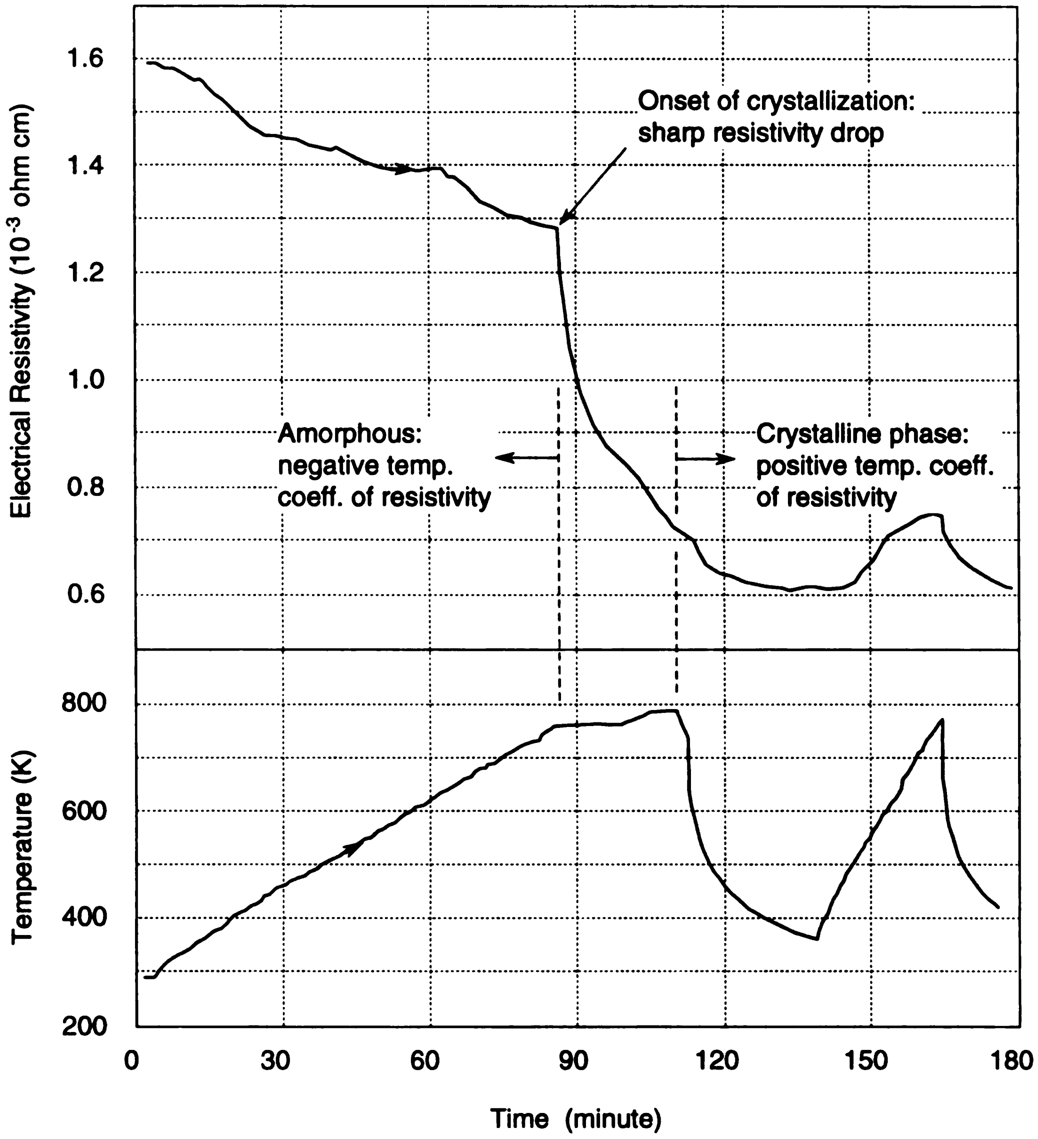

Figure 2-6. The diagram showing the electrical resistivity of NiTi film as a function of temperature during crystallization annealing treatment at a heating rate of 6.7 K/min.

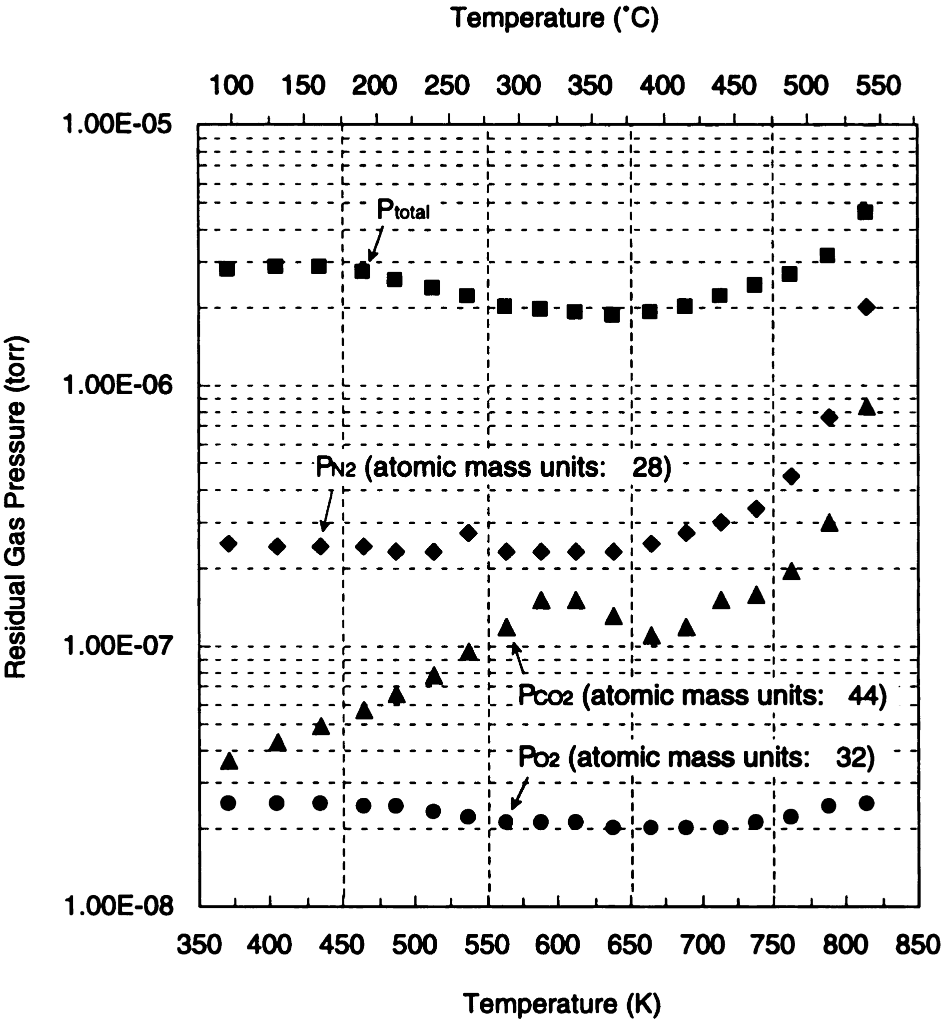

Figure 2-7. Residual gas pressure vs. temperature curves of Kapton film at a heat-up rate of 5 K/min.

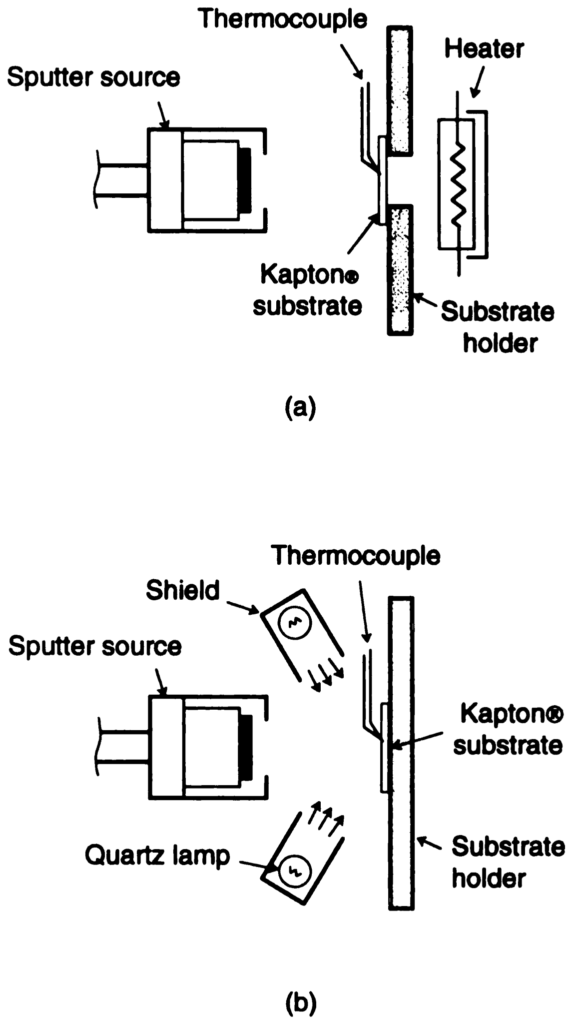

Figure 2-8. Schematic drawings of substrate heating devices which have been tested in this study. (a) A conventional substrate holder with a heater situated under the substrate. (b) A heating device consists of four 625 watt quartz lamps clustered around the sputter source to irradiate the substrate.

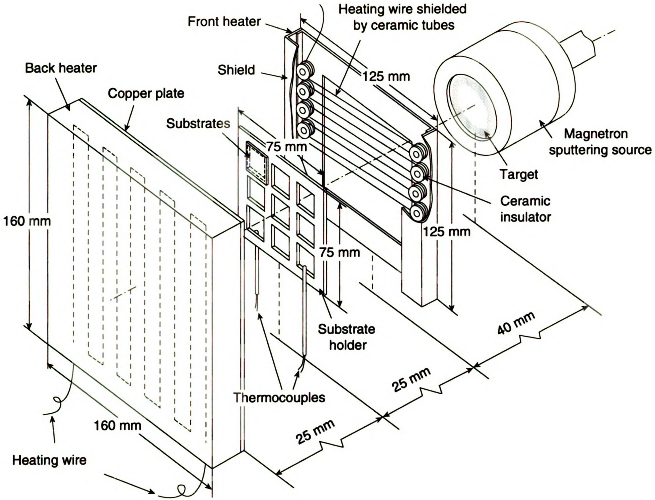

Figure 2-9. Schematic illustration showing the exploded view of two-sided substrate heating device.

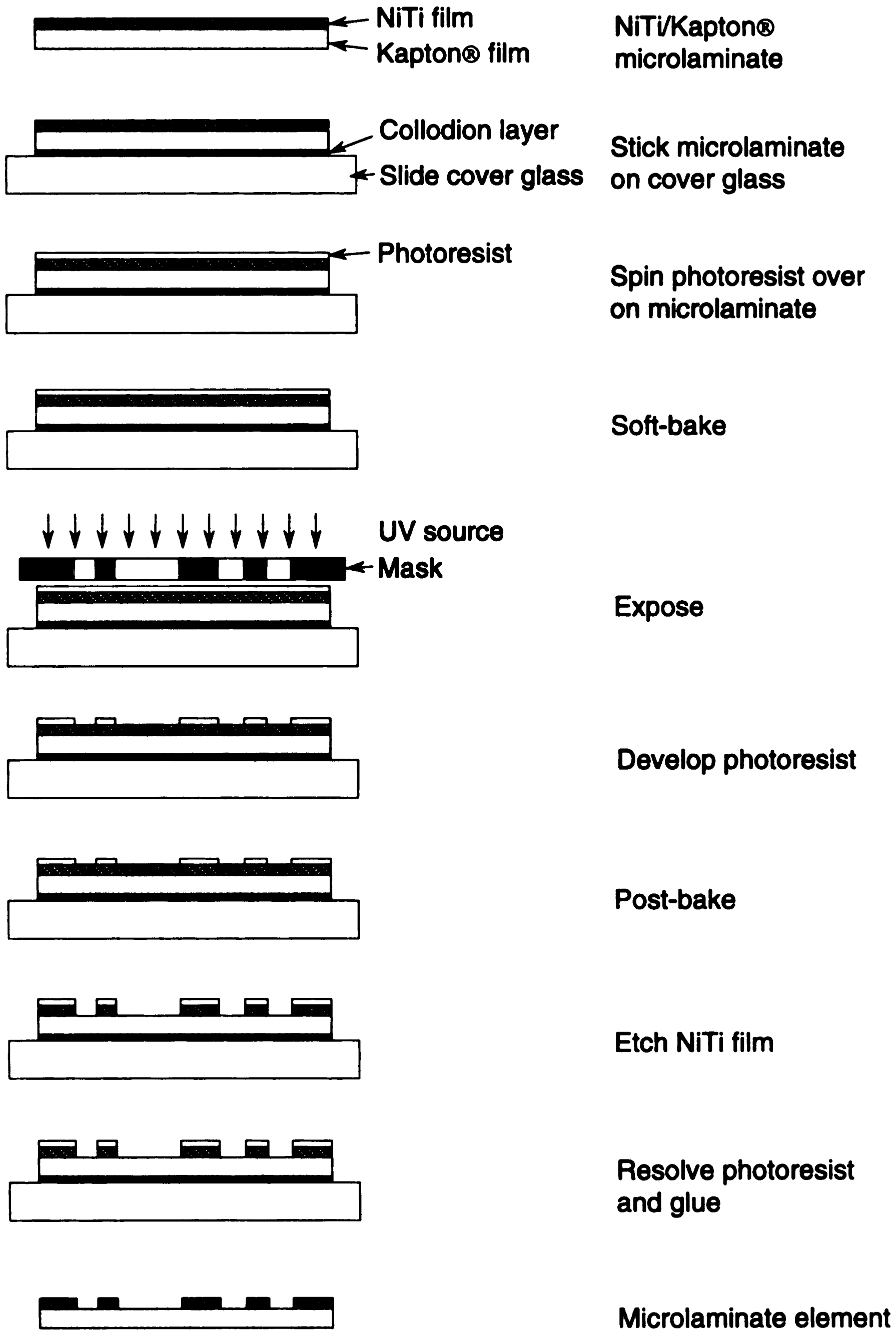

Figure 2-10. A patterning-etching process for fabrication of NiTi/polyimide actuator elements.

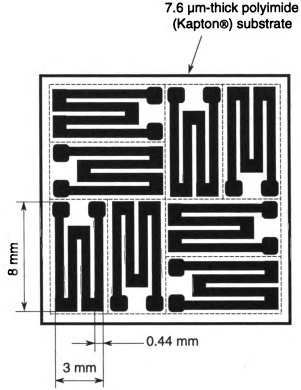

Figure 2-11. Pattern for making eight NiTi/polyimide actuator elements.

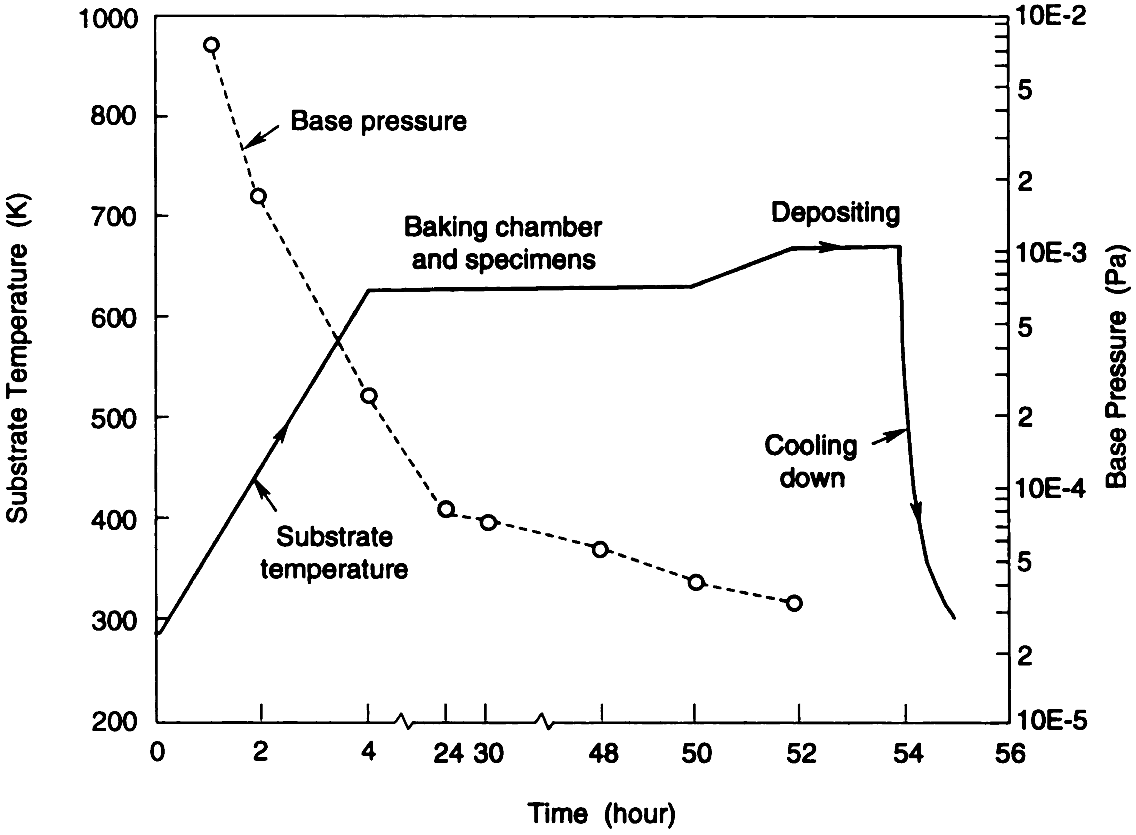

Figure 2-12. A plot of substrate temperature and base pressure vs. time for a typical deposition run ($T = 670$ K).

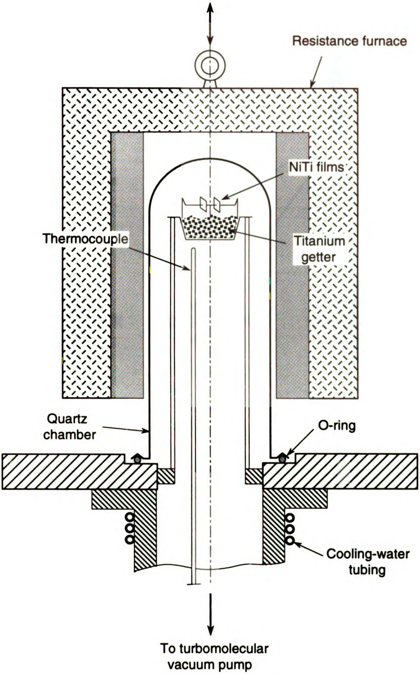

Figure 2-13. A quartz-tube vacuum furnace used for heat-treatment of NiTi films.

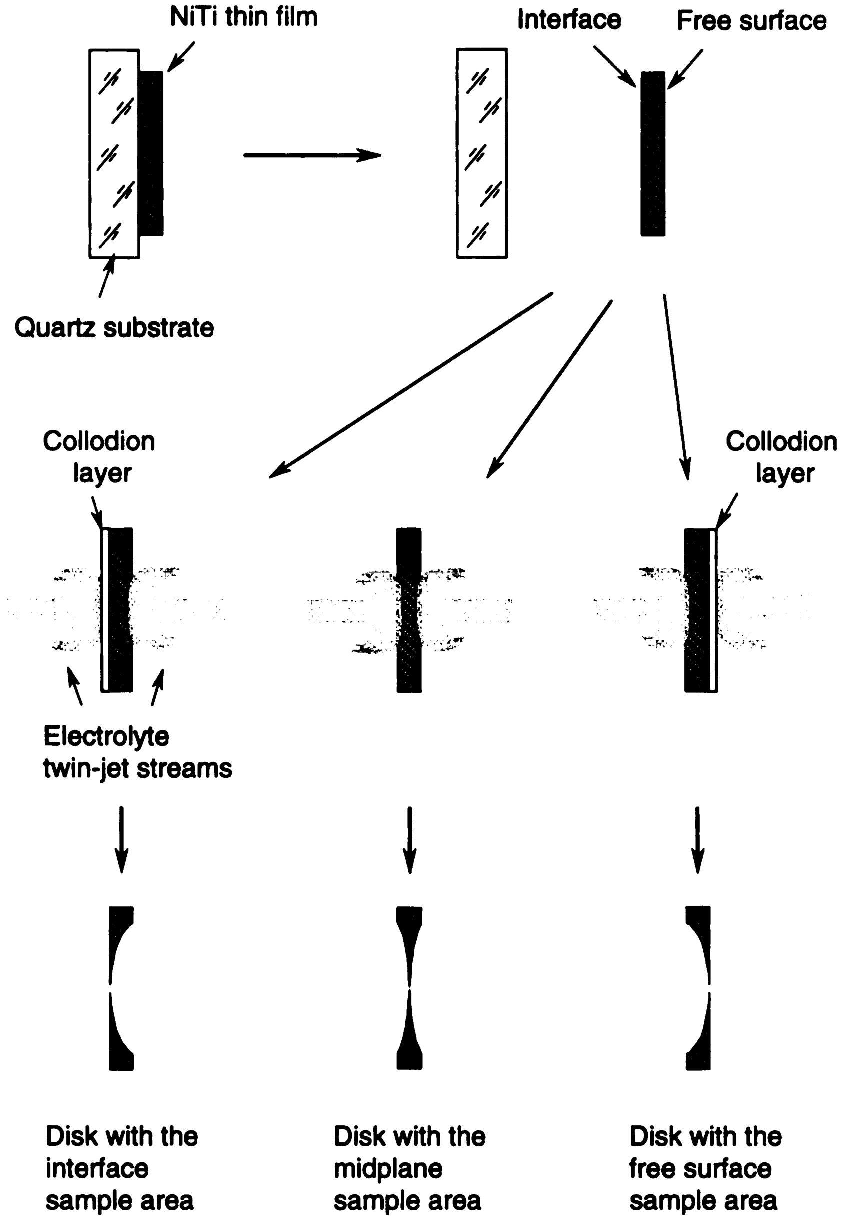

Figure 2-14. A drawing illustrating the preparation of TEM disks. Three sampling locations along the depth of the NiTi thin films could be obtained by a masking technique.

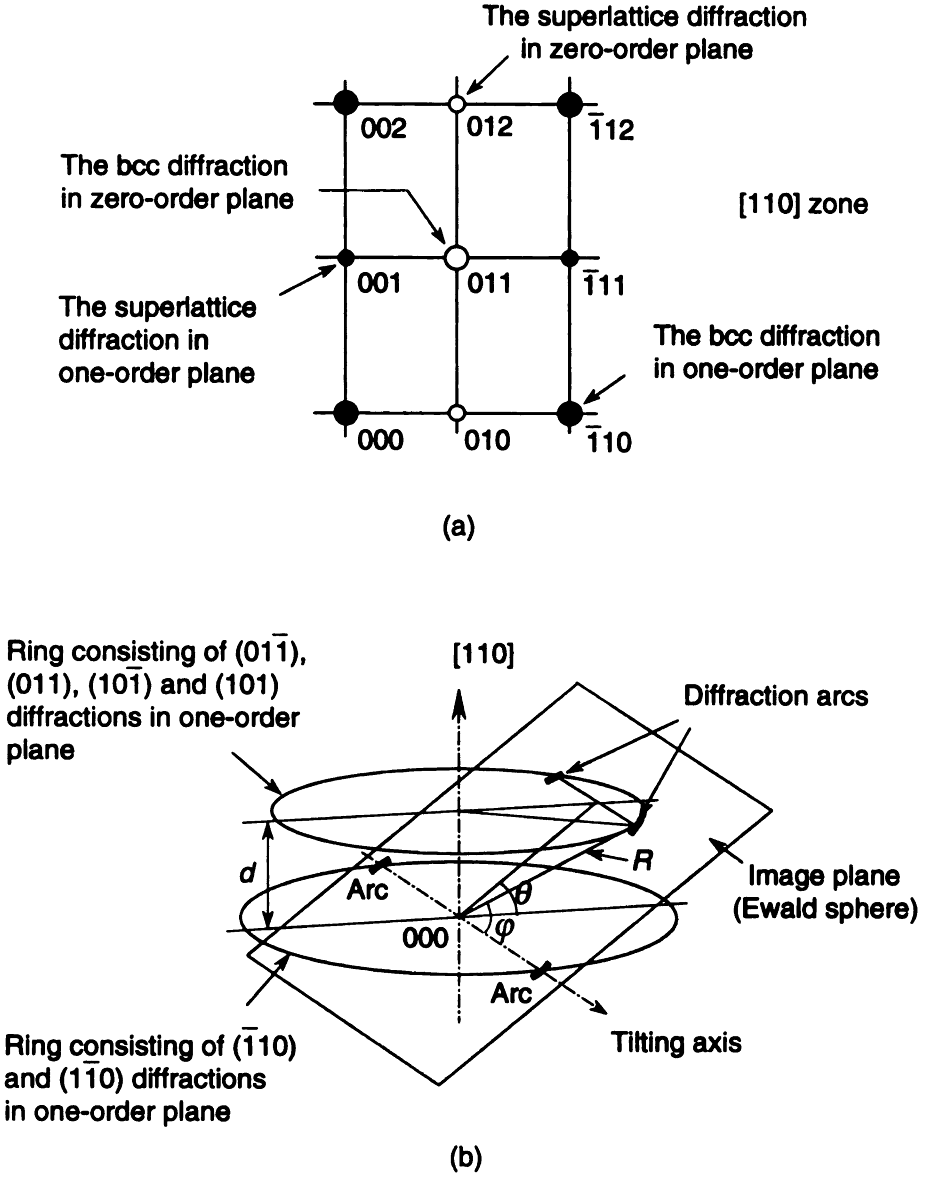

Figure 2-15. (a) The reciprocal lattice of the B2 structure in [110] zone. (b) The geometry for calculating the positions of diffracted arcs upon tilting. Where φ is the angle between tilting axis and the arcs in the image plane, θ is the tilting angle of the specimen, d is the distance between the zero-order reciprocal rings and the higher-order reciprocal rings and R is the radius of arcs in the image plane.

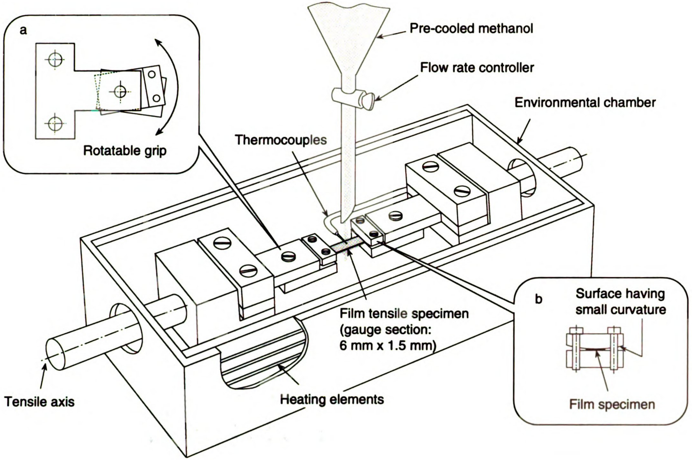

Figure 2-16. Schematic illustration of tensile test apparatus for evaluating thin NiTi films at various temperatures.

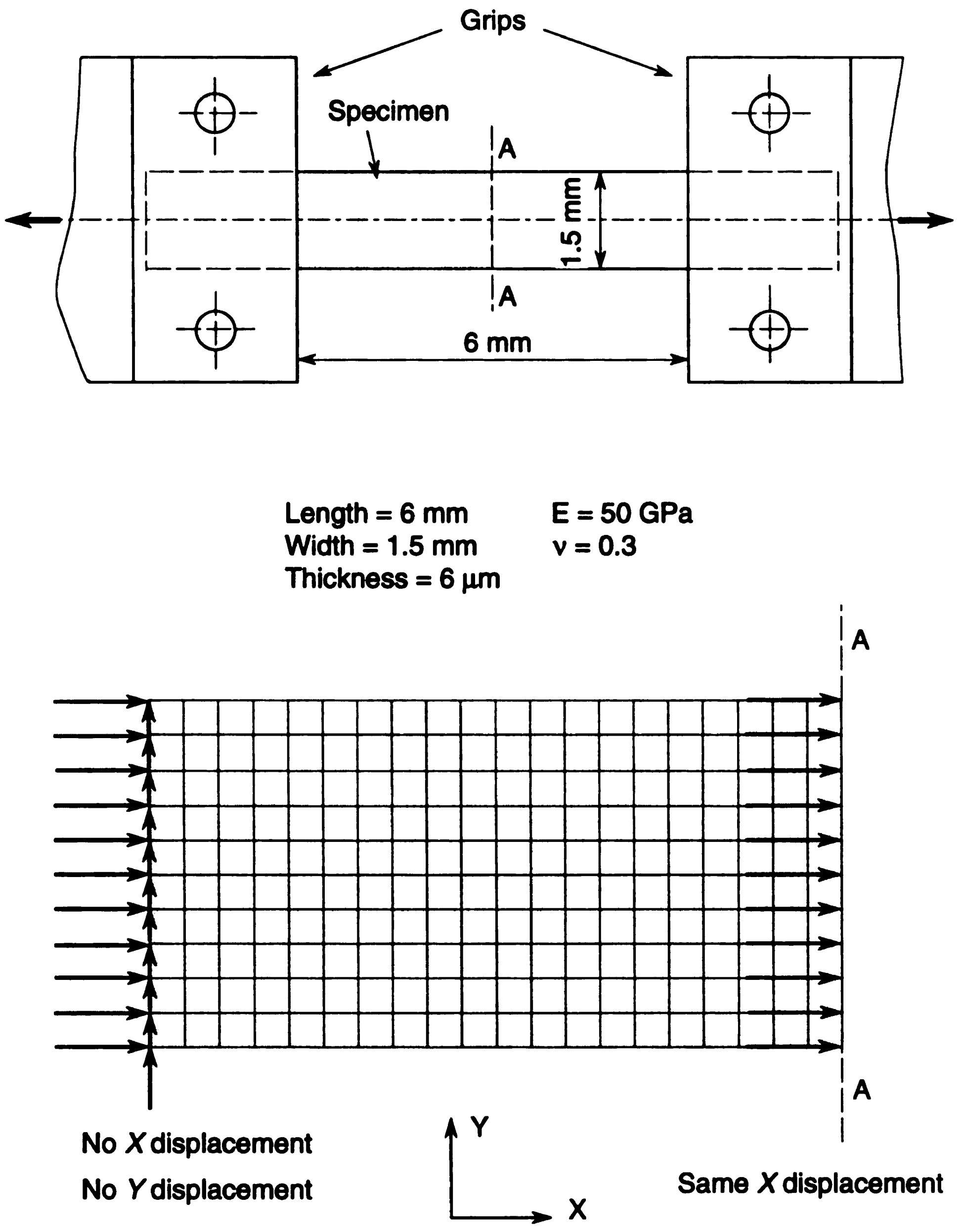

Figure 2-17. Finite element grid for analysis of rectangular thin film tensile specimens.

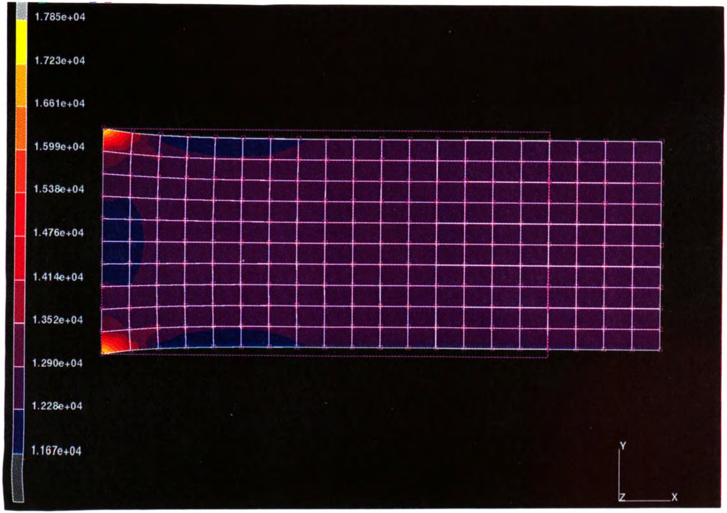

Figure 2-18. A contour map obtained from the finite element analysis showing the maximal principal stress of thin film tensile specimen. It can be seen that the maximal principal stress reaches the maximum at edges near the ends of the gauge section.

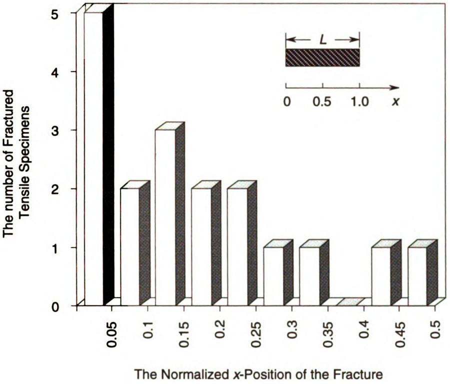

Figure 2-19. A plot of the number of samples fractured versus the normalized x-position where the fracture occurred. Each number is collected from the interval of $(x, x + 0.05)$.

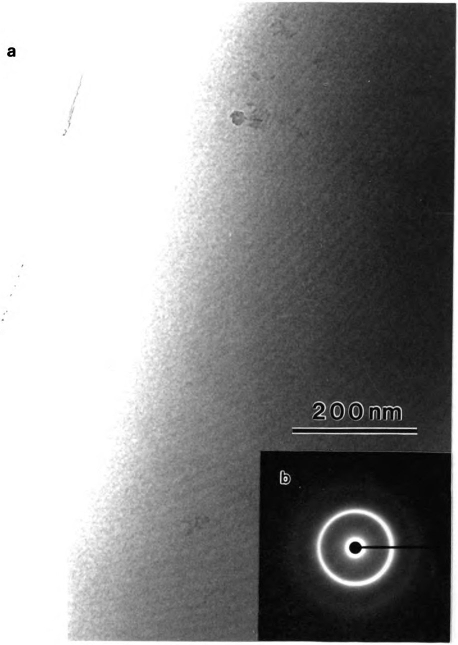

Figure 3-1. TEM bright-field (BF) image in (a) showing a completely featureless structure, and the associated selected area diffraction pattern (SADP) in (b) showing a broad, diffuse halo pattern which are normally observed in the amorphous materials. The micrographs were taken from the midplane of the film H573 at a tilt of 0 degree.

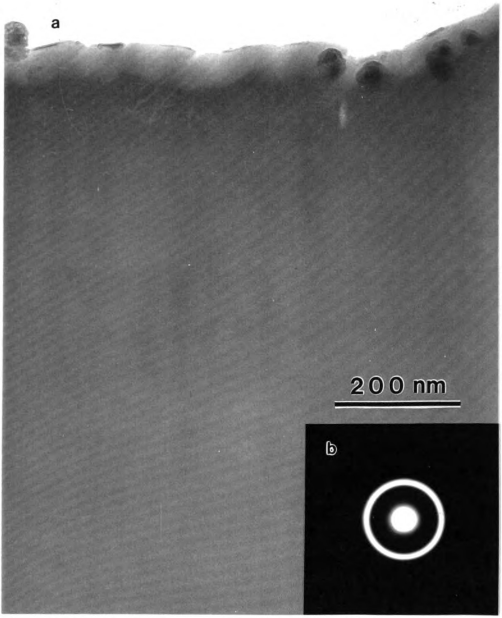

Figure 3-2. TEM BF image in (a) and the associated SADP in (b), taken from the interface of the film H598 at a tilt of 0 degree, showing the amorphous structure.

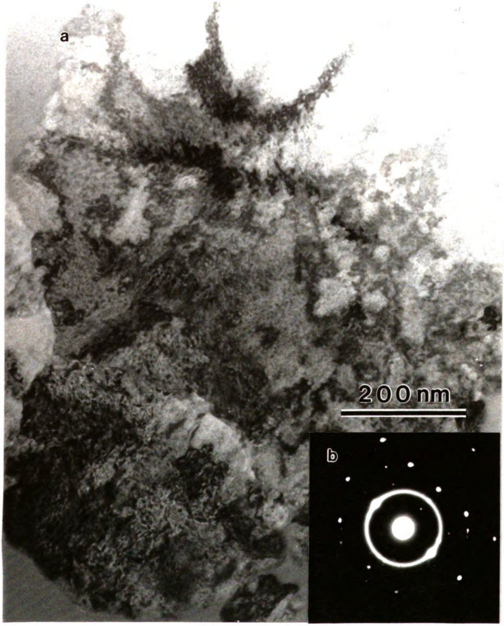

Figure 3-3. TEM BF image and the associated SADP taken from the midplane of the film H598 at a tilt of 0 degree. The SADP reveals a single-crystal diffraction pattern in the $[1\bar{1}0]_{B2}$ zone together with a superimposed diffuse halo pattern scattered from the amorphous background. This initial crystallite has an in-plane size greater than 1 μm.

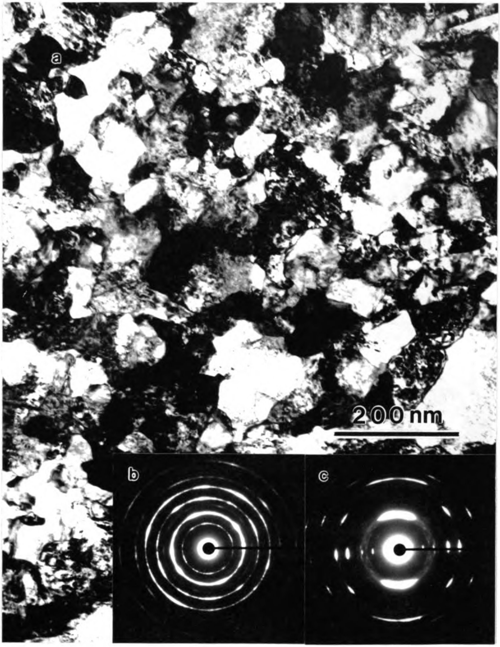

Figure 3-4. TEM BF images and the associated SADP's taken from the surface of the film H598. The BF image (a) and (d), respectively, were recorded at a tilt of 0 and 45 degrees. Elongated grain images in (d) suggests a columnar grain structure. The SADP (b) and (c) were recorded at a tilt of 0 and 30 degrees, respectively, showing a strong (110) fiber-texture. The non-even intensities of the diffraction rings in (b) reflect the restricted in-plane grain orientations.

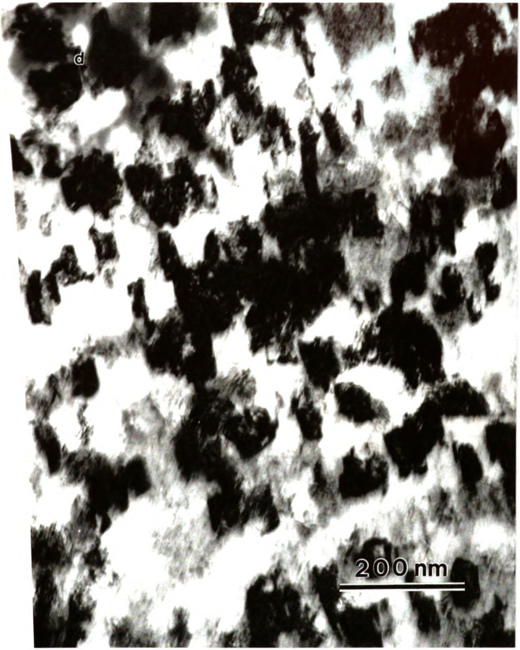

Figure 3-4. (Contiuned) TEM BF images and the associated SADP's taken from the surface of the film H598. The BF image (a) and (d), respectively, were recorded at a tilt of 0 and 45 degrees. Elongated grain images in (d) suggests a columnar grain structure. The SADP (b) and (c) were recorded at a tilt of 0 and 30 degrees, respectively, showing a strong (110) fiber-texture. The non-even intensities of the diffraction rings in (b) reflect the restricted in-plane grain orientations.

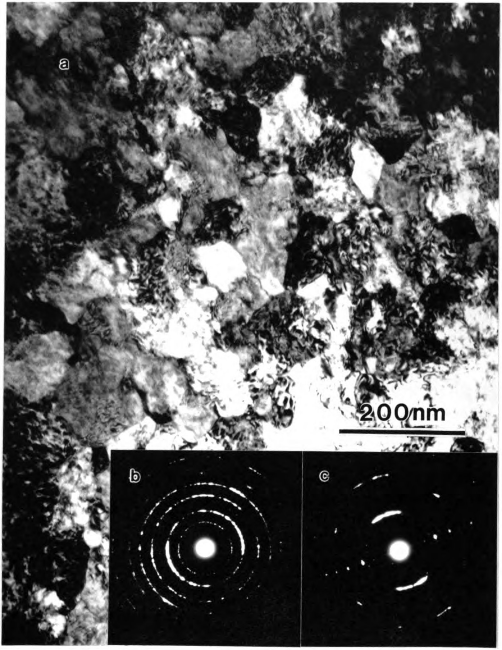

Figure 3-5. TEM BF image and the associated SADP's taken from the interface of the film H623. The SADP (b) and (c) were recorded at a tilt of 0 and 30 degrees, respectively, showing a strong (110) fiber-texture.

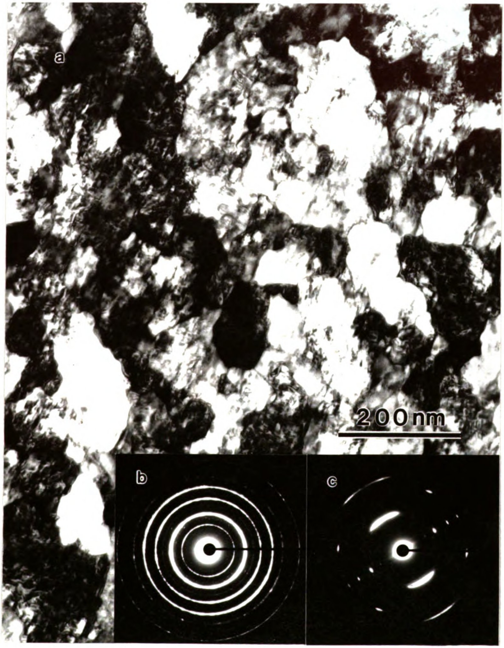

Figure 3-6. TEM BF images and the associated SADP's taken from the midplane of the film H623. The BF image (a) and (d), respectively, were recorded at a tilt of 0 and 45 degrees. Elongated grain images in (d) implies a columnar grain structure. The SADP (b) and (c) were recorded at a tilt of 0 and 30 degrees, respectively, showing a strong (110) fiber-texture.

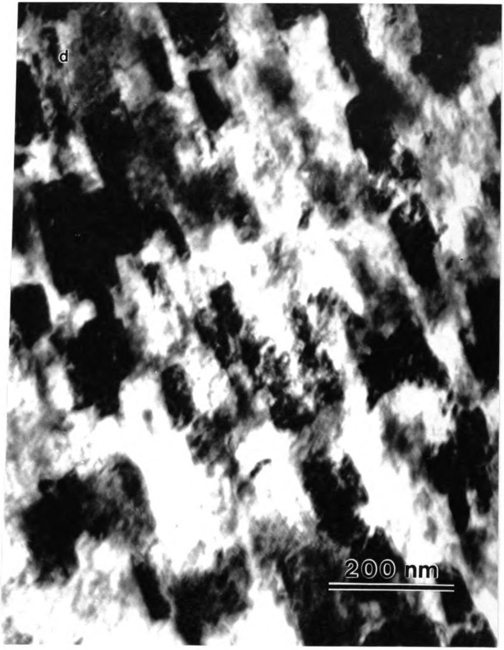

Figure 3-6. (Contiuned) TEM BF images and the associated SADP's taken from the midplane of the film H623. The BF image (a) and (d), respectively, were recorded at a tilt of 0 and 45 degrees. Elongated grain images in (d) implies a columnar grain structure. The SADP (b) and (c) were recorded at a tilt of 0 and 30 degrees, respectively, showing a strong (1 10) fiber-texture.

Figure 3-7. TEM BF image and the associated SADP's taken from the surface of the film H623. The SADP (b) and (c) were recorded at a tilt of 0 and 30 degrees, respectively, showing a strong (110) fiber-texture.

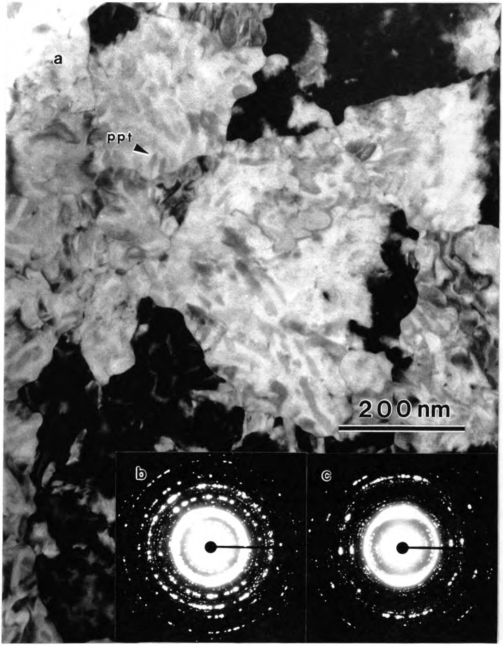

Figure 3-8. TEM BF image and the associated SADP's taken from the interface of the film H673. The lenticular precipitates in (a) can be distinguished (indicated by arrow). The SADP (b) and (c) were recorded at a tilt of 0 and 30 degrees, respectively, showing a strong (110) fiber-texture.

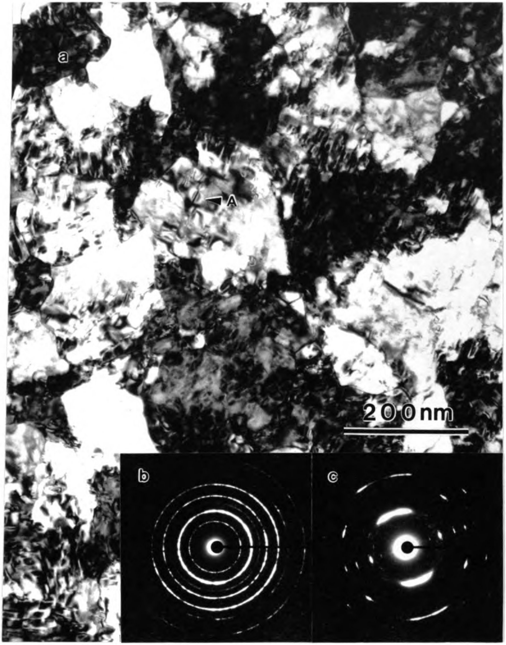

Figure 3-9. TEM BF images and the associated SADP's taken from the midplane of the film H673. The BF image (a) and (d), respectively, were recorded at a tilt of 0 and 45 degrees. A precipitate particle displays a perfect 'butterfly' shape of the image contrast as indicated by the arrow. Again, elongated grain images in (d) implies a columnar grain structure. The SADP (b) and (c) were recorded at a tilt of 0 and 30 degrees, respectively, showing a strong (110) fiber-texture.

Figure 3-9. (Contiuned) TEM BF images and the associated SADP's taken from the midplane of the film H673. The BF image (a) and (d), respectively, were recorded at a tilt of 0 and 45 degrees. A precipitate particle displays a perfect 'butterfly' shape of the image contrast as indicated by the arrow. Again, elongated grain images in (d) implies a columnar grain structure. The SADP (b) and (c) were recorded at a tilt of 0 and 30 degrees, respectively, showing a strong (110) fiber-texture.

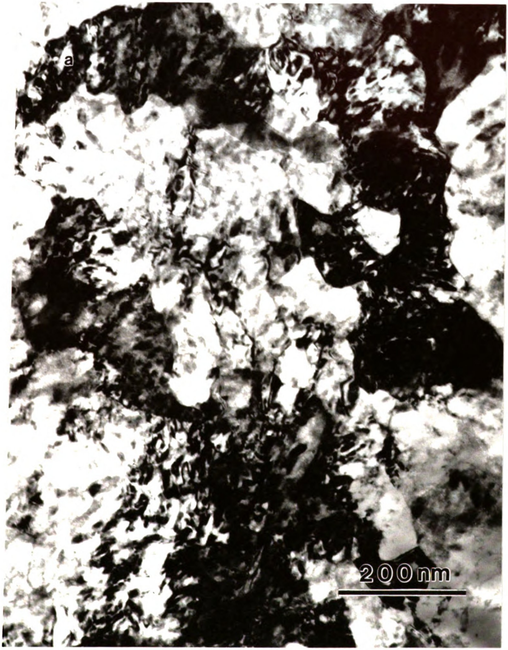

Figure 3-10. TEM BF image taken from the surface of the film H673.

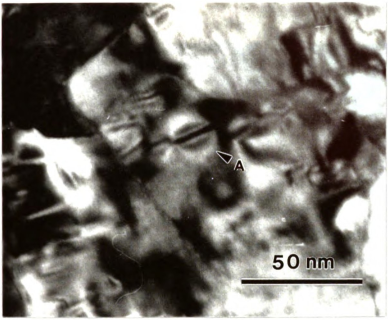

(a)

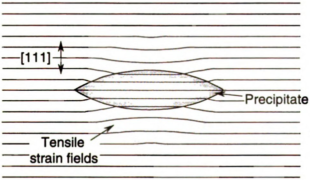

(b)

Figure 3-11. (a) The high magnification image of precipitate with 'butterfly' shaped contrast. The strain fields around Ni_4Ti_3 particles come from the lattice mismatch between particles and B2 matrix. (b) The habit plane of precipitate is $\{111\}_{B2}$ and the maximum mismatch of -2.9 % is along the normal to the precipitate disk. This minus value indicates a tensile strain perpendicular to the precipitate disk. [modified from Kainuma and Matsumoto, 1988]

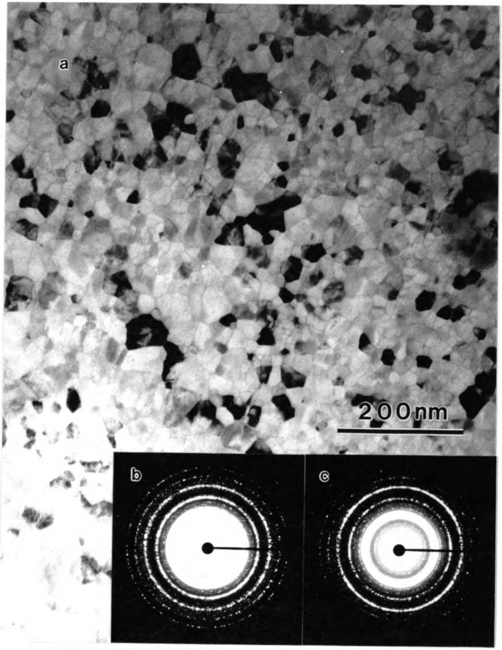

Figure 3-12. TEM BF image and the associated SADP's taken from the interface of the film H723. Extremely fine grains, 25 nm in diameter, were nucleated on very thin initial amorphous layer. The SADP (b) and (c) were recorded at a tilt of 0 and 30 degrees, respectively. The unchanged SADP's upon tilting imply the absence of the grain texture.

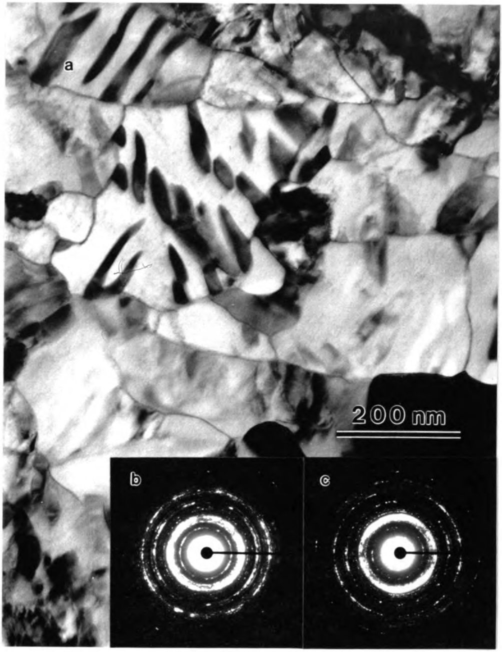

Figure 3-13. TEM BF image and the associated SADP's taken from the midplane of the film H723. The SADP (b) and (c) were recorded at a tilt of 0 and 30 degrees, respectively. The unchanged SADP's upon tilting display the random grain orientations.

Figure 3-14. TEM BF image taken from the surface of the film H723. The precipitates show smaller size than that in the midplane. Three ranges of precipitates can be seen in the low part of the micrograph.

Figure 3-15. The micrograph and associated SADP taken at the midplane of the film H703 revealing crystalline B2 grains and transgranular precipitates (indicated by arrows).

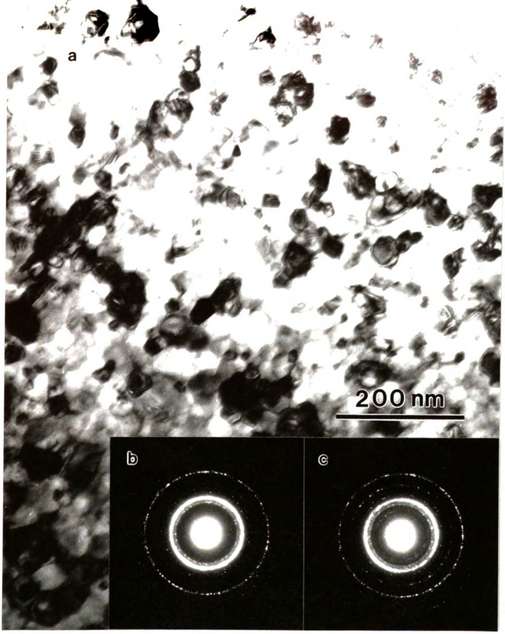

Figure 3-16. TEM BF image and the associated SADP's taken from the interface of the film H773. The SADP (b) and (c) were recorded at a tilt of 0 and 30 degrees, respectively. The micrographs display extremely fine grains and the random grain orientations.

Figure 3-17. TEM BF image and the associated SADP's taken from the midplane of the film H773. The SADP (b) and (c) were recorded at a tilt of 0 and 30 degrees, respectively. The micrographs show coarse precipitates and the random grain orientations.

Figure 3-18. TEM BF image taken from the surface of the film H773 showing the coarse grains and precipitates.

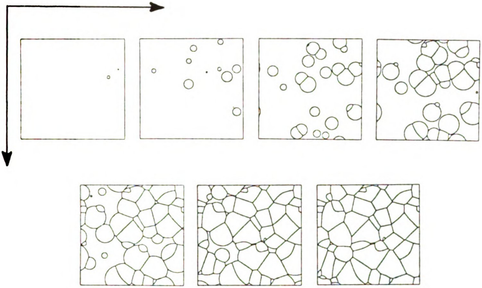

Figure 3-19. Time-lapse sequence illustrating the development of the Johnson-Mehl microstructure from the untransformed body [Mahin, 1980].

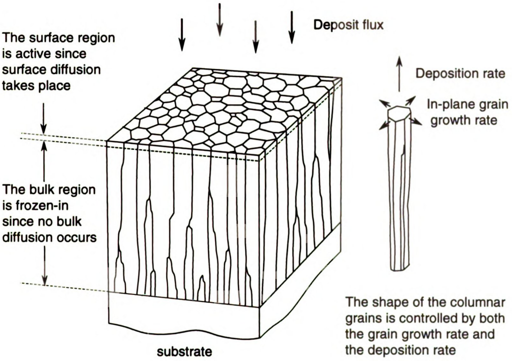

Figure 3-20. A schematic diagram illustrating the formation of columnar grained structures. By means of superposing two-dimension grain growth upon film growth (increasing thickness), a columnar structure can be formed as shown. The shape of the columnar grains is controlled by both the in-plane grain growth rate and the deposition rate.

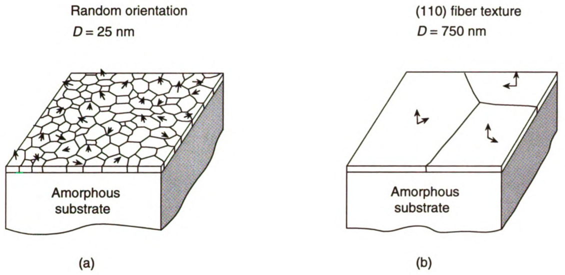

Figure 3-21. A schematic diagram showing the effect of in-plane grain size on texture formation. (a) At higher substrate temperatures the surface and interface energies of grains are not significant due to smaller fraction of the interface and surface areas of the grains and the crystals show random orientations. (b) Films formed at lower temperatures present a strong (110) fiber-texture, i.e., the (110) plane of grains are restricted to parallel to substrate plane, but with no preferred in-plane orientation.

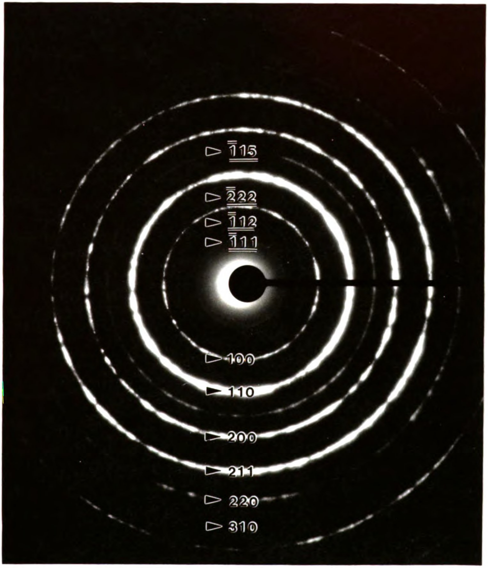

Figure 3-22. SADP sampled at the midplane of the film H673. The indices of Ni_4Ti_3 phase were underlined for purpose of distinguishing them from the B2 reflections. The ring pattern in the figure also shows the (110) grain orientation, since the $(310)_{B2}$ reflection having the radius of 64.3 mm absents.

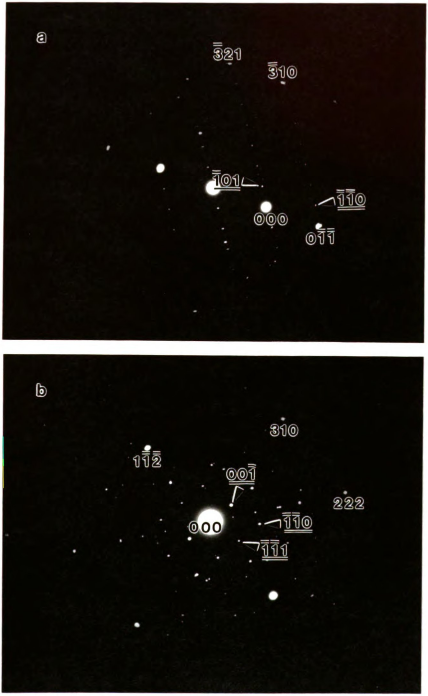

Figure 3-23. Two SADP's, each including approximately one grain, sampled at two areas of the midplane of the film H773. (a) $[13\text{-}3]_{B2}$ // $[1\text{-}11]_{Ni_4Ti_3}$ zone, and (b) $[\text{-}13\text{-}2]_{B2}$ // $[1\text{-}10]_{Ni_4Ti_3}$ zone.

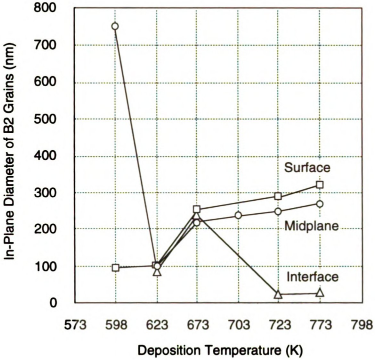

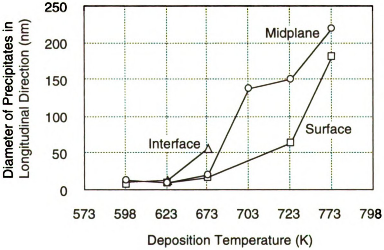

Figure 3-24. Diagrams showing the size changes of B2 grains and precipitates as a function of deposition temperature in three layers.

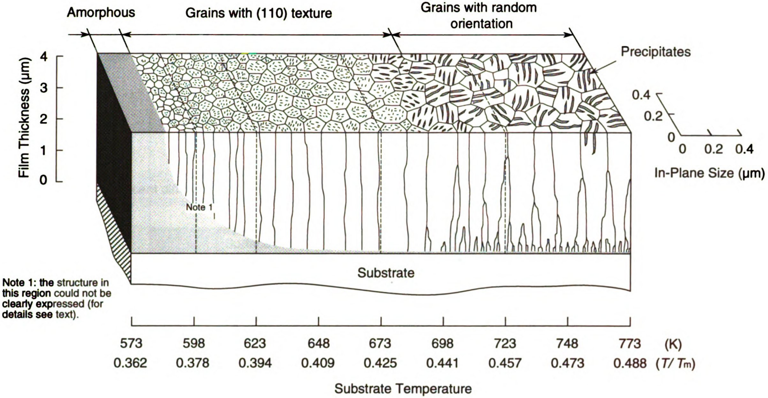

Figure 3-25. A structural model for Ni-rich NiTi films sputter-deposited at a substrate temperature of 573-773 K.

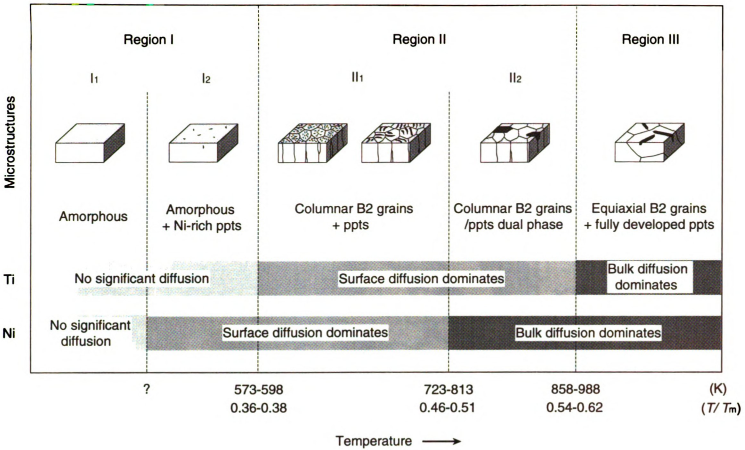

Figure 3-26. Schematic presentations predicting the effects of Ni and Ti diffusions on Ni-rich film microstructure. In Region I, the surface diffusions of Ni and Ti are not active simultaneously. Films deposited at this region are generally amorphous in structure. In sub-region I_2, hyperstoichiometric precipitates may form via Ni surface diffusion in amorphous phase. In Region II, films are mainly of columnar B2 grains. In sub-region II_2, large precipitates may be produced through Ni bulk diffusion and B2/ppt dual-phase may form. In Region III, bulk diffusions for both Ni and Ti start. Films with microstructures similar to that of fully annealed and aged films may result.

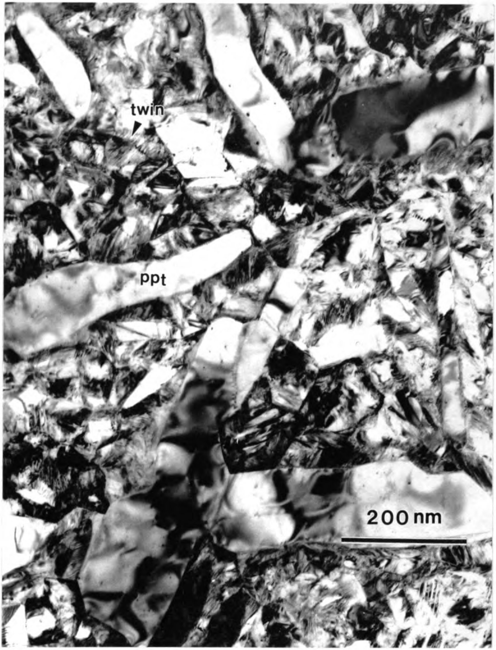

Figure 3-27. TEM bright-field image of film A1 which was produced by aging the film H623 at 858 K for 1 hour and furnace cooling.

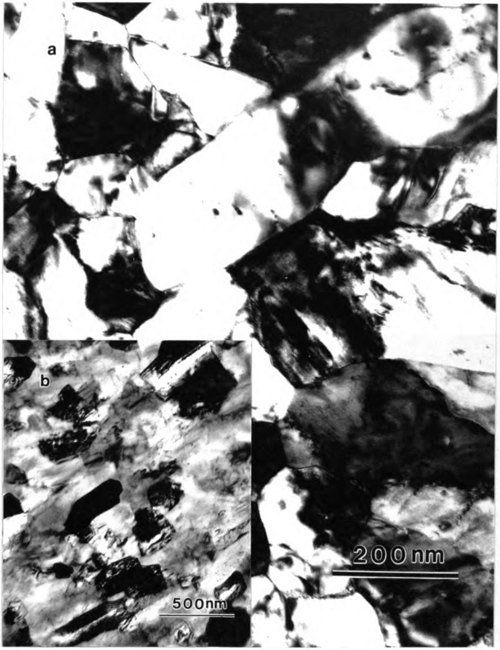

Figure 3-28. (a) TEM bright-field image and SADP's of film A2. (b) The inserted picture taken at 45° specimen tilt revealing columnar grain structure. (c), (d) and (e) are SADP's at three tilt angles 0°, 30° and 45°, respectively, displaying (110) texture. The axis of tilt is indicated in (d) and (e).

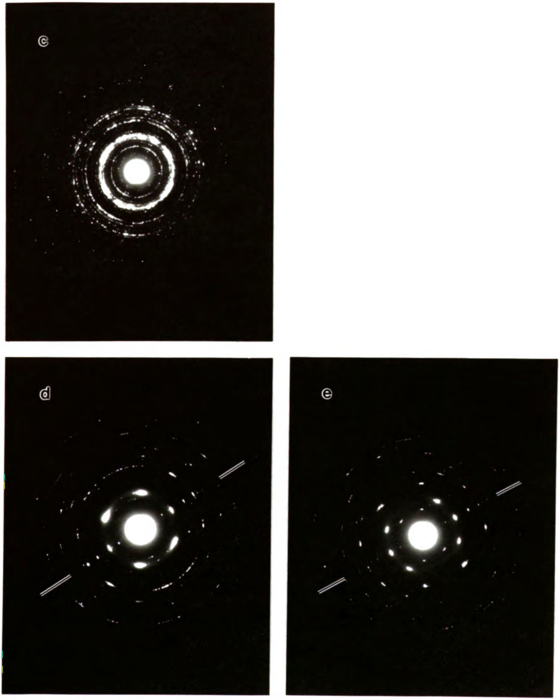

Figure 3-28. (Continued) TEM bright-field image and SADP’s of film A2. (b) The inserted picture taken at 45° specimen tilt revealing columnar grain structure. (c), (d) and (e) are SADP's at three tilt angles 0°, 30° and 45°, respectively, displaying (110) texture. The axis of tilt is indicated in (d) and (e).

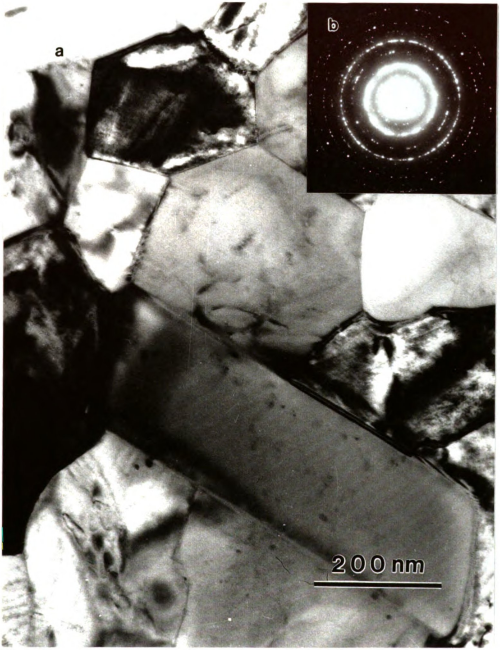

Figure 3-29. TEM bright-field image and SADP of film A3 which was produced by aging the film H723 at 858 K for 1 hour and furnace cooling. The SADP in (b) was taken at 30° tilt showing random grain orientation.

Figure 3-30. TEM bright-field image of film A4 which was produced by aging the film H723 at 813 K for 1 hour and furnace cooling.

Figure 3-31. TEM image of the film A5 obtained by annealing film H673 at 988 K for 1 hour and furnace cooling. The size of grains have increased during annealing. Obviously, the bulk diffusion for NiTi grain growth have occurred.

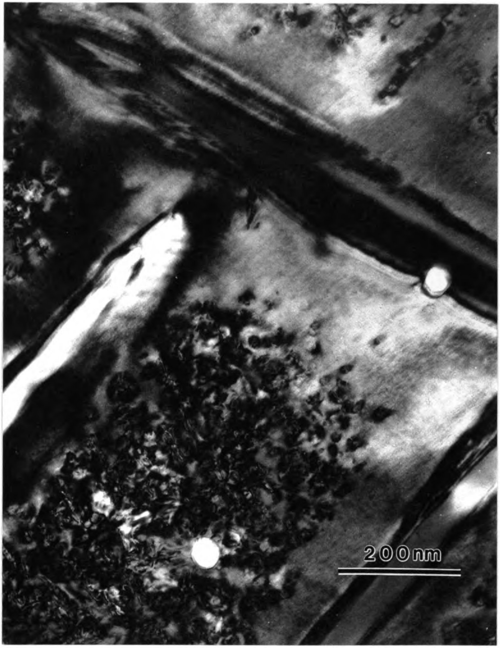

Figure 3-32. TEM image shows the microstructure of film A6 produced by annealing the film H673 at 1123 K for 1 hour and furnace cooling. The film is consist of large grains and lenticular precipitates. The precipitates align along well-defined crystallograghic planes of the matrix. Besides, very fine precipitate particles with strain field contrast also can be noticed in the area between the large precipitates.

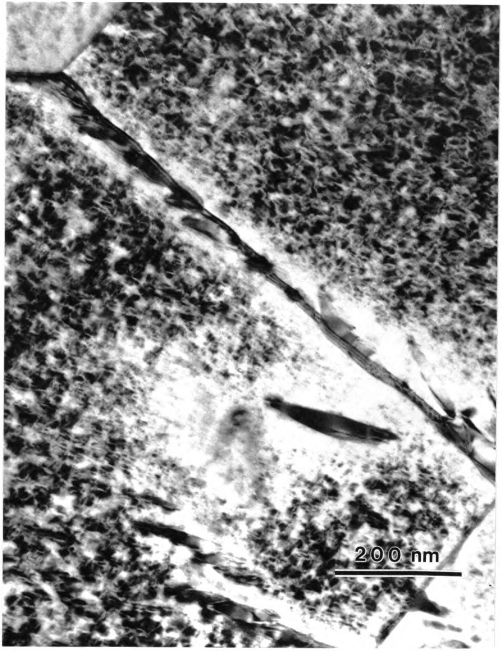

Figure 3-33. TEM image of film A7 obtained by annealing the film H673 at 1073 K for 2 hours and air cooling. The precipitation tends to occur more rapidly at grain boundary areas since the grain boundary is a favorable site for heterogeneous nucleation of precipitation.

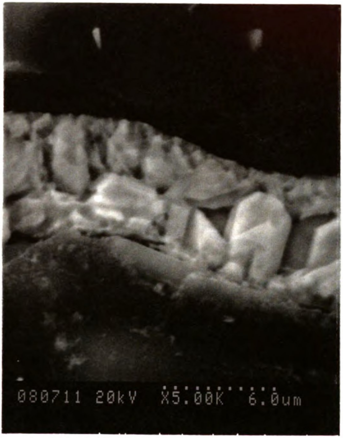

Figure 3-34. Cross-section SEM micrograph of A7 displaying coarse-grained microstructure. Deep etched surface morphology reveals the crystallographic facets of the grains.

Figure 3-35. TEM image of film A8 deposited at 1073 K, 2 hours and 673 K, 1 hour two-stage annealing.

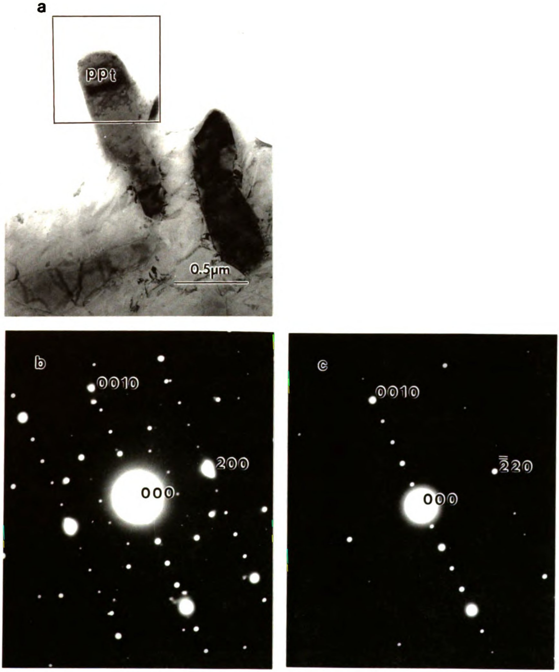

Figure 3-36. BF image and two single-crystal SADP's taken from the large precipitate plate in film A3. (a) An isolated precipitate plate in the edge of the TEM foil was examined in favor of excluding diffraction spots from the matrix. (b) The [0-10] zone of Ni_3Ti_2 phase. (c) The [110] zone of Ni_3Ti_2 phase.

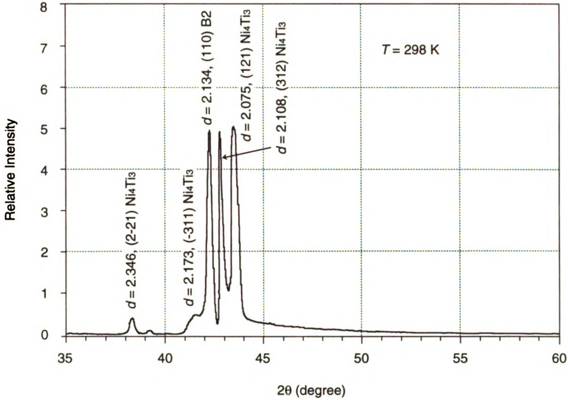

Figure 3-37. XRD curve of the film A5 recorded at the room temperature (298 K). Besides (110) B2 peak, four peaks match the reflections of Ni_4Ti_3 phase at 2θ angle between 35° and 60° within 2 % error.

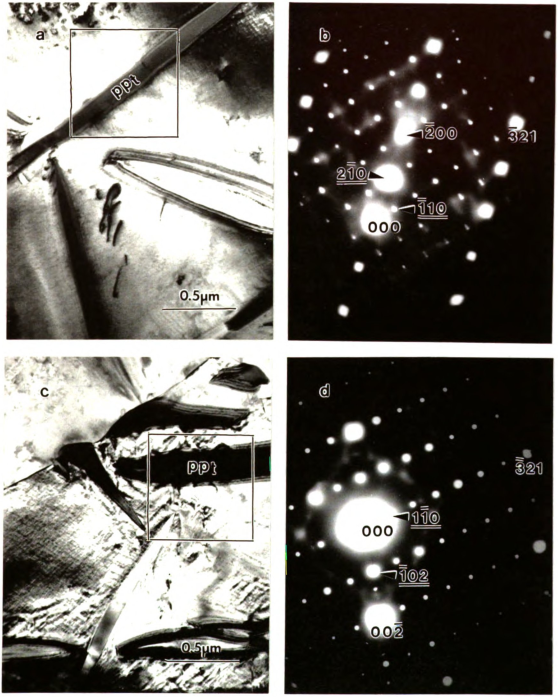

Figure 3-38. BF images and single-crystal SADP's taken from the film A6. The index of large lenticular precipitates could be completed by assuming that they possess the Ni_4Ti_3 structure. (b) and (d) are SADP's of zone $[0\text{-}12]_{B2}$ // $[001]_{Ni_4Ti_3}$ and zone $[230]_{B2}$ // $[221]_{Ni_4Ti_3}$, respectively, taken from indicated areas in (a) and (c). The underlined indices represent the diffractions of precipitates.

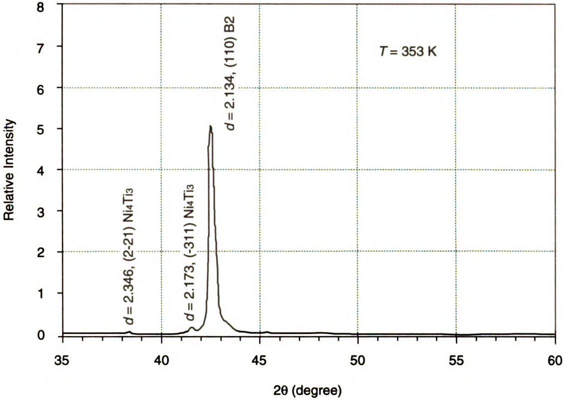

Figure 3-39. XRD curve of the film A7 recorded at 353 K showing (110) B2 peak and two Ni_4Ti_3 phase peaks at 2θ angle between 35° and 60°. The reflections of Ni_4Ti_3 phase are very weak due to its fine size.

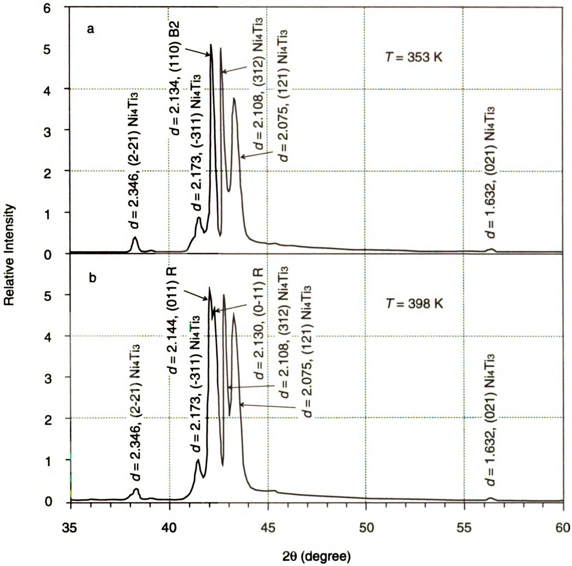

Figure 3-40. The XRD curves of the film A8, taken from the same specimen at 353 K and the room temperature respectively. The curve (a) identifies the (110) B2 peak and five Ni_4Ti_3 peaks in 2θ angle between 35° and 60°. In the curve (b), the same set of the Ni_4Ti_3 reflections appears, however, the (110) B2 peak splits into two NiTi R-phase peaks: (011) and (0-11) with a separation about 0.4°.

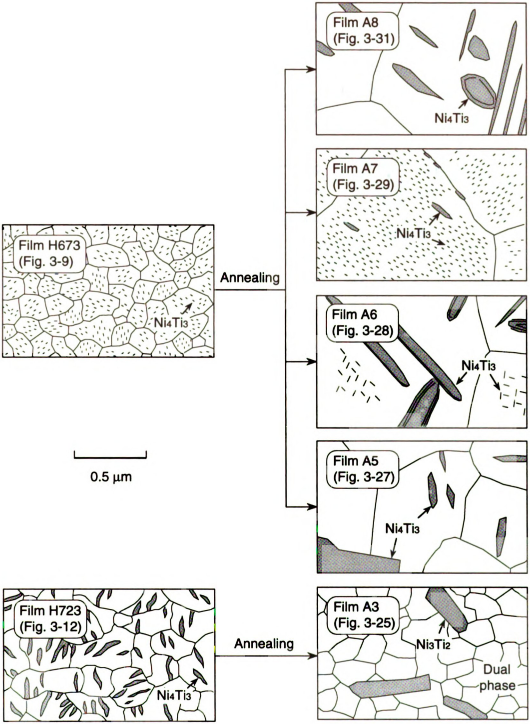

Figure 3-41. Schematic drawings of in-plane views of various microstructure formed in the post-deposition annealing.

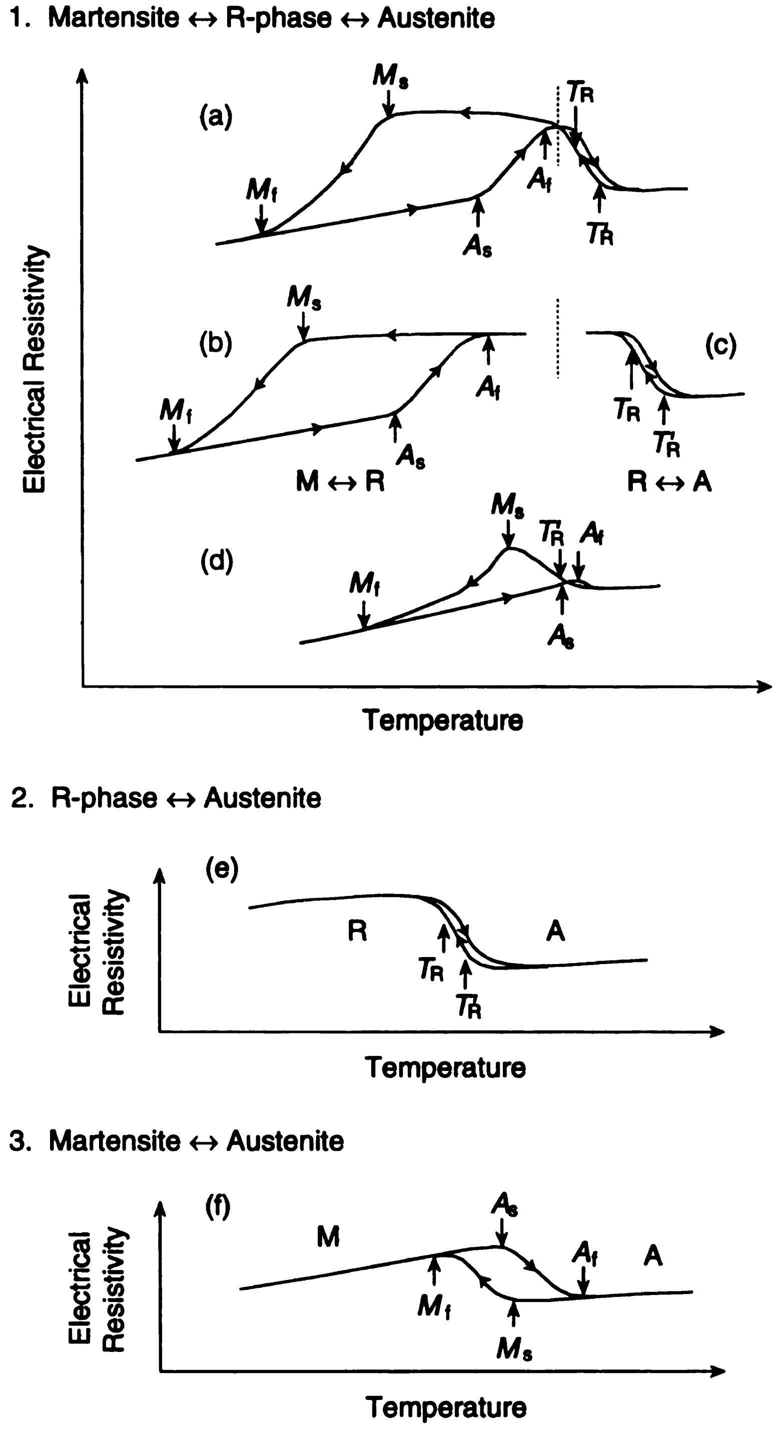

Figure 3-42. Schematic diagrams illustrating the classification of electrical resistivity vs. temperature curves for NiTi alloys. (a) Two-stage curve involving Martensite ↔ R-phase ↔ Austenite phase transformations. (b, c) The M ↔ R and R ↔ A curves decomposed from the curve (a). Curve (d) represents a two-stage curve with an incomplete austenite → R-phase transition. (e) The curve involving R-phase ↔ Austenite transformation which is the same as the curve (c). (f) The curve involving Martensite ↔ Austenite transformation.

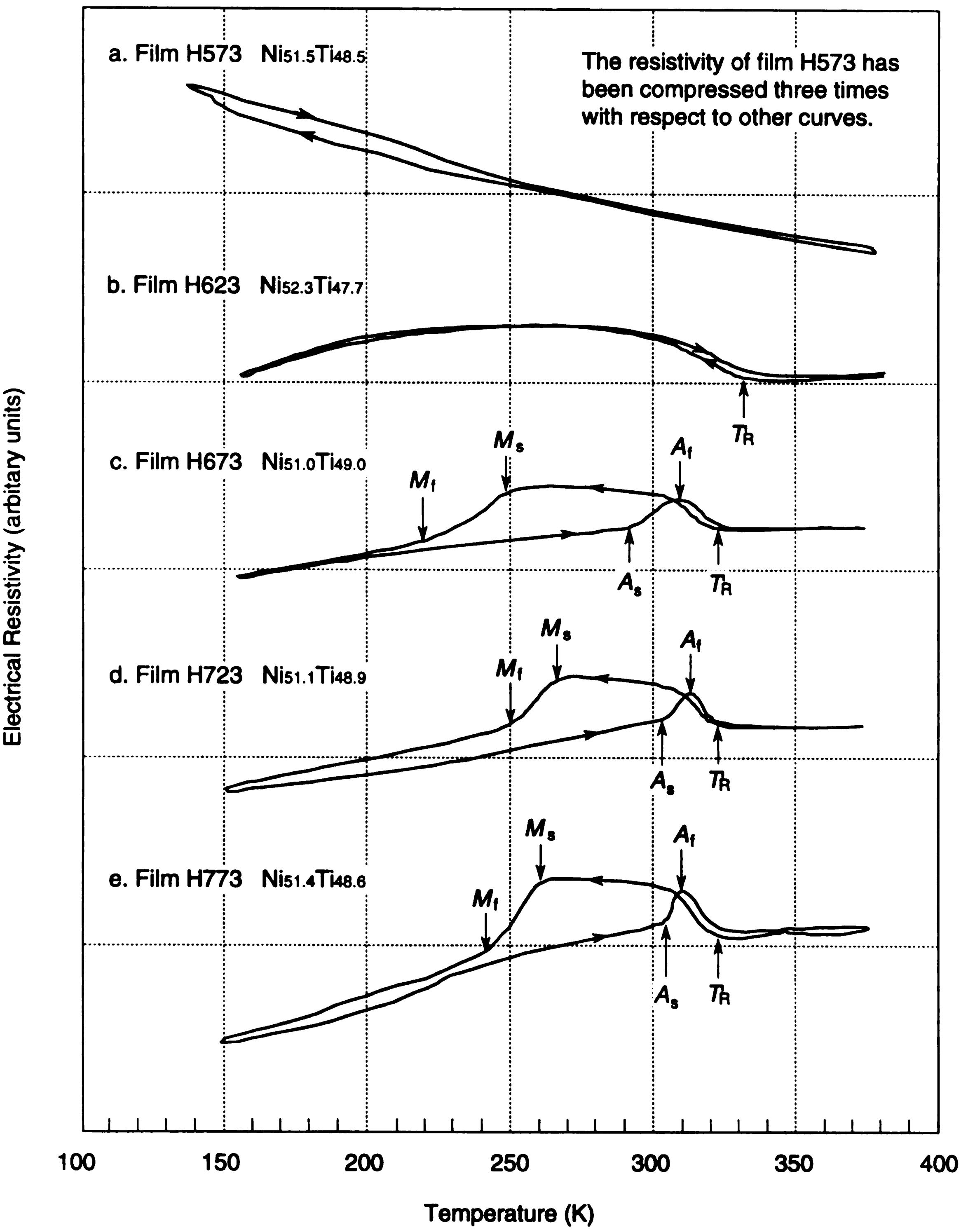

Figure 3-43. Electrical resistivity vs. temperature curves of as-sputtered NiTi films deposited at various substrate temperatures.

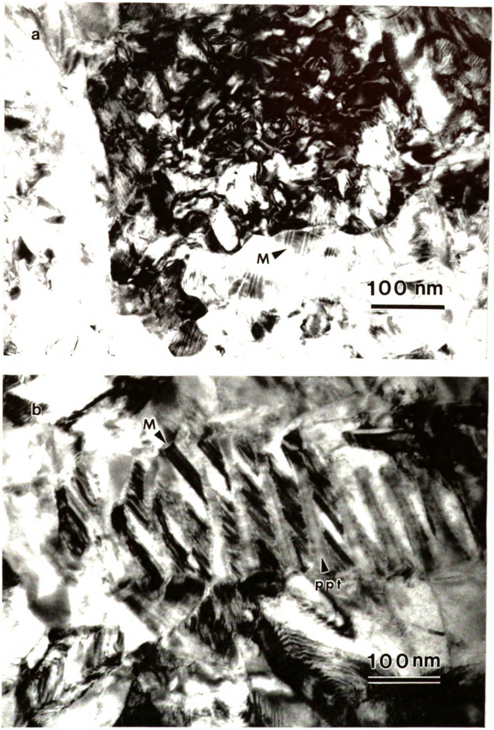

Figure 3-44. Bright-field images of midplane of the films H723 and H673. The micrographs were recorded at 101 K, which is well below their M_s temperatures. (a) The image of film H723. (b) The image of film H673.

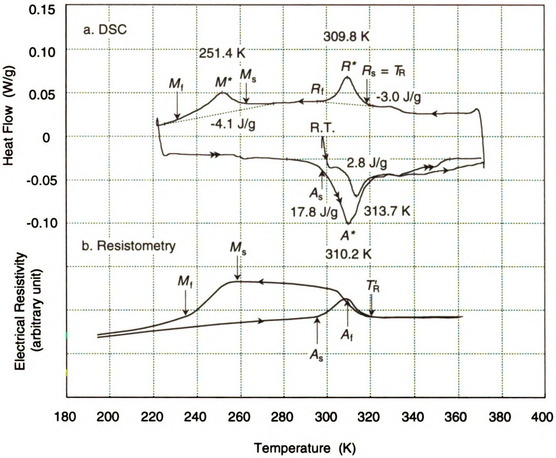

Figure 3-45. DSC scans (a) and electrical resistivity vs. temperature measurements (b) on film H703 having composition of $Ni_{50.8}Ti_{49.2}$. In (a) the second heating scan from 223 to 373 K is indicated by double arrows.

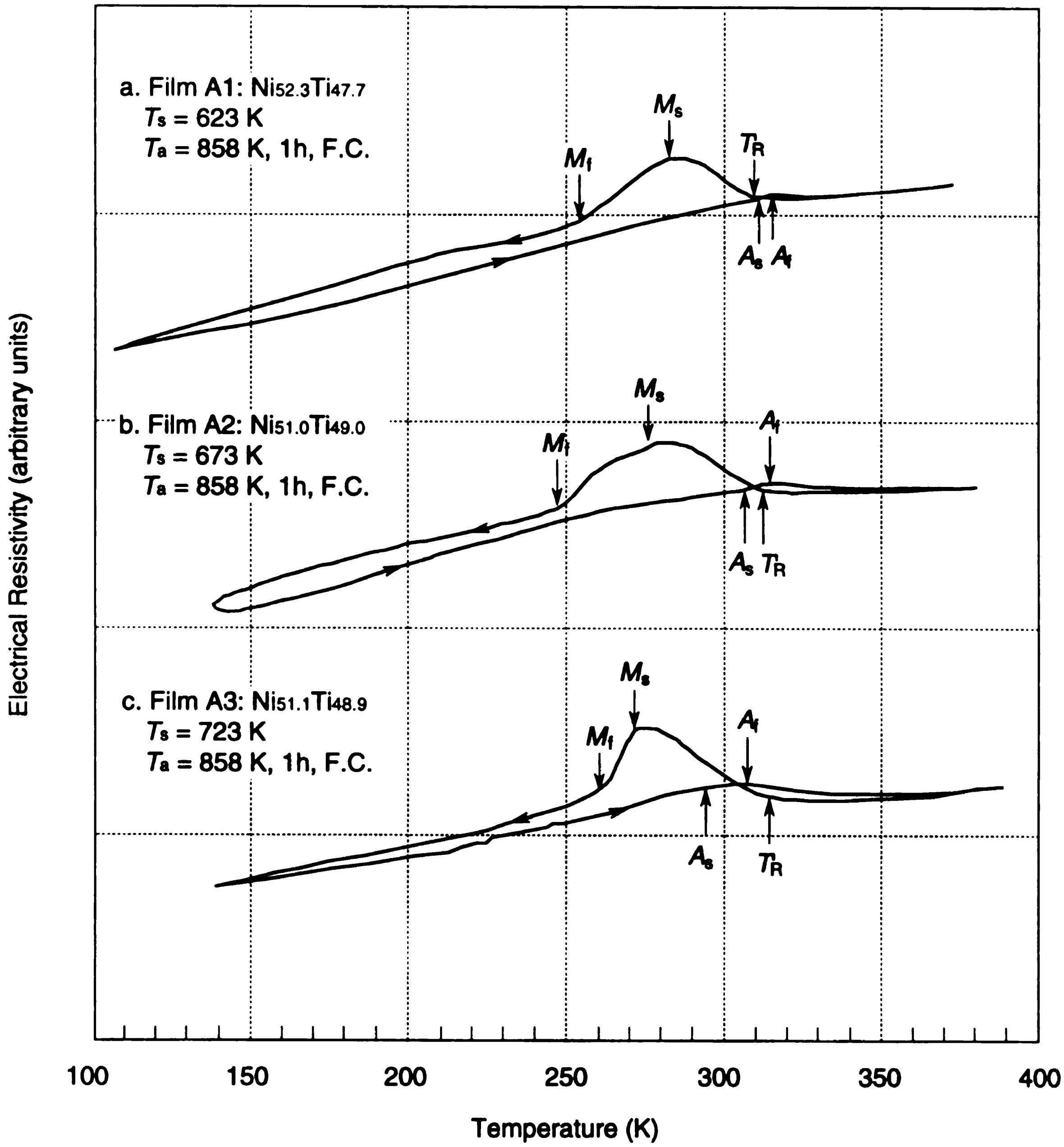

Figure 3-46. Electrical resistivity vs. temperature curves of annealed NiTi films.

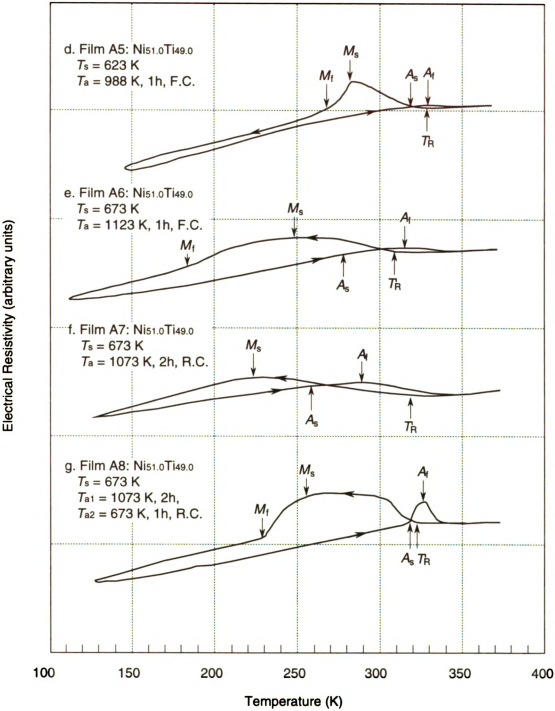

Figure 3-46. (Continued) Electrical resistivity vs. temperature curves of annealed NiTi films.

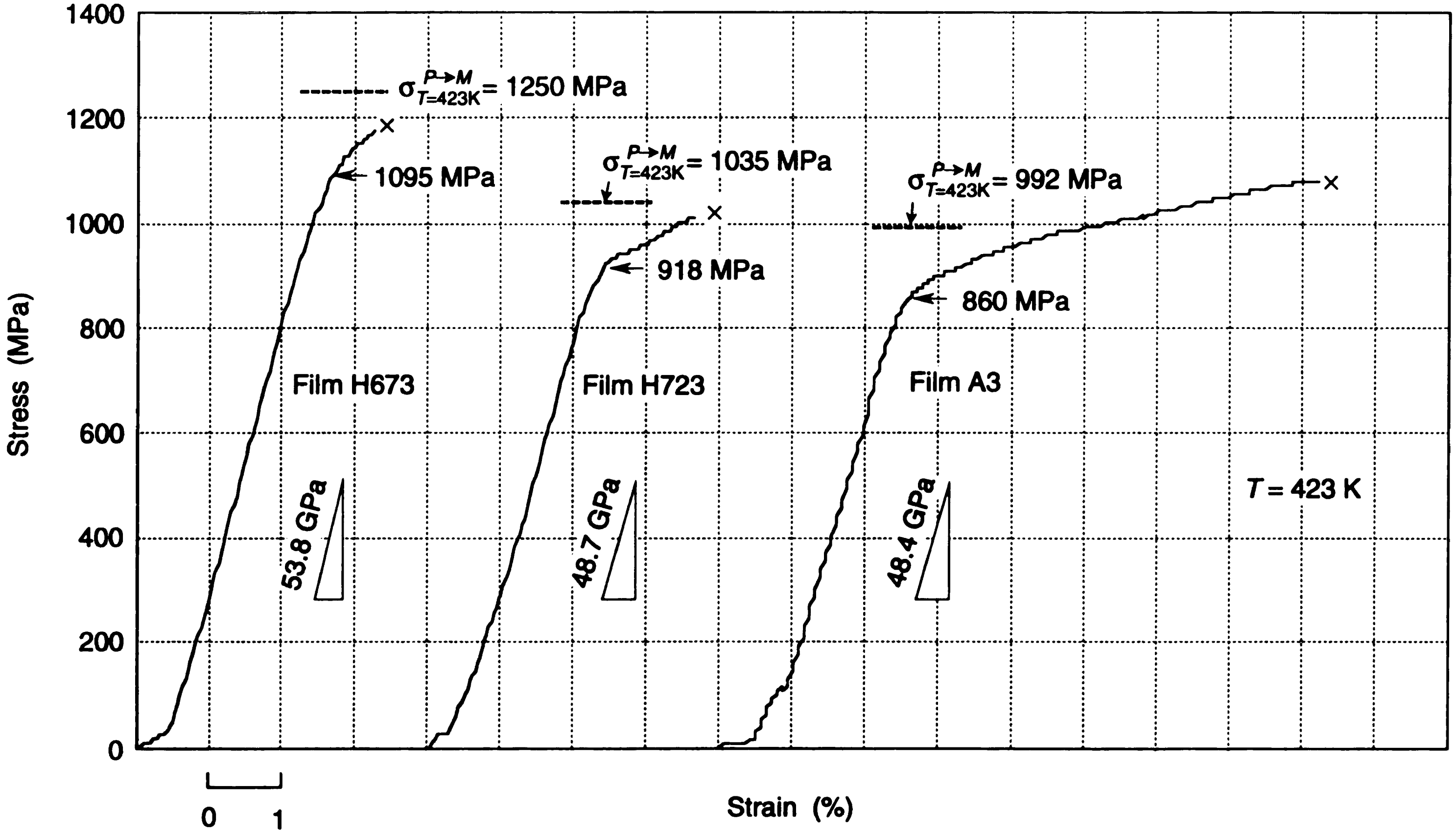

Figure 3-47. Ultimate elongation curves tested at 423 K for films H673, H723 and A3. According to Clausius-Clapeyron relations shown in Figure 3-61, the critical stresses to induce martensite at 423 K would be 1250, 1035 and 992 MPa for H673, H723 and A3 respectively. Clearly, the yield points in the figure were caused by the significant permanent deformation in the parent phase.

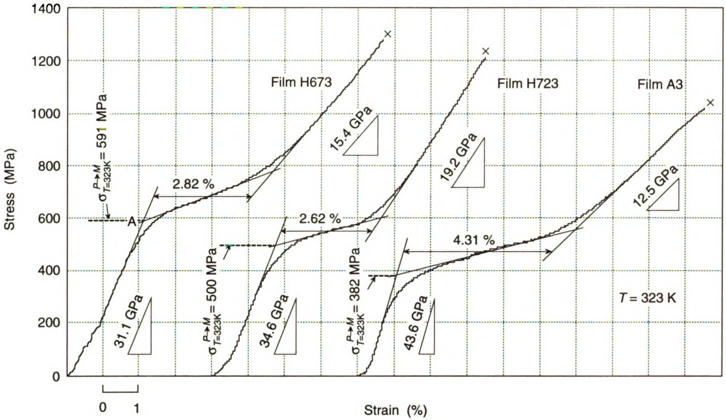

Figure 3-48. Ultimate elongation curves tested at 323 K for films H673, H723 and A3. The curves show well-defined three stages: first the elastic deformation of parent phase, then the plateau of parent-to-martensite transformation and finally the elastic deformation of martensite.

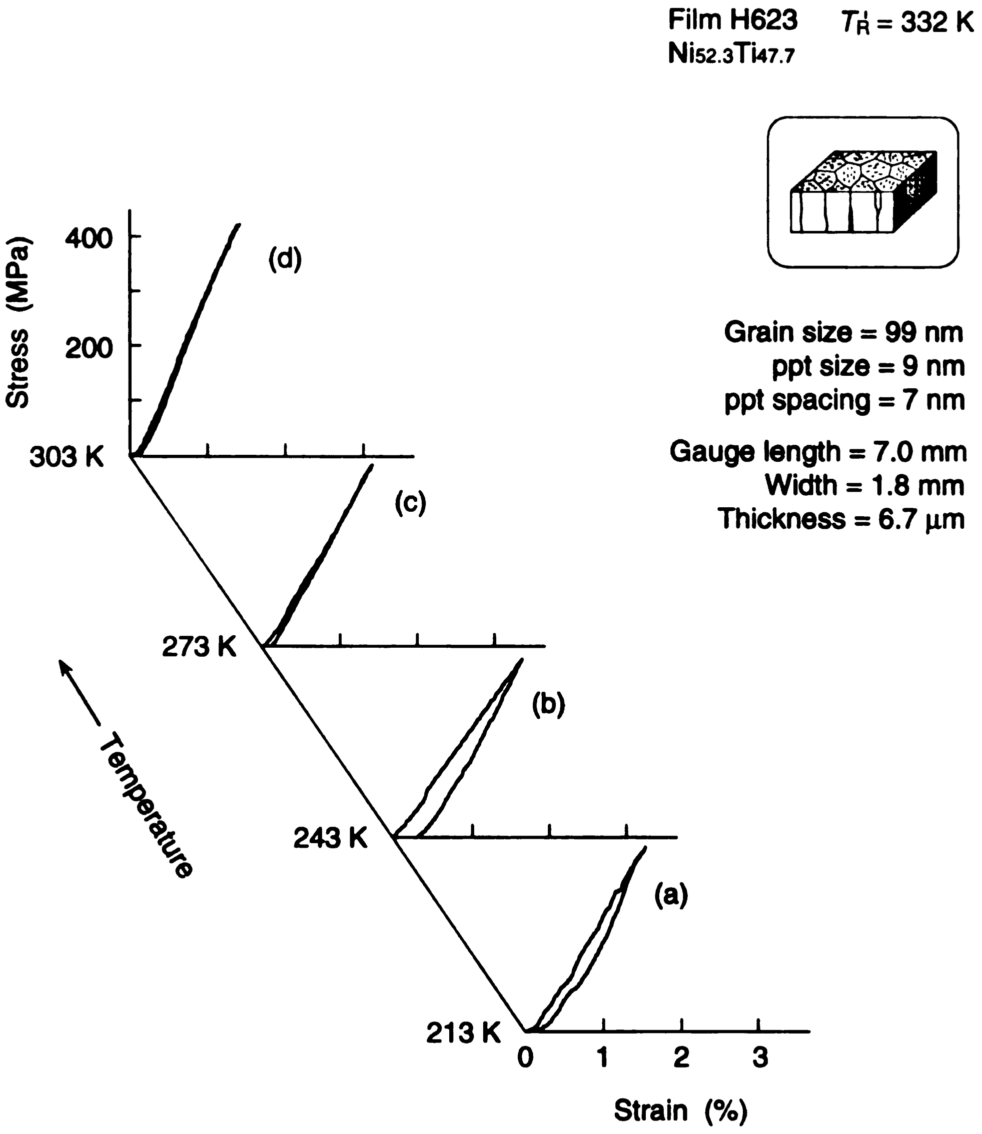

Figure 3-49. Isothermal stress-strain curves of film H623. The yielding due to the detwinning of martensite variants and stress-induced martensitic transformation did not occur at the stress level above 300 MPa. The thin film behaved as an ordinary metallic material.

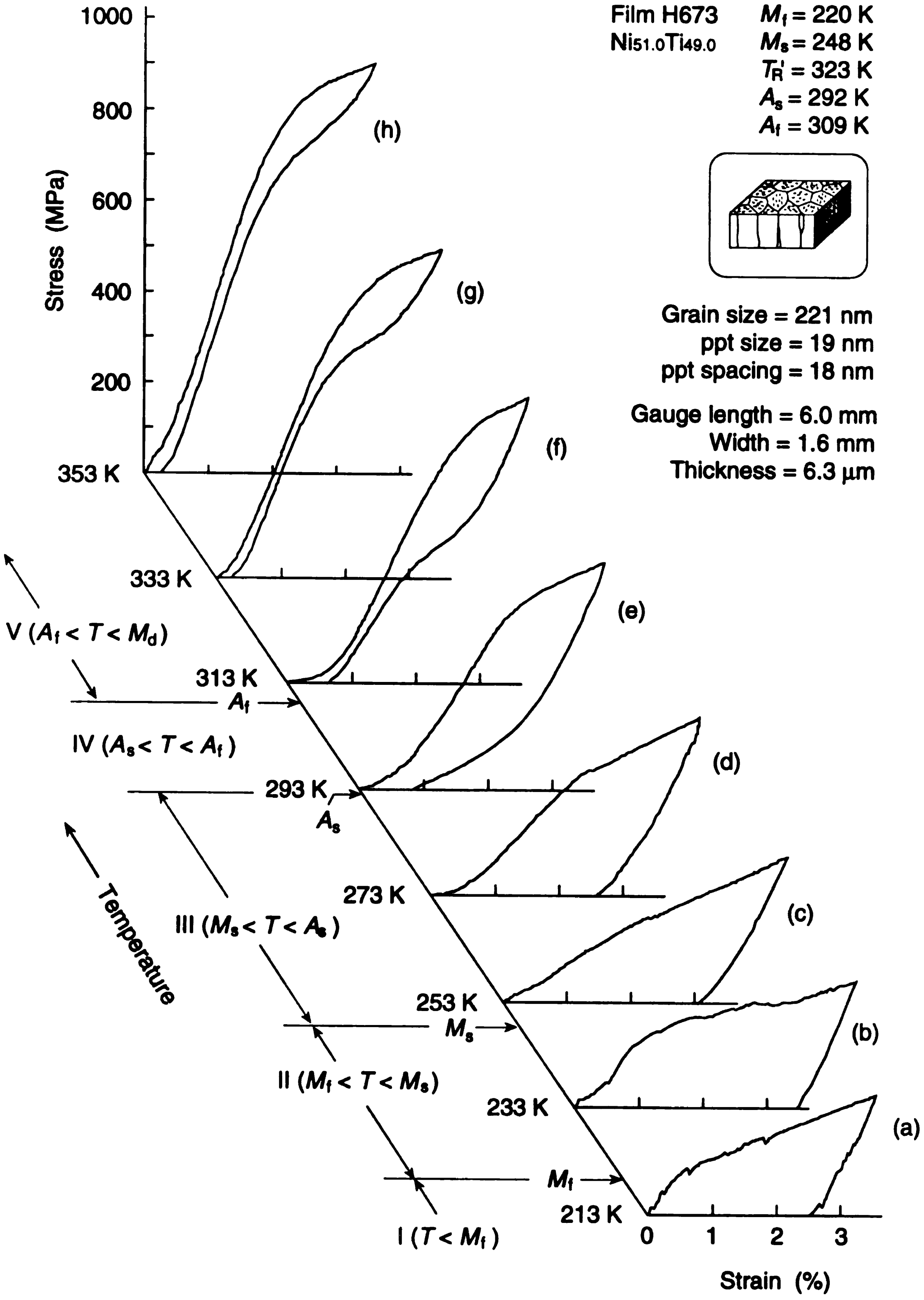

Figure 3-50. Isothermal stress-strain curves of the film H673.

Figure 3-51. TEM bright-field images from deformed film H673. Compared with its original structure, it is seen that the microstructure essentially remained unchanged.

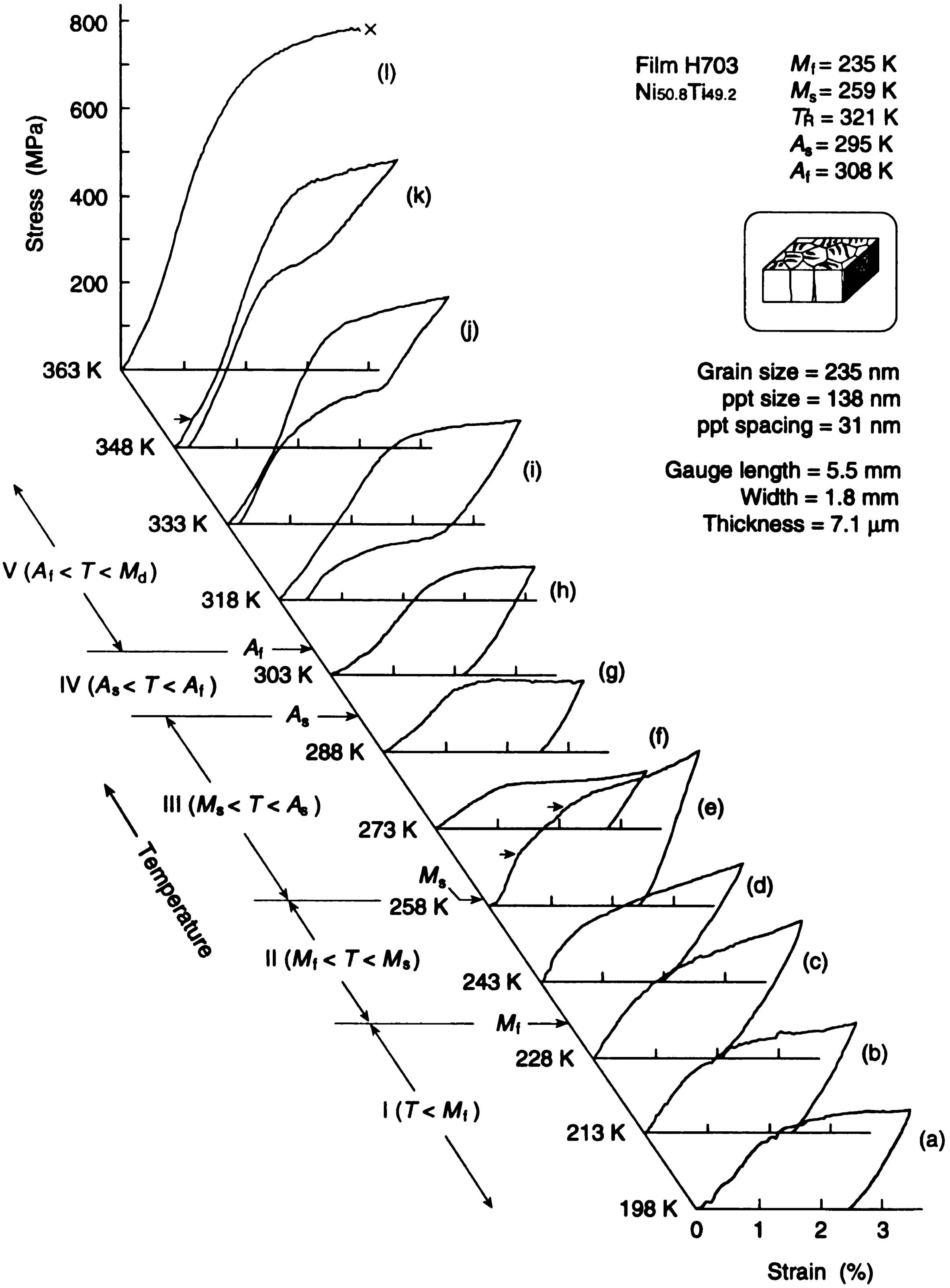

Figure 3-52. A series of isothermal stress-strain curves generated from a single tensile specimen of the film H703 at various test temperatures. Arrows indicate the critical stresses for the first and second yieldings.

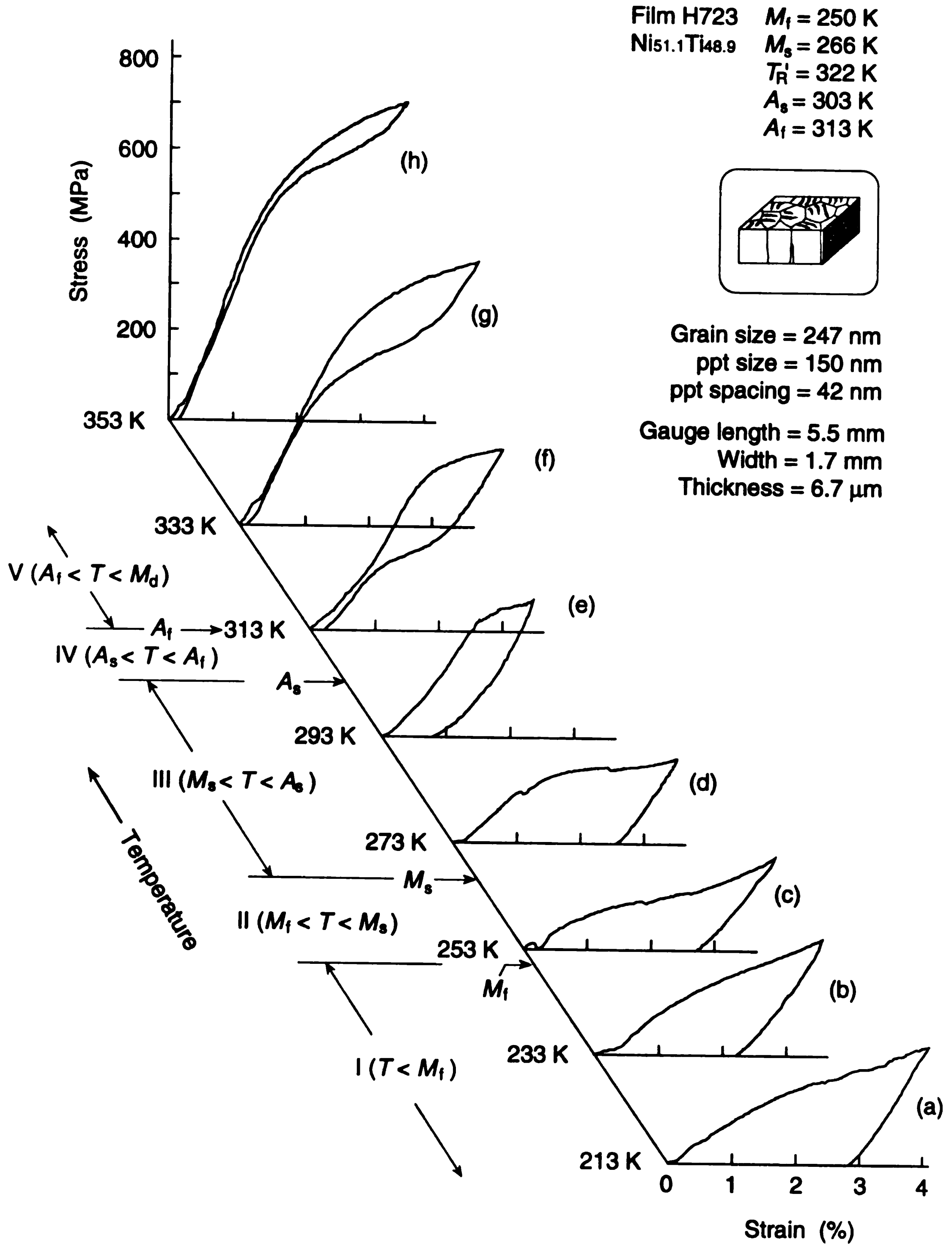

Figure 3-53. Isothermal stress-strain curves of the film H723.

Figure 3-54. TEM bright-field images from deformed film H723. Just like its undeformed structure, well-defined precipitate particles and grains without any dislocation can be seen.

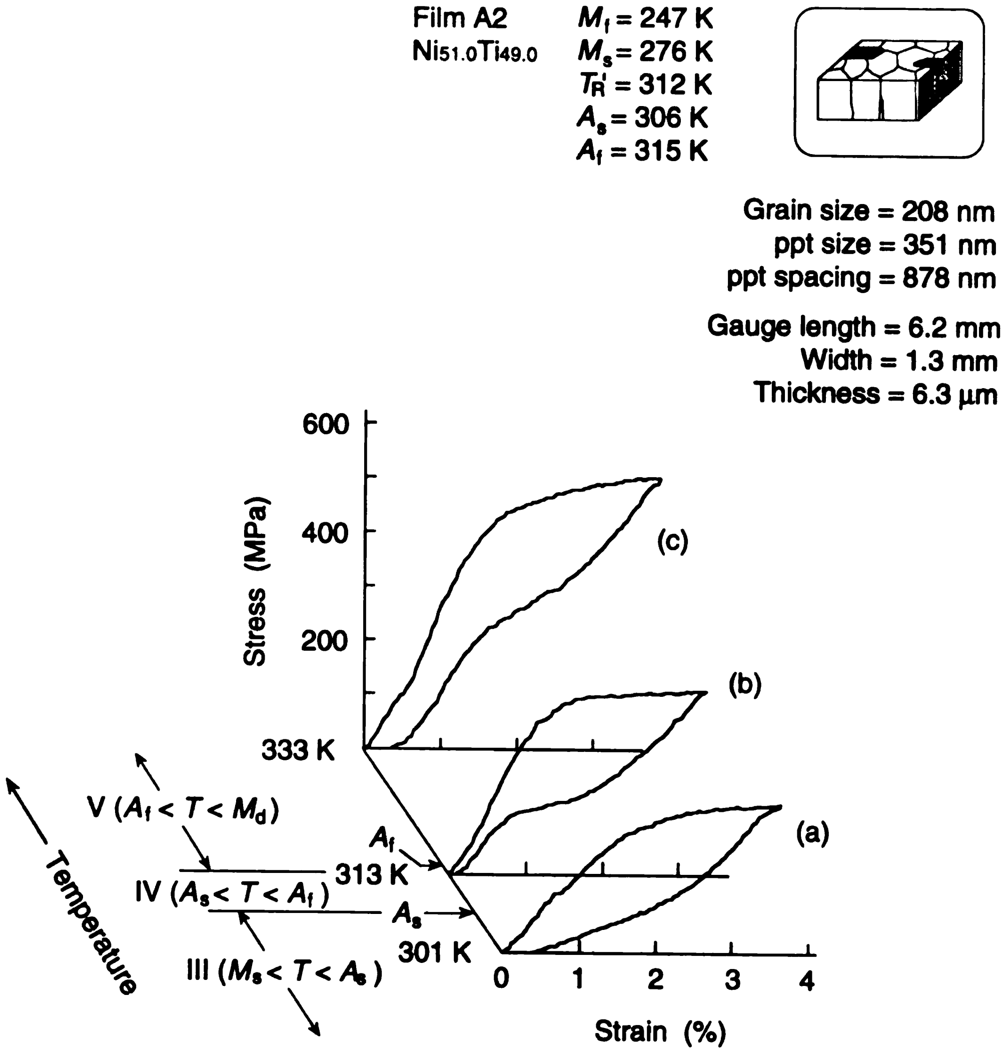

Figure 3-55. Isothermal stress-strain curves of the film A2.

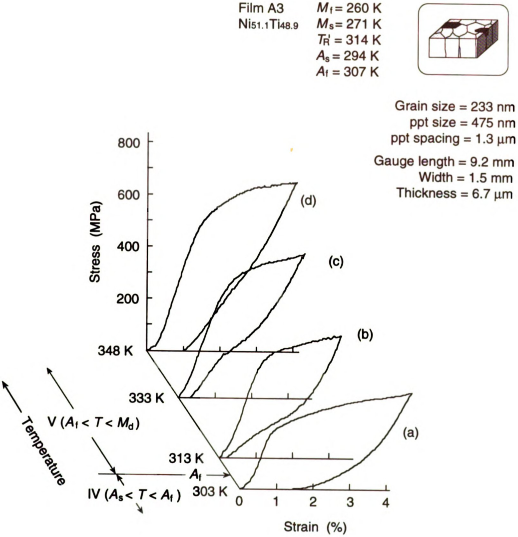

Figure 3-56. Isothermal stress-strain curves of the film A3.

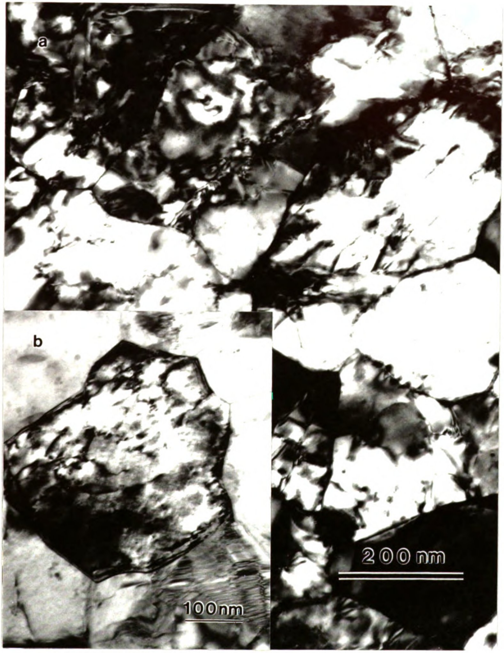

Figure 3-57. (a) and (b) TEM bright-field images taken from the deformed film A3. The absence of precipitates inside grains led the formation of dislocations.

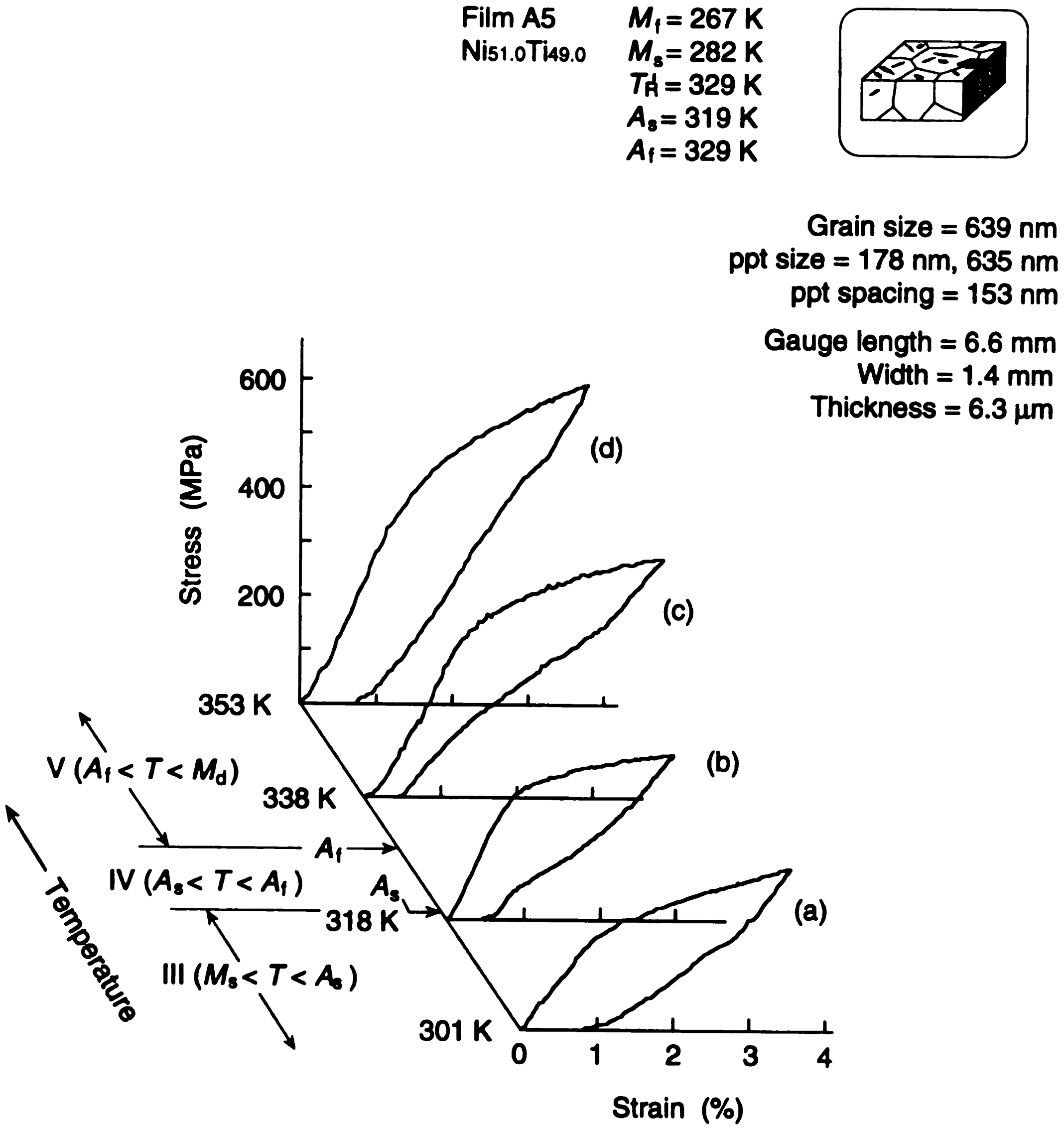

Figure 3-58. Isothermal stress-strain curves of the film A5.

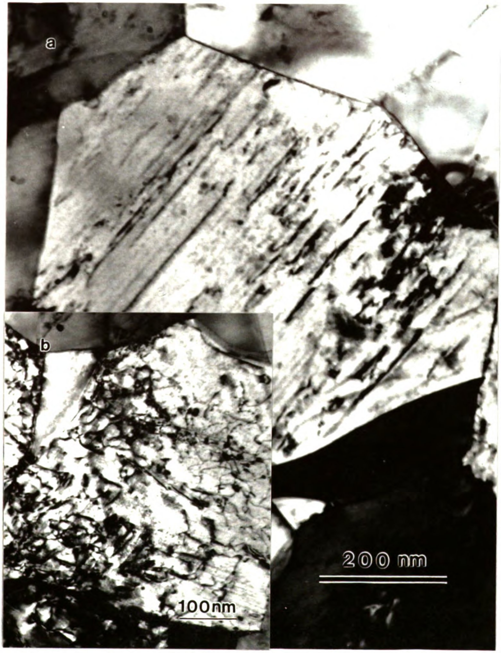

Figure 3-59. TEM bright-field images taken from the deformed film A5. (a) Slip bands which formed by a number of passage of dislocations spread throughout entire grains. The slip bands in different grains tend to align in a common direction which is the direction of maximum shear stress. (b) High density dislocations can be seen.

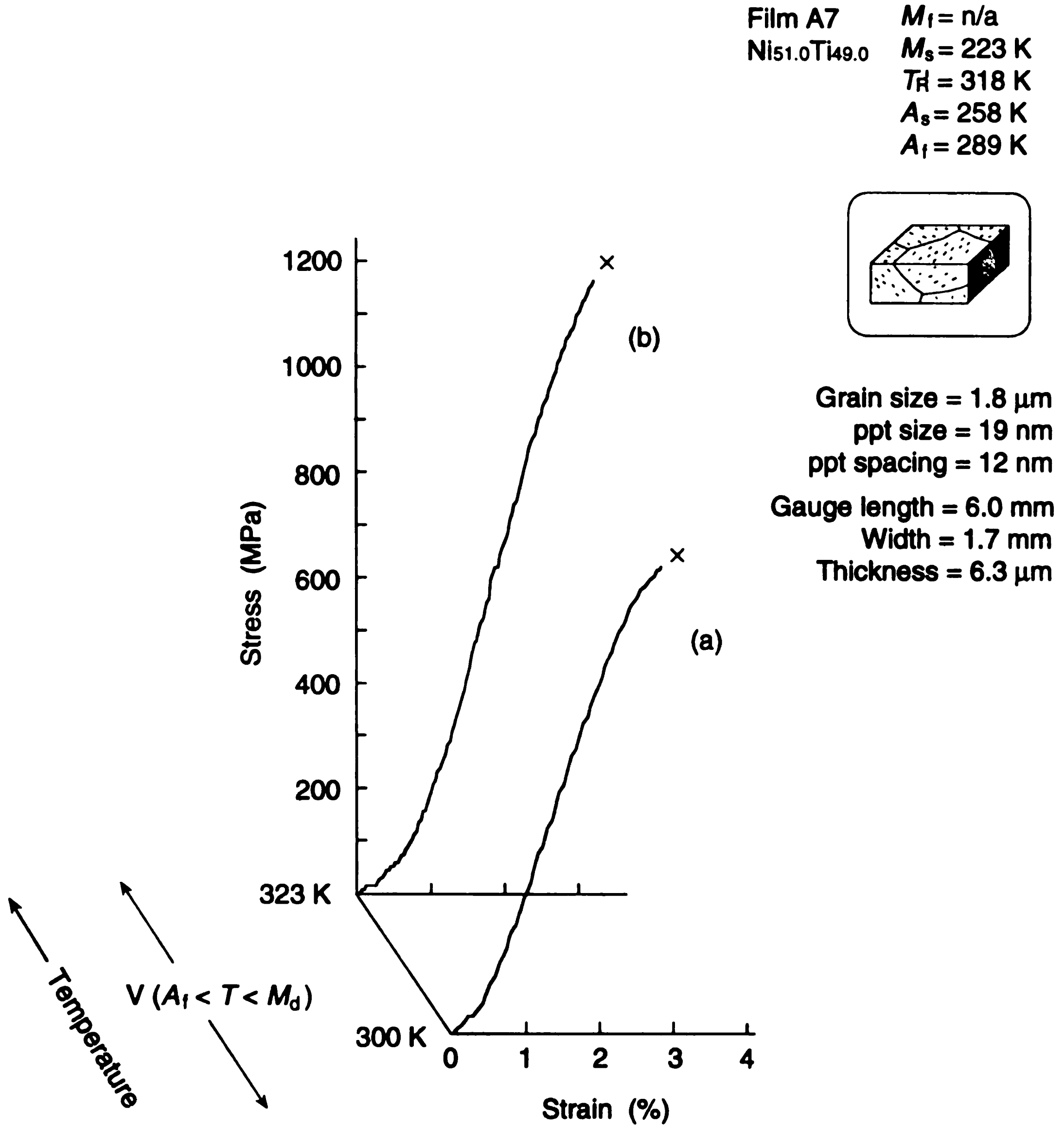

Figure 3-60. Isothermal stress-strain curves of the film A7. The loading curves does not show any transformation yielding due to the extremely fine Ni_4Ti_3 particles.

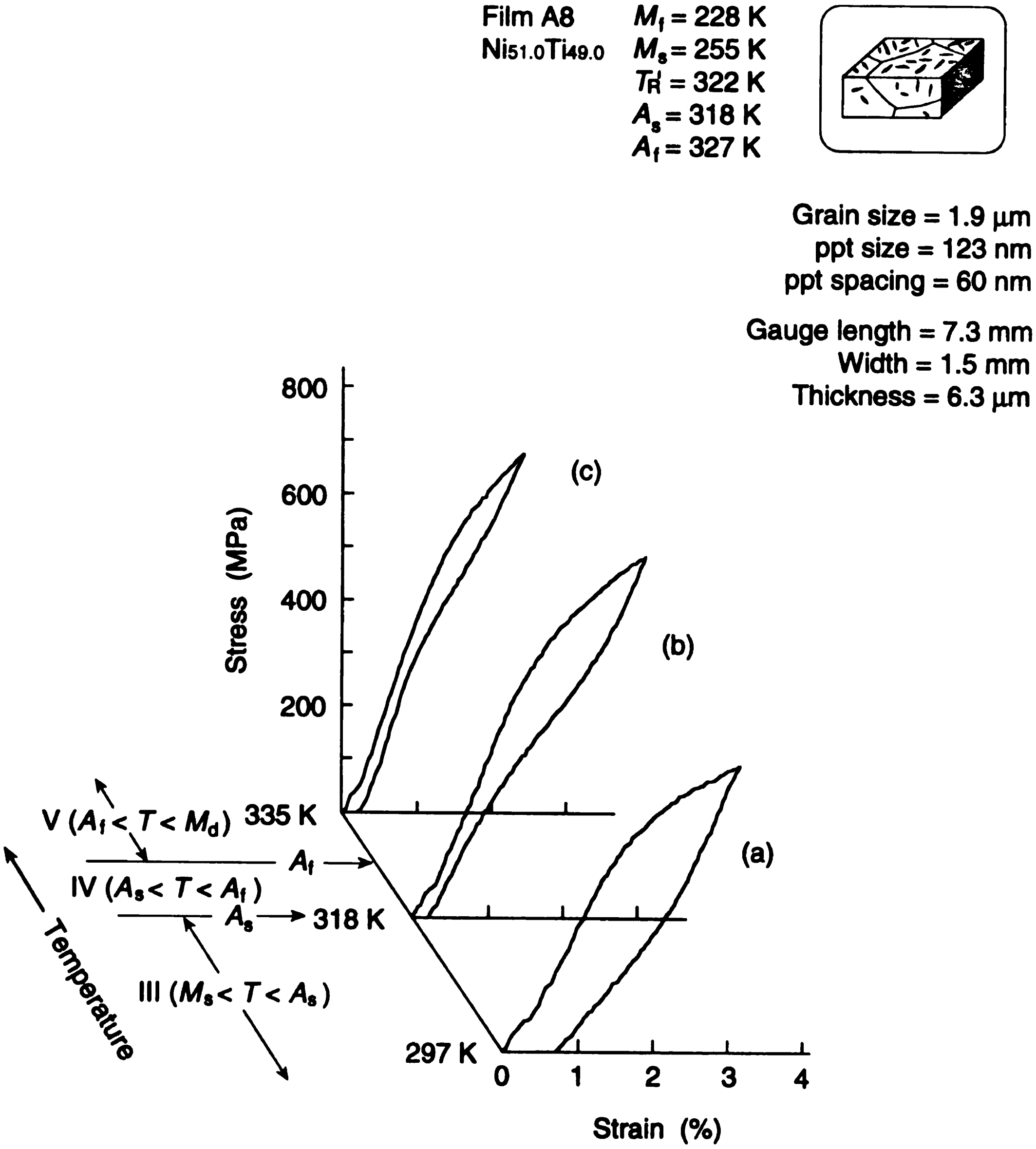

Figure 3-61. Isothermal stress-strain curves of the film A8.

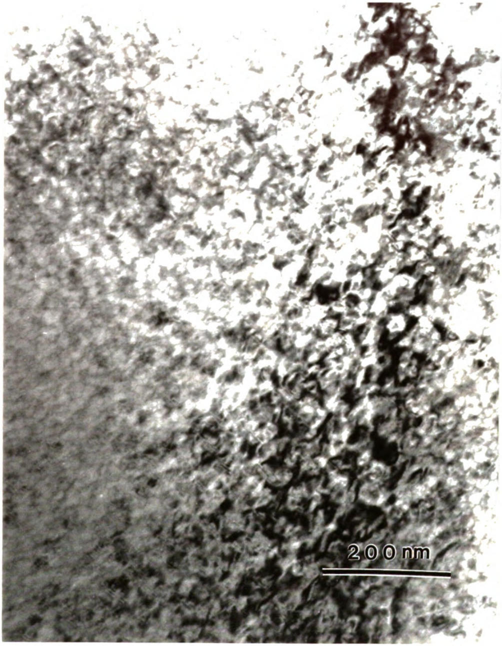

Figure 3-62. TEM bright-field image from the deformed film A7. The microstructure was unchanged in stress-strain cycling.

Figure 3-63. TEM bright-field image taken from the deformed film A8
The microstructure was unchanged in stress-strain cycling.

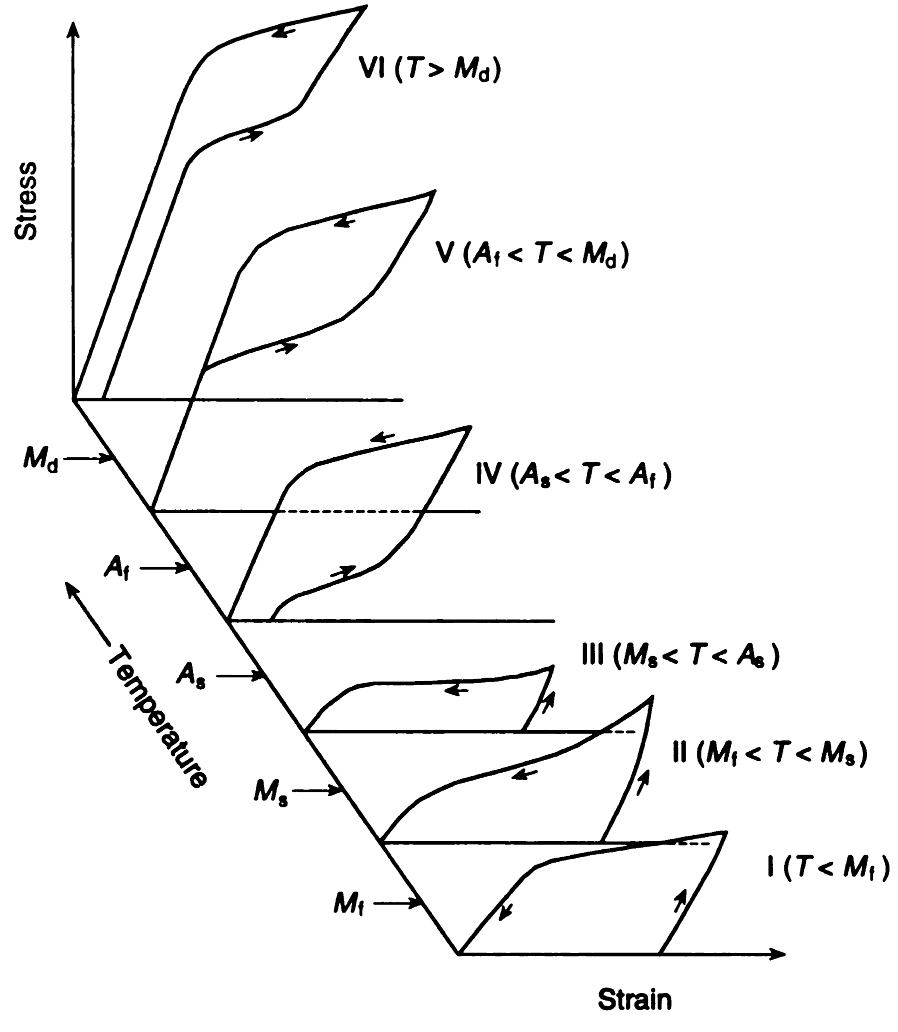

Figure 3-64. A schematic σ-ε-T diagram showing six types of stress-strain behavior depending on the deformation temperature relative to the transformation temperatures in polycrystalline NiTi thin films.

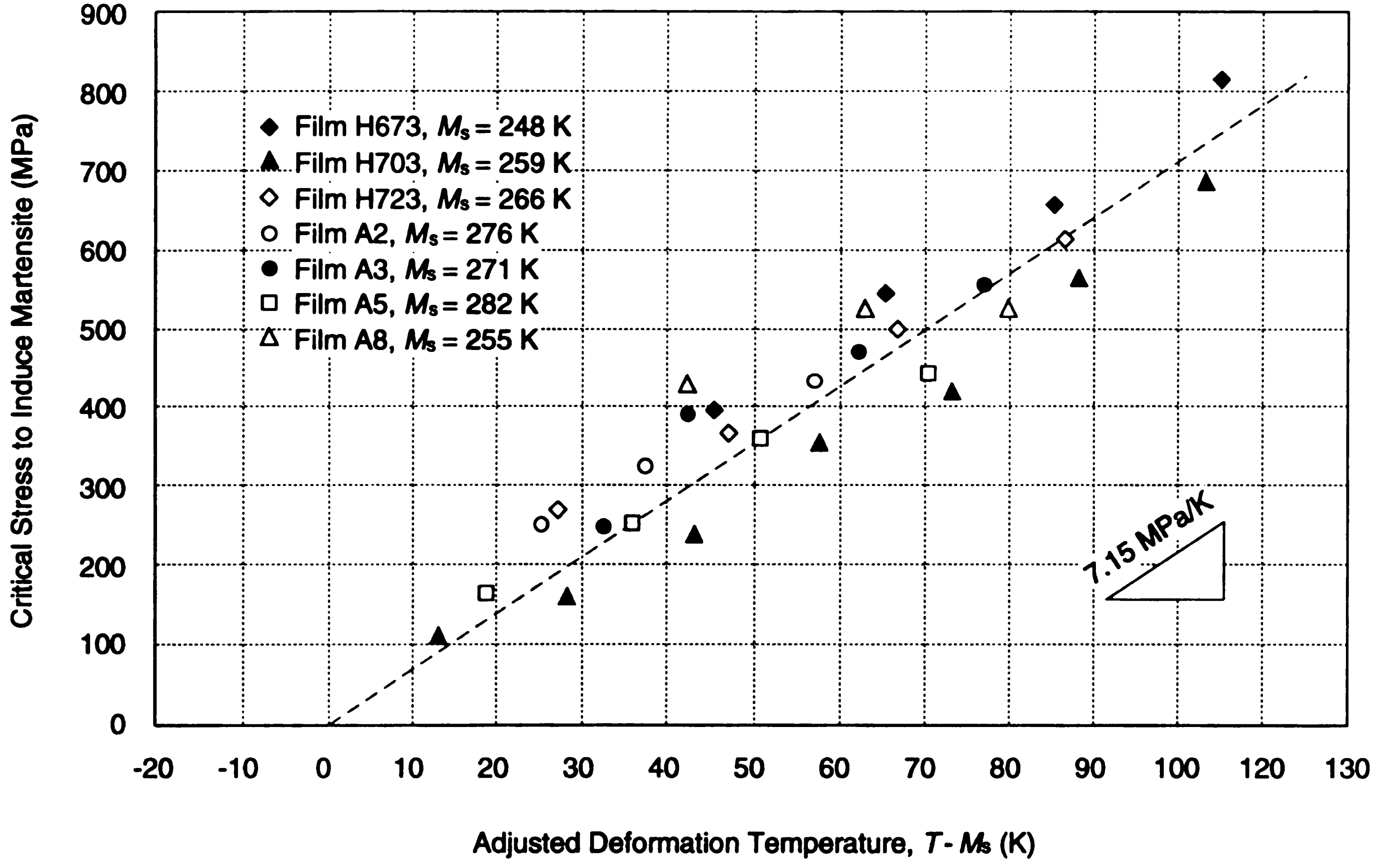

Figure 3-65. Critical stresses to induce the martensite vs. adjusted deformation temperature curves for NiTi films.

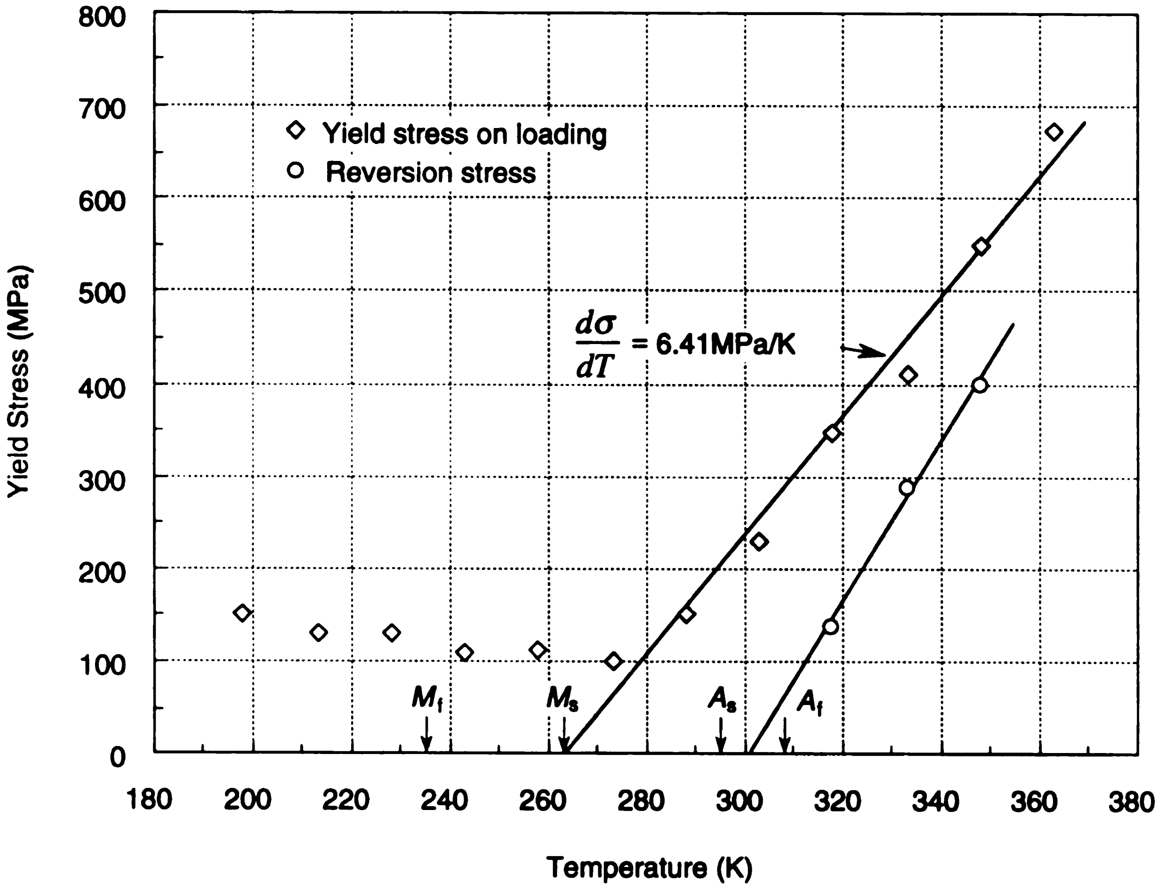

Figure 3-66. Tensile yield stress and reversion stress as a function of test temperature for film H703.

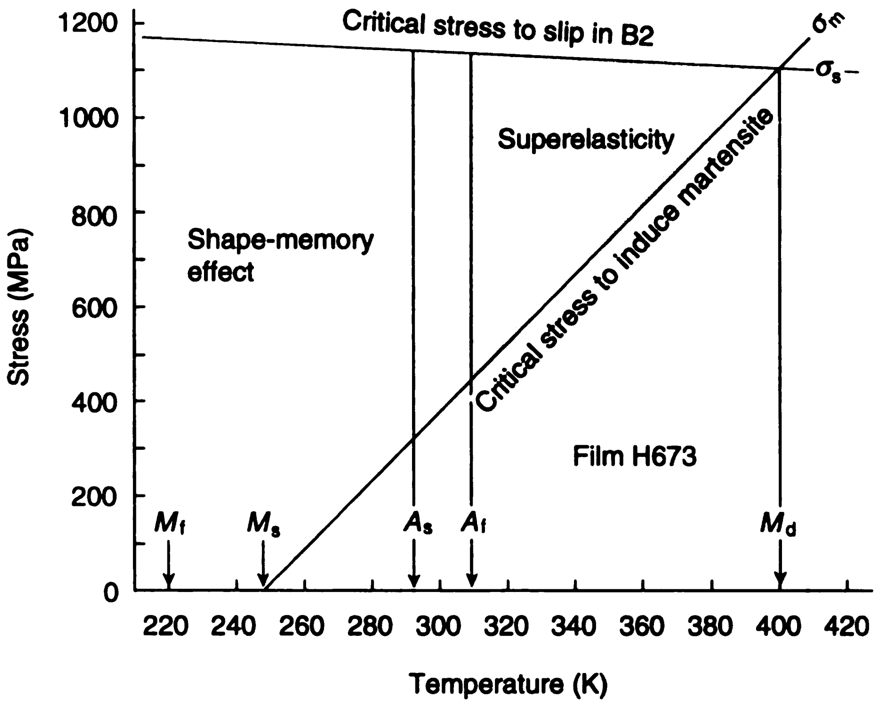

Figure 3-67. Stress-temperature diagram for film H673.

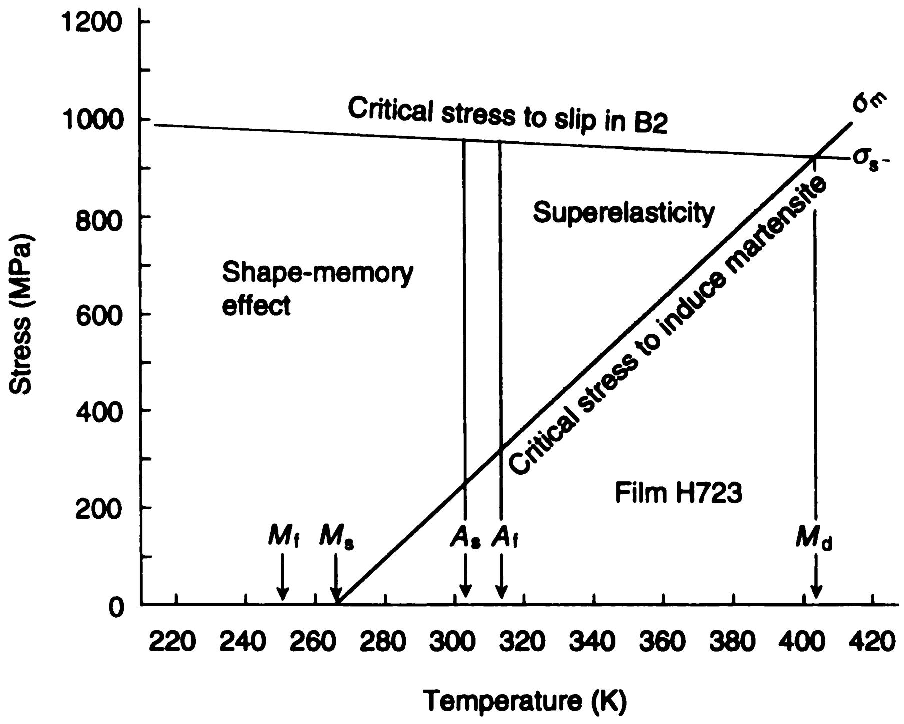

Figure 3-68. Stress-temperature diagram for film H723.

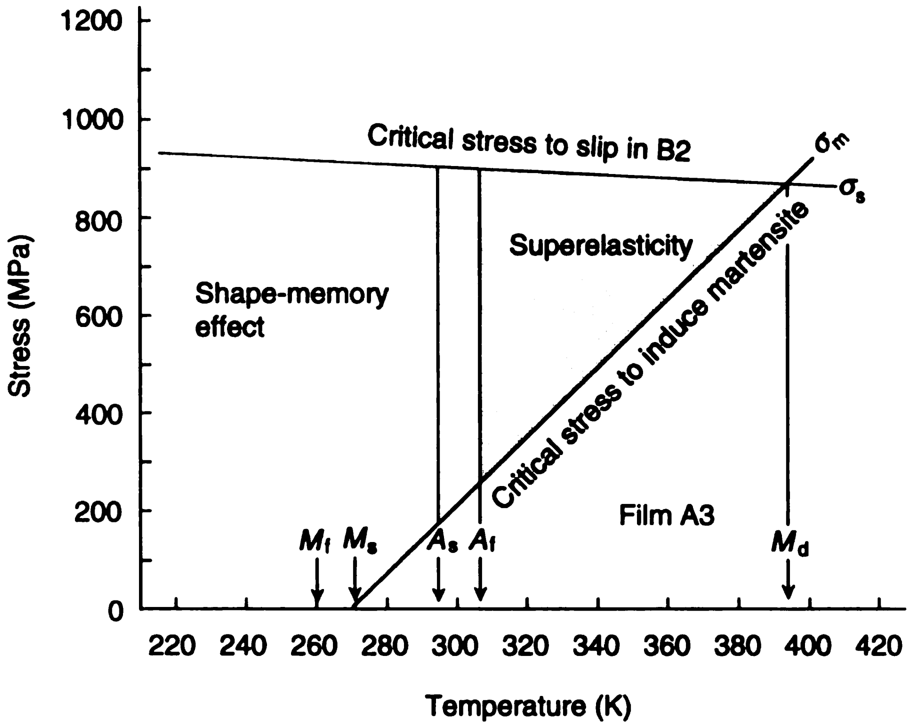

Figure 3-69. Stress-temperature diagram for film A3.

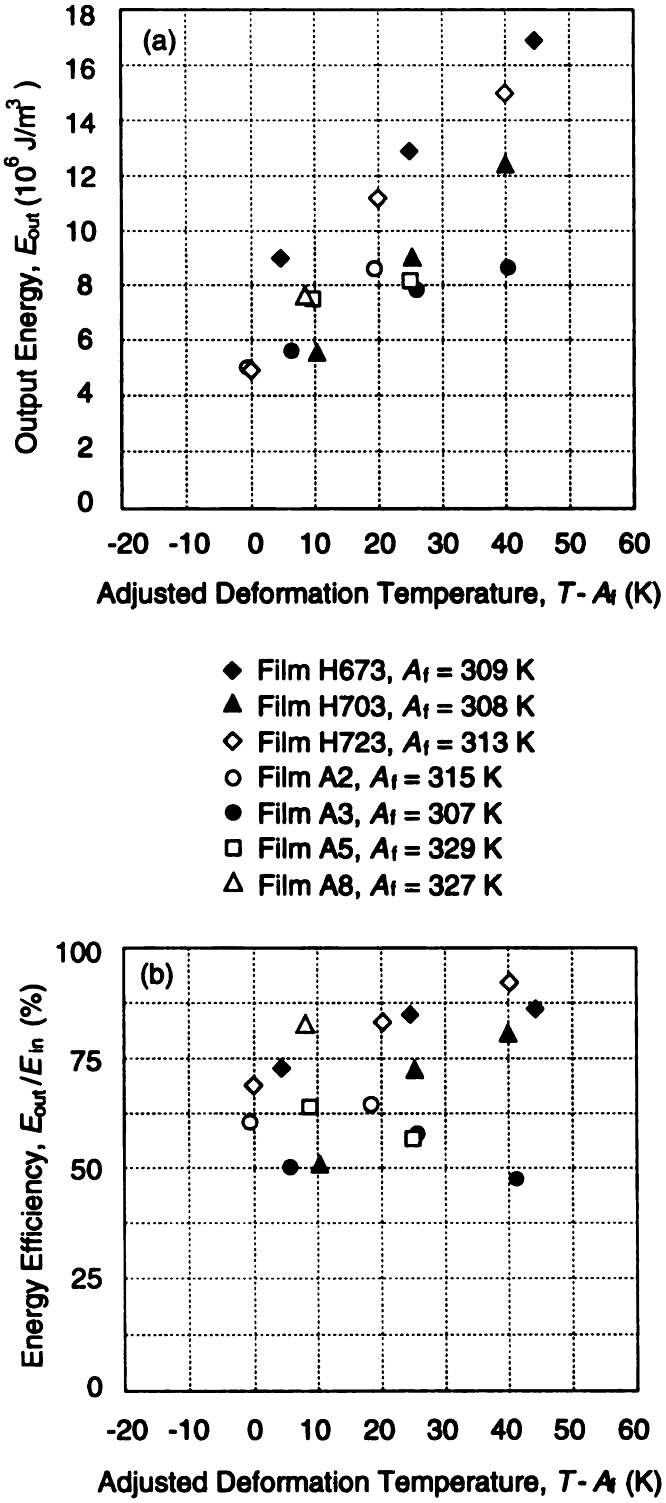

Figure 3-70. (a) Output of mechanical energy vs. adjusted deformation temperature for NiTi films. (b) Energy efficiency vs. adjusted deformation temperature curves.

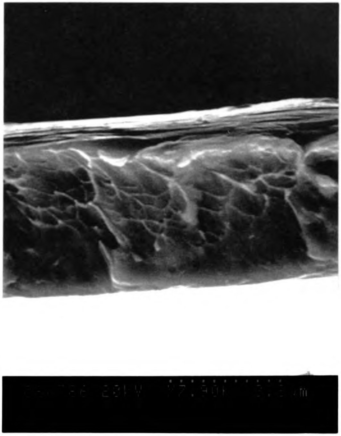

Figure 3-71. SEM image showing the fractography of film H623. The fracture surface consisting of many microdimples exhibits characteristics of mode I (the opening mode) ductile failure. The fracture is a transgranular one since no feature of columnar grain structure can be seen in the fracture surface.

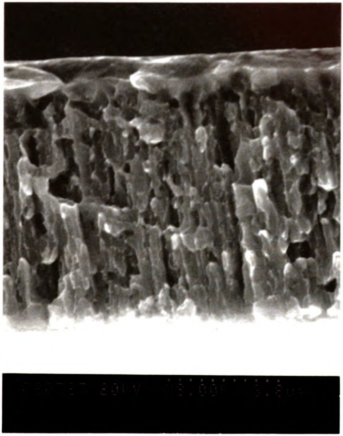

Figure 3-72. SEM image showing the fracture surface of the film H673. The columnar structure is clearly seen and its grain size (abut 0.25 μm) is consistent with that observed by TEM.

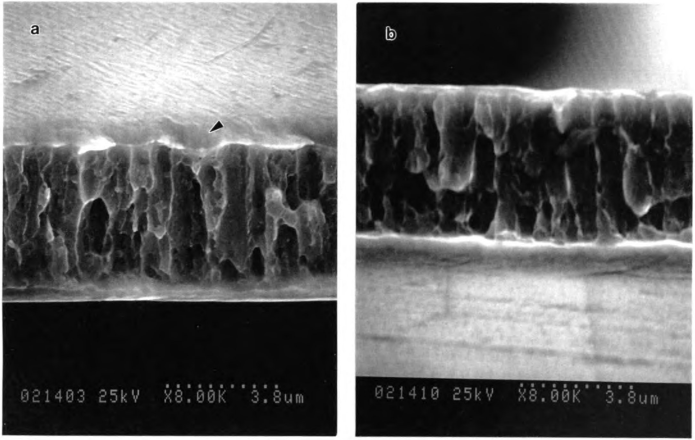

Figure 3-73. SEM images showing the fractography of film H723. (a) is the fracture surface viewed from surface side, and (b) is the fracture surface viewed from substrate side. The external neck area in surface side of the film reveals a serial of valleys as indicated by arrows, but that in substrate side shows even and flat morphology.

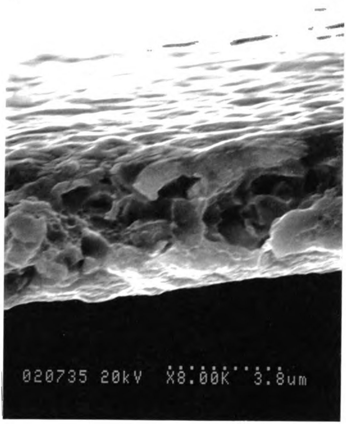

Figure 3-74. SEM image showing the fracture surface of film A3. The fracture is mainly transgrainular type but it is also influenced by equiaxial grain structure which was formed in 858 K, 1 hour annealing (i.e., recrystallization) process.

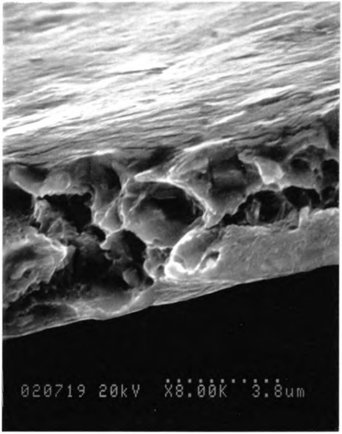

Figure 3-75. The fracture surface of film A5 shows large cup-like feature which is due to a greater grain size. Evidently, the combination of large grains and coarse precipitates posses poor structure stability.

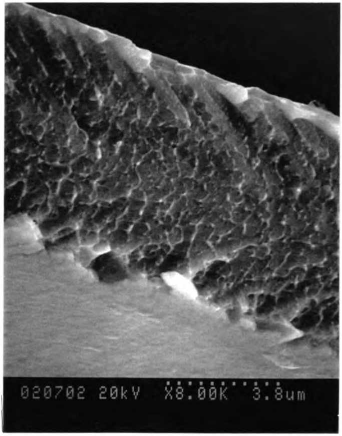

Figure 3-76. The SEM image showing the fracture surface of the film A7. The fractography shows a flat and straight fracture surface with many small dimples. No neck is found in the edge of fracture surface. The free surface of the film is very smooth.

APPENDICES

APPENDICES

A.1. Electrically-Excitable Shape-Memory Actuator

The X-ray diffraction spectrum of NiTi film sputter deposited at 698 K on a 7.6 μm thick Kapton substrate (film H698) shows a fully crystallized NiTi structure (Figure A-1). The recovery temperatures A_s and A_f were 269 K and 293 K respectively which were determined by observing the recovery of a deformed shape during a slow warm up from the liquid nitrogen (LN_2) temperature (104 K). The prototype microactuator displayed an electrical impedance of 30 ohms and was deformed into an approximately 100 μm radius hairpin bend at the LN_2 temperature as shown in Figure A-2a. With the device still immersed in cold nitrogen gas, the application of approximately 3 volts dc induced a rapid and complete recovery of the bending strain as shown in Figure A-2b. The effect was repeatable for a number of cycles, leaving a flat sheet with no evident creasing or delamination.

The NiTi film was also sputtered onto the quartz substrate at a similar temperature of 703 K (film H703). Free-standing NiTi film was prepared for evaluation. The bright-field micrograph and associated SADP of the film H703 shown in Figure 3-15 reveal crystalline B2 grains and transgranular precipitates (the microstructure has been detailed in Section 3.1). A similar bending test was recorded as seen in Figure A-3. A NiTi strap could be sharply bent in near the LN_2 temperature (Figure A-3a). When the LN_2 flask was removed the film restored its original flat shape (Figure A-3b and c).

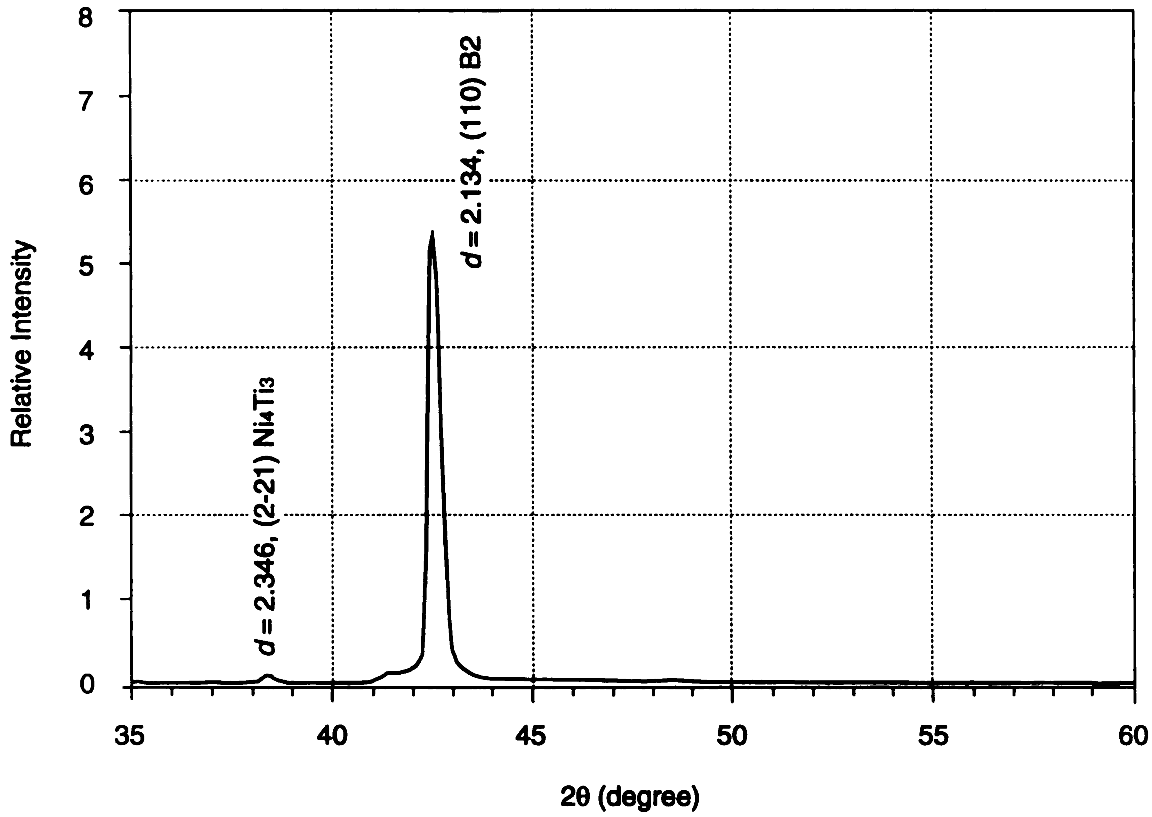

Figure A-1. X-ray diffraction spectra of NiTi film on Kapton substrate sputter deposited at 698 K showing that the NiTi was fully crystallized during the deposition.

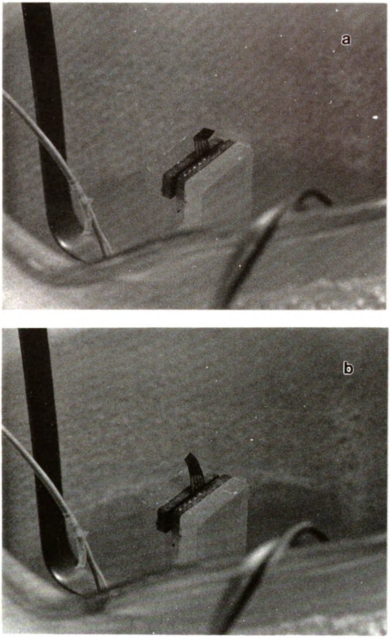

Figure A-2. Photograph demonstrating electrically-excitable NiTi/polyimide actuator. The prototype microactuator displayed an electrical impedance of 30 ohm. (a) The actuator was deformed into an approximately 100 μm radius hairpin bend at the LN_2 temperature. (b) With the device still immersed in cold nitrogen gas, the application of approximately 3 volts dc induced a rapid and complete recovery of the bending strain.

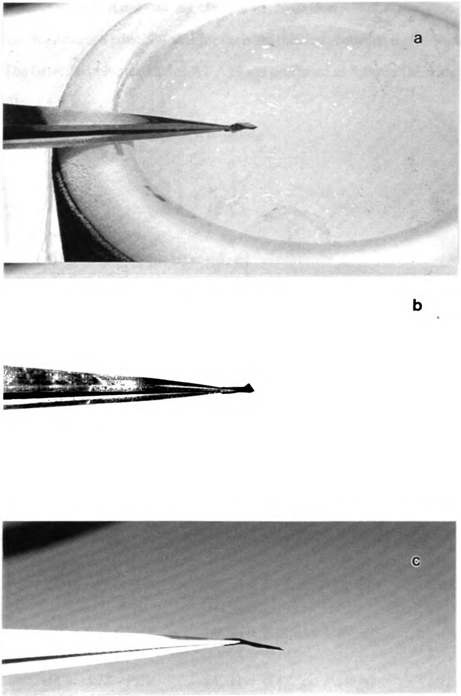

Figure A-3. A series of photographs showing a bending test on a free-standing NiTi strip (film H703). (a) The film could be sharply bent in the LN_2 temperature. (b-c) When the LN_2 flask was removed, the film restored its original flat shape.

A.2. Thermodynamic Analysis by Jacobian Notation

Jacobian notation is a powerful tool for deriving relations between thermodynamic variables. The basic Jacobian equations A1-A19 are presented as follows [Mukherjee and Bieler, 1993]:

Definition and properties of Jacobian notation:

$$\left(\frac{\partial A}{\partial B}\right)_C = \frac{[A,C]}{[B,C]} \tag{A1}$$

$$[A, B] = -[B, A] \tag{A2}$$

$$[A, A] = 0 \tag{A3}$$

$$[A, B]\, dC + [B, C]\, dA + [C, A]\, dB = 0 \tag{A4}$$

$$[A, B]\, [C, x] + [B, C]\, [A, x] + [C, A]\, [B, x] = 0 \tag{A5}$$

$$[A, x] = b\, [B, x] + c\, [C, x] \tag{A6}$$

where $dA = b\, dB + c\, dC$.

Fundamental equations:

$$dU = TdS - PdV \qquad [U, x] = T\,[S, x] - P\,[V, x] \tag{A7}$$

$$dH = TdS + VdP \qquad [H, x] = T\,[S, x] + V\,[P, x] \tag{A8}$$

$$dA = -SdT - PdV \qquad [A, x] = -S\,[T, x] - P\,[V, x] \tag{A9}$$

$$dG = -SdT + VdP \qquad [G, x] = -S\,[T, x] + V\,[P, x] \tag{A10}$$

From Maxwell's equations:

$$[T, S] = [P, V] \tag{A11}$$

If we substitute -*F* for *P* and *V* for *L* in above equations, the relations for *FL*-work can be abtained.

Heat capacities:

$$C_P = T\left(\frac{\partial S}{\partial T}\right)_P = \frac{T[S,P]}{[T,P]} \tag{A12}$$

$$C_V = T\left(\frac{\partial S}{\partial T}\right)_V = \frac{T[S,V]}{[T,V]} \tag{A13}$$

$$C_F = T\left(\frac{\partial S}{\partial T}\right)_F = \frac{T[S,F]}{[T,F]} \tag{A14}$$

$$C_L = T\left(\frac{\partial S}{\partial T}\right)_L = \frac{T[S,L]}{[T,L]} \tag{A15}$$

Volumetric thermal expansion coefficient a:

$$a = \frac{1}{V}\left(\frac{\partial V}{\partial T}\right)_P = \frac{[V,P]}{V[T,P]} \tag{A16}$$

Linear thermal expansion coefficient α:

$$\alpha = \frac{1}{L_0}\left(\frac{\partial L}{\partial T}\right)_F = \frac{[L,F]}{L_0[T,F]} \tag{A17}$$

Isothermal compressibility β:

$$\beta = -\frac{1}{V}\left(\frac{\partial V}{\partial P}\right)_T = -\frac{[V,T]}{V[P,T]} \tag{A18}$$

Adiabatic compressibility β_s:

$$\beta_s = -\frac{1}{V}\left(\frac{\partial V}{\partial P}\right)_s = -\frac{[V,S]}{V[P,S]} \tag{A19}$$

The derivation of Equation 3.3 is shown in the follows. From Equation A1 and A14,

$$\left(\frac{\partial S}{\partial T}\right)_\sigma = \frac{[S,\sigma]}{[T,\sigma]} = \frac{[S,F]}{[T,F]} = \frac{1}{T}\left(\frac{\partial S}{\partial T}\right)_F = \frac{C_F}{T} \tag{A20}$$

$$\left(\frac{\partial \Delta S^{P\rightarrow M}}{\partial T}\right)_\sigma = \frac{\Delta C_F^{P\rightarrow M}}{T} \tag{A21}$$

From Equation A1, A11 and A17,

$$\left(\frac{\partial S}{\partial \sigma}\right)_T = \frac{[S,T]}{[\sigma,T]} = \frac{A[F,L]}{[F,T]} = A\left(\frac{\partial L}{dT}\right)_F = AL_0\alpha = V\alpha \tag{A22}$$

$$\left(\frac{\partial \Delta S^{P\rightarrow M}}{\partial \sigma}\right)_T = V\Delta\alpha^{P\rightarrow M} \tag{A23}$$

Substitute Equation A21 and A23 into Equation 3.2, we obtain the Equation 3.3.

BIBLIOGRAPHY

BIBLIOGRAPHY

Ahmed, N.A.G., *Ion Plating Technology—Development and Applications*, p56, John Wiley & Sons, Ltd., (1987).

Airoldi, G., B. Rivolta and C. Turco, *Proc. Int'l Conf. on Martaensitic Transformations* (ICOMAT- 86), 691 (1986).

Ashby, M.F. and L.M. Brown, *Phil. Mag.*, **8**, 1649 (1963).

Baram, J. and M. Rosen, "Effect of Grain Size on the Acouatic Emission Generated during the Plastic Deformation of Aluminium," *Phil. Mag.*, **A44**, 895 (1981).

Bastin, G.F. and G.D. Rieck, "Diffusion in the Titanium-Nickel System—II. Calculations of Chemical and Intrinsic Coefficients," *Metall. Trans.*, **5**, 1827-1831 (1974).

Bhattacharya, K. and R.V. Kohn, "Symmetry, Texture and the Recoverable Strain of Shape-Memory Polycrystals," *Acta Metall.*, **44**, 529-542 (1996).

Brophy, J.H., R.M. Rose and J. Wulff, *The Structure and Properties of Materials*, Vol. 2. John Wiley & Sons, Inc., New York (1964).

Buckel, W., "Some Remarks on Crystal Growth in Thin Films," *Structure and Properties of Thin Films*, eds. C.A. Neugebauer, J.B. Newkirk and D.A. Vermilyea, John Wiley & Sons, Inc., New York, 53-57 (1959).

Buehler, W.J. and F.E. Wang, "A Summary of Recent Research on the Nitinol Alloys and Their Potential Application in Ocean Engineering," *Ocean Eng.*, **1**, 105-120 (1968).

Bunshah, R.F. in *Deposition Technologies for Films and Coatings*, eds. R.F. Bunshsh, *et al.* Noyes Publications, New Jersey, 139 (1982).

Busch, J.D., A.D. Johnson, C.H. Lee and D.A. Stevenson, "Shape-Memory Properties in Ni-Ti Sputter-Deposited Film," *J. Appl. Phys.*, **68**, 6224-6228 (1990).

Cahn, R.W., "Recovery and Recrystallization," *Physical Metallurgy*, eds. R.W. Cahn and P. Haasen, 1654 (1983).

Chang, F., Unpublished Data, Michigan State University (1998).

Chang, L., C.H. Simpson and D.S. Grummon, *Mat. Res. Soc. Symp. Proc.*, **194**, 301 (1989).

Chang, L., C.H. Simpson, D.S. Grummon, W. Pratt and R. LoLoee, "Structure and Phase Transformation in Thermoelastic $Ni_{(1-x)}TiCu_{(x)}$ Thin Films Prepared by DC Magnetron Sputtering," *Mat. Res. Soc. Symp. Proc.*, **187**, 137-142 (1990).

Chang, L. and D.S. Grummon, "Elevation of Premartensitic Transformation Temperature by $(Ni+Cu)_2Ti$ Precipitation in Sputtered $Ni_{(1-x)}TiCu_{(x)}$ Thin Films," *Scripta Metall.*, **25**, 2079-2084 (1991).

Chang, L. and D.S. Grummon, "Orthorhombic Martensite, Intermetallic Precipitates and Retained Austenite in Ti-Rich Ti(Ni+Cu) Sputtered Thin Films," *Mat. Res. Soc. Symp. Proc.*, **246**, 141-146 (1992).

Chang, L. and D.S. Grummon, "Structure Evolution in Sputtered Thin Films of $Ti_x(Ni, Cu)_{1-x}$—I: Diffusive Transformations," *Phil. Mag.*, **A76**, 163-189 (1997).

Chang, L. and D.S. Grummon, "Phae Transomations in Sputtered Thin Films of $Ti_x(Ni, Cu)_{1-x}$—II: Displacive Transformations," *Phil. Mag.*, **A76**, 191-219 (1997).

Chang, L., "Phase Transformations in Thin Films of TiNi Thermoelastic Alloys," *Ph.D. Thesis*, Michigan State University (1993).

Delaey, L., R.V. Krishnan and H. Tas, Review: "Thermoelasticity, Pseudoelasticity and the Memory Effects Associated with Martensitic Transformations," *J. Mater. Sci.*, **9**, 1521-1535 (1974).

Dodd, B. and Y. Bai, *Ductile Fracture and Ductility*, Academic Press, 1987.

Duerig, T.W. and R. Zadno, "An Engineer's Perspective of Pseudoelasticity," *Engineering Aspects of Shape Memory Alloys*, eds. T.W. Duerig, K.N. Melton, D. Stockel and C.M. Wayman, Butterworth-Heinemann, London, 369-393 (1990).

Du Pont, Product Bulletin, 1993.

Du Pont, Product Bulletin, 1995.

Edmonds, K.R. and C.M. Hwang, "Phase Transformations in Ternary TiNiX Alloys," *Scripta Metall.*, **20**, 733-737 (1986).

Enami, K., V.V. Martynov, T. Tomie, L.G. Khandros and S. Nenno, *Trans. Jap. Inst. Metals.*, **22**, 357 (1981).

Eucken, S. and J. Hirsch, *Mat. Sci. Forum.*, **56-58**, 487 (1990).

Fan, L.S., S.J. Woodman, R.C. Moore, L. Crawforth, T.C. Reiley and M.A. Moser, in *Proc. Solid-State Sensor and Actuator Workshop*, Hilton Head, SC, 38 (1994).

Filip, P. and K. Mazanec, "Influence of Work Hardening and Heat Treatment on the Substructure and Deformation Behaviour of TiNi Shape Memory Alloys," *Scripta Metall.*, **32**, 1375 (1994).

Gil, F.J., J.M. Manero and J.A. Planell, "Effect of Grain Size on the Martensitic Transformation in NiTi Alloy," *J. Mater. Sci.*, **30**, 2526-2530 (1995).

Gilbert, E.N., *Ann. Math. Stat.*, **33**, 958 (1962).

Gilman, J.J., "Deformation of Symmetric Zinc Bicrystals," *Acta Metall.*, **1**, 426-427 (1953).

Gisser, K.R.C., J.D. Busch, A.D. Johnson and A.B. Ellis, "Oriented Nickel-Titanium Shape Memory Alloy Filmsprepared by Annealing During Deposition," *Appl. Phys. Lett.*, **61**, 1632-1634 (1992).

Gokin, K.K., *Shape Memery Alloys*, Gordon and Breach, Science Publishers, 1984.

Goo, E., T. Duerig, K. Melton and R. Sinclair, "Mechanical Twinning in $Ti_{50}Ni_{47}Fe_3$ and $Ti_{49}Ni_{51}$ Alloys," *Acta Metall.*, **33**, 1725 (1985).

Grummon, D.S., L. Hou, Z. Zhao and T.J. Pence, *J. de Physique* **IV**, Colloque C8 665-670 (1995).

Grummon, D.S., S. Nam and L. Chang, "Effect of Superelasticcally Deforming NiTi Surface Microalloys on Fatigue Crack Nucleation in Copper," *Mat. Res. Soc. Symp. Proc.*, **246**, 259-264 (1992).

Guckel, H., T.R. Christenson, T. Earles, J. Klein, J.D. Zook, T. Ohnstein and M. Karnowski, in *Proc. Solid-State Sensor and Actuator Workshop*, Hilton Head, SC, 49 (1994).

Gyobu, A., Y. Kawamura, H. Horikawa and T. Saburi, "Martensitic Transformations in Sputter-Deposited Shape Memory Ti-Ni Films," *Materials Trans.*, Japan Inst. Metals **37**, 697-702 (1996).

Haasters, J., G.V. Salis-Solio and G.Bensmann, "The Use of Ni-Ti as an Implant Material in Orthopedics," *Engineering Aspects of Shape Memory Alloys*, eds. T.W. Duerig, K.N. Melton, D. Stockel and C.M. Wayman, Butterworth-Heinemann, London, 426-444 (1990).

Hale, D.V., M.J. Hoover and M.J. O'Neil, NASA Contractor Rep., CR-61363, 1971

Hall, E.O., *Proc. Phys. Soc.*, **64B**, 747 (1951).

Hasiguchi, R.R. and K. Iwasaki, "Interal Friction and Related Properties of the TiNi Intermetallic Compound," *J. Appl. Phys.*, **39**, 2182-2186 (1968).

Hedayat, A., J. Rechtien and K. Mukherjee, "The Effect of Surface Constraint on the Phase Transformation of Nitinol," *J. Mat. Sci.*, 27, 5306-5314 (1992).

Hehemann, R.F. and G.D. Sandrock, "Relations between the Premartensitic Instability and the Martensite Structure in TiNi," *Scripta Metall.*, **5**, 801-806 (1971).

Heimendahl, M.V., *Electron Microscopy of Materials, An Introduction,* p116, New York, NY. Academic Press, 1980.

Hirsch, P., A. Howie, R. Nicholson, D.W. Pashley and M.J. Whelan, *Electron Microscopy of Thin Crystals*, Krieger Publishing Company, Malabar, Florida (1977).

Hirth, J.P., "The Influence of Grain Bounderies on Mechanical Properties," *Met. Trans.*, **3**, 3047-3067 (1972).

Honeycombe, R.W.K., *The Plastic Deformation of Metals,* William Clowes and Sons, p223, p235 (1968).

Hook, R.E. and J.P. Hirth, "The Deformation Behavior of Non-Isoaxial Bicrystals of Fe-3% Si," *Acta Metall.*, **15**, 535, 1099-1110 (1967).

Hou, L. and D.S. Grummon, "Transformational Superelasticity in Sputtered Titanium-Nickel Thin Films," *Scripta Metall.*, **33**, 989-995 (1995).

Hou, L., T.J. Pence and D.S. Grummon, "Structure and Thermal Stability in Titanium-Nickel Thin Films Sputtered at Elevated Temperature on Organic and Polymeric Substrates," *Mat. Res. Soc. Symp. Proc.*, **360**, 369-374 (1995).

Hua, S.Z., C.M. Su and M. Wuttig, "The Transformation Characteristics in Thin Film SMA Heterostructures," *Mat. Res. Soc. Symp. Proc.*, **308**, 33-37 (1993).

Hwang, C.M., M. Meichle, M.B. Salamon and C.M. Wayman, "Transformation Behaviour of A $Ti_{50}Ni_{47}Fe_3$ Alloys, I. Premartensitic Phenomena and the Incommensurate Phase," *Phil. Mag.*, **A47**, 9-30 (1983).

Hwang, C.M., M. Meichle, M.B. Salamon and C.M. Wayman, "Transformation Behaviour of A $Ti_{50}Ni_{47}Fe_3$ Alloys, II. Subsequent Premartensitic Behaviour and the Commensurate Phase," *Phil. Mag.*, **A47**, 31-62 (1983).

Hwang, C.M., M.B. Salamon and C.M. Wayman, "Transformation Behaviour of A $Ti_{50}Ni_{47}Fe_3$ Alloys, III. Martensitic Transformation," *Phil. Mag.*, **A47**, 177-191 (1983).

Ikuta, K., H. Fujita, M. Ikeda and S. Yamashita, "Crystallographic Analysis of TiNi Shape Memory Alloy Thin Film for Microactuator," *Proc. of IEEE MEMS*, Napa Valley, CA, 38-39 (1990).

Ishida, A., A. Takei and S. Miyazaki, "Shape memory Thin Film of Ti-Ni Formed by Sputtering," *Thin Solid Films*, **228**, 210-214 (1993).

Ishida, A., A. Takei, M. Sato and S. Miyazaki, "Shape Memory Behavior of Ti-Ni Thin Films Annealed at Various Temperatures," *Mat. Res. Soc. Symp. Proc.*, **360**, 381-386 (1995).

Ishida, A., M. Sato, A. Takei, Y. Kase and S. Miyazaki, "Effect of Heat Treatment on Shape Memory Behavior of Ti-Ni Thin Films," *J. de Physique Colloque,* **C8**, 701-705 (1995).

Ishida, A., M. Sato, A. Takei, K. Nomura and S. Miyazaki, "Effect of Aging on Shape Memory Behavior of Ti-51.3 at. pct Ni Thin Films." *Metall. Mater. Trans.*, **27A**, 3753-3759 (1996).

Jardine, A.P., "Cycling Times of Thin-Film NiTi on Si," *Mat. Res. Soc. Symp. Proc.*, **246**, 427-431 (1992).

Jean, R., and J. Duh, "The Thermal Cycling Effect on Ti-Ni-Cu Shape Memory Alloy," *Scripta Metall.*, **32**, 885-890 (1995).

Johnson, A.D., "Vacuum-Deposited TiNi Shape Memory Film: Characterization and

Applications in Microdevices," *J. Micromech. Microeng.*, **1**, 34-41 (1991).

Johnson, A.D., J.D. Busch, C.A. Ray and C.L. Sloan, *Mat. Res. Soc. Symp. Proc.*, **276**, 151 (1992).

Johnson, W.A. and R.F. Mehl, "Reaction Kinetics in Processes of Nucleation and Growth," *Trans. Am. Inst. Min. Engrs.*, **135**, 416-458 (1939).

Johnson, A.D., V.V. Martynov and R.S. Minners, Sputter deposition of high transition temperature in Ti-Ni-Hf alloy thin films, Abstracts of Proc. ICOMAT, Lausanne, Switzerland (1995).

Kainuma, R. and M. Matsumoto, "Shape Memory Effect by Diffusional Transformation in Ti-52% Ni Alloy," *Scripta Metall.*, **22**, 457-478 (1988).

Kessler, H. and W. Pitsch, "On the Nature of the Martensite to Austenite Reverse Transformatiom," *Acta Metall.*, **15**, 401-405 (1967).

Kim, J.J., P. Moine and D.A. Stevenson, "Crystallization Behavior of Amorphous Ni-Ti Alloys Prepared by Sputter Deposition," *Scripta Metall.*, **20**, 243-248 (1986).

Kim, Y.D. and C.M. Wayman, "Shape Recovery and Phase Transformation Behavior in Ni-Al Alloys," *Metall Trans.*, **23A**, 2981-2986 (1992).

Kim, T., Q. Su and M. Wuttig, "Thermo-Mechanical $Ni_{50}Ti_{50}$/Si Composite Thin Film Switch," *Mat. Res. Soc. Symp. Proc.*, **360**, 375-380 (1995).

Knowles, K.M. and D.A. Smith, "The Crystallography of the Martensitic Transformation in Equiatomic Nickel-Titanium," *Acta Metall.*, **29**, 101 (1981).

Kocks, U.F., "Polyslip in Polycrystals," *Acta Metall.*, **6**, 85-94 (1958).

Kocks, U.F., "The Relation between Polycrystal Deformation and Single-Crystal Deformation," *Met. Trans.*, **1**, 1121-1143 (1970).

Koskimaki, D., M.J. Marcinkowki and A.S. Sastri, *Trans. Amer. Inst. Min. Engrs.*, **245**, 1883 (1969).

Krulevitch, P., A.P. Lee, P.B. Ramsey, J.C. Trevino, J. Hamilton and M.A. Northrup, "Thin Film Shape Memory Alloy Microactuators," *J. Microelectromech. Sys.*, **5**, 270-282 (1996).

Krulevitch, P., P.B. Ramsey, D.M. Makowiecki, A.P. Lee, M.A. Northrup and G.C. Johnson, "Mixed-Sputter Deposition of Ni-Ti-Cu Shape Memory Films," *Thin Solid Films*, **274**, 101-105 (1996).

Kudoh, Y., M. Tokonami, S. Miyazaki and K. Otsuka, "Crystal Structure of the Martensite in Ti-49.2 at.% Ni Alloy Analyzed by the Single Crystal X-Ray Diffraction Method, *Acta Metall.*, **33**, 2049 (1985).

Kuribayashi, K., T. Taniguchi, M. Yositake and S. Ogawa, "Reversible SMA Actuator for Microsized Robot," *Proc. IEEE of MEMS, An Investigation of Micro Structures, Sensers, Actuators, Machines and Robots*, 217-221 (1990).

Kurt J. Lesker Company, Technical Tables, Vacuum Product, 1993.

Li, D.Y. and L.Q. Chen, "Selective Variant Growth of Coherent $Ti_{11}Ni_{14}$ Precipitate in A TiNi Alloy under Applied Stresses," *Acta Mater*, **45**, 471-479 (1997).

Li, D.Y. and J.A. Szpunar, "The Slip System in Ordered Tini Alloy," *J. Mater. Sci. Lett.*, **11**, 510-511 (1992).

Lieberman, D.S., M.S. wechsler and T.A. Read, "Cubic to Orthorhombic Diffusionless Phase Change—Experimental and Theoretical Studies of AuCd," *J. appl. Phys.*, **26**, 473 (1955).

Lin, H.C., S.K. Wu, T.S. Chou and H.P. Kao, "The Effects of Cold Rolling on the Martensitic Transformation of an Equiatomic TiNi Alloy," *Acta Metall.*, **39**, 2069-2080 (1991).

Ling, H.C. and R. Kaplow, "Macroscopic Length Changes during the B2 ↔ R and M → B2 Transitions in Equiatomic Ni-Ti Alloys," *Metall. Trans.*, **11A**, 77 (1981).

Ling, H.C. And R. Kaplow, "Stress-Induced Shape Changes and Shape Memory in the R and Martensite Transformations in Equiatomic NiTi," *Metall. Trans.*, **12A**, 2101 (1981).

Livingston, J.D. and B. Chalmers, "Multiple Slip in Bicrystal Deformation," *Acta Metall.*, **5**, 322-327 (1957).

Loloee, R., Private communication, (1995).

Mader, S., A.S. Nowick and H. Widmer, "Metastable Evaporated Thin Films of Cu-Ag and Co-Au Alloys, I. Occurrence and morphology of Phase," *Acta Metall.*, **15**, 203-214 (1967).

Madsen, J.S. and A.P. Jardine, "The Effect of Cold-Working on the Crystallization Temperature of Thin-Film Shape Memory TiNi," *Mat. Res. Soc. Symp. Proc.*, **308**, 45-49 (1993).

Mahin, K.W., K. Hanson and J.W. Morris, Jr, "Comparative Analysis of the Cellular and Johnson-Mehl Microstructures Through Computer Simulation," *Acta Metall.*, **28**, 443-453 (1980).

Martin, J.W., *Micromechanisms in Particle-Hardened Alloys*, Cambridge University Press, 1980.

Massalski, T.B., *Binary Alloy Phase Diagrams*, American Metals Society, Metals Park, Vol. 2, 1768 (1987).

Matsumoto, O., S. Miyazaki, K. Otsuka and H. Tamura, "Crystallography of Martensitic Transformation in Ti-Ni Single Crystals," *Acta Metall.*, **35**, 2137 (1987).

Melton, K.N., "Ni-Ti Based Shape Memory Alloys," *Engineering Aspects of Shape Memory Alloys*, eds. T.W. Duerig, K.N. Melton, D. Stockel and C.M. Wayman, Butterworth-Heinemann, London, 21-35 (1990).

Meyers, M.A. and K.K. Chawla, *Mechanical Metallurgy*, Prentice-Hall, Inc., 1984.

Michal, G.M. and R. Sinclair, *Acta Cryst.*, **B37**, 1803 (1981).

Mises, R.Von, *Z. Ang. Math. Mech.*, **8**, 161 (1928),

Miyazaki, S., T. Hashinaga, K. Yumikura, H. Horikawa, T. Ueki and A. Ishida, "Shape Memory Characteristics of Sputter-Deposited Ti-Ni-Base Thin Films," *Smart Mater.*, SPIE **2441**, 156-164 (1995).

Miyazaki, S., Y. Igo and K. Otsuka, "Effect of Thermal Cycling on the Transformation Temperatures of Ti-Ni Alloys," *Acta Metall.*, **34**, 2045-2051 (1986).

Miyazaki, S., T. Imai, Y. Igo and K. Otsuka, "Effect on Cyclic Deformation on the Psedoelasticity Characteristics of Ti-Ni Alloys," *Metal. Trans.*, **17A**, 115-120 (1986).

Miyazaki, S., S. Kimura and K. Otsuka, "Shape-Memory Effect and Pseudoelasticity Associated with the R-Phase Transition in Ti-50.5 at.% Ni Single Crystals," *Phil. Mag.*, **A57**, 467-478 (1988).

Miyazaki, S., S. Kimura, K. Otsuka and Y. Suzuki, "The Habit Plane and Transformation Strains Associated with the Martensitic Transformation in Ti-Ni Single Crystals," *Scripta Metall.*, **18**, 883-888 (1984).

Miyazaki, S., S. Kimura, F.S. Takei, T. Miura, K. Otsuka and Y. Suzuki, "Shape Memory Effect and Pseudoelasticity in a Ti-Ni Single Crystal," *Scripta Metall.*, **17**, 1057 (1983).

Miyazaki, S., Y. Kohiyama and K. Otsuka, "Plastic Deformation of Ti-Ni Alloys," *Proc. Inter. Symp. on Intermetallic Compounds, Structure and Mechanical Properties*, Sendai, Japan, JIM, 691-695 (1991).

Miyazaki, S., O. Matsumoto, K. Otsuka and Y. Suzuki, *Abstract Bulletin, 95th Meeting of the Japan Institute of Metals*, Hiroshima, Japan, 143 (1983).

Miyazaki, S. and K. Nomura, "Development of Perfect Shape Memory Effect in Sputter-Deposited Ti-Ni Thin Films," Proc. MEMS-94, Oiso, Japan, 176-181 (1994).

Miyazaki, S., K. Nomura and H. Zhirong, "Shape Memory Effect and Superelasticty Developed in Sputter-Deposited Ti-Ni Thin Films," *Proc. SMST*, Pacific Grove, California, USA, 19-24 (1994).

Miyazaki, S., Y. Ohmi, K. Otsuka and Y. Suzuki, "Characteristics of Deformation and Transformation Pseudoelasticity in Ti-Ni Alloys," *J. de Physique Colloque*, **C4**, 255-260 (1982).

Miyazaki, S. and K. Otsuka, "Deformation and Transition Behavior Associated with the R-Phase in Ti-Ni Alloys," *Metall. Trans.*, **A17**, 53-63 (1986).

Miyazaki, S. and K. Otsuka, "Mechanical Behaviour Associated with the Premartensitic Rhombohedral-Phase Transition in a $Ti_{50}Ni_{47}Fe_3$ Alloy," *Phil. Mag.*, **A50**, 393-408 (1988).

Miyazaki, S., K. Otsuka and Y. Suzuki, "Transformation Pseudelasticity and Deformation Behavior in a Ti-50.6 (at.%) Ni Alloy," *Scripta Metall.*, **15**, 287-292 (1981).

Miyazaki, S., K. Otsuka and C.M. Wayman, "The Shape Memory Mechanism Associated with the Martensitic Transformation in Ti-Ni Alloys—I. Self-Accommodation," *Acta Metall.*, **37**, 1873 (1989).

Miyazaki, S., K. Otsuka and C.M. Wayman, "The Shape Memory Mechanism Associated with the Martensitic Transformation in Ti-Ni Alloys—II. Variant Coalescence and Shape Recovery," *Acta Metall.*, **37**, 1885 (1989).

Miyazaki, S., K. Shibata and H. Fujita, "Effect of Specimen Thickness on Mechanical Properties of Polycrystalline Aggregates with Various Grain Sizes," *Acta Metall.*, **27**, 855-862 (1979).

Miyazaki, S., Sugaya, Y. and K. Otuska, *MRS International Meeting on Advanced Materials*, **9**, 251 (1989).

Miyazaki, S. and C.M. Wayman, "The R-phase Transition and Associated Shape Memory Mechanism in Ti-Ni Single Crystals," *Acta Metall.*, **36**, 181-192 (1988).

Moberly, W.J., J.D. Busch, A.D. Johnson and M.H. Berkson, "*In situ* HVEM of Crystallization of Amorphous TiNi Thin Films," *Mat. Res. Soc. Symp. Proc.*, **230**, 85-90 (1992).

Moberly, W.J., J.L. Proft, T.W. Duerig and R. Sinclair, "Deformation, Twinning and Thermo-Mechanical Strengthening of $Ti_{50}Ni_{47}Fe_3$," *Acta Metall.*, **38**, 2601-2612 (1990).

Mori, H. and H. Fujita, in *Proc. of Yamada Conf. 9 on Dislocations in Solids*, Japan, 1984.

Motohashi, Y. K. Ohsawa, T. Hoshiya, Y. Okamoto and M. Ohmori, "Grain Refinement of a Ti-Ni Shape Memory Alloy and its Influence on Phase Transformation Characteristics," *J. Jpn. Inst. Met.*, **55**,132-140 (1991).

Movchan, B.A. and A.V. Demchishin, *Phys. Met. Metallogr.*, **28**, 83 (1969).

Mukherjee, K., and T. Bieler, Notes of the course MSM 851: *Thermodynamics of Materials*, fall 1993, instructor T. Bieler, Michigan State University.

Mukherjee, K., S. Sircar and N.B. Dahotre, "Thermal Effects Associated with Stress-Induced Martensitic Transformation in a Ti-Ni Alloy," *Mater. Sci. Eng.*, **74**, 75-84 (1985).

Murr, L.E., "Some Observations of Grain Boundary Ledges and Ledges as Dislocation Sources in Metals and Alloys," *Met. Trans.*, **6A**, 505-515 (1975).

Nam, S., "Effect of Ion-Sputtered Thermoelastic NiTi Coatings on Fatigue Crack Initiation in Copper," *Ph.D. Thesis*, Michigan State University (1995).

Neugebauer, C.A., "Tensile Preperties of Thin, Evaporated Gold Films," *J. Appl. Phys.*, **31**, 1096-1101 (1960).

Nevitt, M.V., *Trans. AIME*, **218**, 327 (1980).

Nishida, M. and T. Honma, "All-Round Shape Memory Effect in Ni-Rich TiNi Alloys Generated by Constrained Aging," *Scripta Metall.*, **18**, 1293-1298 (1984).

Nishida, M. and C.M. Wayman, "Phase Transformations in Ti_2Ni_3 Precipitates Formed in Aged Ti-52 at. pct Ni," *Met. Trans.*, **18A**, 785-799 (1987).

Nishida, M. and C.M. wayman, "Electron Microscopy Studies of Precipitation Processes in Near-Equiatomic TiNi Shape Memory Alloys," *Mater. Sci. Eng.*, **93**, 191-203 (1987).

Nishida, M., C.M. Wayman and T. Honma, "Electron Microscopy Studies of the All-Round Shape Memory Effect in a Ti-51.0 (at.%) Ni Alloys," *Scripta Metall.*, **18**, 1389-1394 (1984).

Nishida, M., C.M. Wayman and T. Honma, "Precipitation Processes in Near-Equiatomic TiNi Shape Memory Alloys," *Metall. Trans.*, **A17**, 1505-1515 (1986).

Nishida, M., C.M. Wayman, R. Kainuma and T. Honma, "Further Electron Microscopy Studies of The $Ti_{11}Ni_{14}$ Phase in an aged Ti-52 at.% Ni Shape Memory Alloy," *Scripta Metall.*, **20**, 899-904 (1986).

Nomura, K. and S. Miyazaki, "The Stability of Shape Memory Characteristics against Cyclic Deformation in Ti-Ni Sputter-Deposited Thin Films," *Smart Mater.*, SPIE **2441**, 149-155 (1995).

Orowan, E., *Symposium on Internal Stresses in Metals*, Institute of Metals, London, p451, 1948.

Ortin, J. and A. Planes, "Thermodynamic Analysis of Thermal Measurements in Thermoelastic Martensitic Transformations," *Acta Metall.*, **36**, 1873-1889 (1988).

Ortin, J. and A. Planes, "Thermodynamic and Hysteresis Behaviour of Thermoelastic Martensitic Transformations," *Journal de Physique* IV, **C4**, 13-23 (1991).

Otsuka, K., T. Sawamura and K. Shimizu, "Crystal Structure and Internal Defects of Equiatomic TiNi Martensite," *Physica Status Solidi*, **5**, 457-470 (1971).

Otsuka, K. and K. Shimizu, "On the Crystallographic Reversibility of Martensitic Transformations," *Scripta Metall.*, **11**, 757 (1977).

Otsuka, K. and K. Shimizu, "Pseudoelasticity and Shape Memory Effects in Alloys," *International Metals Reviews*, **31**, 93-114 (1986).

Otsuka, K., C.M. Wayman, K. Nakai, H. Sakamoto and K. Shimizu, "Superelasticity Effects and Stress-Induced Martensitic Transformations in Cu-Al-Ni Alloys," *Acta Metall.*, **24**, 207-226 (1976).

Palmer, J.E., Thompson, C.V. and H.I. Smith, "Grain Growth and Grain Size Distributions in Thin Germanium Films," *J. Appl. Phys.*, **62**, 2492-2497 (1987).

Pence, T.J. and Y. Ivshin, "Building Proper Behavior into Mathematical Models for Shape Memory Alloys," SPIE Proc. *Mathematics and Control in Smart Structures*, ed. H.T. Banks, Vol. 2192 (1994).

Perkins, J., *The Principles of Chemical Equilibrium*, p197-203, Cambridge University Press (1966).

Petch, N.J., *J. Iron Steel Inst.*, **173**, 25 (1953).

Philip, T.V. and P.A. Beck, "CsCl-Type Ordered Structures in Binary Alloys of Transition Elements," *Trans. Am. Inst. Min. Engrs.*, **209**, 1269-1271 (1957).

Quandt, E., C. Halene, H. Holleck, K. Feit, M. Kohl and P. Schlobmacher, "Sputter Deposition of TiNi and TiNiPd Films Displaying the Two Way Shape Memory Effect," *Proc. 8th Int. Conf. on Solid-State Sensors and Actuators, and Eurosensors IX*, Stockholm, Sweden, June 25-29, 202-205 (1995).

Robinson, C., "Shape Memory Alloys Find Expanding Applications," *InTech*, **March**, 55-58 (1987).

Ray, C.A., C.L. Sloan, A.D. Johnson, J.D. Busch and B.R. Petty, *Mat. Res. Soc. Symp. Proc.*, **276**, 161 (1992).

Reed-Hill, R.E., *Physical Metallurgy Principles*, ed. W.W. Hagerty, D. Van Nostrand Company, Inc., p250, p404, 1964.

Robbins, W.P., D.L. Polla, T. Tamagawa, D.E. Glumac and J.W. Judy, in *Int.Conf. Solid-State Sensor and Actuator Transducers* '91, San Francisco, CA, 55 (1991).

Saburi, T. and S. Nenno, *Proc. Int. Conf. on Solid-Solid Phase Transformations*, eds H.I. Aaronson, D.E. Laughlin, R.F. Sekerka and C.M. Wayman, The Metallurgical Society of AIME, Pittsburgh, p1455 (1981).

Saburi, T., S. Nenno and T. Fukuda, "Crystal Structure and Morphology of the Metastable X phase in Shape Memory Ti-Ni Alloys," *J. Less Common Met.*, **125**, 157-166 (1986).

Saburi, T., T. Tatsumi and S. Nenno, "Effects of Heat Treatment on Mechanical Behavior of Ti-Ni Alloys," *J. de Physique Colloque*, **C4**, 261-266 (1982).

Saburi, T., M. Yoshida and S. Nenno, "Deformation Behavior of Shape Memory Ti-Ni Alloy Crystals," *Scripta Metall.*, **18**, 363-366 (1984).

Salzbrenner, R.J. and M. Cohen, "On the Thermodynamics of Thermoelastion Martensitic Transformations," *Acta Metall.*, **27**, 739-748 (1979).

Schmid, E. and W. Boas, *Plasticity of Crystals*, Hughes (1950).

Schroeder, T.A., and C.M. Wayman, *Scripta Metall.*, **11**, 225 (1977).

Shaw, J.A. and S. Kyriakides, "Thermomechanical Aspects of NiTi," *J. Mech. Phys. Solids.*, **43**, 1243-1281 (1995).

Shugo, Y., S. Hanada and T. Honma, *Bull. Res. Inst. Min. Met.*, **41**, 23 (1985).

Smidth, F.A., "Use of Ion Beam Assisted Deposition to Modify the Micro-Structure and Properties of Thin Films," *International Materials Reviews,* **35**, 61-128 (1990).

Smith, C.S. ASM Seminar, *Metal Interfaces*, 65 (1952).

Smith, M.C., *Principles of Physical Metallurgy*, Harper & Brothers, 191, (1956).

Srolovitz, D.J., "Grain Growth Phenomena in Films: A Monte Carlo Approach," *J. Vac. Sci. Technol.*, **A4**, 2925 (1986).

Stachowiak, G.B. and P.G. McCormick, "Shape Memory Behaviour Associated with the R and Martensiyic Transformations in a NiTi Alloy," *Acta Metall.*, **36**, 291-297 (1988).

Swalin, R.A., *Thermodynamics of Solid*, p88 (1961).

Tang, L. and G. Thomas, "Microstructure and Texture Evolution of Cr Thin Films with Thickness," *J. Appl. Phys.*, **74**, 5025-5032 (1993).

Taylor, A. and R.W. Floyd, *J. Inst. Metals.*, **80**, 577-587 (1952).

Taylor, G.I., *J. Inst. Metals.*, **62**, 307 (1938).

Thompson, C.V., "Grain growth in Thin Films," *Ann. Rev. Mater. Sci.*, **20**, 245-268 (1990).

Thompson, C.V., "Grain Growth in Polycrystalline Thin Films," *Mat. Res. Soc. Symp. Proc.*, **343**, 3-12 (1994).

Thompson, C.V. and H.I. Smith, *Appl. Phys. Lett.*, "Surface-Energy-Driven Secondary Grain Growth in Ultrathin (< 100 nm) Films of Silicon," **44**, 603-605 (1984).

Thornton, J.A., *J. Vac. Sci. Technol.*, **11**, 666 (1974).

Thornton, J.A., "High Rate Thick Film Growth," *Ann. Rev. Mater. Sci.*, **7**, 239-260 (1977).

Thornton, J.A., in *Deposition Technologies for Films and Coatings,* eds. R.F. Bunshsh, *et al.* Noyes Publications, New Jersey, 190 (1982).

Tjhen, W., T. Tamagawa, C.P. Ye, C.C. Hsueh, P. Schiller and D.L. Polla, in *Proc. IEEE Conf. Micro Electro Mechanical Systems*, MEMS 1991, Nara, Japan, 114 (1991).

Tong, H.C. and C.M. Wayman, "Characteristic Temperatures and Other Properties of Thermoelastic Martensites," *Acta Metall.*, **22**, 887-896 (1974).

Van Humbeeck, J., R. Stalmans, M. Chandrasekaran and L. Delaey, "On the Stability of Shape Memory Alloys," *Engineering Aspects of Shape Memory Alloys* eds T.W. Duerig, K.N. Melton, D. Stockel and C.M. Wayman, Butterworth-Heinemann, London, 96 (1990).

Van Loo, F.J.J., G.F. Bastin and A.J.H. Leenen, "Phase Relations in the Ternary Ti-Ni-Cu System at 800 and 870°C," *J. Less Common Met.*, **57**, 111-121 (1978).

Walker, J.A., K.J. Gabrieland and M. Mehregany, *Sensor and Actuators*, **A21**, 24 (1990).

Walles, B., L. Chang and D.S. Grummon, "Residual Stress, Adhesion and Crystallization of Ion-Sputtered and IBED Processed NiTi films," *Mat. Res. Soc. Symp. Proc.*, **246**, 349-354 (1992).

Wang, F.E., W.J. Buehler and S.J. Pichart, "Crystal Structure and a Unique 'martensitic' Trandformation of TiNi," *J. Appl. Phys.*, **36**, 3232-3239 (1965).

Wasilewski, R.J., S.R. Butler, J.E. Hanlon and D. Worden, *Metall. Trans.*, **2**, 229 (1971).

Wayman, C.M., "Phase Transformations, Nondiffusive," *Physical Metallurgy*, eds. R.W. Cahn and P. Haasen, 1032-1074 (1983).

Wayman, C.M. and H.C. Tong, "On the Equilibrium Temperature in Thermoelastic Martensitic Transformations," *Scripta Metall.*, **11**, 341-343 (1977).

Wolf, R.H. and A.H. Heuer, "*TiNi (Shape Memory) films on Silicon for MEMS Applications*", J. Microelectromechanical Systems, **4**, 206-212 (1995).

Wollants, P., J.R. Roos and L. Delaey, "On the Stress-Dependence of the Latent Heat of Transformation as Related to the Efficiency of a Work Performing Cycle of a Memory Engine," *Scripta Metall.*, **14**, 1217-1223 (1980).

Wollants, P., J.R. Roos and L. Delaey, "Thermally- and Stress-Induced Thermoelastic Martensitic Transformations in the Reference Frame of Equilibrium Thermodynamics," *Progress in Materials Science*, **37**, 227 (1993).

Wollants, P., M. DeBonte and J.R. Roos, *Z. Metallkd.*, **70**, 113 (1979).

Wong, C.C., H.I. Smith and C.V. Thompson, "Surface-Energy-Driven Secondary Grain Growth in Thin Au Films," *Appl. Phys. Lett.*, **48**, 335-337 (1986).

Wu, S.K., H.C. Lin and T.S. Chou, "Transformation Temperatures of Martensite and Premartensite in an Aged $Ti_{49}Ni_{51}$ Alloy," *Scripta Metall.*, **23**, 2043-2048 (1989).

Wu, S.K., H.C. Lin and T.S. Chou, "A Study of Electrical Resistivity, Internal Friction and Shear Modulus on an Aged $Ti_{49}Ni_{51}$ Alloy," *Acta Metall.*, **38**, 95-102 (1990).

Xie, C.Y., L.C. Zhaoand and T.C. Lei, "Effect of Precipitates on the Electrical Resistivity-Temperature Curves in an Aged Ti-51.8 at.% Ni Shape Memory Alloy," **23**, 2131-2136 (1989).

Zadno, G.R. and T.W. Duerig, "Linear Superelasticity in Cold-Worked Ni-Ti," *Engineering Aspects of Shape Memory Alloys*, eds. T.W. Duerig, K.N. Melton, D. and C.M. Wayman, Butterworth-Heinemann, London, 414-419 (1990).

Zdeblick, M.J., R. Anderson, J. Jankowski, B. Kline-Schoder, L.Christel, R. Miles and W. Weber, in *Proc. Solid-State Sensor and Actuator Workshop*, Hilton Head, SC, 251 (1994).

Zhang, J., D.S. Grummon, "Stress Evolution during Crystallization and Isothermal Annealing of Titanium-Nickel on (100) Si," *Mat. Res. Soc. Symp. Proc.*, Y, Advanced Materials for Smart Systems, Boston MA, **459**, 451-457 (1997).

Zhang, J., "Stresses and Stress Relaxation during Annealing and Phase Transformation of NiTi Films on Si," *Master's Thesis*, Michigan State University (1998).

Zhao, Z, "Development of Stress in NiTi Thin Films," *Master's Thesis*, Michigan State University (1996).